Structure of Superdeformed Bands in Cerium and Neodymium Isotopes involving Neutron $i_{13/2}$ (N=6) Intruder States

Thesis submitted in accordance with the requirements of
the University of Liverpool for the degree of Doctor in Philosophy

by

David Thomas Joss

Oliver Lodge Laboratory

January 1998

What curious eye doth quote deformities ?

Mercutio, [Romeo and Juliet, I.iv]

William Shakespeare

This thesis is dedicated to my Mum and Dad.

Abstract

The quadrupole moments Q_t of five superdeformed bands in ^{131,132}Ce have been established using the Doppler shift attenuation method; for the first time, we can compare the relative deformations of yrast and excited bands in neighbouring nuclei to an accuracy of $\approx$(5-7)%. Four of five bands have very similar deformations, while the excited band in ^{131}Ce has a somewhat larger quadrupole moment. Important new information is presented on the shape-driving force of the $\nu i_{13/2}$ orbital, the relative deformation of rotational bands, the nature of sidefeeding and the time-scale of the decay mechanism.

The Doppler shift attenuation method has been used to determine the transition lifetimes of a triaxial band belonging to the γ-soft nucleus, ^{133}Ce. Doppler broadened lineshape (DBLS) analysis has revealed the magnitude of the Q_t value to be approximately 2.4 eb. This work provides new information of (i) the lifetimes of in-band and sidefeeding transitions, (ii) the transition quadrupole moment of this band and, (iii) the relative deformations of coexisting nuclear shapes. The results are discussed in terms of calculations based on the total Routhian surface (TRS) formalism.

High-spin states have been studied in neutron deficient ^{132}Nd, produced in the ^{105}Pd(^{35}Cl, $x\alpha$, yp, zn) reaction, using the GAMMASPHERE γ-ray spectrometer in conjunction with the MICROBALL charged particle detector array. Three new, weakly populated rotational bands have been found, which are believed to be associated with a superdeformed prolate shape. Comparison of the properties of these bands with Woods-Saxon cranking calculations suggests that they are built upon negative-parity configurations that involve only one intruder orbital ($\nu i_{13/2}$) from the N=6 shell. One of the bands has been linked into the normally deformed states allowing an estimation of the spin, parity and excitation energy of the band.

Acknowledgements

This work would not have been possible without the contribution and support of many people. It is difficult to thank so many is so few words and I fear that these short citations understate my considerable appreciation of all who have contributed in some way. Please accept my apologies if I have missed you out.

- Profs P.J. Twin and E. Gabathuler for allowing the opportunity to pursue research in the Department of Physics at the University of Liverpool.
- Dr. Paul Nolan for accepting me into his research group and for his patient supervision and guidance in the course of this work.
- Dr. Eddie Paul for his invaluable interest in this work, in particular for guiding me through my misconceptions and for many informative discussions. Special thanks are extended to Eddie for reading through this entire work and being so thorough and helpful with his comments.
- Dr. J.R. Cresswell, J. Sampson, L. Pratt, J. Hønsi and more recently Dr. I.M. Hibbert for their help in rescuing me from an assortment of my computing catastrophe's.
- Dr. Dave Cullen for reading the theory and spectroscopy chapters in this thesis and offering advice regarding corrections.
- The GAMMASPHERE group and crew of the 88-Inch cyclotron at Berkeley for keeping beam on target for all the experiments that I have attended.
- Drs. Barna Nyakó, Janos Timár, Laszlo Zolnai and the Debrecen group for their unparalled hospitality during the *Exotic Nuclear Shapes 97* conference.
- The postgraduate CASE studentship provided by EPSRC in conjunction with Gresham Lion Technology Ltd is gratefully acknowledged.
- I would like to thank the nuclear structure group (both past and present) for their enthusiasm and assistance over the years. In particular I would like to thank Dr. Sally Forbes, Dr. Adrian Semple, Andrew Boston and Sarah Shepherd (the A$\sim$130 group) for helping things run smoothly and night shifts pass quickly. Thanks also to my fellow finalists Duncan Appelbe, Kev Cann, Sefa Ertürk and Roger Allatt. I am indebted to Anna Wilson for the many trips hunting for books thoughout Liverpool and John Smith for bits of advice and encouragement.
- Special thanks to my friends for their wit, wisdom and support particularly Duncan Appelbe, Nyree Beeston, Martin Rothery, Sarah Walton and Yvonne Windsor. I would also like to acknowledge the many friends I have made during my time as a tutor at Carnatic, especially Carl Davis for his encouragement and unrelenting inspiration.

Introduction

This thesis documents two experiments in which the GAMMASPHERE γ-ray spectrometer array was used to study the deformation and structure of nuclei in the A$\approx$132 region. In this mass region superdeformed structures are expected to be stabilised by the direct interplay of quantal shell structure and collective rotation. In particular, high-j neutron states originating from the N=6 oscillator shell are predicted to breach the Fermi surface at low rotational frequencies due to the spin-orbit interaction, strengthening the stability of the superdeformed second minimum.

The purpose of this work is to elucidate the structure of superdeformed nuclei believed to involve the N=6 $\nu i_{13/2}$ intruder states by analysing the characteristic rotational γ-ray cascades that are emitted as the highly deformed nucleus dissipates angular momentum.

The first study addresses the role of the $\nu i_{13/2}$ $[660]1/2^+$ intruder orbitals in the isotopes, ^{131,132}Ce. Cranked shell model calculations predict numerous bands based upon particle-hole excitations at the Fermi surface, yet experiment has yielded only two bands in ^{131}Ce and three bands in ^{132}Ce. Experimental evidence based upon the variation of the dynamic moment of inertia with rotational frequency, has suggested that the yrast structures in ^{131}Ce and ^{132}Ce are built on configurations involving one or both of the $\nu i_{13/2}$ $[660]1/2^+$ states. The yrast bands are also predicted to have different deformations attributed to the different neutron intruder configurations. Since the core polarising effects of successively occupying the $\nu i_{13/2}$ neutrons was expected to enhance nuclear deformation, structures based upon single particle excitations might also possess varying degrees of prolate deformation. An experiment was proposed to measure the lifetimes and relative deformations of all five bands under the same experimental conditions with a view to determining the deformation driving role of configurations involving the N=6 neutron states and providing more definite information on the configurations upon which the bands are built. Using the present generation of highly efficient γ-ray spectrometers, it has also been possible to determine the role of unknown sidefeeding transitions and assess their contribution to the deformation properties of the yrast bands. Furthermore, a triaxial band in ^{133}Ce that was once believed to possess a configuration involving a single $\nu i_{13/2}$ orbital was populated in the same experiment as the ^{131,132}Ce bands. Nuclei involving 73 or 75 neutrons are known to be shape-sensitive to the position of the Fermi surface in a high-j sub-shell. An investigation has been performed

to measure the lifetimes and deformation of this triaxial structure and estimate the relative deformations of coexisting nuclear shapes.

The second experiment details the results from an experiment that aimed to study the global deformation properties of the A≈135 region. The reaction ^{105}Pd(^{35}Cl, $x\alpha, yp, zn$) was used to populate high-spin states in praseodymium, neodymium, samarium and promethium nuclei. The MICROBALL charged particle detector array was used to select the various reaction channels and this work documents the results of the analysis of the $\alpha p3n$ channel leading to ^{132}Nd. The neodymium isotopes are predicted to have similar superdeformed structures to the nearby cerium isotopes involving the $\nu i_{13/2}$ intruder states. With decreasing neutron number it becomes energetically favourable to occupy N=5 valence states rather than the second $\nu i_{13/2}$ intruder state. The observation of superdeformed bands in ^{132}Nd and investigation into their properties provides a valuable opportunity to investigate the role of the $\nu i_{13/2}$ neutron intruder orbitals in the stabilising large quadrupole deformations. Furthermore, in many neodymium isotopes linking transitions between the superdeformed and normally deformed states have been observed. Since linking transitions have been found in ^{132}Nd it is possible to suggest possible decay mechanisms and gain valuable insight into the role of specific neutron configurations in stabilising the superdeformed minimum.

The unifying theme between the experimental studies detailed in this thesis is the shape driving role of the $\nu i_{13/2}$ $[660]1/2^+$ states and the various orbitals in the immediate vicinity of the Fermi surface at high spin. Both studies rely on comparison with theoretical models in two regimes; deformation and rotation. The relevant ideas regarding the origins of deformation and electromagnetic nuclear properties that reflect the highly deformed character of certain nuclei are addressed in Chapter 1. The work documented in this thesis is performed at high-spin and so Chapter 2 is devoted entirely to rotation. The studies reported here have only been possible because of major advances in the development of techniques and apparatus over recent years. Chapter 3 is dedicated to the major tools of current γ-ray spectroscopy. The results, analysis and discussions are treated in a self-contained manner in Chapters 4 and 5. The relative deformation measurements in ^{131,132,133}Ce are documented in Chapter 4, and the observation of multiple superdeformed bands in ^{132}Nd is contained within Chapter 5.

Part of this work has been published in [Cla96] and [Jos96].

Contents

Chapter 1

Nuclear Models

In order to understand the structure of the nucleus one must provide a framework with which one can discuss the experimental results. This chapter reviews the development of nuclear models. It starts from the liquid drop and nuclear shell models and describes the necessity and nature of corrections which have to be applied to the models in order to reproduce experimental results.

1.1 The Liquid Drop Model

The liquid drop model was historically the first nuclear model. It is derived from analogies between global nuclear properties and the properties of atomic molecules in a liquid drop. The main success of the model is that it can describe the saturation property of the nuclear force which is extremely short range and therefore, only affects nearest neighbours within the nucleus. The analogy between the nucleus and a liquid drop also extends to describe properties such as low nuclear compressibility and the variation of binding energy per nucleon.

The variation of nuclear binding energy as a function of mass is described by the semi-empirical Bethe-Weizsäcker formula. This formula is derived from considering the nucleus as a charged spherical liquid drop. The formula is stated as

$$BE(A,Z) = a_v A - a_s A^{2/3} - a_c Z(Z-1)A^{-1/3} - a_A(A-2Z)^2 A^{-1} \pm \delta A. \qquad (1.1)$$

The volume term ($a_v A$) expresses the fact that the nuclear force is saturated and so nucleons within the nuclear volume will contribute to the binding energy. This term overestimates the binding energy and the other terms in Eq. 1.1 are required. The volume term does not account for the fact that nucleons at or near to the surface have fewer nearer neighbours and therefore, the surface term ($-a_s A^{2/3}$) provides a reduction proportional to the nuclear surface area. The Coulomb term $-a_c Z(Z-1)A^{-1/3}$ compensates for proton-proton repulsion within the nuclear volume. The protons electromagnetically repel each other and therefore, reduce the binding energy.

The classical liquid drop model requires two further modifications to reproduce the experimental variation of binding energy. The asymmetry term, $-a_A(A-2Z)^2 A^{-1}$ is added to account for the fact that nuclei with N=Z are more stable than nuclei where N > Z. Also, the effect of pairing interactions is accounted for by the pairing term which is positive for even-even nuclei, zero for odd-even nuclei, and negative for odd-odd nuclei.

1.2 The Nuclear Shell Model and the Many-Body Problem

Although the liquid drop model is successful in describing certain bulk properties of the nucleus it is clear that microscopic single-particle effects cannot be ignored. This can be

seen by the necessity of introducing the symmetry and pairing corrections into Eq. 1.1 in order to make the formula consistent with experimental data. There are a number of features that cannot be described by collective models and imply that the nucleus possesses shell structure. For example, it is found that the proton and neutron separation energies are larger at certain 'magic' numbers. The separation energy is analogous to the ionization energy of atomic electrons that are bound in the Coulomb potential of the nucleus. The separation energy is roughly constant around 8 MeV although certain values are noticeably larger at magic and doubly-magic numbers. Also, the excitation energies of the first $I^{\pi}=2^{+}$ state of magic and doubly magic nuclei are distinctly larger than that of their neighbours which indicate an enhanced stability against excitations.

Although it is useful to compare many similar features of the nuclear and atomic shell models, it is obvious that there is a fundamental difference. The atomic electrons move in a central potential generated by an attractive Coulomb force between the electrons and the nucleus, whereas nucleons do not move in such a central potential. It is assumed that each nucleon moves independently in an average potential that is formed by the interactions of all the other nucleons in the nucleus. This mean field approximation allows the many-bodied nuclear problem to be reduced to a two-body problem which is solvable. If the interaction potential between two nucleons, i and j, is $v(r_{ij})$ then the average potential acting on each particle is given by

$$V_i(r_i) = \langle \sum_j v(r_{i,j}) \rangle. \tag{1.2}$$

Consequently the expression for the nuclear Hamiltonian H becomes

$$H = \sum_i T_i + \sum_{ij} v(r_{i,j}). \tag{1.3}$$

Eq. 1.3 can be written as

$$H' = \sum_i [T_i + V_i(r_i)] + \lambda \left[\sum_{ij} v(r_{i,j}) - \sum_i V_i(r_i) \right] \tag{1.4}$$

The second term is a perturbation due to the effect of residual interactions and H' is the perturbed Hamiltonian. For $\lambda = 1$, $H' = H$. The assumption made in the shell model is that $\lambda \rightarrow 1$ since this allows for the fact that the central potential is much greater that residual interactions.

The solutions to the Schrödinger equation using an appropriate potential, yield the energy eigenvalues of the single-particle orbits. The solution to the nuclear many-body problem is extremely complicated and it is difficult to define a total wavefunction microscopically. It is necessary to adjust the form of the potential term in the Schrödinger equation to obtain a realistic model that will describe the observed features of the nucleus. The simplest starting point is the harmonic oscillator potential.

1.2.1 The Harmonic Oscillator Potential

The advantage of the harmonic oscillator potential is that it is possible to solve the Schrödinger equation and obtain single-particle eigenfunctions analytically. The harmonic oscillator potential can be expressed as

$$V_{HO} = -V + \frac{1}{2}m\omega^2 r^2 \tag{1.5}$$

where V is the depth of the potential, m is the particle mass, r is the radius and ω is the frequency of the simple harmonic motion of the particle. The nuclear Hamiltonian can be written as

$$H = \frac{-\hbar^2}{2m}\nabla^2 - V + \frac{1}{2}m\omega^2 r^2. \tag{1.6}$$

The solution of the Schrödinger equation gives the energy eigenvalues

$$E_N = \left[N + \frac{3}{2}\right]\hbar\omega \tag{1.7}$$

where N denotes the principal quantum number.

Successive N shells are evenly spaced and for each N value there are a degenerate group of levels with different angular momentum quantum numbers, ℓ. Each oscillator shell contains states with the same parity, so that

$$\pi = (-1)^N = (-1)^\ell \tag{1.8}$$

Each N level is (N+1)(N+2) degenerate and states are grouped so that

$$\ell = N, \quad N-2, \quad N-4 \ldots \tag{1.9}$$

For example, the N=4 shell will contain degenerate states with ℓ=4, 2, and 0 corresponding to the 1g, 2d, and 3s subshells. The simple harmonic oscillator potential is an unrealistic potential, since the form of the oscillator term in Eq. 1.5 implies that nucleons at the surface

of the nucleus should experience a larger potential than nucleons deep within the core which is clearly untrue. The nuclear potential should be realistic enough to replicate experimentally observed characteristics, however this potential does not reproduce the experimental magic numbers.

1.2.2 The Woods-Saxon Potential

It is clear that the harmonic oscillator represents an unphysical potential since V(r) $\rightarrow \infty$ as r becomes large. The Woods-Saxon potential [WS54] describes a finite potential where $V(r) \rightarrow 0$ when $r > R_0$, i.e.

$$V_{WS}(r) = \frac{-V_0}{1 + exp\left[\frac{r-R_0}{a}\right]}. \tag{1.10}$$

The Woods-Saxon shape is compared with the harmonic oscillator in Fig. 1.1. It is clearly seen that the Woods-Saxon shape well reproduces the flat bottomed potential. This is clearly an advantageous description since nucleons at the centre of the nucleus feel the nuclear forces uniformly and there is no net force ($\frac{\partial V}{\partial r} = 0$). Eq. 1.10 includes a surface diffuseness term, a, to allow for the fact that the nucleus does not have a sharply defined boundary. The radius term, R_0 is equal to the product, $r_0 A^{1/3}$ with $r_0 = 1.2$ fm. The depth of the potential, V_0, can be adjusted to suit experimental measured quantities (usually V_0 $\approx$ 50 MeV).

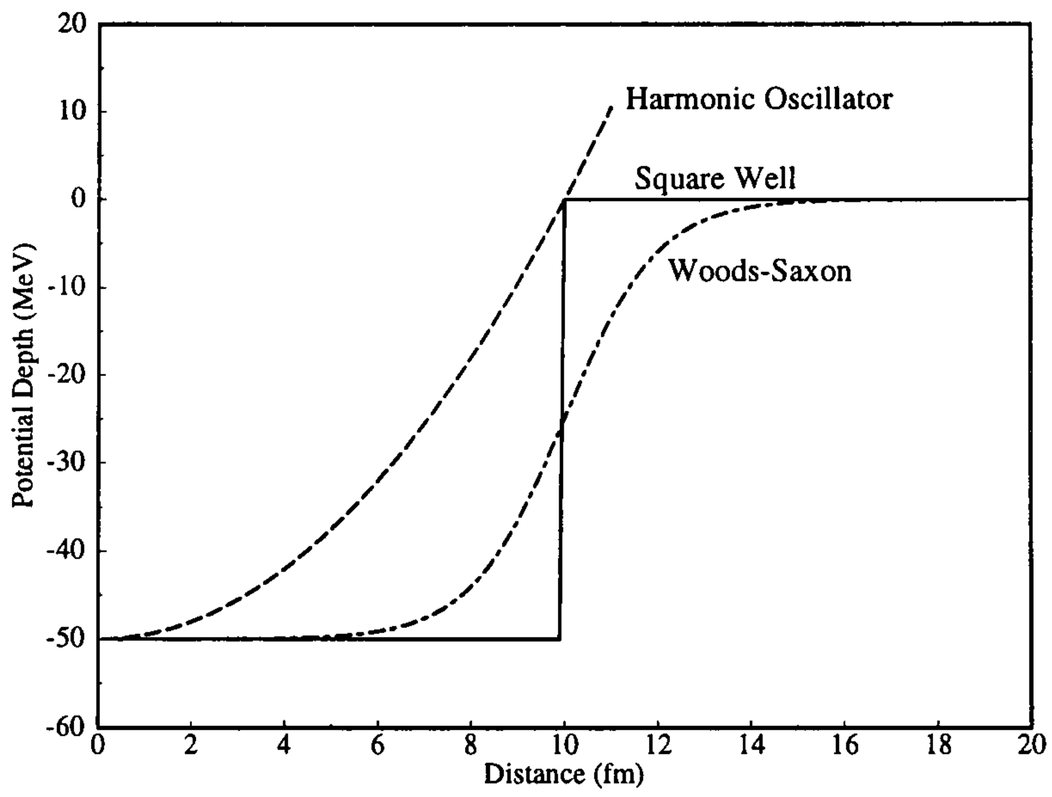

Figure 1.1: Comparison of harmonic oscillator and Woods-Saxon potentials. The square well potential is also added for comparison.

The nuclear Hamiltonian can be rewritten using the Woods-Saxon potential as

$$H_{WS} = \frac{-\hbar}{2m}\nabla^2 + \frac{-V_0}{1 + exp\left[\frac{r-R_0}{a}\right]} \tag{1.11}$$

The Woods-Saxon parameterisation relieves the degeneracy of the harmonic oscillator states, however the magic numbers are still not reproduced correctly.

1.2.3 Spin-Orbit Coupling

A further correction to the nuclear Hamiltonian to reproduce the correct magic numbers is drawn from analogy with atomic physics. A spin-dependent force may be introduced into the Hamiltonian to account for the coupling of the nucleon's intrinsic spin to its orbital angular momentum. The nuclear spin-orbit term was proposed in [Hax49] and [May49] and has the form

$$V_{SO} = -f(r)\ \ell.\mathbf{s}; \quad f(r) \propto \frac{1}{r}\frac{\partial V(r)}{\partial r}, \tag{1.12}$$

where $f(r)$ controls the strength of the coupling. The total angular momentum, $\mathbf{j}$, is defined as the vector sum of the nucleon's orbital angular momentum, ℓ and its intrinsic spin, $\mathbf{s}$. This is displayed in Fig. 1.2. It can be seen that ℓ and $\mathbf{s}$ precess around $\mathbf{j}$, whilst $\mathbf{j}$ precesses about the symmetry axis. The projections of ℓ and $\mathbf{s}$ on the rotation axis (ℓ_x and $\mathbf{s}_x$) are not constants of motion although $\mathbf{j}_x$ remains constant. The spin-orbit coupling relieves the degeneracy of the Woods-Saxon states, by splitting each $\mathbf{j}$-state into two levels with $\mathbf{j} = \ell \pm 1/2$. The spin-orbit interaction must be an attractive force to allow for the observation that $\mathbf{j} = \ell + 1/2$ states have lower lying energies than the $\mathbf{j} = \ell - 1/2$ states, contrary to the atomic case.

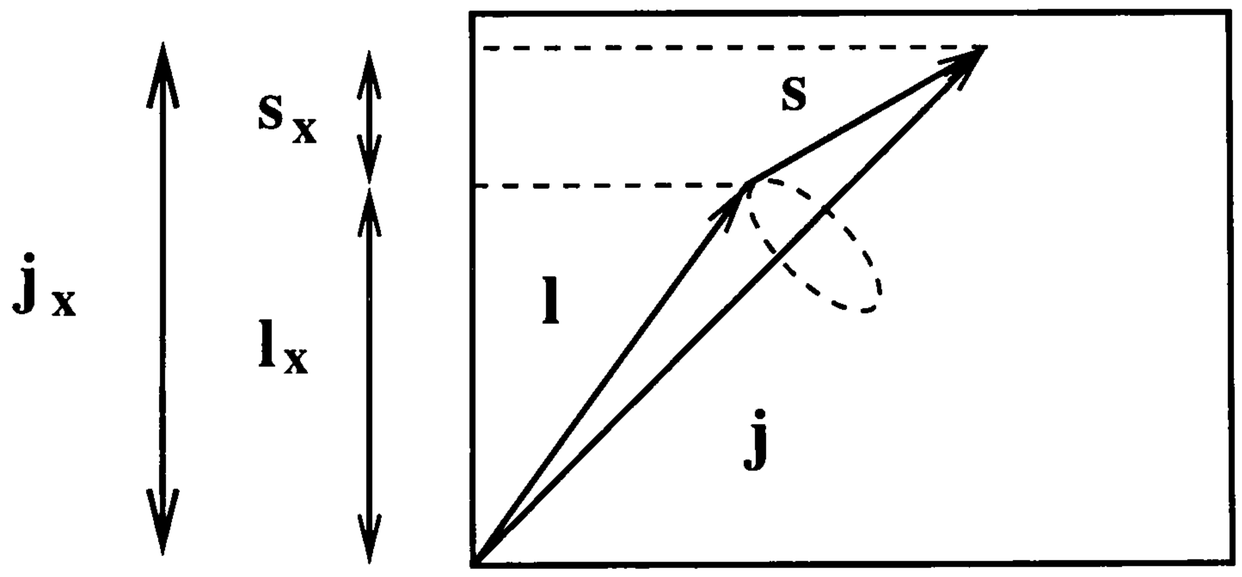

Figure 1.2: $\ell.s$ coupling, components on the rotational axis are shown.

The nuclear Hamiltonian including the spin-orbit term can be written as

$$H = T + V_{WS} + V_{SO}, \tag{1.13}$$

$$H = \frac{-\hbar}{2m}\nabla^2 + \frac{-V_0}{1 + exp\left[\frac{r-R_0}{a}\right]} - f(r)\ \ell.\mathbf{s}. \tag{1.14}$$

It can been seen from Eq. 1.14 that the spin-orbit term is proportional to ℓ. High-j (j=ℓ+s) states for which the spin-orbit interaction is sufficiently large may be depressed in energy so that they 'intrude' on the next lowest major oscillator shell. Such depressed states are called unnatural parity or intruder states and are particularly important in the large-deformation / high-angular-momentum regime.

1.3 Deformation Parameters and Nuclear Shapes

For magic nuclei, the individual orbitals are oriented equally in all directions and the nucleus is spherical. The orbits of individual particles in partially filled shells (j>1/2) are strongly anisotropic and the mean field deviates from sphericity. The resultant nuclear shape is created by the interplay of the deformation driving effects of individual nucleons and the residual pairing interactions between nucleons. Deformation arises when a number of anisotropic orbitals act coherently and if sufficiently many particles behave collectively, the nucleus favours an ellipsoidal shape.

Nuclear deformation is conveniently characterised by describing the nuclear surface in terms of a radius vector defined in spherical harmonics from the centre of the nucleus to its surface;

$$R(\theta,\phi) = R_0\left(1 + \alpha_{0,0} + \sum_{\lambda=1}^{\infty}\sum_{\mu=-\lambda}^{\lambda}\alpha_{\lambda,\mu}Y_{\lambda,\mu}(\theta,\phi)\right), \tag{1.15}$$

where R_0 is the radius of a sphere that would contain the same volume as the ellipsoid and $\alpha_{0,0}$ is introduced to conserve volume. The terms, $\alpha_{\lambda,\mu}$ describe changes in nuclear volume, with λ defining the deformation type. In this study quadrupole deformation ($\lambda = 2$) is especially important. Quadrupole shapes are parameterised by the coefficients

$$\alpha_{2,2} \quad \alpha_{2,1} \quad \alpha_{2,0} \quad \alpha_{2,-1} \quad \alpha_{2,-2} \tag{1.16}$$

For axially symmetric shapes, the $\alpha_{\lambda,\mu}$ coefficients are constrained such that;

$$\alpha_{2,2} = \alpha_{2,-2}; \qquad \alpha_{2,1} = \alpha_{2,-1} = 0. \tag{1.17}$$

The $\alpha_{2,2}$, and $\alpha_{2,0}$ coefficients together with the three Euler angles that govern the transformation to the intrinsic frame completely define the nuclear shape.

In the intrinsic frame, $\alpha_{2,2}$, and $\alpha_{2,0}$ can be expressed in an alternative parameterisation using the polar coordinates β and γ through the relations

$$\alpha_{2,2} = \frac{1}{\sqrt{2}}\beta_2 \sin\gamma, \tag{1.18}$$

$$\alpha_{2,0} = \beta_2 \cos\gamma, \tag{1.19}$$

such that

$$\sum_{\mu} |\alpha_{2,\mu}|^2 = \beta_2^2. \tag{1.20}$$

The quadrupole deformation parameter, β_2, describes the RMS deviation of the nuclear surface from a sphere of radius, R_0, while the triaxiality parameter, γ, describes how the deviation is distributed over the surface. The new parameterisation of the nuclear shape in terms of β_2 and γ is given by;

$$R(\theta,\phi) = R_0\left(1 + \sqrt{\frac{5}{16\pi}}\beta_2 \cos\gamma(3\cos^2\theta - 1) + \sqrt{3}\sin\gamma\sin^2\theta\cos 2\phi\right). \tag{1.21}$$

The usual definition of parameters defining quadrupole shapes is the Lund Convention [And76]. The definition of the β_2 and γ coordinates and the shapes they represent is displayed in Fig. 1.3.

The triaxiality of any quadrupole deformed shape is adequately defined by the sector spanning $-60° \leq \gamma \leq 0°$. If rotations are considered, this range must be extended three-fold in order to specify rotations about the three principal axes.

The collective regime is defined as the range encompassing $-60° \leq \gamma \leq 0°$, while single-particle motion is described by $\gamma = 60°$ and $-120°$ where rotation and symmetry axes coincide.

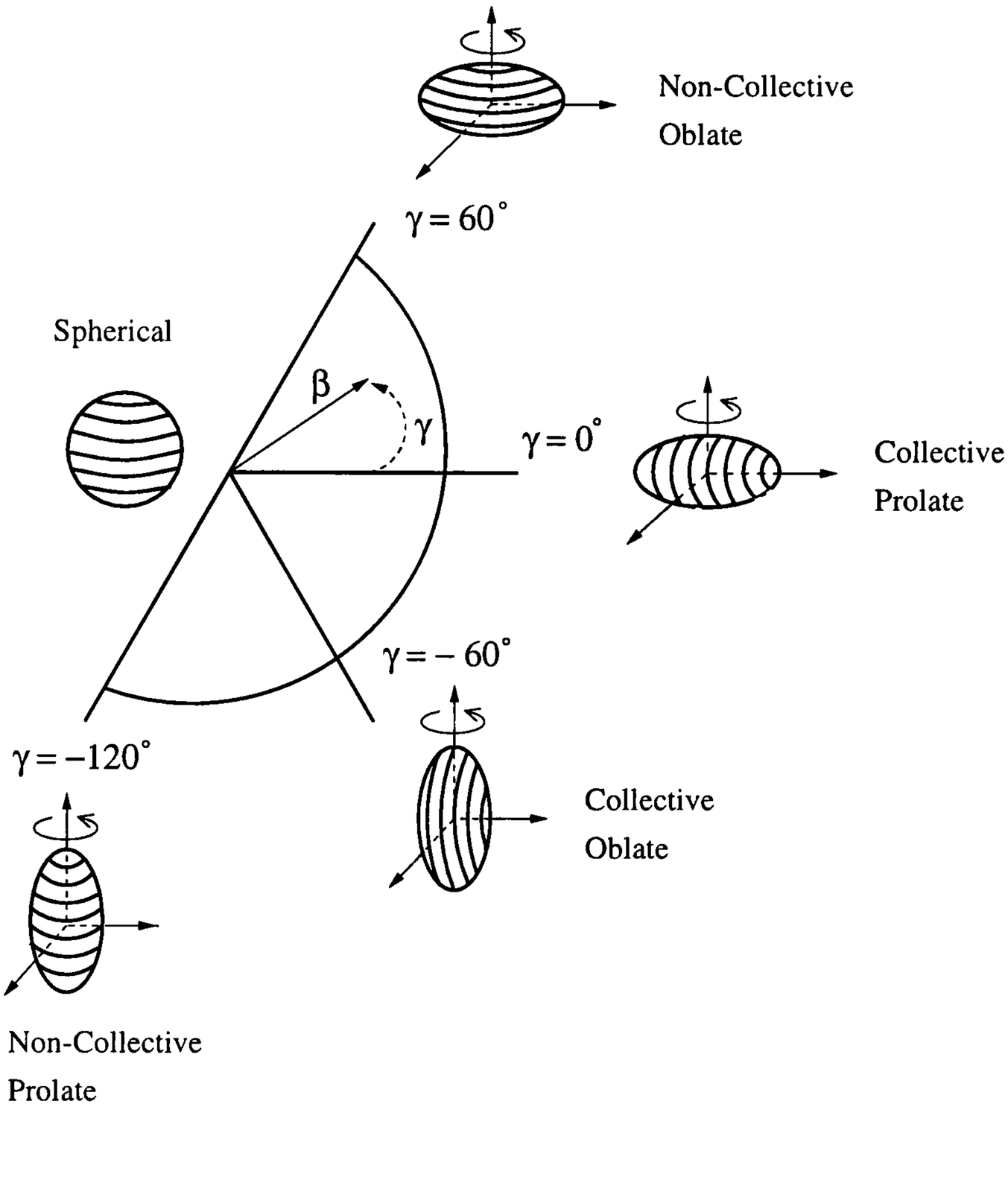

Figure 1.3: The Lund Convention for describing quadrupole shapes.

1.4 The Deformed Shell Model

The central theme of the shell model is that nucleons move independently in orbits that are contained by a spherical potential which is generated by the interactions of all the other nucleons. This is true for nuclei in the vicinity of the magic numbers, however, there is experimental evidence to suggest that a spherical potential does not adequately describe many nuclei. For example, it is known that nuclei with partially filled shells possess very large quadrupole moments which implies that nucleons within the core are moving collectively in a deformed potential. In spherical nuclei, the rotation and symmetry axes coincide and collective rotation is quantum mechanically forbidden, therefore, the observation of rotational bands is another characteristic feature of deformed nuclei. The transition probabilities obtained from experimental lifetime measurements of states in rotational bands are observed to be much greater than the single-particle estimates which provides further

evidence for deformed nuclear shapes.

If the shell model is to be extended to describe nuclei with non-spherical shapes, the potential in the nuclear Hamiltonian must be deformed. The more realistic deformed potentials are adapted from the harmonic oscillator and Woods-Saxon average potentials and are described in sections 1.4.1 and 1.4.2.

1.4.1 The Modified Oscillator or Nilsson Potential

Nilsson proposed that a deformed nuclear potential can be described by an anharmonic oscillator [Nil55] with an ellipsoidal potential,

$$V_{MHO} = \frac{m}{2}(\omega_x^2 x^2 + \omega_y^2 y^2 + \omega_z^2 z^2). \tag{1.22}$$

The oscillator frequencies are inversely proportional to the half axes a_v, of the ellipsoid such that

$$\omega_v = \frac{1}{a_v} \qquad v = x, y, z. \tag{1.23}$$

The conservation of volume prerequisite is

$$\omega_x \omega_y \omega_z = \omega_0^3. \tag{1.24}$$

The spacing between oscillator shells defines the oscillator frequencies with an isospin dependence as

$$\hbar\omega_0 = 41 A^{-\frac{1}{3}} \left(1 \pm \frac{1}{3}\frac{(N-Z)}{A}\right), \tag{1.25}$$

with the minus sign for protons and the plus sign for neutrons. The anharmonic oscillator potential can be separated into one dimensional potentials in x, y and z, where the eigenvalues are analytically calculable as

$$E(n_x, n_y, n_z) = \hbar\omega_x \left(n_x + \frac{1}{2}\right) + \hbar\omega_y \left(n_y + \frac{1}{2}\right) + \hbar\omega_z \left(n_z + \frac{1}{2}\right). \tag{1.26}$$

The expression for the modified oscillator potential is simplified by considering axially symmetric shapes such that

$$\omega_\perp = \omega_x = \omega_y, \tag{1.27}$$

$$V_{MHO} = \frac{m}{2}[\omega_\perp^2 (x^2 + y^2) + \omega_z^2 z^2]. \tag{1.28}$$

The anisotropies in the potential are introduced by defining the oscillator frequencies in terms of nuclear deformation, δ.

$$\omega_\perp \approx \omega_0 \left(1 - \frac{2}{3}\delta\right); \quad \omega_z \approx \omega_0 \left(1 + \frac{1}{3}\delta\right); \quad \delta = \frac{\Delta R}{R_0}, \tag{1.29}$$

where ΔR is the difference between the radii parallel and perpendicular to the symmetry axis and R_0 is the mean radius. To avoid complications inherent in using cartesian coordinates, the stretched coordinate system is introduced with

$$\xi = x\sqrt{\frac{m\omega_\perp}{\hbar}}; \qquad \eta = y\sqrt{\frac{m\omega_\perp}{\hbar}}; \qquad \zeta = z\sqrt{\frac{m\omega_z}{\hbar}}. \tag{1.30}$$

In the stretched coordinate system, the nuclear surface can be described by the parameters ρ (radius in stretched coordinate system) and θ_t (angle between ρ and the symmetry axis now described by ζ coordinate). These parameters are defined as

$$\rho^2 = \sqrt{\xi^2 + \eta^2 + \zeta^2}\ ; \qquad \cos\theta_t = \frac{\zeta}{\rho}. \tag{1.31}$$

The modified oscillator potential can be written in terms of Eq. 1.31 and deformation, ϵ_λ as

$$V_{MHO} = \frac{1}{2}\hbar\omega_0(\epsilon_2)\rho^2 \left[1 - \frac{2}{3}\epsilon_2 P_2 \cos\theta_t\right]. \tag{1.32}$$

The deformation parameters δ and ϵ_2 are related to the parameter β_2 through the relations [LVH70]

$$\beta_2 \approx \sqrt{\frac{\pi}{5}}\left(\frac{4}{3}\delta + \frac{2}{3}\delta^2\right) \approx \sqrt{\frac{\pi}{5}}\left(\frac{4}{3}\epsilon_2 + \frac{4}{9}\epsilon_2^2\right). \tag{1.33}$$

Higher multipole orders of deformation can be included into Eq. 1.32 by adding terms proportional to $\epsilon_\lambda \rho^2 P_\lambda(\cos\theta_t)$. The solutions of the modified oscillator problem are given by

$$E_{n_z N_\perp} = \left(n_z + \frac{1}{2}\right)\ \hbar\omega_z + (n_\perp + 1)\ \hbar\omega_\perp \tag{1.34}$$

or in terms of deformation, δ,

$$E_{N n_z N_\perp} \approx \left(N + \frac{3}{2}\right)\ \hbar\omega_0 - \frac{1}{3}\delta\,(2n_z - n_\perp)\ \hbar\omega_0, \tag{1.35}$$

where $N = n_z + n_\perp$. Equation 1.35 simply yields the energies of the spherical harmonic oscillator with a deformation dependent correction term added.

In order to reproduce the correct magic numbers, Nilsson added terms proportional to ℓ^2 and $\ell.\mathbf{s}$. The resulting Nilsson potential is defined as

$$V_{Nil} = V_{MHO} - \kappa\hbar\omega \left[2\ell.\mathbf{s} + \mu(\ell^2 - \langle\ell^2\rangle_N)\right], \tag{1.36}$$

where $\ell.\mathbf{s}$ is the spin-orbit term in the stretched coordinate system and the $\mu(\ell^2 - \langle\ell^2\rangle_N)$ term flattens the potential for the centre of the nucleus. The coefficients κ and $\kappa\mu$ define the strength of the spin-orbit coupling and the squareness of the potential, respectively, and are chosen by fitting to experimental energy levels. The parameters κ and μ are different for each major shell.

The Nilsson - Modified Oscillator eigenstates are labelled by the asymptotic quantum numbers for large deformation and axially symmetric shapes.

$$[\ N\ n_z\ \Lambda\ ]\ \Omega^\pi \tag{1.37}$$

where

N = Total number of oscillator quanta

n_z = Number of oscillator quanta along the symmetry axis

Λ = Component of orbital angular momentum (ℓ) along symmetry axis

Ω = Component of total angular momentum (j) along symmetry axis

π = Parity of the State = $(-1)^N$

The quantities $\mathbf{j}$ and ℓ are no longer good quantum numbers, although their projections, Ω and Λ are conserved in the deformation regime. Figure 1.4 relates the vector quantities to their projections on the symmetry axis.

The onset of deformation relieves the degeneracies of the spherical harmonic oscillator. Consider the N = 3 spherical shell that has a degeneracy of (N + 1)(N + 2) = 20 with ℓ = 3 and 1 in the harmonic oscillator potential. In the Nilsson model deformation causes the spherical levels to split into (N + 1) levels each of $2(n_\perp + 1)$ degenerate states. The splitting of the energy levels depends on the spatial orientation of the orbital. Figure 1.5 shows the possible orientations of a state with j = $\frac{7}{2}$ for prolate and oblate deformations. A nucleon with j = $\frac{7}{2}$ can have eight possible components of $\mathbf{j}$ along the symmetry axis ranging from $-\frac{7}{2}$ to $\frac{7}{2}$. For reflection symmetric shapes, such as prolate and oblate nuclei, the $-\Omega$ and $+\Omega$ projections are degenerate. States with different n_z (Eq. 1.35) are split.

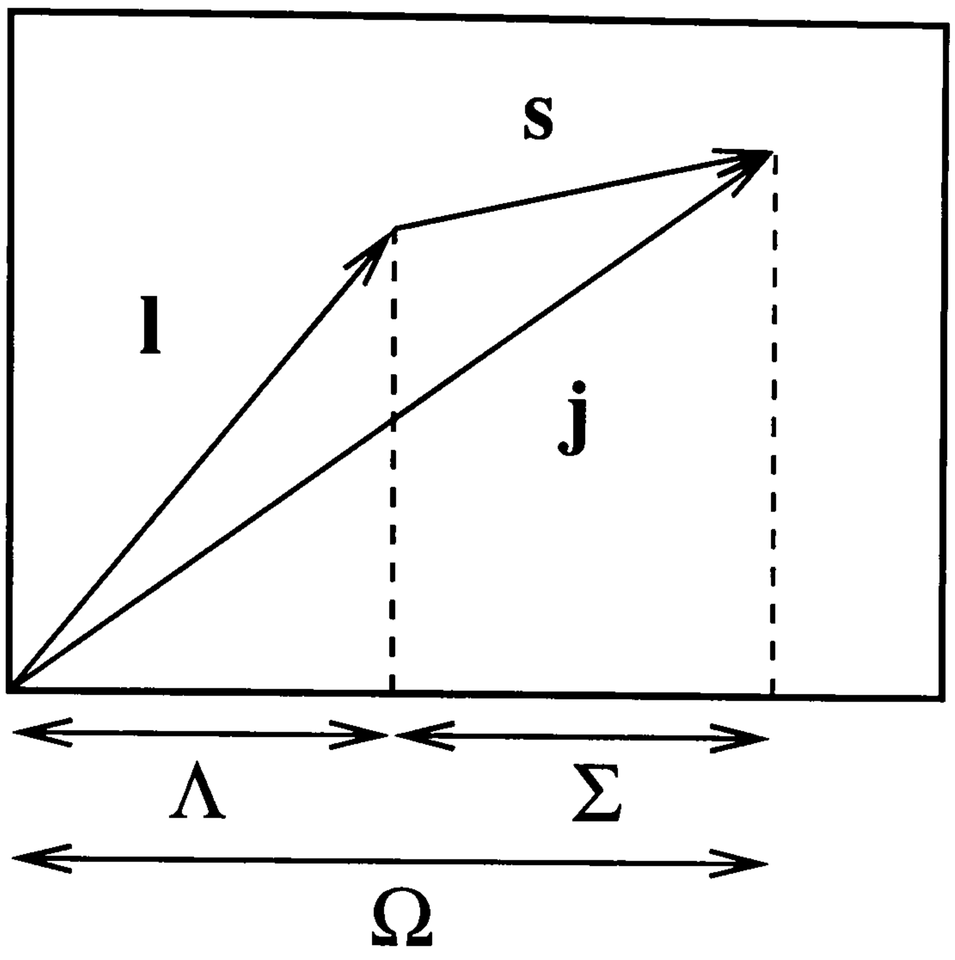

Figure 1.4: Figure to illustrate spin-orbit ℓ .**s** coupling. The components of ℓ, **s** and **j** on the symmetry axis are shown.

Figure 1.5 illustrates the splitting for prolate and oblate deformations. For prolate deformation, the low-Ω component has the maximum overlap with the core and is, therefore, lower in energy. The opposite is true for oblate deformations, where the high-Ω component is lowered in energy.

Although the Nilsson model is successful in reproducing the observed experimental properties, the deformed Woods-Saxon potential is thought to be more accurate when extrapolating to neutron deficient nuclei.

1.4.2 The Deformed Woods-Saxon Potential

The Nilsson model in its original form, included a term proportional to $|\ell^2|$ in order to reproduce a flat bottomed potential. On comparison with experimental data, it was found for heavy nuclei, i.e. states with large N quantum numbers, that the single-particle energies were shifted too strongly [GLN67]. The advantage of using a deformed Woods-Saxon parameterisation is the absence of any term dependent on ℓ^2, thus eliminating the overestimation found in the Nilsson model. The deformed Woods-Saxon potential is defined as,

$$V_{DWS}(r,\beta) = \frac{-V_0}{1 + exp\left[\frac{dist_\Sigma(r,\beta)}{a}\right]}, \tag{1.38}$$

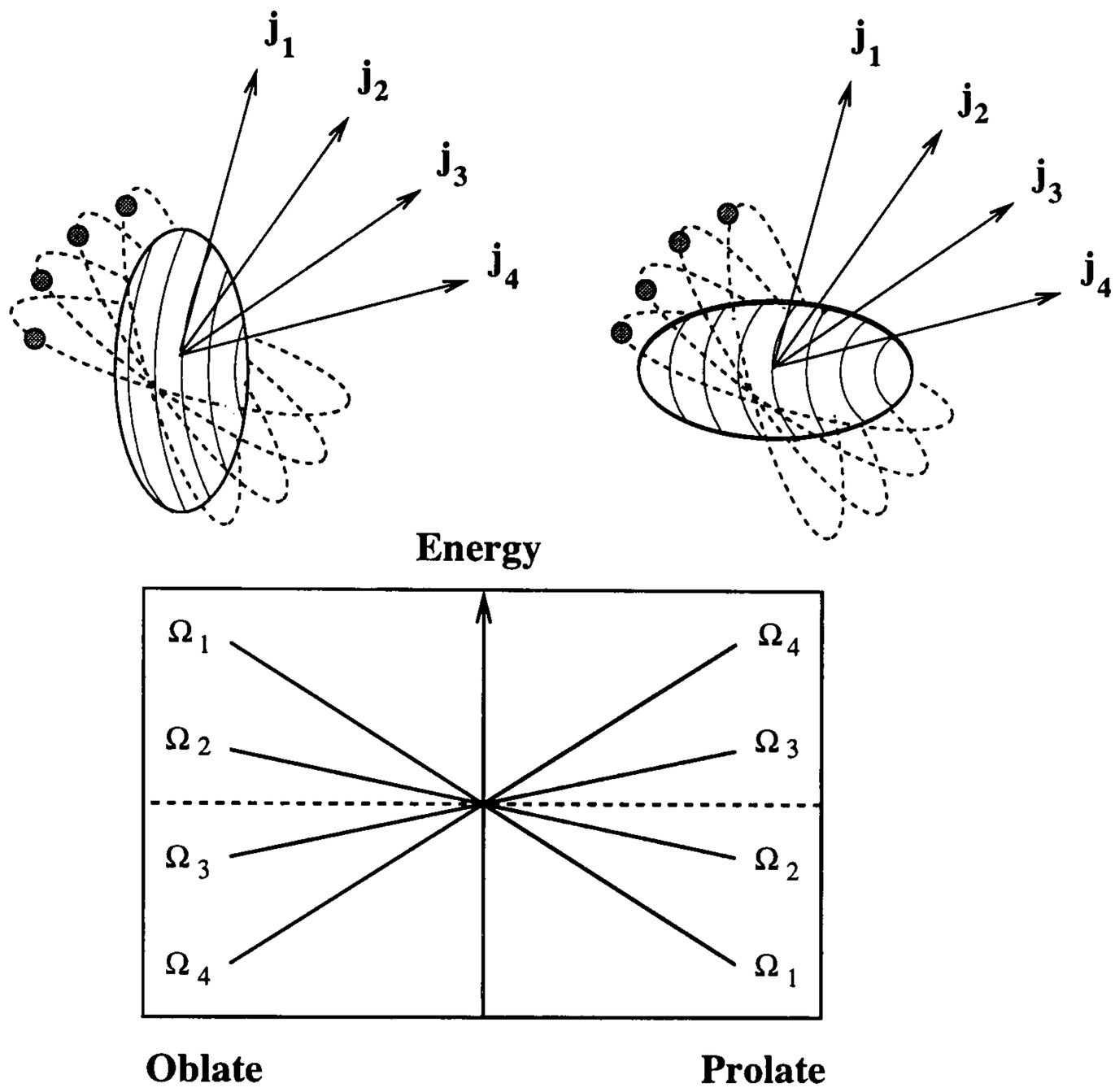

Figure 1.5: Figure illustrating the possible orientations of states originating from a shell with j= $\frac{7}{2}$ for prolate and oblate deformations.

where $dist_\Sigma(r,\beta)$ is a function of the distance r from the nuclear surface Σ and β denotes the shape parameters that uniquely define Σ. The expression for the Hamiltonian is defined as

$$H = \frac{-\hbar}{2m}\nabla^2 + \frac{-V_0}{1 + exp\left[\frac{dist_\Sigma(r,\beta)}{a}\right]} - f(r)\ \ell.\mathbf{s}. \tag{1.39}$$

Single particle energies included in this work have been calculated assuming a deformed Woods-Saxon potential using the code WSBETA [Cwi87] with the universal parameter set [Naz85].

Whichever potential is ultimately used, the plots of single-particle energies as a function of quadrupole deformation parameter are generally termed Nilsson diagrams.

1.4.3 Nilsson Diagrams

A Nilsson diagram for neutrons, calculated with parameters suitable for a neutron deficient rare-earth nucleus is pictured in Fig. 1.6. There are a number of characteristic features

which result from using an axially symmetric deformed potential:

1. The spherical shell model magic numbers are reproduced at $\beta_2 = 0$ in regions of low level density. At higher deformations the spherical shell closures disappear and new shell closures occur at different particle numbers corresponding to stable deformed shapes e.g. N=72.

2. At certain deformations, the single-particle levels may change their slope as the result of an interaction between states originating from different j-shells but holding the same quantum numbers (Ω, π). Such states are not allowed to cross according to the Pauli exclusion principle. For example, the $[402]5/2^+$ originating from the $2d_{5/2}$ shell and the $[413]5/2^+$ emerging from the $1g_{7/2}$ shell approach each other with decreasing prolate deformation as displayed in Fig. 1.6. Since they have the same parity and Ω quantum numbers they are not permitted to cross and exchange character at the crossing point.

3. Orbitals with high-j are lowered in energy by the spin-orbit interaction so that they reside amongst levels with opposite parity. An example of this phenomena is found in Fig. 1.6 where the negative parity $1h_{11/2}$ states are lowered among the positive parity $1g_{7/2}$ and $2d_{5/2}$ levels. States such as those originating from the $1h_{11/2}$ shell are termed unnatural parity states (intruder states).

4. The slope of the levels is related to the single-particle matrix element of the quadrupole operator.

$$\frac{dE}{d\beta_2} = -\langle\psi|r^2 Y_{20}|\psi\rangle. \tag{1.40}$$

1.5 The Strutinsky Shell Correction Procedure

In the previous sections, it has been shown that there are two distinct models that describe the nucleus. The liquid drop model assumes that a uniform nucleon density with a well-defined surface can be used to describe bulk properties that vary smoothly with mass. The alternative view is the shell model which embraces the premise of quantised independent orbits moving in an average potential. The shell model is known to reproduce

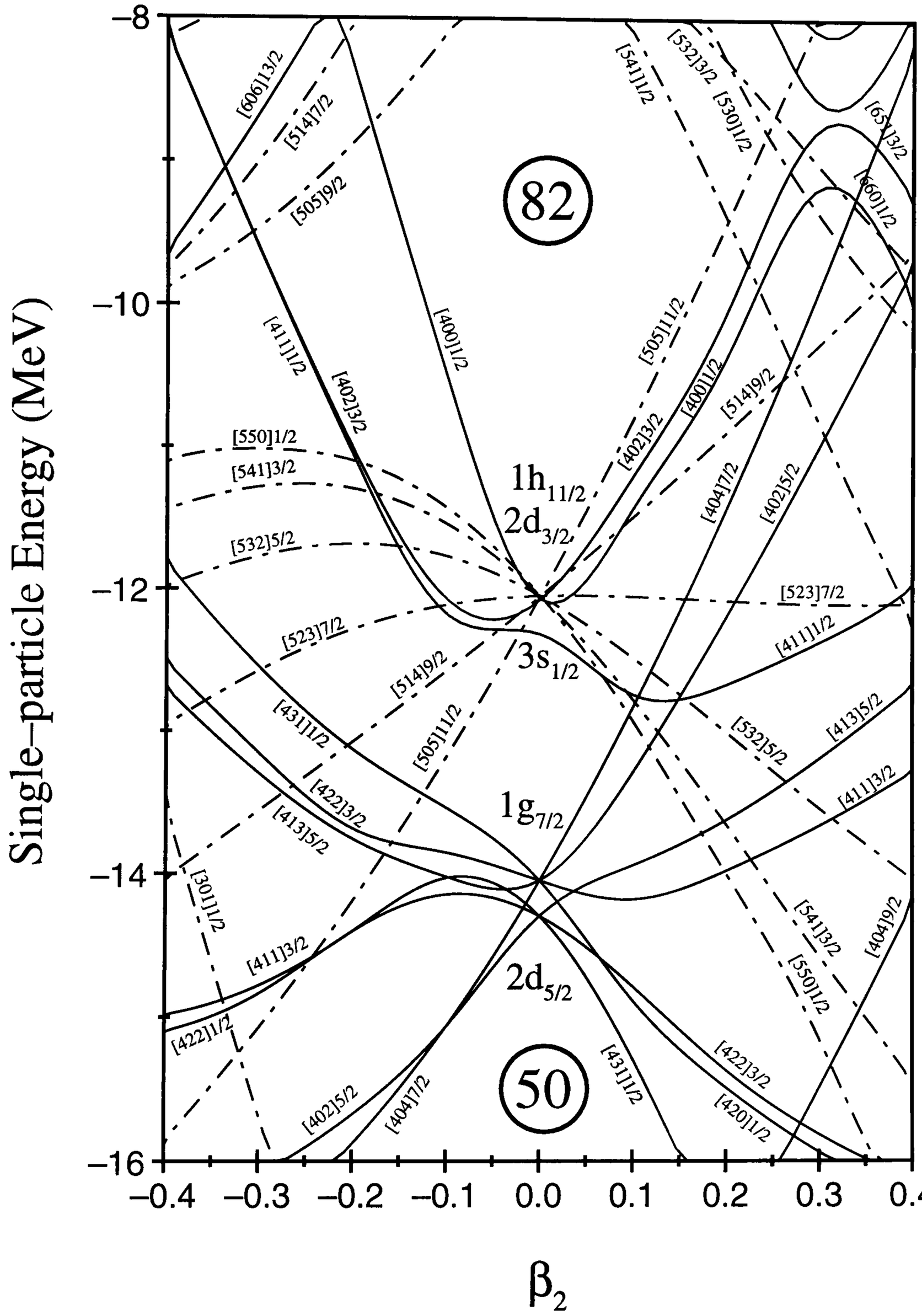

Figure 1.6: Nilsson diagram for neutrons calculated for nuclei in the A≈130 region.

nuclear properties where only the nucleons at the Fermi surface are involved. However, phenomenological shell models fail to correctly account for collective properties in which all nucleons contribute. This is highlighted by the shell models inability to correctly represent the ground state energy as the sum of all the single-particle energies from the bottom of the potential well to the Fermi surface. The Strutinsky shell correction procedure [Str66] [Str67] was presented as a solution to this problem. The great success of Strutinsky's procedure is that it can correctly replicate the binding energy of the nucleus and also the dependence of the binding energy on deformation parameters.

The dependence of the nuclear binding energy, E, as a function of mass A, can be separated into two parts comprised of the smooth variation of the Bethe-Weizsäcker formula (Eq. 1.1), E_{LDM} and an oscillatory part, E_{osc} so that

$$E = E_{LDM} + E_{osc}. \tag{1.41}$$

The oscillations about the smooth component E_{osc} are due to the occurrence of shell closures where the binding energy is at a local maximum. Similar oscillations would be found to occur if it were possible to calculate the exact energy of the many-body system as a function of deformation. The oscillatory term in Eq. 1.41 cannot be taken directly from a solution of the shell model. In the shell model, the total energy, E_{sh}, is also constructed from two components with smooth and fluctuating character.

$$E_{sh} = E_{osc} + \tilde{E}_{sh} = \sum_{i=1}^{A} \epsilon_i. \tag{1.42}$$

In the shell model, levels bunch together to form regions of high and low level densities. A simplified view in terms of level densities suggests that in regions of high level density with sufficiently smooth distribution of levels, the binding energies will vary smoothly as a function of the position of the Fermi surface. A comparison of an evenly spaced level density to a shell-like density, where the average densities are equal, shows that if the Fermi level is below (above) the shell closure the binding energy is greater (less) than the Fermi level for the evenly spaced density. In short, it is noted that the binding energies of the shell-like density oscillate about those obtained from the average level density. In the shell model representation (Eq. 1.42), the total energy is comprised of the average level density component across the shells that is perturbed by the oscillations in energy around the shell closures. The average component of Eq. 1.42 relates directly to the average behaviour of

the binding energy. It has already been stated that phenomenological shell models do not correctly represent the variation of binding energy since the smoothly varying term in the shell model representation is incorrect.

The Strutinsky shell correction calculates the total energy by adding the smooth variation of the liquid drop model to the oscillating component of the shell model approach. The remaining problem is to separate the average and oscillating components. At this stage it is crucial to adequately mathematically define the smoothly varying average density for a given level density. The mathematical prescription must also ensure that the oscillatory behaviour is not reproduced in the mean component.

Allowing for these considerations, the total energy of the nucleus can be written as

$$E = E_{LDM} + E_{sh} - \tilde{E}_{sh}. \tag{1.43}$$

The Strutinsky calculations can also be adapted for rotational nuclei. Cranked Strutinsky calculations are often displayed as deformation contours and will be described in more detail in Chapter 2.

1.6 Electromagnetic Nuclear Properties

Electromagnetic transitions in nuclei, from an initial state to a final state, can occur by the emission of a γ ray photon. Since the nuclear system is partly assembled from discrete charges, these transitions take place in the presence of an associated electromagnetic field. The inclusion of the electromagnetic fields into the total Hamiltonian yields

$$H = H_{shell} + H_{field} + H', \tag{1.44}$$

where H_{shell} describes the shell model Hamiltonian, H_{field} is the Hamiltonian of the electromagnetic field and H' is a time-dependent perturbation which describes the interaction between the field and a system of charges. If two states ψ_i and ψ_f are related by a transition then

$$\langle \psi_i | H' | \psi_f \rangle \neq 0, \tag{1.45}$$

i.e. a transition between the states will be lead to a non-zero matrix element. If the interaction relating states $|\psi_i\rangle$ and $|\psi_f\rangle$ is small, the probability per unit time of a transition

between the states is given by

$$T_{if} = \frac{2\pi}{\hbar}|\langle\psi_i|H'|\psi_f\rangle|^2\rho_E \tag{1.46}$$

where ρ_E is the density of states per unit energy at the transition energy.

Electromagnetic perturbations such as γ-ray emission can be defined by an infinite power series known as a multipole expansion and is defined by its constituent components known as the multipole moments which are either electric or magnetic in nature:

$$H' = \sum_{\lambda\mu} a_{\lambda\mu}Q_{\lambda\mu} + b_{\lambda\mu}M_{\lambda\mu}, \tag{1.47}$$

where $Q_{\lambda\mu}$ and $M_{\lambda\mu}$ are the electric and magnetic operators, respectively.

Electromagnetic moments arise from charge and current densities in the nucleus. As the nucleus deviates from sphericity, the contributions of terms in Eq. 1.44 also change and thus measurements of the electromagnetic moments can reveal much about the matrix elements and deformation properties of the nucleus. This work is primarily concerned with axially symmetric prolate shapes and so the lowest multipole that is considered is the electric quadrupole which is directly related to the charge distribution within the nucleus.

1.6.1 Quadrupole Moments

The quadrupole moment operator is defined in terms of the nuclear charge density and its distribution throughout the nuclear volume,

$$Q(r) = e\int \rho_e(r)r(3\cos^2\theta - 1)dV, \tag{1.48}$$

where $Q(r)$ is the electric quadrupole operator, ρ_e is the charge density and θ is the angle subtended by the radius vector, r. If the nucleus is spherical, the integral over the entire nuclear volume will be zero. Positive quadrupole moments are characteristic of prolate deformed shapes and can be related to the quadrupole deformation parameter β_2 through

$$Q_0 = \frac{3}{\sqrt{5\pi}}ZR^2\beta_2\left[1 + \frac{1}{8}\sqrt{\frac{5}{\pi}}\beta_2\right]. \tag{1.49}$$

1.6.2 Lifetimes and Transition Strengths

Selection rules obtained for γ-ray emission arise from symmetry and conservation considerations. If an excited state decays via γ-ray emission, conservation of angular momentum gives the following selection rule

$$|I_i - I_f| \leq L \leq (I_i + I_f); \quad L \neq 0 \tag{1.50}$$

where I_i and I_f are the angular momenta of the initial and final states and L defines the multipolarity of the γ ray. The transition is referred to as stretched if the photon carries away the maximum possible angular momentum from the transition ($I_\gamma = I_f - I_i$) and non-stretched if the photon carries away some lesser value. For example, superdeformed cascades are composed of a series of stretched E2 γ rays.

Since the electromagnetic interaction is parity-conserving, a further selection rule is applied to transitions between states

$$\pi_i \pi_f = \pi_L \tag{1.51}$$

where π_i and π_f are the parities of the initial and final states and L is the multipolarity of the γ ray. The parity is related to the individual multipole operators by the following rules

$$\pi(ML) = (-1)^{L+1}, \tag{1.52}$$

$$\pi(EL) = (-1)^{L}, \tag{1.53}$$

where (ML) and (EL) are the magnetic and electric multipoles of the L'th order. The multipole expansion converges rapidly for higher multipole orders and usually only the lower order terms are considered.

The probabilities of γ-ray emission per unit time can be estimated theoretically from the single-particle Weisskopf estimates (in Weisskopf units, Wu). The single-particle transition rates for different multipolarities are listed in Table 1.1 for the lower multipole orders.

Experimentally, the intrinsic quadrupole moment can also be used to extract reduced transition probabilities $B(E2; I \rightarrow I-2)$ through

$$B(E2; I \rightarrow I-2) = \frac{5}{16\pi} \langle I\ 2\ 0\ 0 | I-2\ \ 0 \rangle^2 Q_t^2, \tag{1.54}$$

L	Electric Transitions	$\Delta\pi$	Magnetic Transitions	$\Delta\pi$
1	$\mathrm{T(E1)}_{sp} = 1.0 \times 10^{14}\ \mathrm{A}^{2/3}\mathrm{E}_\gamma^3$	Yes	$\mathrm{T(M1)}_{sp} = 5.6 \times 10^{13}\mathrm{E}_\gamma^3$	No
2	$\mathrm{T(E2)}_{sp} = 7.3 \times 10^{7}\ \mathrm{A}^{4/3}\mathrm{E}_\gamma^5$	No	$\mathrm{T(M2)}_{sp} = 3.5 \times 10^{7}\ \mathrm{A}^{2/3}\mathrm{E}_\gamma^5$	Yes
3	$\mathrm{T(E3)}_{sp} = 3.4 \times 10^{1}\ \mathrm{A}^{2}\mathrm{E}_\gamma^7$	Yes	$\mathrm{T(M3)}_{sp} = 1.6 \times 10^{1}\ \mathrm{A}^{4/3}\mathrm{E}_\gamma^7$	No
4	$\mathrm{T(E4)}_{sp} = 1.1 \times 10^{-5}\ \mathrm{A}^{8/3}\mathrm{E}_\gamma^9$	No	$\mathrm{T(M4)}_{sp} = 4.5 \times 10^{-6}\ \mathrm{A}^{2}\mathrm{E}_\gamma^9$	Yes

Table 1.1: Weisskopf single-particle estimates for electric and magnetic γ-ray transitions. E_γ and $T(\lambda, L)$ are expressed in MeV and s^{-1}, respectively.

where $\langle I\ 2\ 0\ 0|I-2\ \ 0\rangle$ is a Clebsch-Gordan vector addition coefficient and Q_t is the quadrupole moment.

The lifetime is related to the collective transition strength (T(E2)) by

$$\frac{1}{\tau} = T(E2) = 1.23 \times 10^{13} E_\gamma^5 B(E2), \tag{1.55}$$

where T(E2) is defined in s^{-1} E_γ in MeV and B(E2) in $(\mathrm{eb})^2$. Consequently, substituting Eq. 1.54 into Eq. 1.55 gives

$$\frac{1}{\tau} = 1.223 \times 10^{12} E_\gamma^5 \langle I\ 2\ 0\ 0|I-2\ \ 0\rangle^2 Q_t^2. \tag{1.56}$$

The nature of γ-ray transitions between states depend on the multipole expansion of the nuclear electromagnetic field and as such depends strongly on the nuclear deformation. Lifetime and quadrupole moment measurements of rotational bands allow an understanding of the deformation properties of the nucleus and the underlying structures that influence these properties.

1.7 Summary

Fig. 1.7 displays schematically the corrections made to the spherical shell model that lead to a realistic nuclear model. The final column in Fig. 1.7 shows that for a deformed nucleus, there are rotational degrees of freedom and the interplay of Coriolis and centrifugal forces leads to new symmetries in the nuclear Hamiltonian (π, α). The effects of rotation are of fundamental importance in the results presented in this thesis and are discussed separately in Chapter 2.

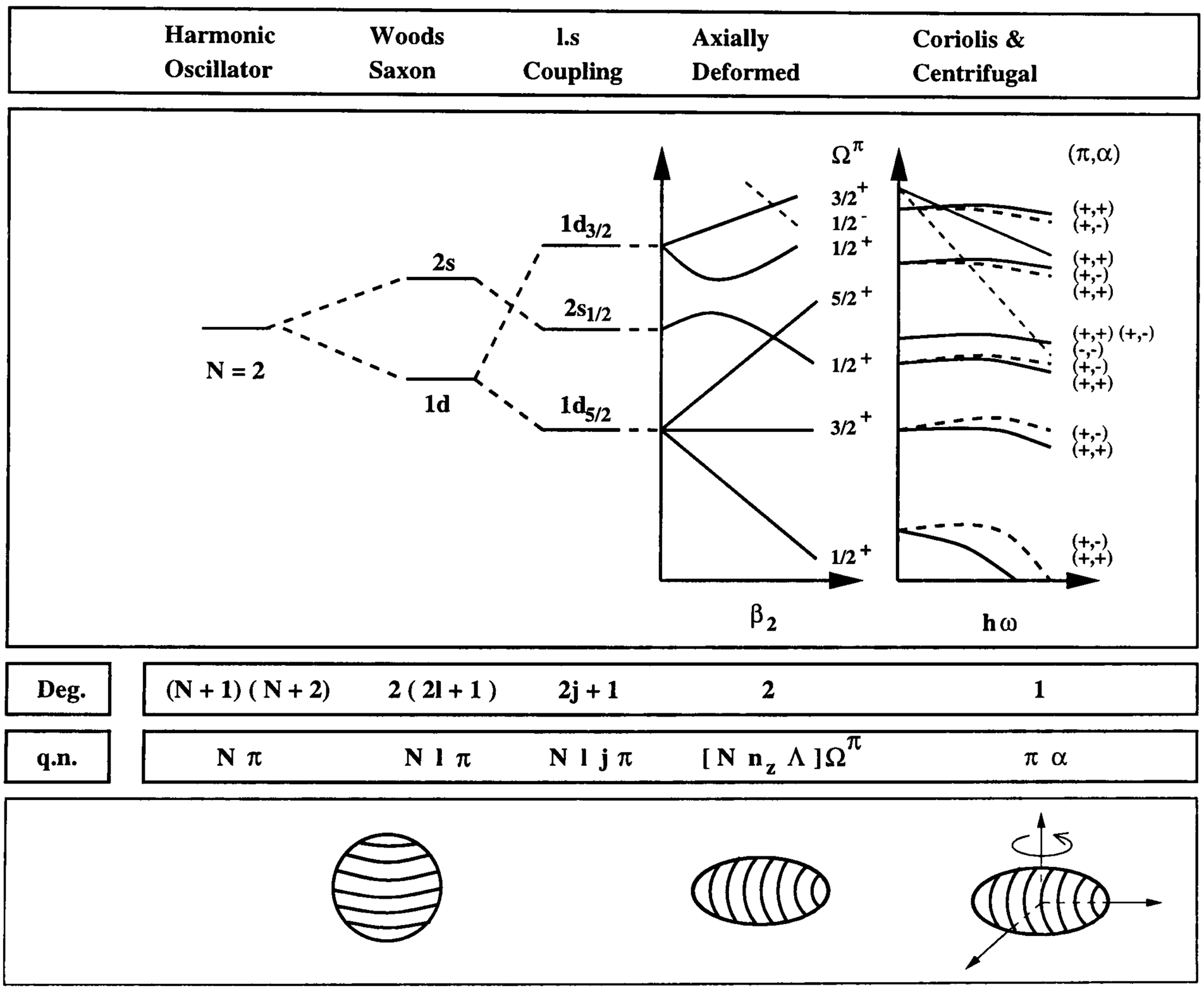

Figure 1.7: The N=2 level scheme. The top box describes the factors that relieve the (N+1)(N+2) degeneracy of the spherical harmonic oscillator, while the effect on the single-particle energies are shown schematically in large box. The lower boxes state the degeneracies and the remaining good quantum number labels. The lowest section illustrates the nuclear shape in the various regimes.

Chapter 2

Nuclear Rotation

In deformed nuclei, it is possible for rotation to occur about an axis perpendicular to the symmetry axis. The effects of rotational forces relieve the degeneracies of the deformed shell model potentials and lead to new symmetries in the nuclear Hamiltonian. This chapter reviews nuclear rotation and introduces the origin of experimental quantities which are relevant to the results presented in this work.

2.1 Collective Nuclear Rotation

Nuclear deformation originates from anisotropies of the single-particle orbitals. If the nucleus possesses deformation, it is possible to define nuclear orientations which lead to degrees of freedom that are not available to the spherically symmetric nucleus. In deformed nuclei collective rotation about an axis perpendicular to the symmetry axis, in which all the nucleons make a coherent contribution, leads to the expression;

$$E(I) = \frac{\hbar^2}{2\Im} I(I+1), \tag{2.1}$$

where $E(I)$ is the excitation energy of collective states, $\Im$ is the moment of inertia and I is the total spin. A rotational frequency can be defined as

$$\hbar\omega = \frac{dE}{dI_x} \approx \frac{1}{2}(E_{I+1} - E_{I-1}) \tag{2.2}$$

where I_x is the projection of the total angular momentum on the rotation axis

$$I_x = \sqrt{I(I+1)^2 - K^2}. \tag{2.3}$$

Eq. 2.2 is obtained for quadrupole γ-rays that carry away $2\hbar$ of spin with each transition between levels in a rotational band defined by Eq. 2.1.

For axially symmetric shapes, the intrinsic nuclear wavefunction can be characterised by the spin component on the symmetry axis, K. The rotational motion of the nucleus can be completely defined by I^2, $I_{Z_{Lab}} = M$ and K. The eigenfunctions of I^2, M and K operators are given by

$$\psi_{rot} = |IMK\rangle = \sqrt{\frac{2I+1}{8\pi^2}} D^I_{MK}(\Theta, \Phi, \Psi), \tag{2.4}$$

where the functions $D^I_{MK}(\Theta, \Phi, \Psi)$ are the rotation matrices that contain the wavefunctions describing the orientation of the rotational system with respect to the angular momentum quantum numbers I^2, M and K. Fig. 2.1 displays the relationship between these quantities.

Depending on the K value, different rotational bands may be formed. For K=0, the $D^I_{MK}(\Theta, \Phi, \Psi)$ functions reduce to spherical harmonics Y_{IM} and the total nuclear wavefunction is given by

$$\Psi_{r,IMK=0} = \frac{1}{\sqrt{2}} \psi_{r,K=0} Y_{IM}, \tag{2.5}$$

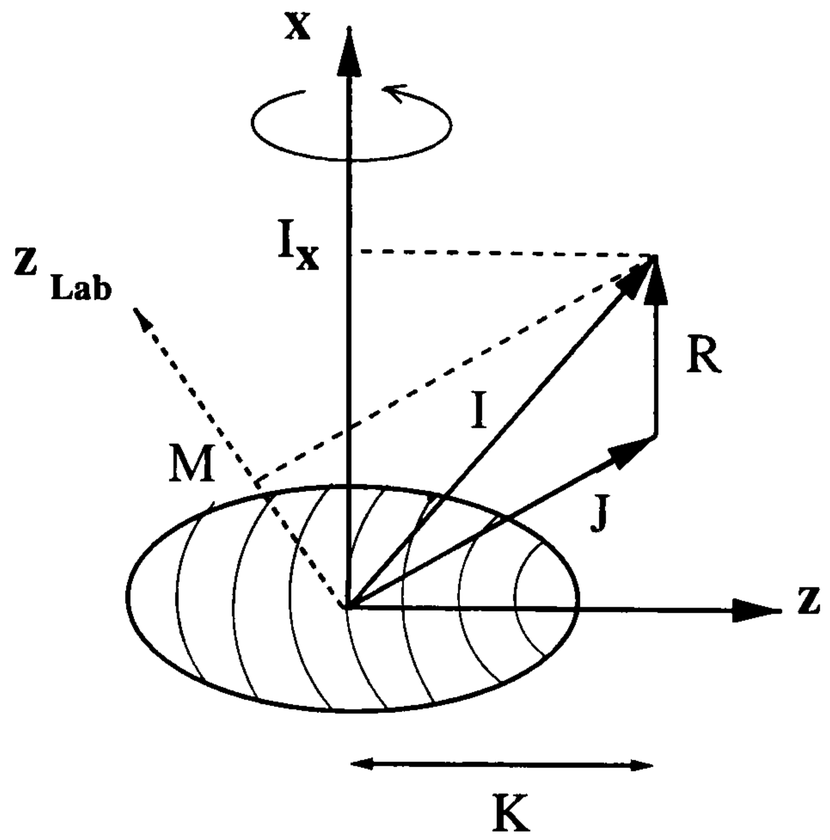

Figure 2.1: Angular momentum coupling describing the quantities used to define the rotational motion of the collective nuclear system.

where r is introduced to describe the reflection invariance of the axial system with respect to the plane perpendicular to the symmetry axis. The values of r are obtained through the expression.

$$r = (-1)^I. \tag{2.6}$$

The selection rules obtained from Eq. 2.6 are defined as

$$I = 0, 2, 4 \quad ... \qquad K = 0 \qquad r = +1$$
$$I = 1, 3, 5 \quad ... \qquad K = 0 \qquad r = -1$$

These spin sequences are defined as rotational bands. For the cases where $K \neq 0$ the nuclear wavefunction is anti-symmetrised to account for the reflection symmetry so that it takes the form

$$\Psi^I_{MK} = \sqrt{\frac{2I+1}{16\pi^2}} \left[\psi_k D^I_{MK}(\Theta, \Phi, \Psi) + (-1)^{I+K} \psi_{\bar{K}} D^I_{M-K}(\Theta, \Phi, \Psi)\right] \tag{2.7}$$

where $\psi_{\bar{K}}$ is the wavefunction that corresponds the projection of the angular momentum $-K$. This projection can be obtained from ψ_K by a rotation through 180° about the rotation axis. As a consequence of rotational invariance, the components of $\psi_{\bar{K}}$ and ψ_K ($-K$ and K respectively) are degenerate and constitute a single sequence of rotational states with spins

$$I = K, K+1, K+2 \quad ...$$

The term $(-1)^{I+K}$ in Eq. 2.7 is a phase factor and is generally referred to as the signature. The signature changes sign for alternate states in the band sequence mentioned above. A

rotational band of this type can be separated into two bands of opposite signature with spin sequences

$$I = K,\ K{+}2,\ K{+}4 \quad ...$$
$$I = K{+}1,\ K{+}3,\ K{+}5 \quad ...$$

The energy of rotational motion is defined as

$$E_{rot} = \frac{\hbar^2}{2\Im}(\mathbf{I}-\mathbf{J})^2 = \frac{\hbar^2}{2\Im}(\mathbf{I}.\mathbf{I}+\mathbf{J}.\mathbf{J}-2\mathbf{I}.\mathbf{J}). \tag{2.8}$$

In Eq. 2.8, the term **I.J** couples the angular momentum of the valence nucleons to the rotational motion. The coupling of valence nucleons to a deformed core depends on how the angular momenta of the components are added. This coupling of angular momentum is addressed in section 2.2.

2.1.1 Moments of Inertia

Eq. 2.1 defined the static moment of inertia, $\Im$. When describing the rotating nucleus, the moment of inertia is not a static function and varies as a function of rotational frequency. The nuclear moment of inertia $\Im_{Nucl}$ is found to be approximately 30% less than the value calculated for a rigid rotating ellipsoid body ($\Im_{Rig}$). If the nucleus is viewed from the other extreme as an irrotational fluid, the $\Im_{Nucl}$ value is underestimated and so $\Im_{Nucl}$ is defined by the inequality,

$$\Im_{Irr} < \Im_{Nucl} < \Im_{Rig}. \tag{2.9}$$

Eq. 2.9 suggests that there are residual interactions between nucleons and pairing is introduced in section 2.3.2. Since $\Im_{Nucl}$ is a dynamic quantity, two other moments of inertia are introduced to provide more information on rotational effects. The quantities $\Im^{(1)}$ and $\Im^{(2)}$ are defined from the first and second derivatives of Eq. 2.8. The following formulae are obtained by assuming that for a nucleus at high spin $I >> K$ and $I_x \approx I$ where I_x is defined in Eq. 2.3. The kinematic moment of inertia, $\Im^{(1)}$, is defined as the first derivative of Eq. 2.8,

$$\Im^{(1)} = \frac{\hbar^2}{2}\left[\frac{dE}{dI_x}\right]^{-1} = \hbar\frac{I_x}{\omega}. \tag{2.10}$$

The dynamic moment of inertia, $\Im^{(2)}$, is defined the second derivative of Eq. 2.8,

$$\Im^{(2)} = \hbar^2\left[\frac{d^2E}{dI_x^2}\right]^{-1} = \hbar\frac{dI_x}{d\omega}. \tag{2.11}$$

The kinematic and dynamic moments of inertia are related via the expression,

$$\Im^{(2)} = \Im^{(1)} + \omega \frac{d\Im^{(1)}}{d\omega}. \tag{2.12}$$

For a rigid body the $\Im^{(1)}$ value is independent of ω and $\Im^{(1)} \approx \Im^{(2)} \approx \Im_{Rig}$.

The $\Im^{(1)}$ and $\Im^{(2)}$ values can be obtained from experiment. If a rotational band is assumed to decay by stretched electric quadrupole (E2) γ-rays, Eq. 2.10 and Eq. 2.11 can be written as

$$\Im^{(1)} = \hbar^2 \frac{(4I-2)}{2E_\gamma} \tag{2.13}$$

$$\Im^{(2)} = \frac{4\hbar^2}{\Delta E_\gamma} \tag{2.14}$$

where ΔE_γ corresponds to the energy separation between peaks in the band. It can be seen from Eq. 2.14 that the dynamic moment of inertia is independent of spin.

The $\Im^{(2)}$ values are sensitive to single-particle alignments and can reveal much about the internal structure of the nucleus. The $\Im^{(2)}$ parameter is of particular interest when discussing superdeformed bands where the spin and excitation energy are not definitely assigned.

2.2 Angular Momentum and the Particle-Rotor Model

The particle-rotor model describes the coupling between the single-particle motion of a few independent valence nucleons to a deformed nuclear core. The angular momentum in the nuclear system is composed of a collective component attributed to the rotation of the deformed core and a single-particle component generated by the intrinsic motion of the valence nucleons. This is defined in Eq. 2.15 and illustrated in Fig. 2.2.

$$\mathbf{I} = \mathbf{R} + \mathbf{J} \tag{2.15}$$

where J is explicitly defined as the sum of the intrinsic angular momenta of the individual valence nucleons

$$\mathbf{J} = \sum_i \mathbf{j_i}. \tag{2.16}$$

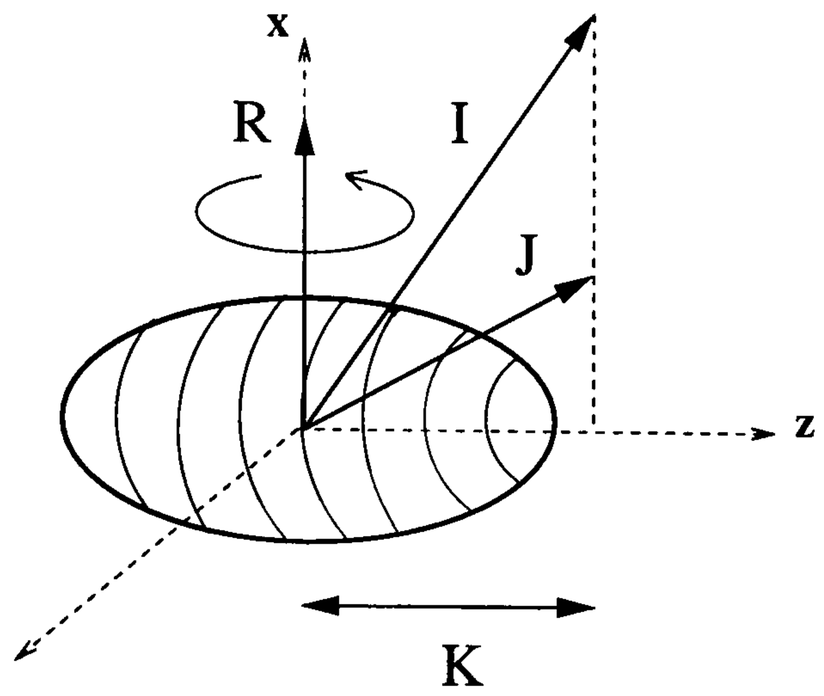

Figure 2.2: Angular momentum coupling in the particle-rotor model. The rotation and symmetry axes are labelled x and z, respectively. The projection of the total spin onto the symmetry axis is labelled K in the figure.

The axial symmetry of the nucleus ensures that the total angular momentum (spin), I and its projection on the symmetry axis, K, are conserved. The total spin projection on the symmetry axis is related to the single-particle momentum projection, Ω, by

$$K = \sum_i \Omega_i \tag{2.17}$$

The coupling of the extra nucleons to the core can occur between two extreme regimes, deformation alignment (DAL) and rotational alignment (RAL). These coupling schemes are illustrated in Fig. 2.3. The deformation aligned limit occurs for large deformations and low rotational frequencies where the valence nucleons closely overlap the core. When the angular momentum vector, J is aligned with the deformation, the Coriolis force is not strong enough to align the single-particle orbits with the rotation axis. In this case the single-particle energy eigenvalues in the rotating frame (Routhians) are near degenerate levels with little level splitting. For deformation alignment, Ω is a conserved quantum number.

For smaller deformations and rapid rotation, the particle-rotor system approaches the rotation aligned limit (RAL). In this scheme, the orbitals are strongly affected by the Coriolis force which aligns the nucleon'(s) angular momentum with the rotation axis so that J precesses about the rotation axis and the nucleon orbit lies in the symmetry plane. In the rotation aligned limit, Ω is not conserved.

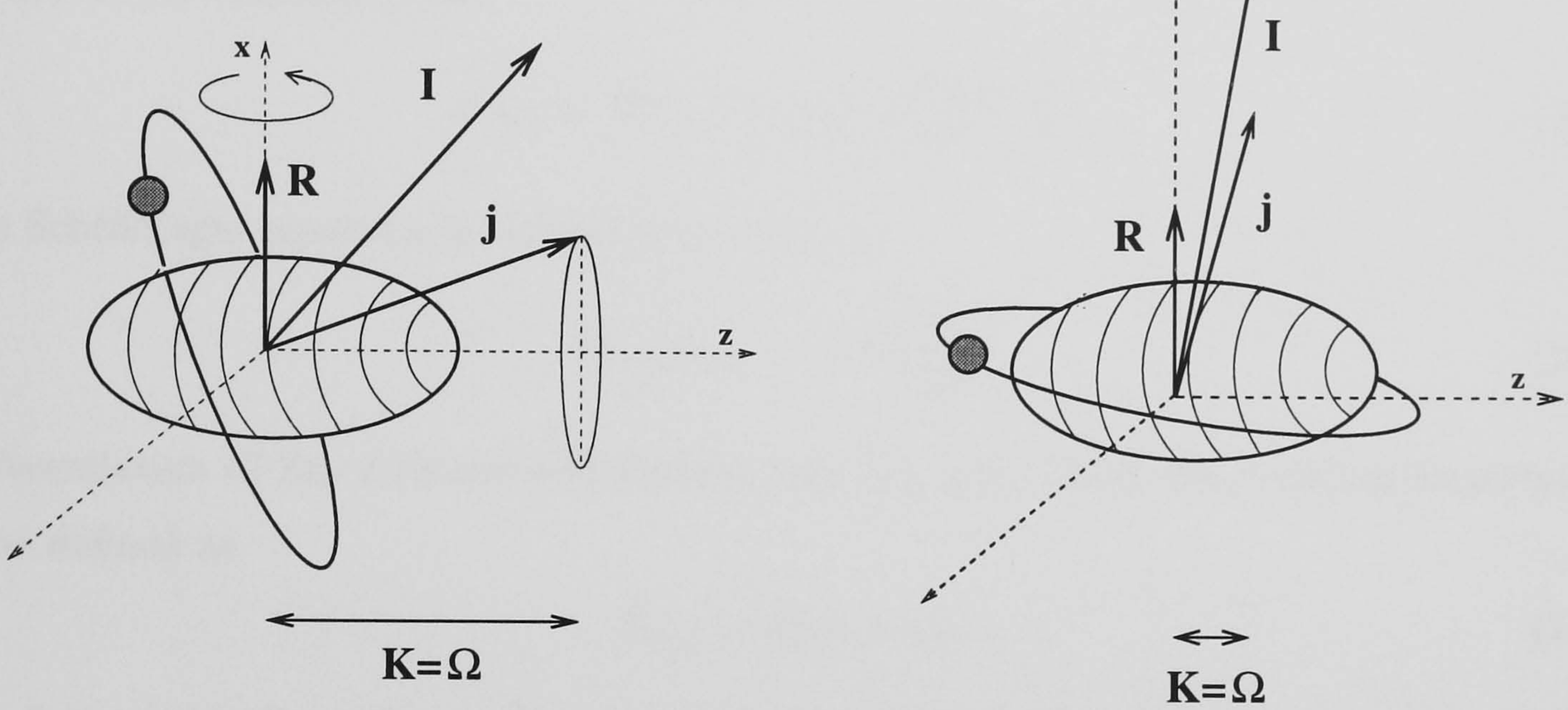

Figure 2.3: Angular momentum coupling in the particle-rotor model. The rotation and symmetry axes are labelled x and z, respectively. The projection of the total spin on the symmetry axis is labelled K in the figure.

2.3 The Cranked Shell Model

The cranked shell model is a fully microscopic description of the rotating nucleus that describes the collective angular momentum as the sum of single particle angular momenta. The advantage of the cranking model is that it can describe the various coupling processes between deformation and rotation aligned limits on an equal basis by including the effects of Coriolis and centrifugal forces. The cranked shell model was derived semi-classically by Inglis [Ing54] by introducing a coordinate system that rotates with a constant angular velocity, ω around a fixed axis in space. With the correct choice of angular frequency, the nucleons can be thought of as independent particles moving in an average potential well that is rotating with the coordinate frame. The transformation of the laboratory wavefunction

into the rotating frame is achieved by the rotation operator $\hat{R}$

$$\hat{R} = \exp\left[\frac{-i\omega t j_x}{\hbar}\right], \tag{2.18}$$

so that in the rotating frame

$$\Psi_{Rot} = \hat{R}\Psi_{Lab} = \exp\left[\frac{-i\omega t j_x}{\hbar}\right]\Psi_{Lab}. \tag{2.19}$$

The Schrödinger equation in the rotating frame is

$$\hat{H}_{Rot}\Psi_{Rot} = -i\hbar\frac{\partial\Psi_{Rot}}{\partial t}. \tag{2.20}$$

Differentiation of Eq. 2.19 and substitution into Eq. 2.20 allows the cranking Hamiltonian to be defined as

$$\hat{H}_{Rot} = \hat{H}_{Lab} - \omega j_x \tag{2.21}$$

The first term in Eq. 2.21 corresponds to the Hamiltonian in the laboratory system which is defined by a deformed single-particle potential such as the deformed Woods-Saxon potential discussed in Chapter 1. The second term models the effects of the Coriolis and centrifugal forces. The Coriolis force modifies the single-particle orbits according to their spatial orientation. The value of $-\omega j_x$ has a different sign depending on whether or not the nucleon is moving in the direction of the collective rotation and this leads to the removal of time reversal symmetry.

The eigenvalues of the single-particle cranking Hamiltonian are defined as

$$e' = \langle u|\hat{H}_{Rot}|u\rangle \tag{2.22}$$

where

$$e' = \langle u|\hat{H}_{Rot}|u\rangle = \langle u|\hat{H}_{Lab}|u\rangle - \omega\langle u|\hat{j}_x|u\rangle \tag{2.23}$$

$$e' = e - \omega j_x \tag{2.24}$$

where u represents eigenstates of the cranking Hamiltonian.

Woods-Saxon cranking calculations have been used to discuss the results in this work. A typical Routhian diagram calculated for ^{132}Nd is displayed in Fig 2.4

At $\hbar\omega = 0$ MeV, the standard Woods-Saxon levels are reproduced. The Woods-Saxon levels at $\hbar\omega = 0$ MeV are two-fold degenerate with respect to time reversal symmetry. If

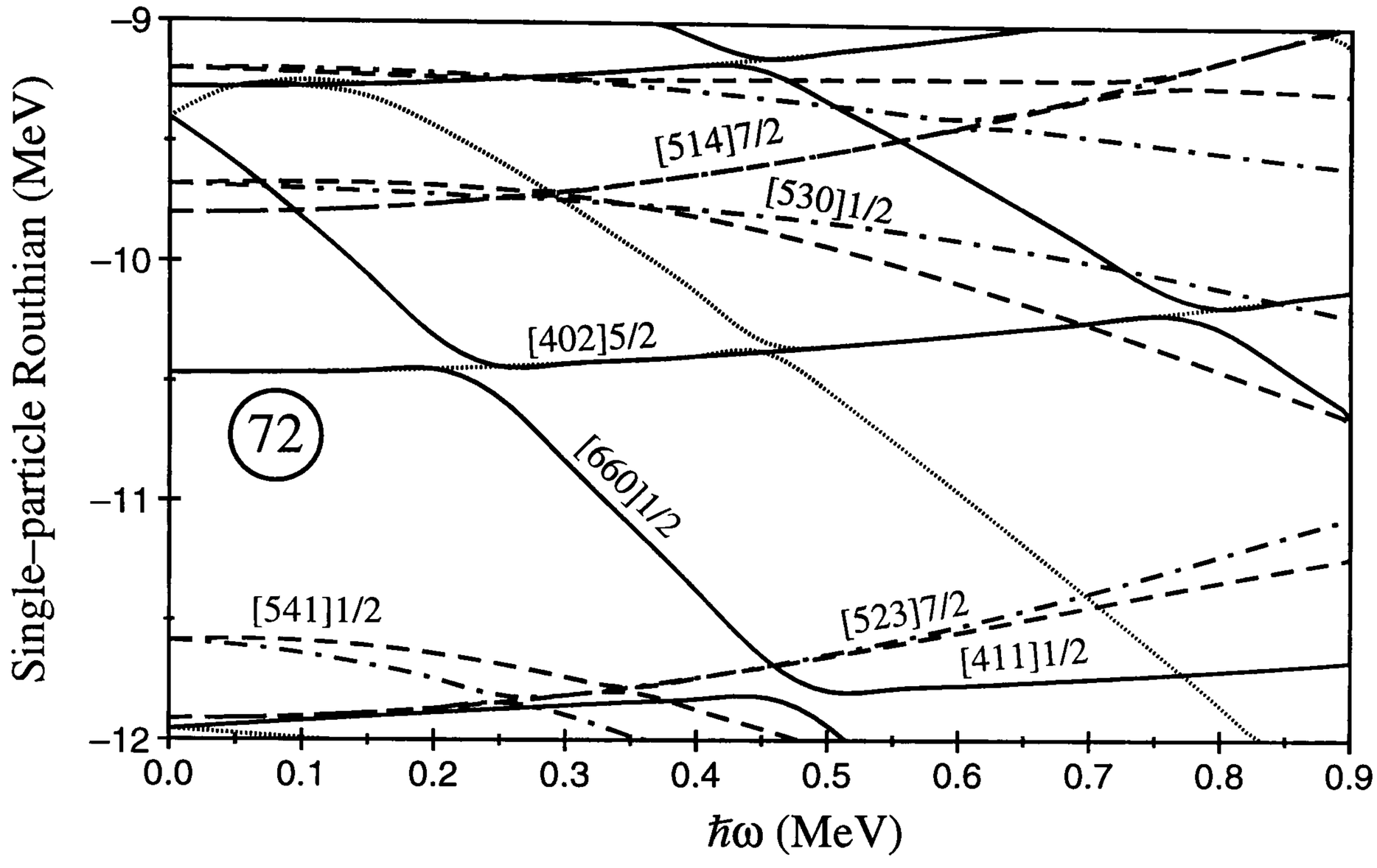

Figure 2.4: Single-particle Routhians calculated for ^{132}Nd at β_2=0.340 , β_4=0.022, γ=2°. Although, the levels are labelled by asymptotic quantum numbers each orbital should be labelled by its signature and parity (π, α): solid line (+,+1/2), dotted line (+,–1/2), dot-dash line = (–,+1/2) and dashed line = (–,–1/2).

the Coriolis force becomes sufficiently strong to align nucleons with the rotation axis with increasing rotational frequency, the time reversal symmetry is broken and the degeneracy is relieved. This results in the splitting of each level into two levels of opposite signature (section 2.3.1). The Coriolis and centrifugal forces are strongest for high-j, low-Ω orbitals. Single-particle Routhian diagrams are similar to Nilsson diagrams since the levels in both obey the Pauli exclusion principle. In the Nilsson model levels with the same quantum numbers (Ω, π) cannot cross, but exchange their trajectories and characteristics at the crossing. In Routhian diagrams, levels with the same parity and signature cannot cross. For example, the [402]5/2 (α=1/2) level and the [660]1/2 (α=1/2) level in Fig. 2.4 repel

each other at $\hbar\omega$=0.25MeV. Level interactions such as these correspond to large changes in the dynamic moment of inertia, $\Im^{(2)}$.

The total energy in the rotating frame is

$$E' = \sum_u e_u - \omega \sum_u \langle u|\hat{j_x}|u\rangle \tag{2.25}$$

The total angular momentum projection on the rotation axis, I_x is defined by

$$I_x = \sum_u \langle u|\hat{j_x}|u\rangle. \tag{2.26}$$

Certain orbitals are very sensitive to changes in rotational frequency and the slope of the orbitals in Fig. 2.4 are directly related to the rotational alignment of those orbits such that

$$\frac{de'}{d\omega} = -\langle u|\hat{j_x}|u\rangle = i_x \tag{2.27}$$

In Eq. 2.27, the quantity i_x is known as the single-particle alignment and the variation of i_x with rotational frequency is especially useful, for elucidating the nucleon configurations of rotational bands.

2.3.1 Symmetries in the Cranking Hamiltonian

Certain symmetries are preserved by the cranking Hamiltonian. At $\hbar\omega > 0$ MeV, the two-fold degeneracy of the Nilsson states is removed and each level splits into two levels of opposite *signature*. The signature quantum number defines reflection symmetry of the single-particle Routhian which is invariant with respect to rotation of 180° about the rotation axis. The rotation operator and its eigenvalues are defined as

$$\hat{R}\, u_\alpha = e^{-i\pi j_x} u_\alpha = e^{-i\pi\alpha} u_\alpha \tag{2.28}$$

where α is signature exponent quantum number. The signature exponent is an additive quantity and is hereafter called the signature. The eigenvalues restrict the spin sequences such that

$$\begin{array}{llll} I = 0, 2, 4 & \ldots & \alpha = 0 & r = +1 \\ I = 1, 3, 5 & \ldots & \alpha = 1 & r = -1 \\ I = \frac{1}{2}, \frac{5}{2}, \frac{9}{2} & \ldots & \alpha = +1/2 & r = -i \\ I = \frac{3}{2}, \frac{7}{2}, \frac{11}{2} & \ldots & \alpha = -1/2 & r = +i \end{array}$$

These sequences can be expressed succinctly as

$$\alpha \ = I \ mod 2 \tag{2.29}$$

The only other symmetry that remains in the cranking Hamiltonian is parity. Parity defines the symmetry with respect to space reflections through the origin. The parity operator $\hat{\pi}$ operates on the single-particle wavefunction with the following results.

$$\hat{\pi}\Psi(x) \ = \Psi(-x) \quad Odd. \tag{2.30}$$

$$\hat{\pi}\Psi(x) \ = \Psi(x) \quad Even. \tag{2.31}$$

The total signature and parity of a configuration is given by

$$\pi_{tot} \ = \prod_i \pi_i; \quad \alpha_{tot} = \sum_i \alpha_i. \tag{2.32}$$

2.3.2 Pairing and Rotation

The effects of rotational forces on relieving the two-fold degeneracy of the deformed Woods-Saxon potential has been discussed in the previous section. The role of attractive residual interactions between nucleons has not been considered. There is experimental evidence that suggests that nucleons couple so that their angular momenta sum to zero. The easiest way that this can be achieved is by pairing nucleons in time reversed orbits. It is observed that all even-even nuclei have ground state spins of $I{=}0\hbar$, whilst in odd-A nuclei the ground state spin is determined by the spin of the last nucleon. It is also observed that the binding energy of odd-even nuclei is less that the mean value of the neighbouring even-even nuclei. Further evidence for pairing can be found from the observations that the nuclear moment of inertia is generally 30% lower than the rigid body moment of inertia and the excitation energy of the first non-collective state in even-even nuclei is consistently greater than odd-even energies.

Time-reversal symmetry requires that for a particular angular momentum state $|j_{\nu 1}, \Omega_{\nu 1}\rangle$, there exists a time reversed state $|j_{\nu 1}, \Omega_{\nu \bar{1}}\rangle$. Both states are degenerate in the absence of rotation. Since both states are occupied simultaneously, the total angular momentum couples to zero. As the $|j_{\nu 1}, \Omega_{\nu 1}\rangle$ and $|j_{\nu 1}, \Omega_{\nu \bar{1}}\rangle$ orbit in opposite directions along the same spatial

path there must be two interactions per orbit. Interactions of this type result in the scattering of the two nucleons into another empty time reversed states ($|j_{\nu 2}, \Omega_{\nu 2}\rangle$, $|j_{\nu 2}, \Omega_{\nu \bar{2}}\rangle$) above the Fermi surface. The scattering into states of different energies smears out the Fermi surface. The inclusion of pairing correlations removes the clear definition between particle-hole states and it is more appropriate to discuss excitations in terms of particle-hole occupation probabilities. In order to include pairing effects in cranked shell model calculations, the Hartree-Fock-Bogoliubov (HFB) formalism is introduced.

2.3.3 HFB Formalism and Quasiparticles

The central idea behind the Hartree-Fock-Bogoliubov formalism stems from the analogy drawn between nucleonic motion and the dynamics of Cooper pairs in a superconducting metal [BMP58]. Bohr, Mottelson and Pines argued that pairing correlations in the nucleus, where a monopole pairing force which couples nucleons into pairs with zero angular momentum, were of a similar type to the Cooper effect in superconductors. The simplest way to couple nucleons is in time reversed orbits. The aim of the HFB formalism is to include the pairing interaction in the nuclear Hamiltonian. The Hamiltonian including a two-body monopole pairing interaction can be written as

$$\hat{H} = \hat{H}_{DWS} + \hat{H}_{Res} \tag{2.33}$$

$$\hat{H} = \sum_{\nu>0} \epsilon_\nu [a^\dagger_\nu a_\nu + a^\dagger_{\bar{\nu}} a_{\bar{\nu}}] - G \sum_{\nu 1, \nu 2} a^\dagger_{\nu 1} a^\dagger_{\bar{\nu 1}} a_{\bar{\nu 2}} a_{\nu 2} \tag{2.34}$$

where $a^\dagger_\nu$ and a_ν are the creation and annihilation operators that create or destroy particles in a state $|\nu\rangle$ and G is the two body interaction strength. The first term in Eq. 2.34 is the sum of the single-particle energies ϵ_ν and describes the motion of nucleons up to the Fermi surface in the deformed Woods-Saxon potential. The second term in Eq. 2.34 refers to the pairing interaction that annihilates of a pair of nucleons in the state $|\nu_2\rangle$ and its time reversed partner $|\bar{\nu_2}\rangle$ and creates the nucleons in the time reversed states $|\nu_1\rangle$ and $|\bar{\nu_1}\rangle$. This corresponds to the scattering of particles at the Fermi surface illustrated in Fig 2.5.

The form of the residual interaction can be rewritten as

$$\hat{H}_{Res} = -\frac{1}{4} G P^\dagger P \tag{2.35}$$

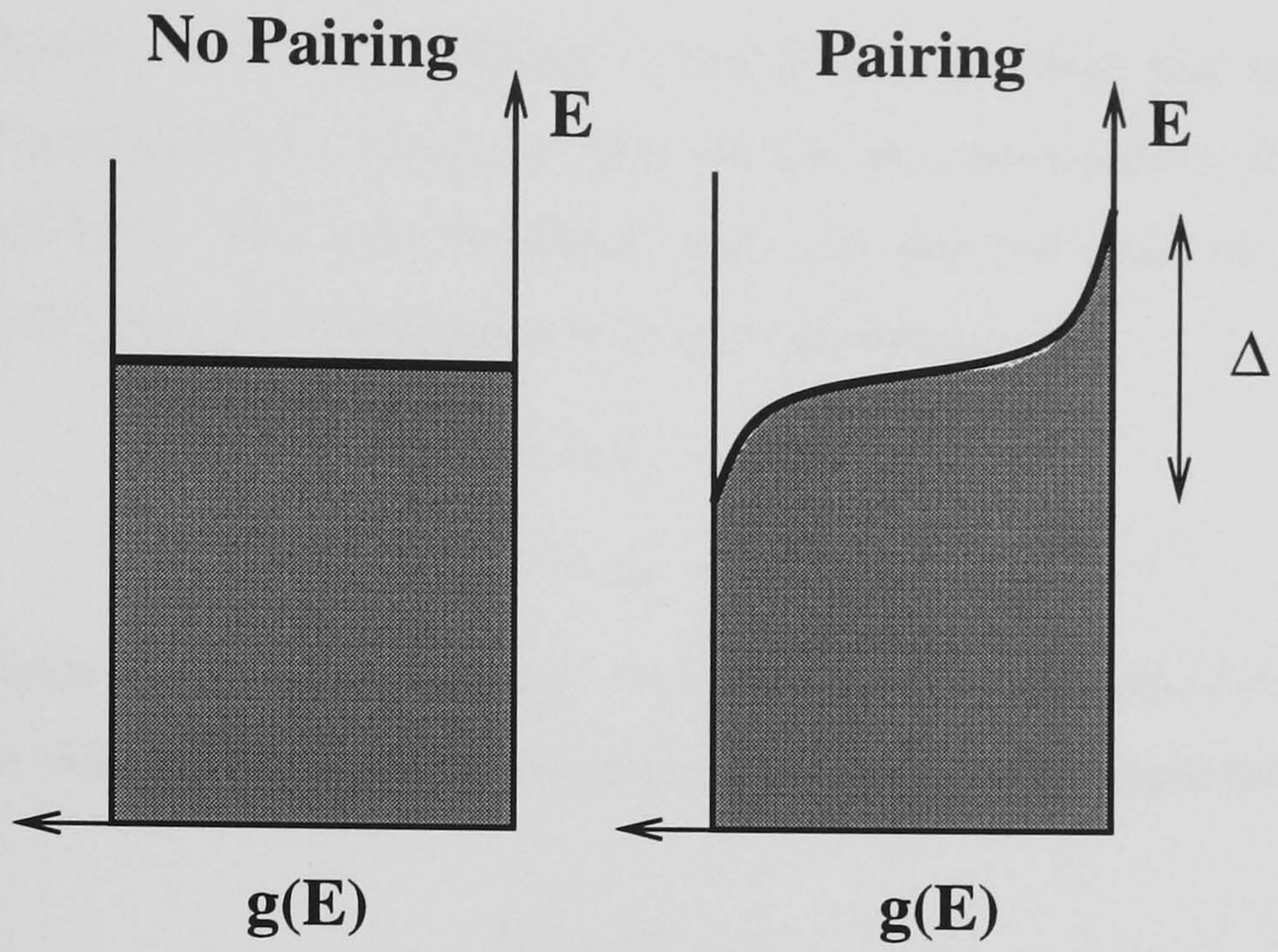

Figure 2.5: Figure illustrating the density of states $g(E)$ as a function of energy E and the effects of the pairing interaction on the Fermi surface. When pairing is not considered the Fermi surface is completely level. When pairing is treated, the nucleons scatter into new time-reversed orbits and smear out the Fermi surface. The smearing of the Fermi level is the origin of the pair gap, Δ.

where $P^\dagger$ and P are the pair creation and annihilation operators and are defined as

$$P^\dagger = \sum_\nu a^\dagger_\nu a^\dagger_{\bar{\nu}}; \qquad P = \sum_\nu a_{\bar{\nu}} a_\nu \tag{2.36}$$

To simplify calculations, the residual interaction is rewritten to account for the energy increase of the condensate per particle added by introducing the chemical potential, λ, so that

$$\hat{H}_{Res} = -\frac{1}{2}\Delta[P^\dagger + P] - \lambda\hat{N} \tag{2.37}$$

where Δ is the pairing gap and $\hat{N}$ is the particle number operator. This formulation of the pairing Hamiltonian allows the pair creation and annihilation operators to be treated separately rather than simultaneously as in Eq. 2.35. If the operators are not operated simultaneously the particle number is not conserved. This corresponds to the transfer of particles to and from the condensate. Since the nucleus has a definite number of particles the chemical potential, λ must be used as a Lagrange multiplier to conserve the number of particles.

A further simplification to the pairing interaction is to treat the nucleus as a non-interacting gas of quasiparticles. Quasiparticles are a linear combination of particle and hole occupation probabilities. The transformation from the particle basis to the quasiparticle basis is obtained through the Bogoliubov-Valatin transformation

$$\alpha_\nu = U_\nu a_\nu^\dagger + V_\nu a_{\bar{\nu}}, \tag{2.38}$$

$$\alpha_{\bar{\nu}} = U_\nu a_{\bar{\nu}}^\dagger - V_\nu a_\nu^\dagger, \tag{2.39}$$

where the coefficients U_ν and V_ν are chosen through the minimisation of expectation values of $\hat{H}$ according to the Hartree-Fock variational method with the constraint

$$U_\nu^2 + V_\nu^2 = 1. \tag{2.40}$$

The solution of the Schrödinger equation requires trial wavefunctions of the form

$$|\Psi_{BCS}\rangle = \prod_\nu \left(U_\nu + V_\nu a_\nu^\dagger a_{\bar{\nu}}^\dagger |0\rangle \right) \tag{2.41}$$

where $|0\rangle$ is the particle vacuum state and $|\Psi_{BCS}\rangle$ is the quasiparticle vacuum. The energy eigenvalues in the quasiparticle basis are defined as

$$E_\nu = \pm\sqrt{(\epsilon_\nu - \lambda) + \Delta^2}. \tag{2.42}$$

Eq. 2.42 suggests that for each single-particle level there are two quasiparticle levels, one positive and one negative, that are reflections of each other about the Fermi surface.

The HFB treatment of the cranking Hamiltonian leads to quasiparticle excitations in the rotating frame, where the Hamiltonian is defined as

$$h_{qp} = h - \hbar\omega j_x - \Delta(P^+ + P) - \lambda\hat{N} \tag{2.43}$$

The eigenvalues of the HFB Hamiltonian are the quasiparticle Routhians. An example of quasiparticle Routhians are displayed in Fig 2.6. The conventional labelling of quasiparticle diagrams follows the convention noted in Table 2.3.3.

Although the quasiparticle diagram (Fig 2.6) has a number of similar features to the single-particle Routhian diagram (Fig 2.4), there are some obvious differences. The quasiparticle diagram is constructed relative to a reference configuration. The reference or vacuum configuration corresponds to the point where all the negative energy states are filled. This is another way of expressing the position of the Fermi surface. The excitation energy of the vacuum is the sum of the energies of the occupied states. If a level in Fig 2.6

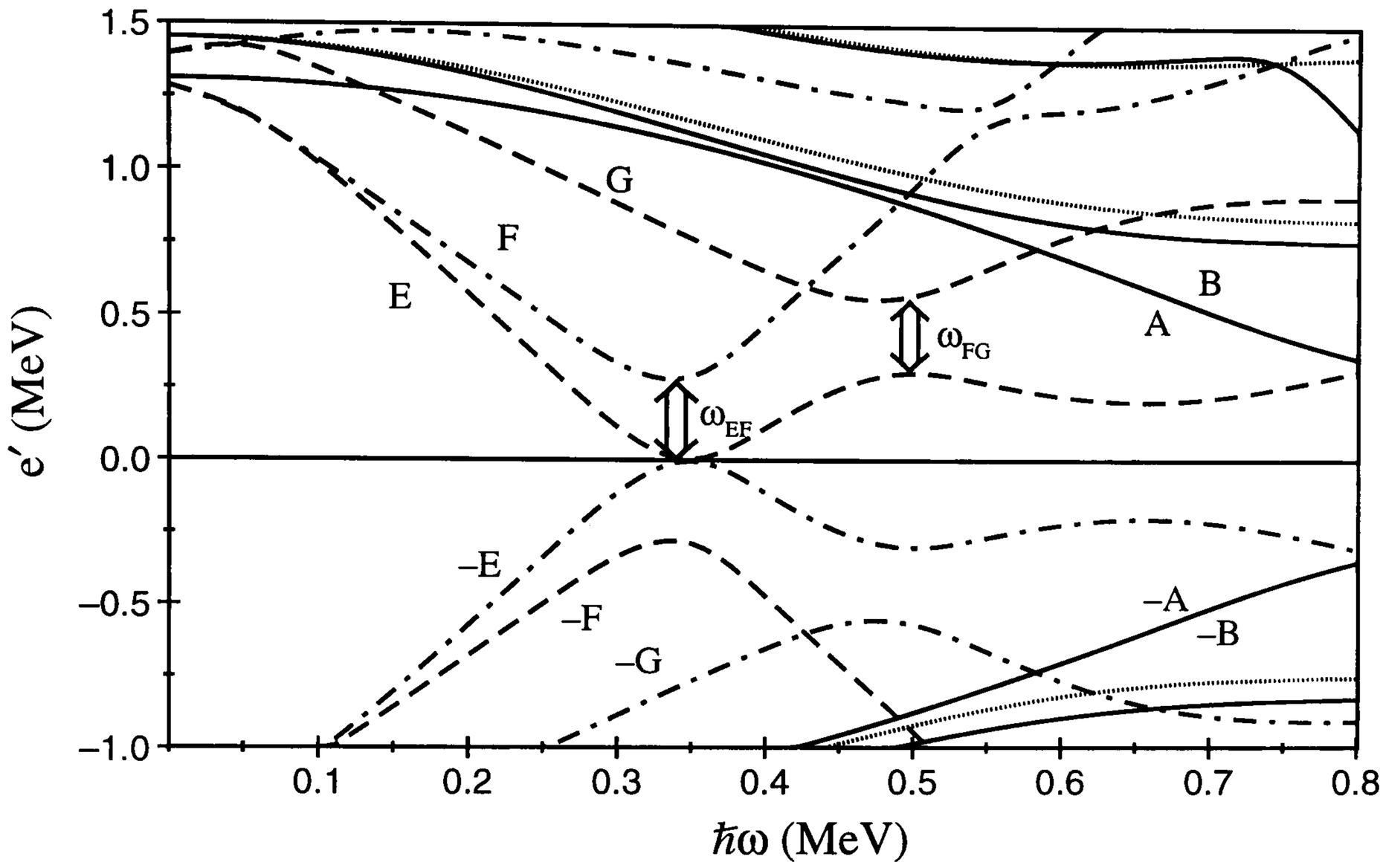

Figure 2.6: Quasiproton Routhians calculated for ^{132}Nd at β_2=0.340 , β_4=0.022, $\gamma = 2°$. Each orbital should be labelled by its signature and parity (π, α): solid line (+,+1/2), dotted line (+,−1/2), dot-dash line = (−,+1/2) and dashed line = (−,−1/2).

(π, α)	Protons	Neutrons
(+, +1/2)	A, C, ...	a, c, ...
(+, −1/2)	B, D, ...	b, d, ...
(−, +1/2)	F, H, ...	f, h, ...
(−, −1/2)	E, G, ...	e, g, ...

Table 2.1: Convention for labelling quasiparticle Routhians

is occupied, its conjugate (reflection in e′ about 0 MeV) is unoccupied. For example if E is occupied in Fig 2.6, then –E is empty. It should also be noted that the conjugate levels have opposite signature. As with Fig 2.4, levels with the same quantum numbers cannot cross and each level will exchange character at the crossing. A crossing occurs when the Coriolis force becomes strong enough to break a pair of nucleons and align their orbital angular momentum with the rotation axis. In Fig 2.6 there is an EF crossing at 0.35MeV. For a crossing to occur both the E and F levels must be unoccupied and the signature must be conserved at the crossing. If there was a quasiproton in the E level, the crossing would not occur and would be described as blocked. In this case, the next available crossing would occur at 0.5 MeV between the F and G levels. Both these crossings are illustrated in Fig 2.6.

The energy required to break a pair of quasiparticles is specified by the energy gap at $\hbar\omega = 0$ MeV. As with its single-particle counterpart, high-j, low-Ω orbitals in Fig 2.6 are lowered in energy by the Coriolis and centrifugal forces. For example the E and F levels originate from the $h_{11/2}$ states and lie at high excitation energies in the absence of rotation. At a crossing the internal structure of the nucleus is changed and a new rotational structure will become yrast.

2.3.4 Total Routhian Surface (TRS) Calculations

The Strutinsky shell correction procedure can be adapted to predict the total energy of a rotating nucleus (total Routhian). This is achieved by altering the static liquid drop term so that it incorporates the smooth energy variation of a rotating liquid drop, E_{RLDM}. The shell model terms in Eq. 1.42 replace the static density of states terms with a spin density dependence so that the expression for the rotating Strutinsky scheme is

$$E = E_{RLDM} + E_{sh}(I) - \tilde{E}_{sh}(I). \tag{2.44}$$

The total Routhian of the nucleus as a function of deformation can be obtained using the formalism of Eq. 2.44 and the pairing correction energies. This is summarised as

$$E^{\omega}(Z,N,\hat{\beta}) = E^{\omega}_{Macro}(Z,N,\hat{\beta}) + \Delta E^{\omega}_{Shell}(Z,N,\hat{\beta}) + \Delta E^{\omega}_{Pair}(Z,N,\hat{\beta}) \tag{2.45}$$

where $\hat{\beta}$ represents all the surface deformation parameters. $E^{\omega}_{Shell}(Z,N,\hat{\beta})$ is taken directly from the Strutinsky procedure and is calculated using a deformed Woods-Saxon potential.

In this work, the pair gap has been calculated at zero rotational frequency ($\Delta = \Delta_{BCS}$) and has been modelled so that the pair gap has decreased to 50% at a critical frequency, ω_c=0.70 MeV/$\hbar$. The pair gap is expressed in terms of the critical frequency in as

$$\Delta(\omega) = \Delta_{BCS}\left[1 - \frac{1}{2}\left(\frac{\omega}{\omega_c}\right)^2\right] \qquad \omega \leq \omega_c. \tag{2.46}$$

$$\Delta(\omega) = \Delta_{BCS}\left[\frac{1}{2}\left(\frac{\omega}{\omega_c}\right)^2\right] \qquad \omega > \omega_c. \tag{2.47}$$

The total Routhian is calculated on a lattice in deformation space ($\hat{\beta} = \beta_2, \beta_4, \gamma$) at a fixed rotational frequency and minimised with respect to the shape parameters to obtain an equilibrium deformation. The results of different rotational frequencies are interpolated between the lattice points.

The results of these calculations are usually displayed as an energy contour in the $\beta_2 - \gamma$ plane, for example see Fig. 2.7. These contours are the Total Routhian Surface (TRS) plots. In these plots, different minima correspond to different nuclear shapes. Fig 2.7 is taken from calculations for ^{133}Ce, a nucleus that is known to be 'soft' with respect to the triaxiality parameter, γ and is extremely sensitive to the alignment of particles in the $h_{11/2}$ shell. This results in a number of different configurations that are represented by the different minima in the plot.

2.4 Superdeformation

Studies of superdeformation have been of great interest in recent years. The phenomenon arises when it becomes possible to populate states in a secondary minimum in the fission barrier. Experimental evidence for a second minimum came initially from spontaneous fission studies. Experiments investigating fission isomers revealed that the fission half-lives of excited states were much shorter than expected for ground state fission [Pol62]. These observations led to the interpretation of the decay process proceeding from metastable states in a secondary minimum through a narrower barrier width, thus increasing the probability of fission (see Fig 2.8). Deformation in fission isomers originates from the strong Coulomb repulsion between the large number of protons in these nuclei (Z≈100).

Superdeformation is also known to occur as the result of the delicate interplay between quantal shell structure and collective rotation. The first evidence for superdeformed bands

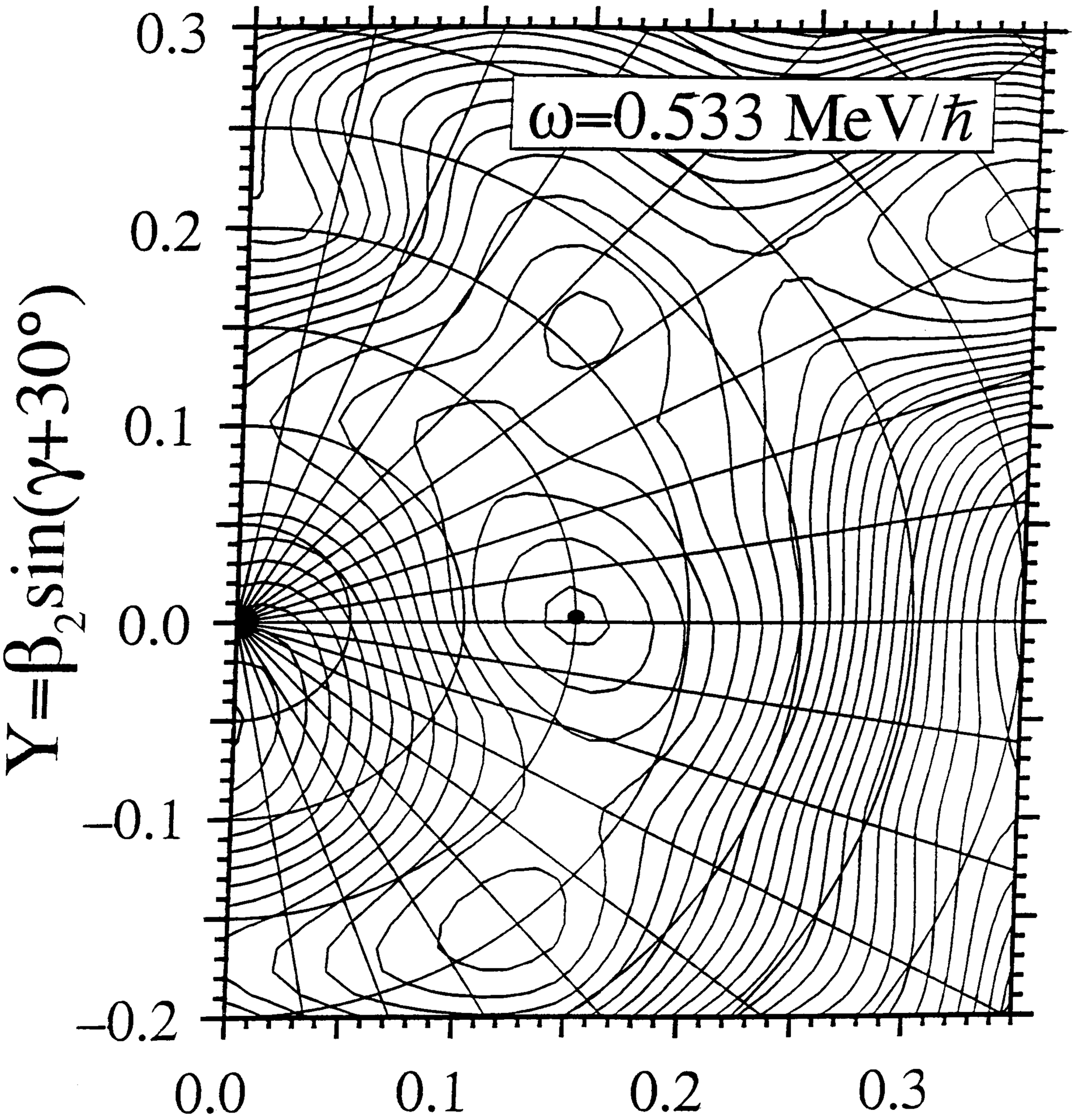

Figure 2.7: Total Routhian surface calculations for the (π, α)= (–,+1/2) quasiparticle configuration in ^{133}Ce.

at high-spin came from analysis of the γ-ray continuum in ^{152}Dy [Nya84] and discrete line spectra were observed later for ^{132}Ce [Nol85]. A deformed simple harmonic oscillator potential shows that with increasing deformation certain levels intrude/extrude into states from different oscillator shells forming new shell closures. Fig 2.9 shows that regions of low level density occur for nuclei possessing integer axis ratios. This is in excellent agreement with the increasing amount of experimental data on superdeformed bands which have revealed nuclei with axis ratios of 3:2 (^{132}Ce) [Kir87] and 2:1 (^{152}Dy) [Twi86]. Rotational forces can also effect the position of the high-j intruder states which may stabilise semi-magic closures (see Fig. 2.4).

At the present time there are five regions of the chart of nuclides that exhibit superdeformation; A≈80 [LaF95], A≈130 [Nol85], A≈150 [Twi86], A≈190 [JK91] and most recently a superdeformed band with a 3:2 axis ratio has been observed in the A≈60 region (^{62}Zn) [Sve97].

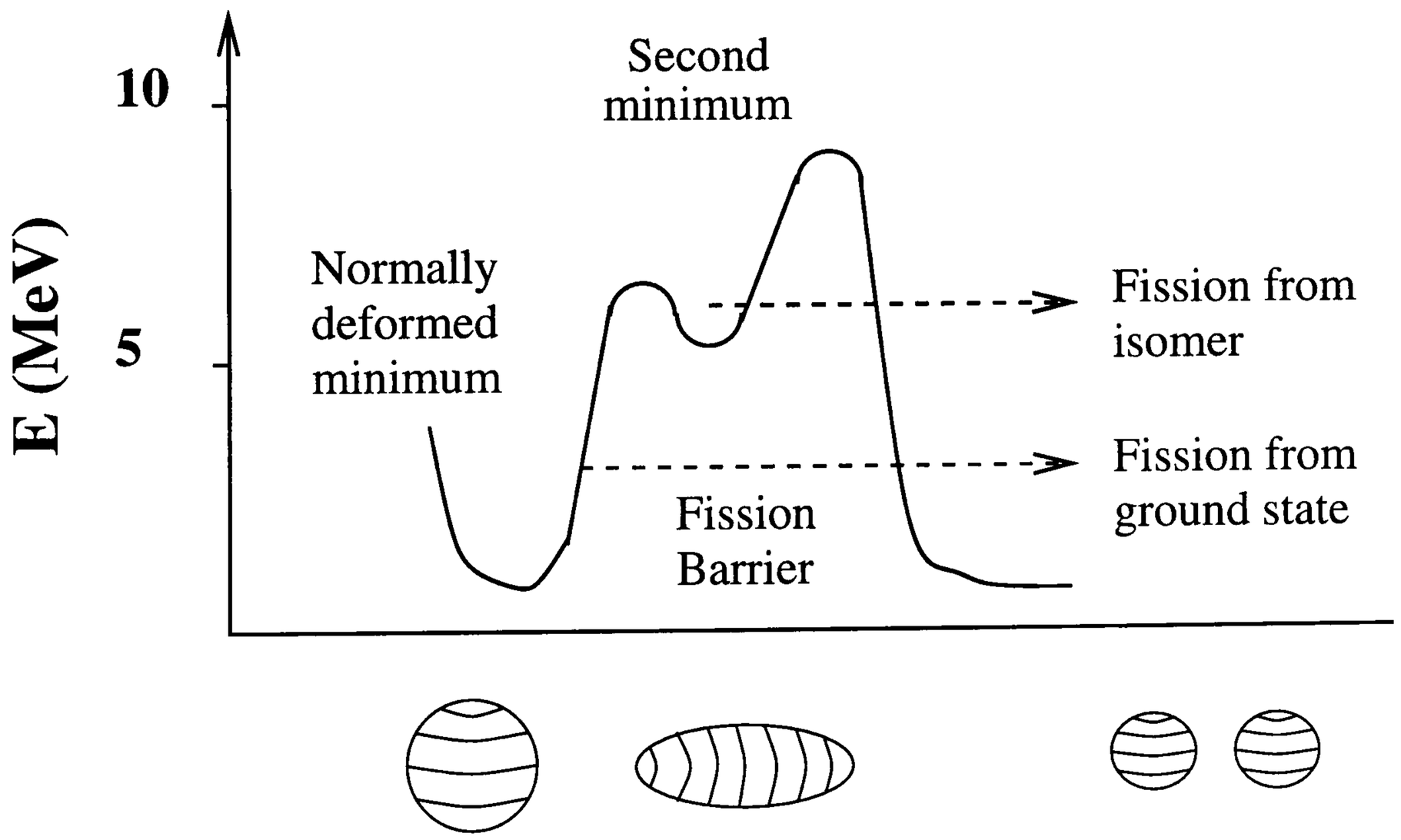

Figure 2.8: Schematic plot of the fission barrier indicating the decay from fission isomers.

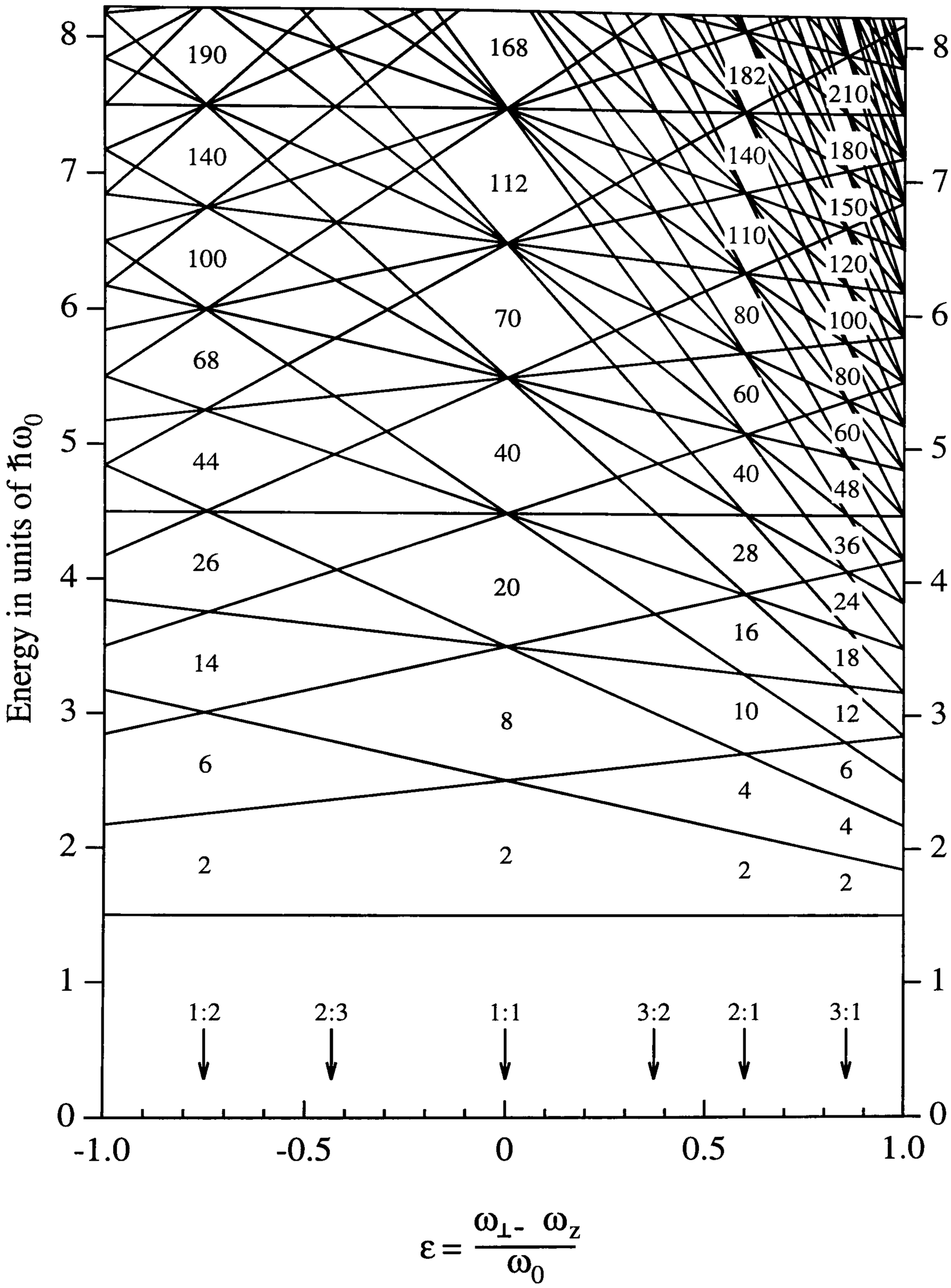

Figure 2.9: Simple harmonic oscillator levels plotted as a function of deformation. New shell closures become apparent at certain major-minor axis ratios.

2.4.1 The A≈130 Region

The A≈130 region is known to accommodate a variety of exotic rotational structures. The normally deformed structures are built upon configurations involving the $h_{11/2}$ shells for both proton and neutrons. Experimental studies have shown that in this mass region, the nuclear cores are soft with respect to γ, the triaxiality parameter in the quadrupole description of rotating shapes [LFM83] (see Fig 2.7). In particular, it has been shown that the soft cores are extremely succeptable to the core polarising effects of valence orbitals. For the low deformation structures, the proton Fermi surface lies at the bottom of the $h_{11/2}$ subshell tending to drive the nucleus to prolate deformations. In contrast, the Fermi level for neutrons lies at the top of the $h_{11/2}$ mid-shell causing the nucleus to adopt an oblate shape.

The presence of intruder states originating from the $f_{7/2}$, $h_{9/2}$ and $i_{13/2}$ subshells and shell closures are thought to be instrumental in producing highly elongated nuclear shapes. Fig. 2.10 displays the known superdeformed bands at the present time in the A≈130 region. The superdeformed region appears to end at the lanthanum isotopes (Z=57). TRS calculations suggested that the barium (Z=56) isotopes do not exhibit a pronounced second minimum shape and to date superdeformed bands have not been found in experimental high-spin studies in these isotopes. The higher Z nuclei have also been shown to possess highly prolate deformed shapes, although fewer experimental high-spin studies have been performed using the present generation of spectrometer arrays.

Superdeformation in the lower-Z region appears to be stabilised by proton shell closures at Z=58 and Z=60 that remain intact with increasing rotational frequency. The low proton level density has implied that the numerous excited bands in this region are formed by neutron excitations with configurations involving the $\nu i_{13/2}$ intruder states. All nuclei in Fig. 2.10 contain some bands that include the N=6 unnatural parity states. The role of high-j intruder orbitals in enhancing deformation is currently of great contemporary interest. The work detailed in this thesis aims to discern directly the shape driving effects of the states originating from the N=6 oscillator shell.

The role of proton levels in the A≈130 region has been investigated in recent years. Ragnarsson [Rag96] suggested that holes in the $g_{9/2}$ states can stabilise superdeformed bands. Evidence for the deformation driving role of the $g_{9/2}$ orbitals in stabilising deformation has

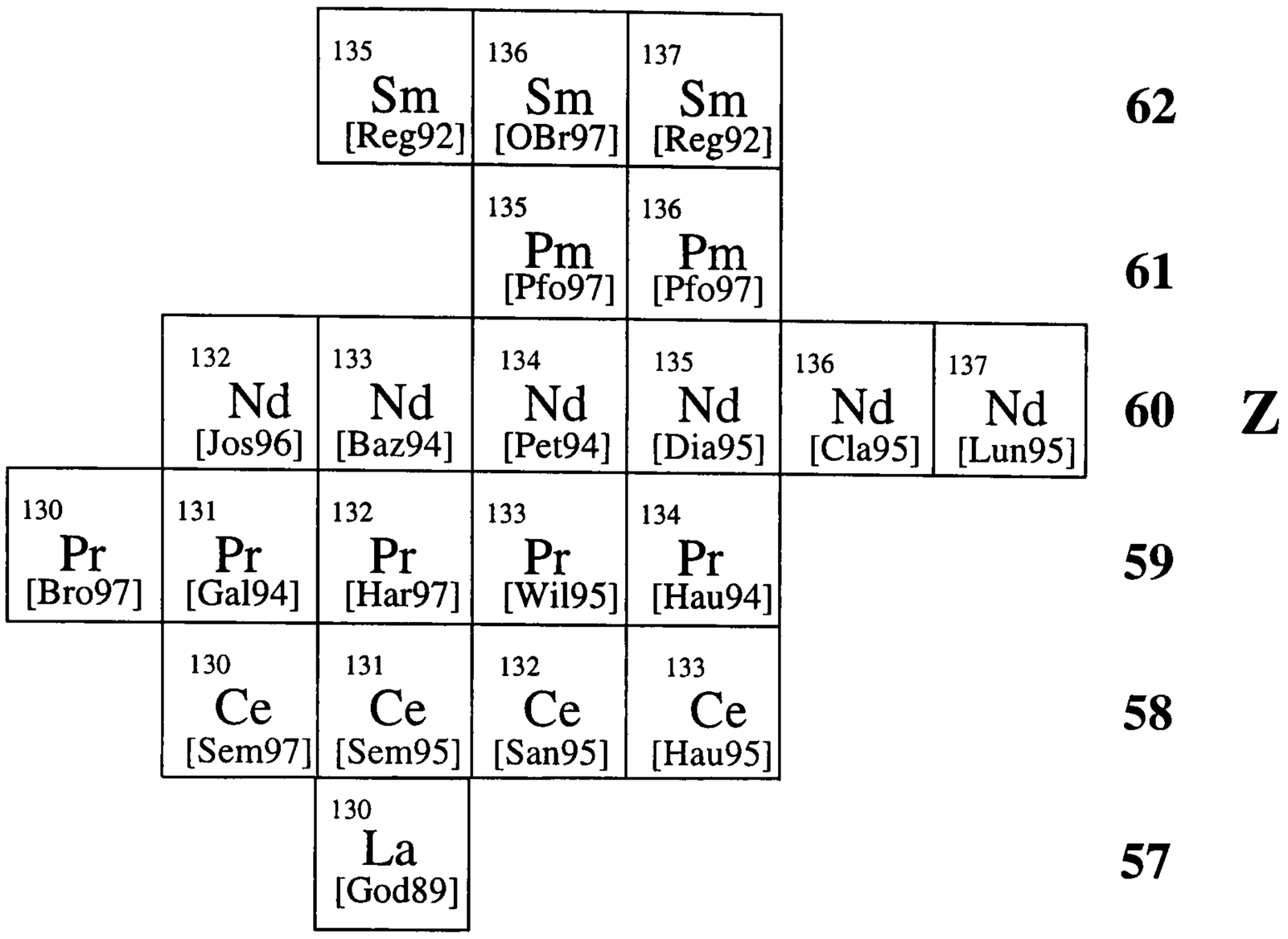

Figure 2.10: The superdeformed A≈130 mass region. These nuclei have superdeformed bands based upon high-j intruder configurations. The references describe results from recent experiments. The references are by no means exhaustive.

been found in the praseodymium isotopes [Wil95], [Gal94]. In the same study as detailed in Chapter 5, superdeformed bands were observed in the low-mass praseodymium (Z=59) [Bro97], [Har97] and higher-mass promethium isotopes (Z=61) [Pfo97]. These data are sure to improve the present understanding of the global systematics of this mass region.

A further intriguing feature of this mass region is the number of second minimum structures that have been linked into the normally deformed level schemes allowing an estimation of the spins, parities and excitation energies of the superdeformed bands. Generally, the decay path from superdeformed bands is, for most cases, highly fragmented, rendering it difficult to link the superdeformed bands into the well defined level schemes. It is interesting to note that many of the neodymium isotopes display linking transitions, whereas for the neighbouring even-Z cerium structures a definite path cannot be discerned.

Chapter 3

Gamma-Ray Spectroscopy

The study of γ rays emitted from highly excited nuclei can reveal much about the internal structure of the nucleus. In recent years the importance of information obtained from γ-ray spectroscopy has lead to the development of large spectrometer arrays comprised of high-resolution germanium detectors. Complementary advances have also been made in the associated techniques in data acquisition and analysis and the development of ancillary detectors.

This chapter introduces the principal concepts behind γ-ray spectroscopy. The interactions of γ-rays and their detection are discussed followed by a description of the germanium spectrometers used in the experiments detailed in this thesis. The desirable properties of large spectrometer arrays and a qualitative description of the GAMMASPHERE are outlined before a general description of high-fold data and the methods employed for its analysis. A description of heavy ion fusion evaporation reactions precedes a qualitative overview of the MICROBALL charged particle detector array. A short summary concludes the chapter.

3.1 Gamma-ray Detection

3.1.1 Gamma-Ray Interactions

There are three major interaction mechanisms for γ rays in matter that are significant in radiation measurement; photoelectric absorption, Compton scattering and pair production. These processes involve the complete or partial transfer of the incident photon energy to the surrounding medium. The fundamental processes are described below and are illustrated in Fig. 3.1.

Photoelectric absorption

Photoelectric absorption occurs when a photon undergoes an interaction with an atom and completely transfers its energy to one of the bound electrons from the inner shells. This results in the electron being ejected from the atom with an energy E_e given by

$$E_e = h\nu - E_b \tag{3.1}$$

where $h\nu$ is the photon energy and E_b is the binding energy of the photoelectron. The photoelectric effect creates an ionised absorber atom in the matter with a vacancy in one of the electron shells. Vacancies are filled by either the capture of a free electron or the rearrangement of electrons from other shells. The rearrangement of electrons between shells produces characteristic X rays that can be reabsorbed by electrons in less bound shells producing secondary photoelectrons. The photoelectric effect predominates at low energies ($E_\gamma \leq 20$keV) and is also enhanced in high Z materials.

Compton scattering

Compton scattering is an interaction between a photon and a loosely bound outer electron in the absorbing medium. In this mechanism the incident photon is deflected through an angle, θ, from its original direction transferring a portion of its energy to an electron. The energy of the scattered photon has an angular dependence and it can be shown through conservation of energy and momentum that

$$E'_\gamma = \frac{E_\gamma}{1 + \frac{E_\gamma}{m_0 c^2}\cos\theta} \tag{3.2}$$

where E_γ and E'_γ are the energies of the incident and scattered photons respectively, θ is the scattering angle of the photon with respect to its initial direction and m_0c^2 is the rest mass

of the electron. It can be seen from Eq. 3.2 that the photon can transfer a range of energies to the electron. The maximum transfer occurs for a scattering angle of 180°. Since the photon only partially transfers energy to the electron, multiple scatters must be detected in order to obtain the total photon energy. If the photon scatters out of the crystal, only a fraction of the total energy will be detected giving a false reading for the γ-ray energy. Compton scattering is the most probable process for the γ-ray energies in the range 200 - 1000 keV and the range of energy values constituting the Compton continuum is the major source of background events in γ-ray spectra. In order to minimise the background due to Compton scattering, escape suppression methods are employed in γ-ray detection, (see section 3.2).

Pair production

A γ-ray can produce an electron-positron pair providing the γ-ray has an energy greater than the rest mass of the pair ($2m_0c$=1.022 MeV). Pair production must take place in the Coulomb field of the absorber atom in order to conserve energy and momentum. If the photon energy is larger than 1.022 MeV then the the excess ($h\nu$ – 1.022 MeV) is equally divided between the electron and the positron as kinetic energy. When the positron has slowed down to the thermal velocity of an atomic electron, it will annihilate with an electron and create two γ rays of energy 511 keV that will move in opposite directions from each other in order to conserve momentum. Pair production is important for γ rays in the energy range 5-10 MeV.

3.1.2 Semiconductor Detectors

A periodic lattice of atoms forming a crystalline solid establishes allowed energy bands that are separated by forbidden energy regions or band gaps. In pure materials, electrons are confined to the allowed energy bands. A simplified representation defines the electrical conductivity in terms of valence and conduction bands separated by an energy gap. The valence band corresponds to electrons that are bound to specific lattice sites and therefore do not contribute to the conductivity. The conduction band represent those electrons that are free to migrate through the crystal. Insulators and semiconductors are characterised primarily by the size of the band gap. The valence band in insulators and semiconductors

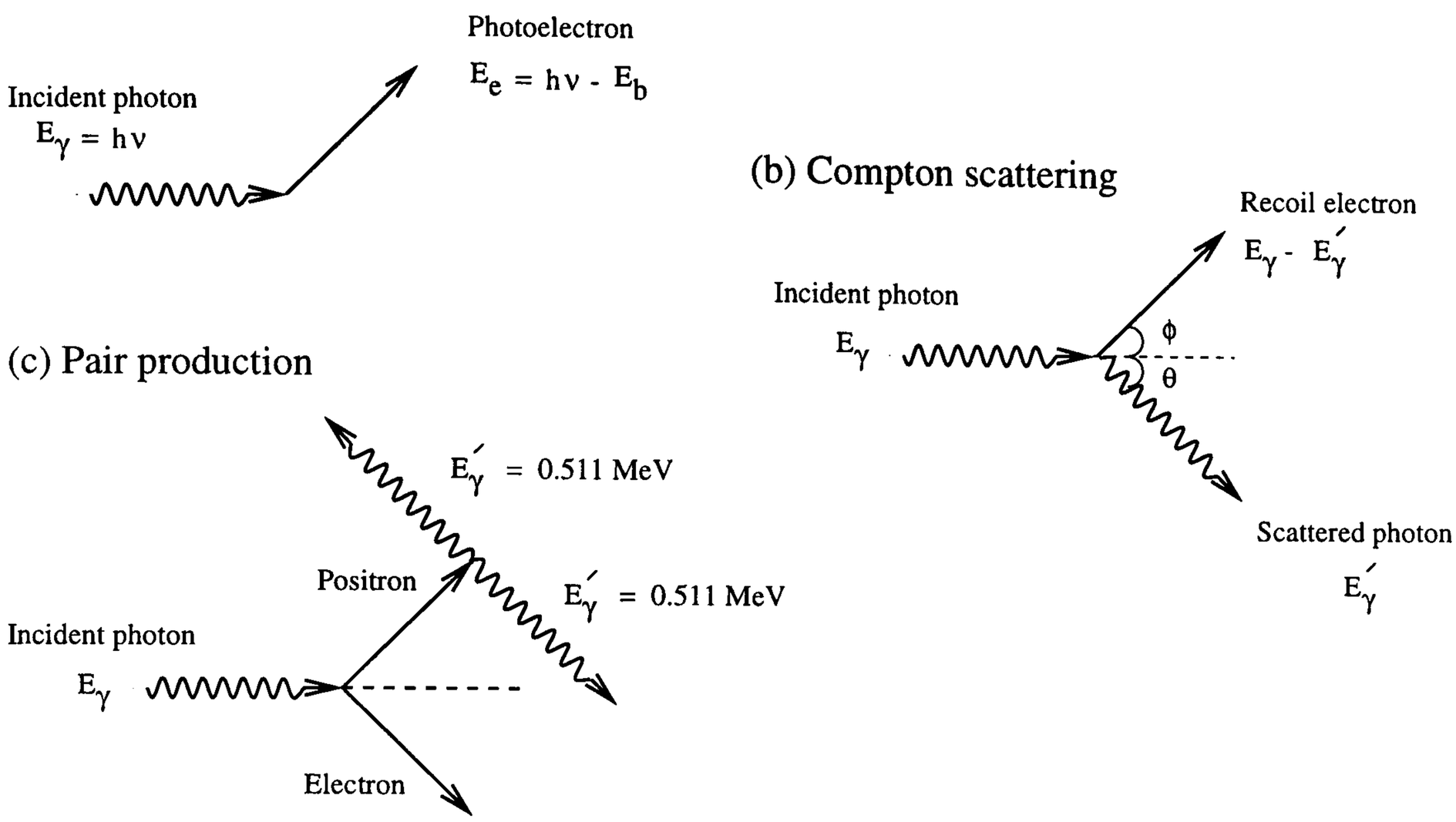

Figure 3.1: Schematic diagram illustrating the interactions of γ rays with matter.

is interpreted as being completely filled, however if the band gap energy is small enough, thermal excitations can promote electrons across the gap into the conduction band. Insulators typically have band gaps that are generally greater than 5eV, while semiconductors have much lower band gaps around 1eV.

When a γ ray passes through a section of semiconductor, electron-hole pairs are formed along the length of the track by one of the processes defined in section 3.1.1. Creation of an electron-hole pair corresponds to the breaking of a covalent bond in the crystal and promoting the electron into the conduction band. The energy expended by creating an electron-hole pair is known as the ionisation energy, ϵ. Since this quantity is independent of the energy of the incident γ ray, the number of pairs created is proportional to the γ-ray energy.

In any crystal there will be an intrinsic charge flow. Such charge flow in the detector is a source of noise and would seriously degrade energy measurements made with the detector. To combat spurious currents, p- and n-type semiconductors are placed in direct contact to form a p-n junction. When a direct contact is made, a discontinuity in the conduction electron density occurs and electrons/holes become free to diffuse from regions of high

concentration to low concentration. Therefore, electrons from the n-type material will diffuse into the p-type material, where they will combine with holes leaving behind regions of immobile positive charges in the form of ionised donor impurities. A complimentary hole charge flow will take place from the p-type material which leaves behind an acceptor site that has picked up an extra electron. The net result is a region of positive space charge in the n-type material and a negative space charge in the p-type material. The establishment of such regions resists further charge flow across the junction. The region over which this charge inbalance exists is depleted of charge carriers and is known as the depletion region. The depletion region is the active volume in which γ-ray detection occurs. The application of a large reverse-bias voltage which in effect makes the p-type side more negative with respect to the n-type side, can increase the size of the depletion region and make γ-ray detection more efficient. Natural germanium can tolerate a depletion region of 2 or 3 mm before electrical breakdown occurs, yet γ rays are deeply penetrating and require as large a depletion region as reasonably possible. The thickness of the depletion region is defined as [Kno89]

$$d = \left[\frac{2\epsilon V}{eN}\right]^{\frac{1}{2}} \tag{3.3}$$

where V is the reverse-bias voltage, N is the net impurity concentration in the material, ϵ is the ionisation energy and e is the electron charge. At a given high reverse-bias voltage, the depletion region can only be increased by decreasing the net impurity concentration. This can be achieved by two methods. The introduction of an equal quantity of dopant material to compensate for the existing impurities will reduce the net impurity concentration. Also, recent advances in detector fabrication have led to the manufacture of hyperpure germanium (HPGe) detectors which have impurity concentrations at the 10^9 atoms/cm^3 level.

3.1.3 Hyperpure Germanium Detectors

It has recently become possible to manufacture large single crystals of hyperpure germanium. As well as having low impurity concentrations, HPGe detectors have the advantage that their purity is not temperature dependent as antecedent lithium drifted germanium detectors were. HPGe detectors must be cooled to liquid nitrogen temperatures during

operation to minimise noise of thermal origin. This is absolutely essential since germanium has a small band gap of 0.67eV. The ability to produce large volume detectors is particularly useful for γ-ray spectroscopy, since γ radiation is extremely penetrating. Detectors used for γ-ray spectroscopy are constructed in a bulletised coaxial configuration. In a coaxial configuration the detector is fabricated so that one electrical contact is formed at the outer surface of a cylindrically shaped germanium crystal, whilst the second contact is formed by removing a section from the core and lining the inner cylindrical surface with another contact. The front end is covered by the outer contact and has rounded edges to eliminate low-field regions. The bulletised coaxial configuration is illustrated in Fig. 3.2. The active detector volume can be as much as 400cm^3, depending on how long the detector is made in the axial direction

A reverse-bias voltage of $\approx$ 3500V can be applied across the crystal to enlarge the depletion layer. The depletion zone extends further into the crystal as the voltage is increased. The increased electric field quickly sweeps the charge carriers to the terminals, where the current flow at the central terminal constitutes the basic electrical signal. The ionisation potential, ϵ, is $\approx$3eV and so the number of charge carrier pairs is large. For example, for a 1MeV γ ray around 30,000 electron-hole pairs would be created. The effect of greater amounts of charge being liberated per γ ray leads to fewer statistical fluctuations (relative

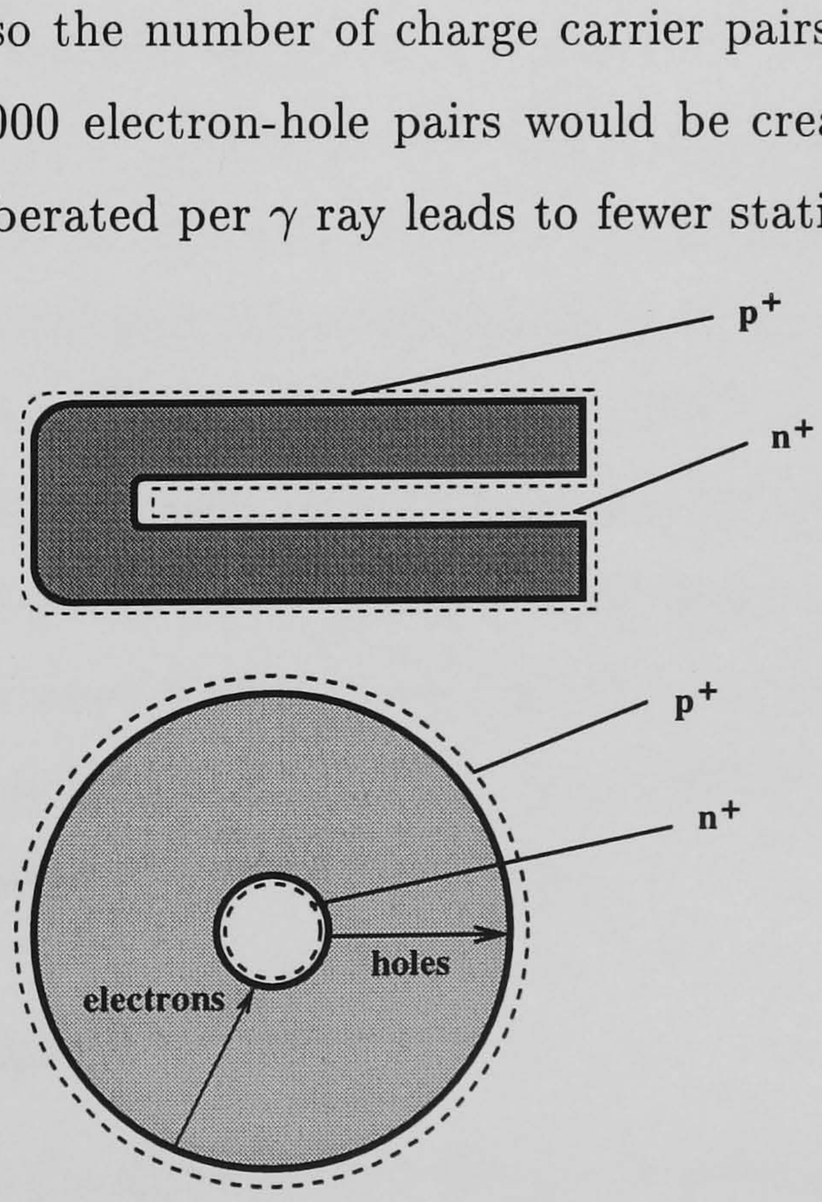

Figure 3.2: Cross section through the axis (top) and perpendicular to the axis (bottom) of an n-type bulletised coaxial germanium detector.

to inorganic scintillators) in the number of carriers produced for a particular event and an improvement in detector resolution by increasing the signal to noise ratio. Typically, HPGe detectors have an energy resolution of ≈2 keV for a characteristic 1.33MeV γ ray from a ^{60}Co radioactive source.

3.1.4 Inorganic Scintillators

Scintillation detectors operate by a different mechanism to semiconductor detectors. In a scintillator, the incident γ rays excite electrons across the band gap of a luminescent crystal, where they de-excite by the emission of a visible photon. The band gap is usually too large for the electron to de-excite to the valence band by emitting a photon in the visible range and so activator materials are usually added. Activators introduce states in the forbidden energy gap so that de-excitation can proceed through the activator states to the valence band by the emission of visible photons. The scintillator material is optically coupled to a photomultiplier tube. Visible photons in the photomultiplier excite photoelectrons at a photocathode, where they are multiplied to produce an adequate current pulse for measurement. Ideally scintillator detectors should be transparent to their own luminescence, and have a linear light output that is proportional to the energy deposited in the detector. The scintillation efficiency should be high and the material must have a similar refractive index to glass to allow efficient coupling of the scintillator light to the photomultiplier tube. Fluctuations in photon emission, photoelectron production and coupling to the photomultiplier indicate that there are a number of inefficient steps and this is reflected by the relatively poor energy resolution of scintillation detectors (approximately 152 keV for a 1.33MeV γ ray from a ^{60}Co radioactive source). The beneficial effects of short decay times encourages the use scintillators in timing applications where recording the presence of a γ ray is more important than a high resolution energy measurement.

3.1.5 Bismuth Germanate $Bi_4Ge_3O_{12}$

Bismuth Germanate (BGO) is a high density inorganic scintillator [WM73]. BGO has many desirable properties that have made it an attractive material to use in escape suppression shields. The high density (7.3 g/cm^3) and large atomic number of the bismuth component (Z=83) increase the stopping and photoelectric absorption probability for γ-ray interactions.

BGO is a pure inorganic scintillator and operates without activator impurities. Photon emission arises from an optical transition in the Bi^{3+} ion. Since there is a large energy shift between absorption and emission in the Bi^{3+} ion, the light output of BGO is transparent to the crystal. Although the BGO light yield is lower than some scintillators, the disadvantages are offset by the ease of fabrication and the stopping characteristics of the material.

3.1.6 Caesium Iodide CsI(Tl)

Caesium Iodide is an alkali-halide scintillator that is usually activated by thallium. The CsI(Tl) light curve has a different decay time for different charged particles that are incident on the detector. This has made CsI(Tl) an appropriate material for differentiating between species of radiation by pulse shape discrimination. Clear separation can be made between light charged particles such as protons and alpha particles and recent developments such as the MICROBALL (section 3.6.1) use CsI(Tl) for these properties.

3.2 Escape Suppression

Section 3.1.1 showed that there are three main mechanisms for γ-ray interactions within a detector. The γ rays of interest are the photoelectric interactions that deposit all their energy in the detector and allow a true measure of the γ-ray energy. Compton scattering is always present in γ-ray detection due to scattering within the detector volume often followed by escape from the detector resulting in an incomplete deposit of energy. The contributions of the Compton scattering in the γ-ray spectrum are considerable and HPGe detectors typically have peak to total values (PT) at the $\approx$20% level. Escape suppression is a method of improving the PT values by rejecting those events which contribute to the Compton continuum. The escape suppression technique involves surrounding the HPGe detector with an inorganic scintillator which detects γ rays that scatter out of the germanium crystal. This configuration is known as an escape suppressed spectrometer. If a γ ray is detected in both the detector crystal and the scintillator, then a Compton scattering event has occurred and the event is vetoed. Using an escape suppression system improves the PT values from $\approx$20% for an unsuppressed detector to $\approx$60% for the escape suppressed spectrometers of the type used in large detector arrays. This can be seen in Fig. 3.4a which compares the spectra collected by a suppressed and unsuppressed spectrometer. The

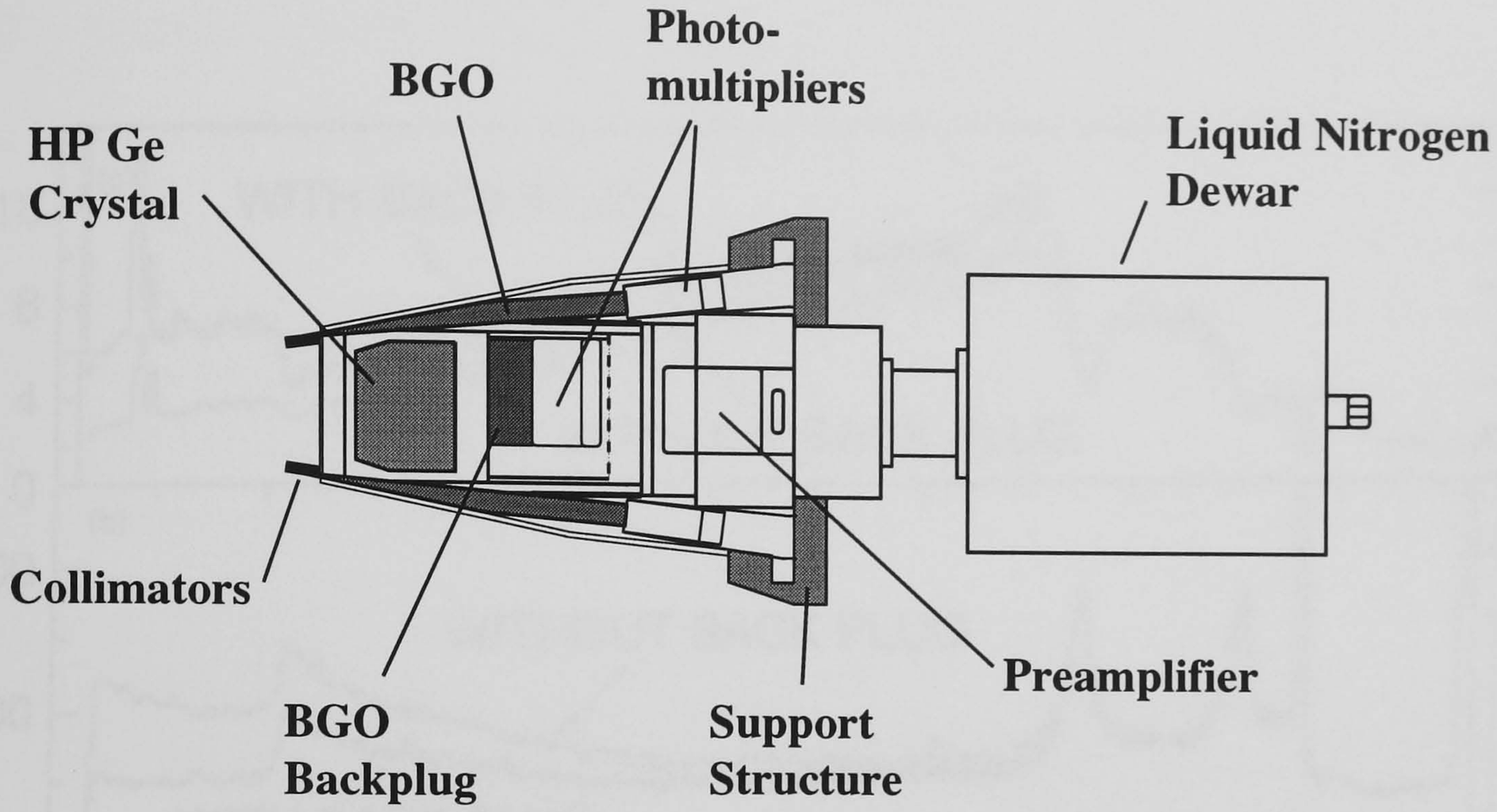

Figure 3.3: A schematic diagram illustrating a escape-suppressed spectrometer used in the GAMMASPHERE γ-ray spectrometer array.

escape suppressed spectrometers used in GAMMASPHERE are comprised of a HPGe detector surrounded by a BGO suppression shield. A GAMMASPHERE escape suppressed spectrometer is displayed in Fig. 3.3. The germanium detector in the spectrometer is a cylindrical crystal of 72mm diameter and 84mm long. The suppression shield consists of 7 optically isolated BGO elements. This includes a BGO backplug to suppress events where the γ ray has forward scattered out of the crystal. The backplug is cylindrical with the same diameter of the germanium crystal except for a slot to accommodate an off-axis tube containing the cold finger and electric cabling to the preamplifier. Prototype tests of the GAMMASPHERE suppression shields [Bax92] (illustrated in Fig. 3.4b) have showed that the peak to total values with the backplug are PT=0.678, approximately 10% better than the suppressed value without the backplug (PT=0.622). The BGO crystals have a tapered lip to allow close packing of the shields. The tapering leaves the germanium crystal with a solid angle of 0.418% and a opening angle of 7.4°.

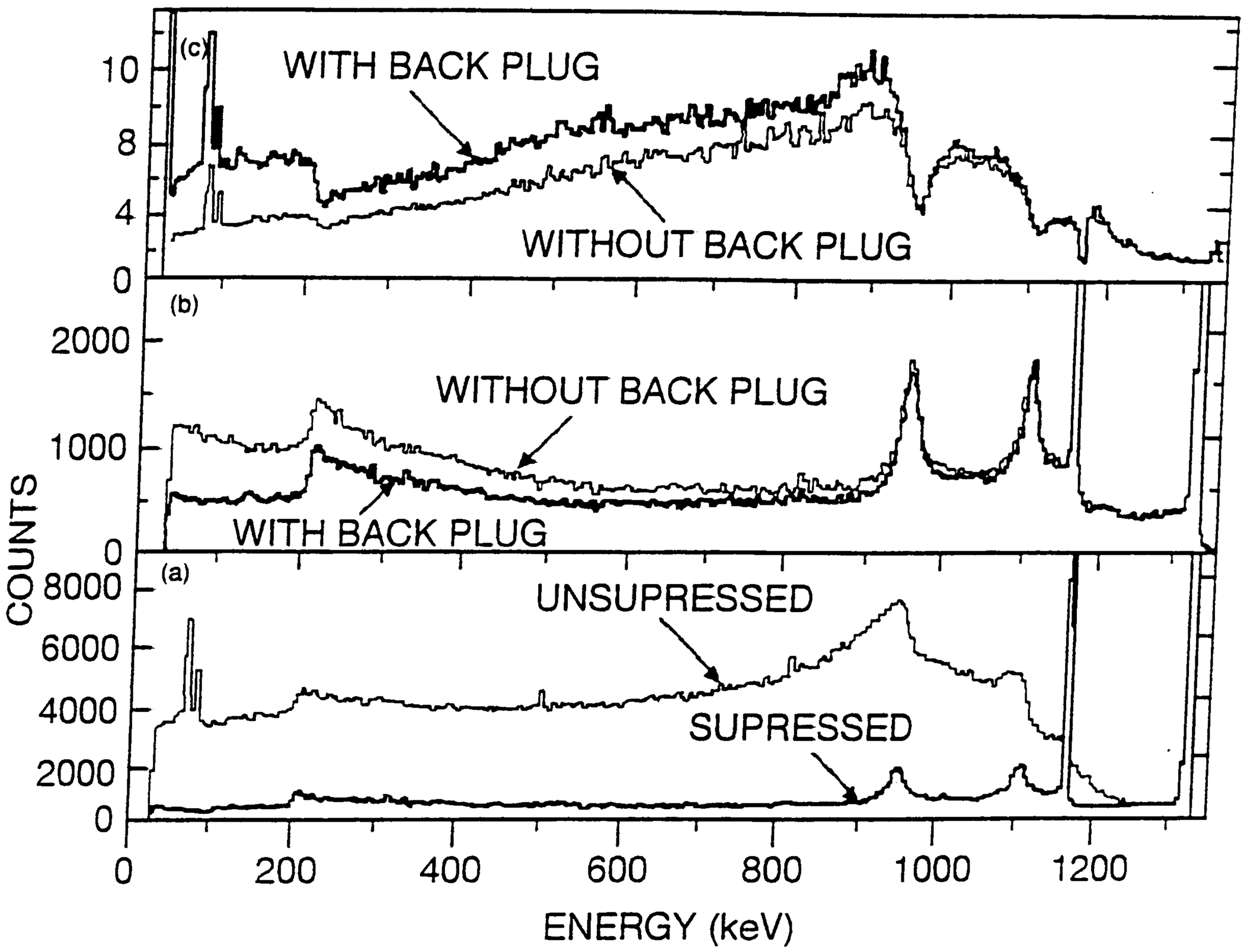

Figure 3.4: Compton suppression tests using ^{60}Co radioactive source. (a) Suppressed and unsuppressed versions of the same spectra are compared. (b) Suppressed spectra are shown with and without the backplug contributing to the suppression; these two spectra are normalised so that the full-energy peaks have the same areas. (c) The ratio of the unsuppressed to the suppressed spectrum is shown with and without the backplug contributing to the suppression. Spectra taken with backplug suppression are given in bold lines. Taken from [Bax92].

3.3 Large Spectrometer Arrays

The development of a new generation of highly efficient γ-ray spectrometers has been made possible by major advances in detector technology and associated integrated circuitry. The aim of these spectrometers is to measure the energies and intensities of γ rays and the correlations between them efficiently. The measure of spectrum quality, resolving power R, gives a good indication of the desirable properties of this generation of spectrometer arrays and the prospects of developing improvements in future spectrometers. The resolving power is defined as

$$R = \left[\frac{SE_\gamma}{\Delta E}\right] PT \tag{3.4}$$

where SE_γ is the energy separation between γ rays in a complex sequence (for example γ-ray energy spacing in a superdeformed band), ΔE is the resolution of the detector and PT is the peak to total ratio. As SE_γ is defined by the intrinsic nuclear structure of the system under investigation, the resolving power of the array can only be improved by increasing the resolution thereby diminishing ΔE or by increasing the peak to total ratio. In practice, it is difficult to increase the peak to total. It has been shown in the review articles [NBF94] and [BS96] that the PT value can be dramatically increased by collecting high-fold coincidences (section 3.4). This is indicated by defining the peak to background in terms of the resolving power.

$$\left[\frac{N_p}{N_b}\right]_F = \alpha_0(0.76R)^F \tag{3.5}$$

where $\left[\frac{N_p}{N_b}\right]_F$ is the peak to background value when a fold selection criterion has been placed on the data and α_0 is the limit of observation for the array. A further improvement can be made to the PT value by using an ancillary detector which introduces a background reduction factor, R_0 into Eq. 3.5 so that

$$\left[\frac{N_p}{N_b}\right]_F = \alpha_0 R_0(0.76R)^F. \tag{3.6}$$

Although, the intrinsic resolution of an HPGe escape suppressed spectrometer can be measured to have values around 2 keV at 1332 keV, the observed resolution in a high spin γ-ray spectroscopy experiment is much worse. In high-spin experiments where the lifetime of the states are shorter that the slowing down time in the target, the peaks tend to be Doppler broadened due to different recoil velocities (ΔE_{vel}). Also the angular distribution

of decaying recoils in the target contributes to reducing the total resolution (ΔE_{ang}) . The opening angle of the detector also Doppler broadens the peak (ΔE_{open}). The total resolution of the spectrometer is defined in terms of these contributions and the intrinsic resolution of the detector and associated signal processing (ΔE_{int}) as

$$\Delta E_{\gamma} = (\Delta E_{int}^2 + \Delta E_{open}^2 + \Delta E_{ang}^2 + \Delta E_{vel}^2)^{\frac{1}{2}}. \tag{3.7}$$

A high photopeak efficiency is achieved by using large volume germanium detectors that cover a large fraction of the 4π solid angle. The photopeak efficiency is reduced by more than one coincident γ ray striking a detector at the same time. This has been limited in the latest generation of spectrometer arrays by increasing the granularity through segmentation. High granularity means that the solid angle is covered by many detectors each covering a small segment of the solid angle. Improving the granularity increases the isolated hit probability and reduces the Doppler broadening due to the opening angle of the detector.

The review articles [NBF94] and [BS96] chart the development and properties of the current generation of arrays and discuss some of the advances in nuclear structure studies that have been made possible by these innovations.

3.3.1 GAMMASPHERE

The work detailed in this thesis has been collected using the GAMMASPHERE spectrometer array [Lee90] based at the Lawrence Berkeley National Laboratory (LBNL), USA. The GAMMASPHERE spectrometer in its full implementation will be comprised of 110 escape suppressed HPGe spectrometers packed closely in a 4π arrangement. The array was designed as a 122 element polyhedron composed of 110 hexagonal faces and 12 pentagonal faces. The detectors and their suppression shields are placed in the hexagonal faces whilst the remaining pentagons are used for beam access and exit and support structures. The polyhedral frame is composed of two hemispheres, each containing 55 detectors, that can be retracted a distance of 75cm from each other to allow access to the target chamber. Each hemisphere can also be rotated through $\pm$90 degrees to allow easier access to the detector positions at the top and bottom of the array. When the array is closed the target detector distance is $\approx$25cm. Each GAMMASPHERE detector covers 0.418% of 4π solid angle and so with the full complement of 110 detectors the array covers 46% of 4π. The total photopeak efficiency is

9.4%. There are approximately 80 segmented detectors in the GAMMASPHERE spectrometer located about the central region of the array. Segmented detectors are the standard n-type reversed bias detectors, where the energy signal is taken from the central contact. The outer p contact is segmented into two parts. Using the low resolution signal from the segmented contacts, it is possible to determine whether the incident γ ray was isolated to one half of the crystal or shared between the crystals. Segmentation increases the isolated hit probability and reduces Doppler broadening by diminishing the opening angle of the detector. Currently tests are being performed to assess the use of these detectors in linear polarisation measurements [Sch97]. Segmented detectors have a comparable efficiency to unsegmented detectors, however the resolving power is increased.

The target chamber is designed so that ancillary detectors such as the MICROBALL [Sar96] (section 3.6.1) can be used to provide channel selection.

3.3.2 Electronics and Data Acquisition

GAMMASPHERE is a complicated system and requires an electronics setup that is maintained by a dedicated support staff. A thorough description of the electronics and data acquisition system would be very complex and beyond the scope of this work. A general overview of the electronics and data acquisition is described here and more detailed descriptions are referenced.

Since GAMMASPHERE contains 110 escape suppressed spectrometers being used simultaneously, the associated electronics must process many hundreds of signals at a rate of $\approx$10000 events/s. Conventional NIM electronics are not feasible for GAMMASPHERE due to the large volume of the modules and the number of cables required. To overcome this problem highly integrated circuitry based on the VXI standard has been introduced to handle the necessary signal processing. VXI cards have the advantages of being compact, more reliable and allow adjustment of electronics parameters by software control.

Each VXI card allows the processing of both analogue and digital signals for two germanium detectors and their fourteen BGO suppression elements. The entire array requires six VXI crates to hold 55 VXI cards to process a total of 110 germanium and 770 BGO signals. A further master crate holds the master trigger and readout electronics.

A concise overview of the Ge-BGO VXI card is illustrated schematically in Fig. 3.5.

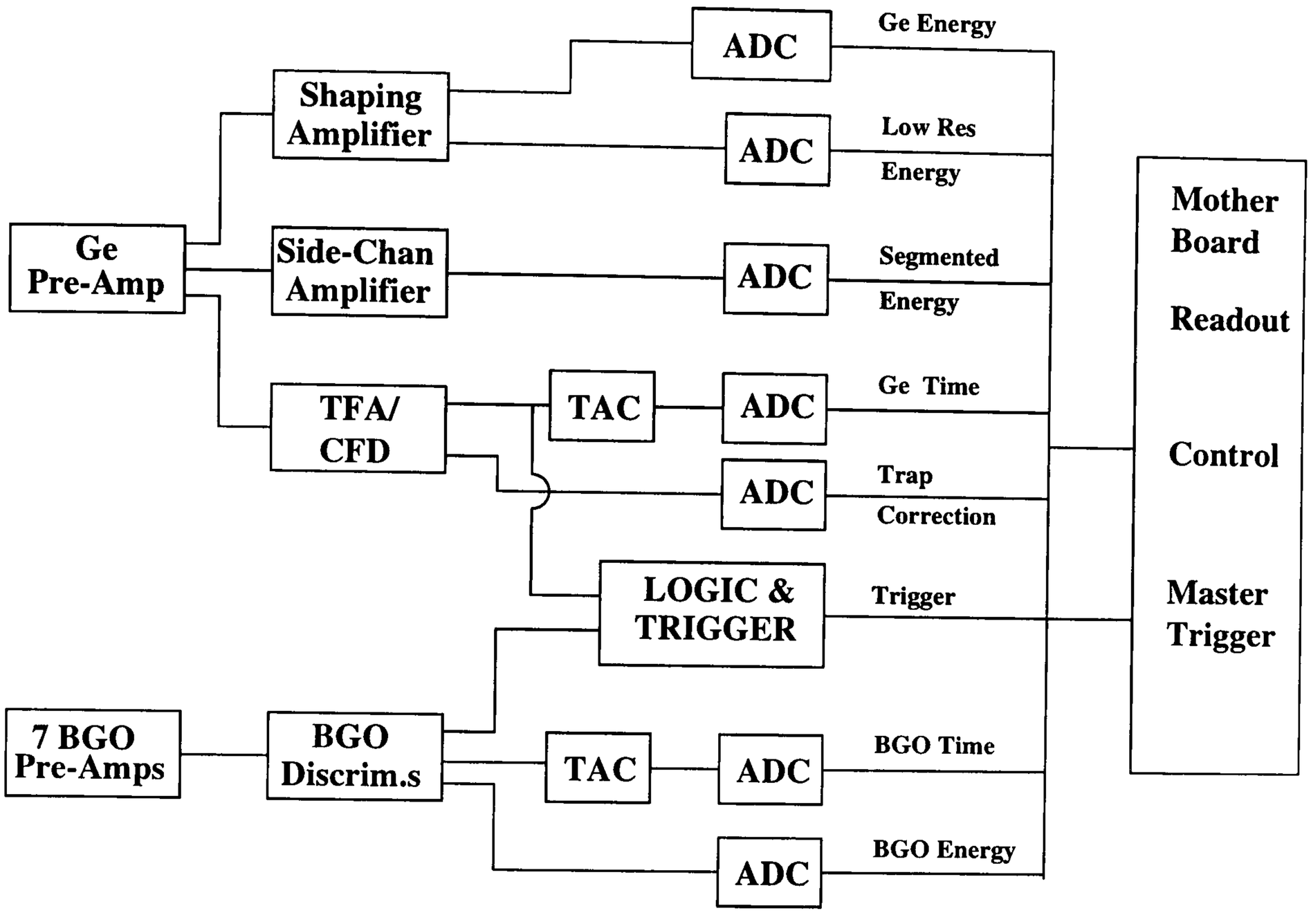

Figure 3.5: Block diagram of a single Ge-BGO channel in the VXI card. Adapted from a figure in [Go94c].

The germanium preamplifier signal is sent through a shaping amplifier with a 4μs shaping time to produce a trapezoidal pulse with a total width of 10μs. The use of a quasi-trapezoidal shaping amplifier limits ballistic deficit [Go94a] at the pre-ADC stage. A lower resolution parallel channel with a shaping time of 2μs is taken from the shaping amplifier to allow fast energy decisions. In segmented detectors, an additional signal is taken from the outer electrode and passed to an ADC. A fast signal from the germanium detector is passed through a timing filter amplifier (TFA) which is not concerned with shaping the signal as much as detecting its presence. The fast output of the TFA is sent to a constant fraction discriminator (CFD) that ensures good relative timing between the germanium detectors and discards signals that do not reach a minimum fold/multiplicity threshold. Consequently, the CFD prevents the system from processing noise signals as true events. The CFD converts the analogue pulse into a logic signal, which is then passed to a time to amplitude convertor (TAC) where timing properties of the signal are recorded with re-

spect to a master trigger signal. The shape of the CFD signal can be used to determine the radial position of the maximum energy interaction and may be analysed to provide a charge trapping correction [Go94b]. The fast germanium signal provides a standard current to a SUM bus where it is added to other detector signals. The SUM signal is used to make multiplicity decisions. The BGO signals from single electron discriminators are used to provide fast timing information. The BGO information is also added together to give a total BGO energy. The germanium and BGO signals are supplied to a local SUM bus in the VXI card. The local trigger data is sent to the master trigger where the final multiplicity and Compton suppression decisions are made. The trigger system is initiated by a clean fast germanium signal from any detector and 800ns is is allowed for the master trigger to make its multiplicity decision. If the required multiplicity is not achieved the system will be reset. If the master trigger validates an event, the complete processing and readout of the event is initiated. The readout time is approximately 10μs, however a buffer system allows the pulse processing of the next event to begin whilst the preceding event is read out.

When the pulses have been shaped and digitised on the VXI cards, the signals are passed into the data acquisition system which is illustrated schematically in Fig. 3.6. Each operation in a VXI crate is controlled by a CPU called the resource manager. A readout controller (ROC) is also present in each crate and relates information to the master ROC. The master ROC contains a dual processor that sequentially passes data as 32-bit packages along fibre optic bundles to the event builder housed in a VME crate. The event builder transforms each event into a suitable format for storage and online sorting using a software routine provided by the user. The data is then randomised in a first in first out (FIFO) module and processed by a sequence of CPU's and fed into a 64 megabyte memory buffer. A further CPU can acquire the data and write the information to one of the eight available tape drives. All eight drives can operate in parallel and collect data at a rate of 4 megabytes/s.

3.4 High-Fold Coincidence Data

A typical heavy-ion fusion evaporation reaction has a high multiplicity consisting of 20-30 γ rays. The number of γ rays that are detected and recorded in a single coincidence event is known as the fold of the event. For example if three γ rays are detected in three different detectors then a single three-fold coincidence event will be recorded. It has been shown

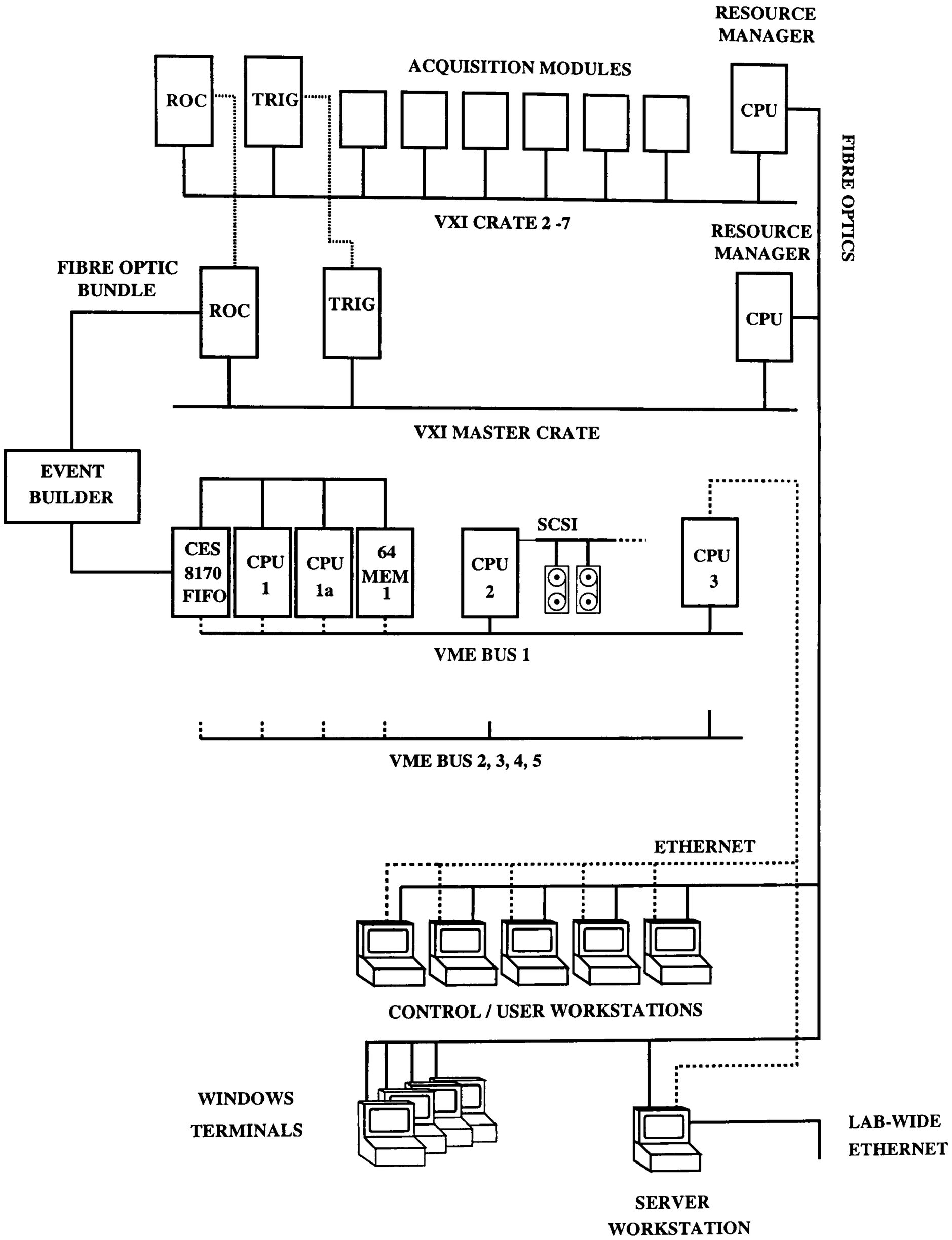

Figure 3.6: Architecture of the GAMMASPHERE data acquisition system.

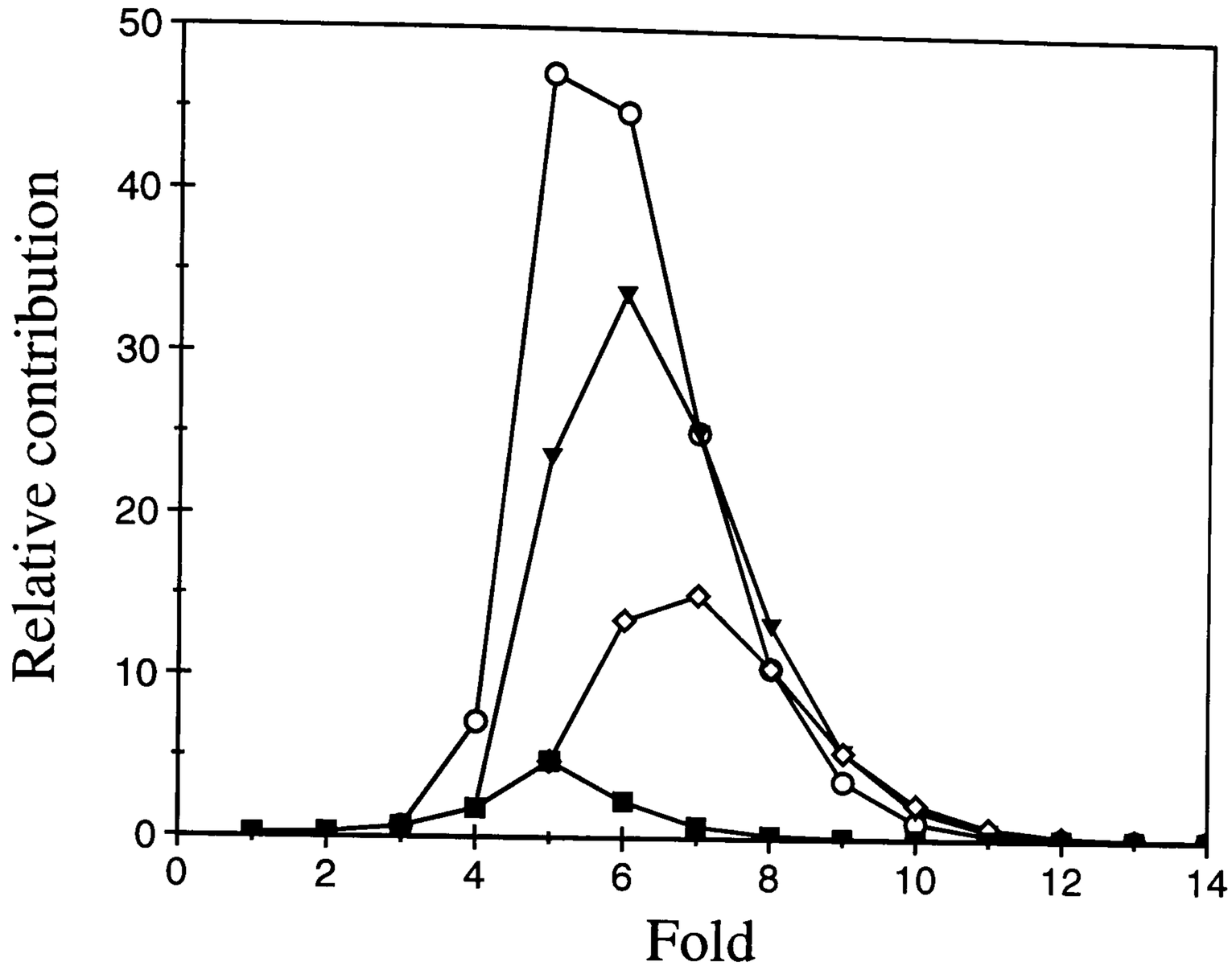

Figure 3.7: The measured contribution to each fold from a GAMMASPHERE data set (filled squares). The effect of unpacking high-fold events into their constituent triple (open circles), quadruple (filled triangles) and quintuple (open diamonds) coincidences is also displayed.

that with increasing photopeak efficiency the probability of detecting high-fold events increases [BS96]. Using the present generation of γ-ray spectrometers it has become possible to exploit the advantages of increased photopeak efficiency and detect higher fold coincidences. A typical fold distribution from a GAMMASPHERE experiment is pictured in Fig. 3.7. It can be seen that the most probable event contains 5 γ rays with the probability of detecting higher folds decreasing with increasing fold number. Although higher-fold coincidences are less probable, they can be unpacked into lower fold coincidences and contribute significantly to the number of lower fold events. In general an n-fold event can be generated into m-fold subevents according to

$$ {}^{n}C_{m} = \frac{n!}{m!(n-m)!}. \tag{3.8} $$

According to Fig. 3.7, the majority of triple coincidences are obtained by unpacking 5-fold coincidences, whereas the major contribution to 4- and 5-fold events comes from unpacking 6- and 7-fold events respectively. Coincidence data is usually sorted into 1-D, 2-D or 3-D spectra.

3.4.1 γ - γ Correlation Matrices

The most convenient way to visualise coincidence data is to create spectra of some fixed fold dimension. With high statistics experiments, data is usually unpacked into $\gamma - \gamma$ coincidences and incremented into a 2-D spectrum known as a $\gamma - \gamma$ correlation matrix. Increasing the number of dimensions of the spectrum allows gates to be set after sorting has taken place. If an event contains two γ rays in coincidence with energies $E_{\gamma 1}$ and $E_{\gamma 2}$ then the coincidences are incremented into the 2-D matrix at the positions ($E_{\gamma 1}$, $E_{\gamma 2}$) and ($E_{\gamma 2}$, $E_{\gamma 1}$). If an event contains three γ rays in coincidence ($E_{\gamma 1}$, $E_{\gamma 2}$, $E_{\gamma 3}$), the event will be unpacked into its constituent two-fold coincidences and incremented at two positions in the matrix per γ ray, with six increments in total. This ensures that the matrix is symmetric about the main diagonal with γ-ray energies defined on both x and y axes. 1-D spectra can be projected on one axis of the matrix by gating on a narrow energy region on the other axis. The resultant spectrum will consist of all γ rays in coincidence with the gate. High-fold data can also be sorted so that events can be unpacked into constituent triple coincidences and stored in 3-D arrays known as cubes. 1-D spectra can be generated from a cube by gating on two axes defining the cube and projecting out coincidences on the remaining axis.

In order to be more selective, gated matrices may be sorted. In a gated matrix, certain gating conditions must be satisfied before the event is incremented in the matrix. In order to observe coincidences with a particular γ ray, $E_{\gamma 1}$, the data must be sorted event by event using the method proposed by Beausang *et al* [Bea95]. If an event contains $E_{\gamma 1}$ then the remaining γ rays in the event are incremented into the spectrum. If $E_{\gamma 1}$ is not present the entire event is ignored.

The lifetime measurements detailed in this work employ asymmetric matrices consisting of coincidences between one ring of detectors with constant θ against all other detectors. For example, the GAMMASPHERE array contains 17 rings of detectors so if an event is validated and contains an event where one γ ray was detected at a specific angle with respect to the beam, then $E_{\gamma\theta}$ is associated with one axis and the γ-rays detected at other angles will be identified with the other axis.

3.5 Heavy Ion Fusion Evaporation Reactions

Collective properties of nuclei are often investigated by the characteristic γ-decay of the nucleus under investigation. Ideally, for high-spin studies, it is desirable to use a reaction mechanism that populates channels with as much angular momentum as possible. The best method of populating states with large angular momentum and significant cross-sections has been to use heavy-ion fusion evaporation reactions [New69]. These reactions fuse a projectile-like nucleus at an energy sufficient to overcome the Coulomb barrier between itself and a stationary target nucleus to produce a highly excited compound system. States high in excitation energy are populated and can decay by particle emission followed by γ-ray emission.

The amount of angular momentum that can be transferred from the projectile to the target depends on the relative momentum of the two nuclei and the impact parameter, b between them. For example, if the projectile has a large relative momentum and a large impact parameter, the compound nuclear system will be formed with a large angular momentum. Classically, the amount of angular momentum that may be transferred between two bodies is given by

$$l_{max} = \sqrt{2A_pE_pb} \tag{3.9}$$

where l_{max} is the maximum angular momentum that the compound nucleus can possess when a beam of projectile ions of mass A_p is bombarding a target with an energy E_p at an impact parameter of b. Eq. 3.9 implies that an optimum angular momentum transfer will occur for reactions involving a heavy projectile ion, however, there are limitations to this rule. It is important to limit the maximum angular momentum to avoid fragmentation and centrifugal fission of the compound nucleus. A further spin restriction is placed on the value of the impact parameter; a sharp cut-off occurs where no further angular momentum will be transferred to the compound nucleus. This corresponds to the boundary beyond which only Coulomb excitation can occur. The impact parameter threshold is defined empirically as

$$b_{thres} = 1.16(A_p^{\frac{1}{3}} + A_t^{\frac{1}{3}} + 2.07)fm \tag{3.10}$$

where A_t is the mass of the target nucleus. These considerations are included in the defin-

ition of maximum angular momentum transfer as

$$l_{max} = 0.219 b_{thres} \sqrt{\mu(E_{CM} - E_{CB})}\hbar \tag{3.11}$$

where μ is the reduced mass, E_{CM} is the beam energy in the centre of mass frame and E_{CB} is the height of the Coulomb barrier given by

$$E_{CB} = \frac{Z_p Z_t e^2}{4\pi\epsilon_0 r}; \quad r = r_0 A^{\frac{1}{3}} fm. \tag{3.12}$$

3.5.1 Preformation and Decay of Compound Nuclei

The preformation and decay of the compound nucleus occurs in a number of stages that are illustrated in this section by describing a heavy-ion reaction used in this work; ^{100}Mo(^{36}S,4n)^{132}Ce. The decay of the compound nucleus is usually described with respect to the variation of energy E, as a function of spin I as shown in Fig. 3.8 relative to the yrast-line (the contour defining the lowest energy for a particular spin value). The population, decay and structure of near-yrast collective γ-ray sequences are of great contemporary interest and will form the content of this thesis.

At the preformation stage, the ^{36}S nuclei are accelerated in the 88-Inch cyclotron to an energy (155 MeV) that is in excess of the Coulomb barrier produced between projectiles and the ^{100}Mo targets (E_{CB}=115 MeV). Fusion occurs $\approx 10^{-22}$ seconds later and forms a highly excited compound nucleus that is spinning rapidly. The compound nucleus is formed at a high excitation energy and it is energetically favourable to lose energy by emitting particles. Neutrons are emitted in this reaction and typically carry away 8-10 MeV per neutron.

De-excitation through particle emission cannot occur indefinitely and beyond a certain threshold the 'cooling' process proceeds via statistical γ-ray emission. Statistical γ rays remove a large amount of energy but very little angular momentum. Yrast-like decays now arise that dissipate angular momentum. At this stage ($\approx 10^{-12}$ seconds after formation), electric quadrupole (E2) γ-ray cascades composed of discrete transitions may be discerned. Eventually after 10^{11} rotations and $\approx$1 ns, the nucleus decays to a final ground-state energy.

3.6 Ancillary Charged Particle Detectors

In the neutron deficient A$\approx$130 region, the highly excited compound nucleus can decay not only by neutron decay, but also by charged particle emission. This results in the population

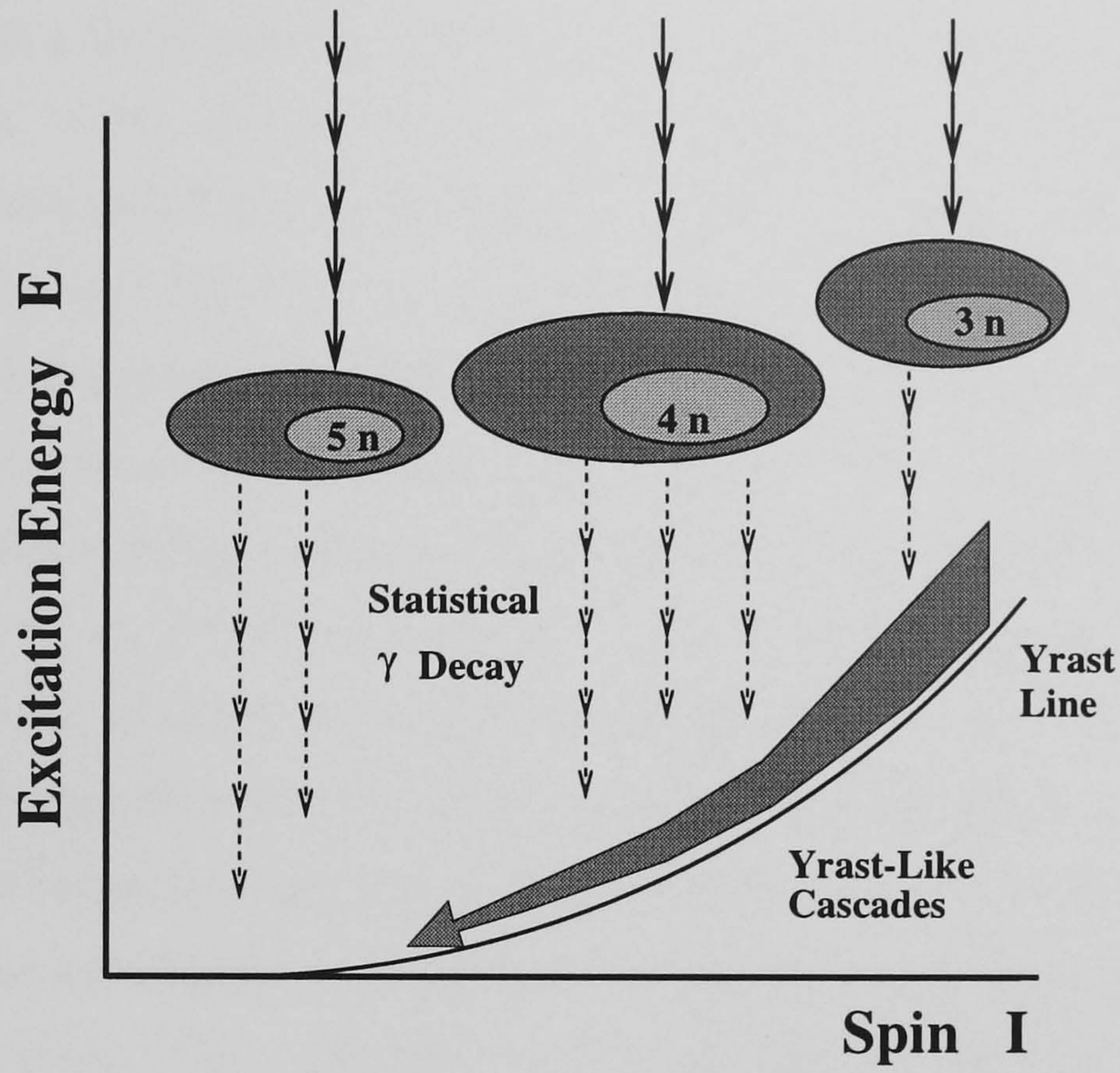

Figure 3.8: Schematic diagram illustrating the decay of the compound nucleus formed in a heavy-ion fusion evaporation reaction.

of a large number of open α, p and n channels with comparable cross-sections. It was stated in section 3.4 and references therein, that the use of an ancillary detector that facilitates channel selection, improves the peak to total values in the associated γ-ray spectra by eliminating γ-ray coincidences specific to other channels.

A 4π charged particle detection system called MICROBALL [Sar96] has been developed by Washington University at St Louis, USA, with a design specification to be compatible with high resolution γ-ray spectroscopy experiments using the GAMMASPHERE spectrometer. Ideally such a detector should not impair the response of the spectrometer and should be capable of functioning at the high counting rates of the system.

The work detailed in this thesis is concerned with the role of the MICROBALL as a channel selection device. The following sections review the detector properties and channel selection methods employed. More detailed information on the MICROBALL and the response of GAMMASPHERE with or without the MICROBALL can be found in [Sar96] and [Dev96].

3.6.1 MICROBALL

The MICROBALL is a 4π charged particle detection device composed of 95 planar CsI(Tl) detectors (pictured in Fig. 3.9 and Fig. 3.10). The CsI(Tl) has two decay components; the first component has a mean light decay time of $\tau = 0.4$ - 1.0μs where the amplitude and fall time depends on the type of incident radiation. The second component has a decay time of $\tau = 7.0$ μs and is independent of the radiation type. The long component limits the counting rate that can be achieved without particle identification (PID) deterioration due to pileup. To reduce the effects of pileup and ensure high counting rates, a highly segmented approach has been adopted in the MICROBALL design. Each detector is shaped as a compound arc to allow close packing of detectors without any shadowing by detectors from neighbouring rings. There are 9 rings of detectors that cover an angular range from 4° to 171°. Detectors are separated by 0.12mm in a ring while the gap between adjacent rings is 0.1mm. Allowing for beam entry and exit, target insertion and the gaps between rings, the total solid angle coverage is 96.5% of 4π. The rings that hold the detectors in place are made from plastic to reduce γ-ray absorption and are supported by legs attached to a rail, along which the rings can be positioned. The detectors are optically coupled to Si photodiodes to collect the scintillation light. The outer surface of the detectors is covered by a thin aluminium leaf and lead or tin absorber to stop scattered heavy-ions. The absorber thickness was varied from 15 mg/cm^2 for forward angles to 5 mg/cm^2 for the extreme backward angles. An earth is applied between the absorbers and the target chamber via the aluminium legs to prevent sparking from target electrons produced by the beam.

3.6.2 MICROBALL Electronics and Data Acquisition

The MICROBALL electronics system is discussed in a similar manner to section 3.3.2. A qualitative overview of the signal processing and the data acquisition is included here. More detailed descriptions of the electronic design of the system can be found in [Sar96] and the references therein.

The signal processing chain is pictured schematically in Fig. 3.11. The setup is similar to GAMMASPHERE since the preamplifier signal is processed via two parallel channels; the slow channel provides the essential PID information while a faster parallel channel is used to provide information to the external particle-γ logic system. A charge sensitive preamplifier

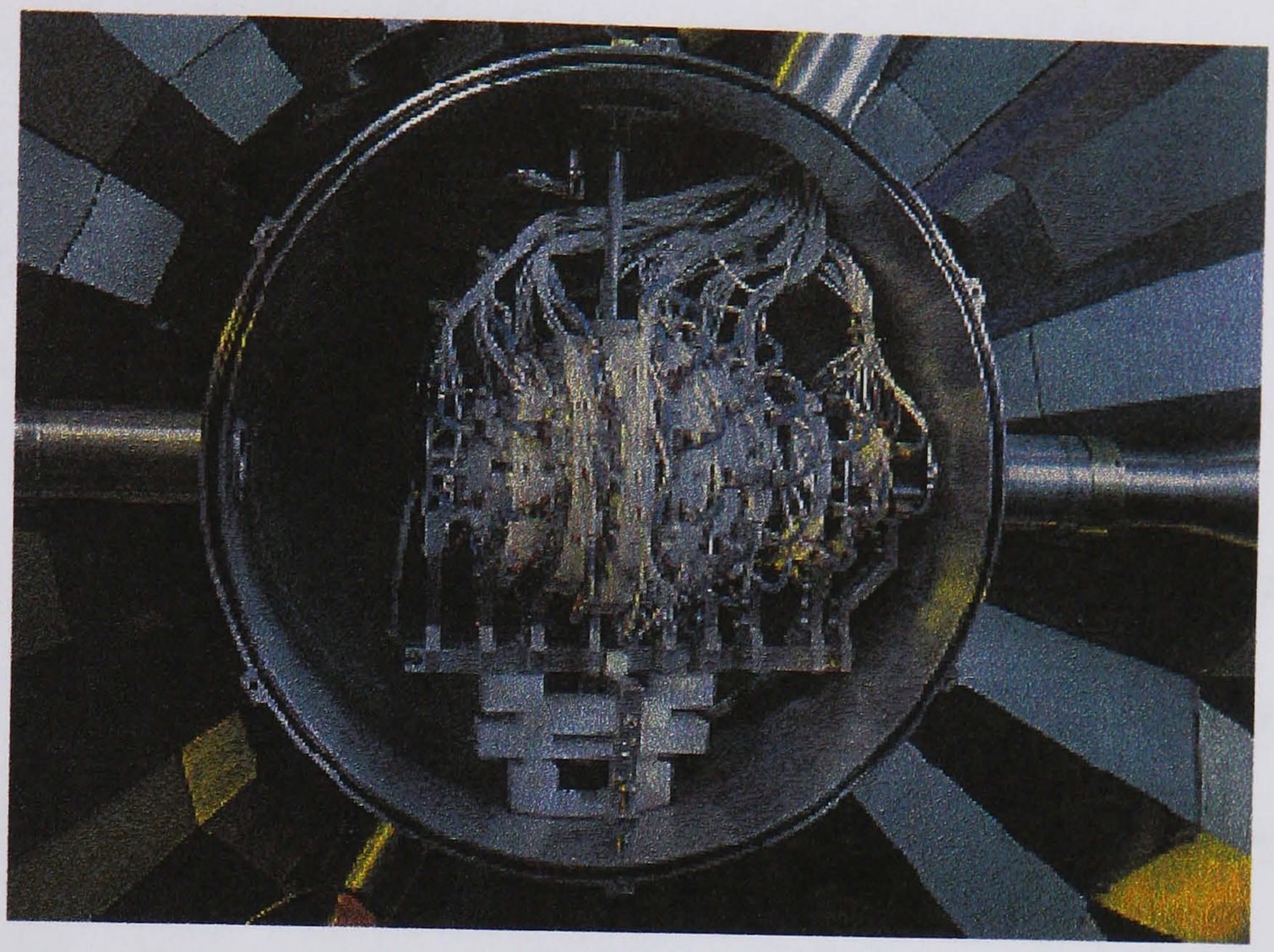

Figure 3.9: Close-up picture of the MICROBALL inside the GAMMASPHERE target chamber.

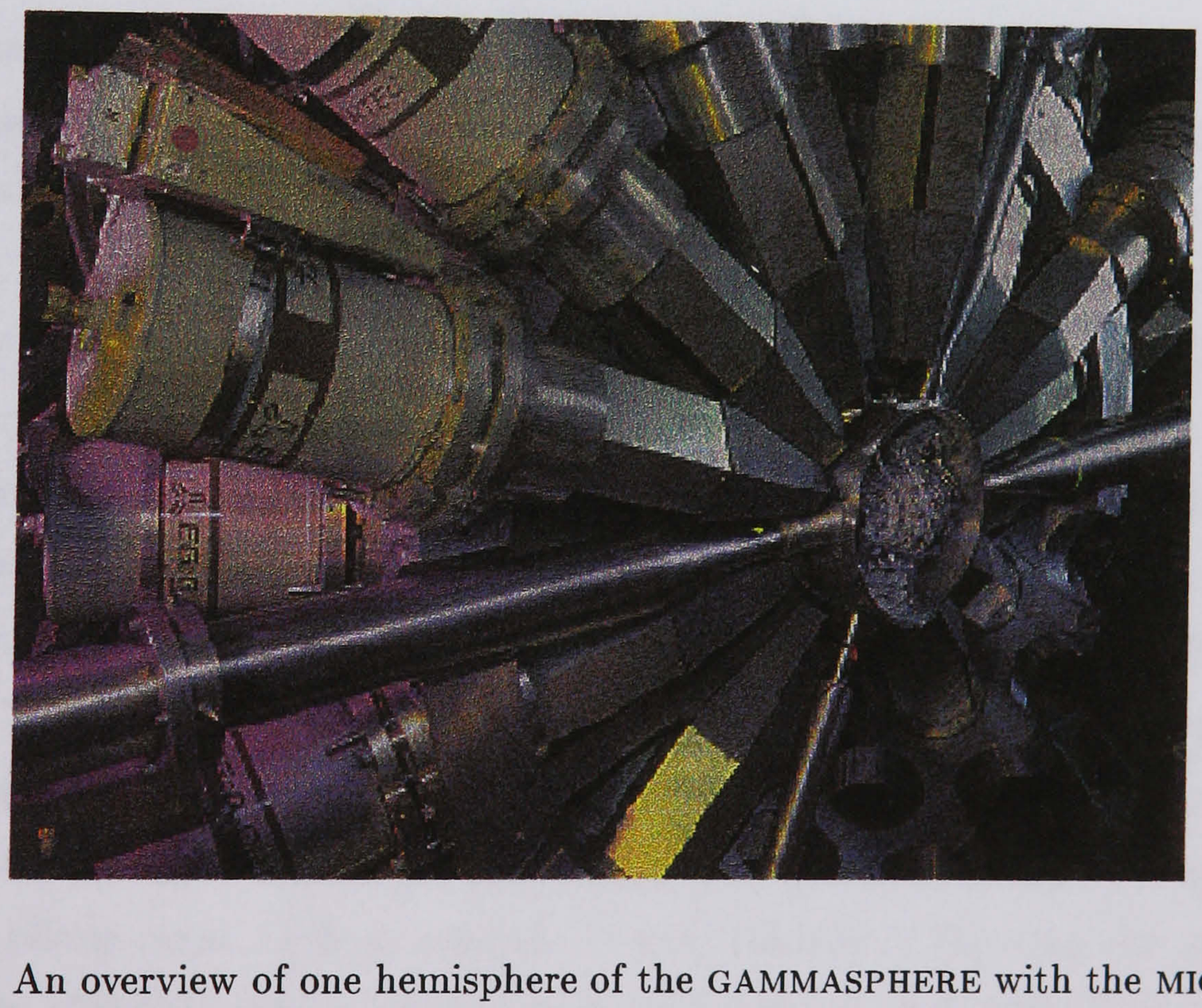

Figure 3.10: An overview of one hemisphere of the GAMMASPHERE with the MICROBALL in place. The germanium detectors and suppression shields surround the target chamber and the support hemisphere structure can be seen at the lower right of the picture. The beam enters from the left and exits from the right.

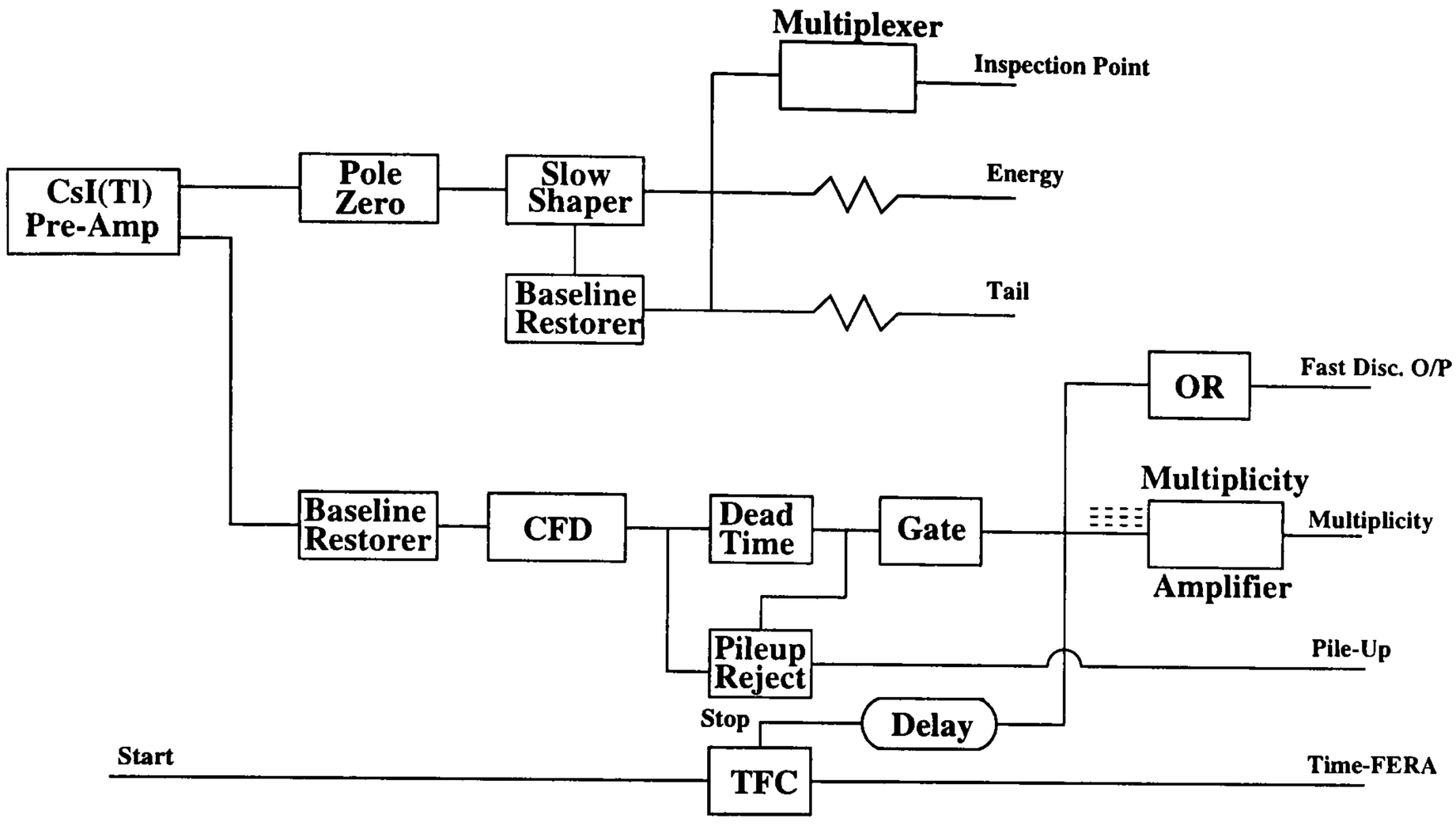

Figure 3.11: Block diagram of a single CsI(Tl) channel in the MICROBALL signal processing system. Adapted from a figure in [Sar96].

integrates the photodiode signals to produce pulses with a 600ns rise time and a 300μs decay time. The slow signal branch uses a pole zero cancellation stage to adjust the length of the pulse tail before using a two stage amplifier to shape the signals to obtain energy and PID information. Pole zero cancellation is essential to minimise pileup at high counting rates. A baseline restorer circuit is included before a two-way DC coupled splitter. The splitter exposes the signal to different processing stages from which energy (fast pulse component) and tail (slow pulse component) signals are derived. The fast signal branch passes through a fast shaper and CFD to produce a logic output pulse. A pileup rejection circuit checks that there are no pileup distorted signals. The output from the CFD is allowed a fixed time period (labelled dead time in Fig. 3.11). If the pileup rejector does not detect another CFD pulse after the dead period the event will pass the gate and move onto the next signal process. Alternatively, if another pulse is detected by the rejector logic the event will be tagged as a pileup event. Pileup rejection is only capable of reducing the problem and cannot totally eliminate pileup events passing the gate. It is possible that two or more events will occur within time resolution of the fast branch and be processed as a single pulse, while the slower branch processes a number of amplitudes from a variety of events. If the gate is passed the signal will pass through a delay and initiate a 'stop' to a time to

FERA convertor (TFC) which was started at some earlier time by the external logic system. The timing of the event is then readout after this stage. The same gate signal will provide multiplicity information and act as an input to an OR gate where the gate output signals from the MICROBALL are used in the particle-γ coincidence logic.

Each discriminator OR passes into a final OR gate where it feeds one input of an AND gate in the external logic circuit. The other AND input is provided by the local triggers from the GAMMASPHERE detector channels. The AND signal is fanned back to the TFC start to provide a readout where the germanium detectors have determined the timing. A second overlap coincidence is formed to allow the CsI(Tl) detectors determine the timing. The second timing AND is used to set energy and tail gates for all the FERA ADCs.

3.6.3 Pulse Shape Discrimination

It was mentioned in section 3.6.1 that CsI(Tl) has two decay components. The first component is dependent on the radiation type, whereas the second, longer component is independent of particle type. Particle identification (PID) can be achieved through measurements of the integrated charge over the two time regions of the pulse. The particle species can be differentiated by gating on the distinct fast component and the slower tail component at the splitter stage of the slow signal processing branch (see section 3.6.2). The PID resolution is indicated in Fig. 3.12a which shows a plot of the fast-gate component versus the slow-gate component. Two major jets can be seen each with a characteristic slope for particles with a common pulse shape. In order to use this information to obtain a good particle identification, two methods can be employed. The zero crossover time of the differentiated fast signal of the MICROBALL constant fraction discriminator using the cyclotron radiofrequency as a reference time will be different depending on the type of particle. Reasonable separation can be obtained by plotting the fast component which defines the particle energy against zero crossover time (ZCT). It can be seen in Fig. 3.12b that α-particles have a better time resolution than protons and a shorter zero crossing time. Better PID definition can be obtained by plotting the ratio of the fast/slow gate signals versus the fast gate (Fig. 3.12c). An optimum identification is obtained by combining the two methods and plotting the ratio versus ZCT. Placing polygonal gates around the high density regions in the ratio-ZCT plane allows correct PID and reduces the fraction of random coincidences that are incremented

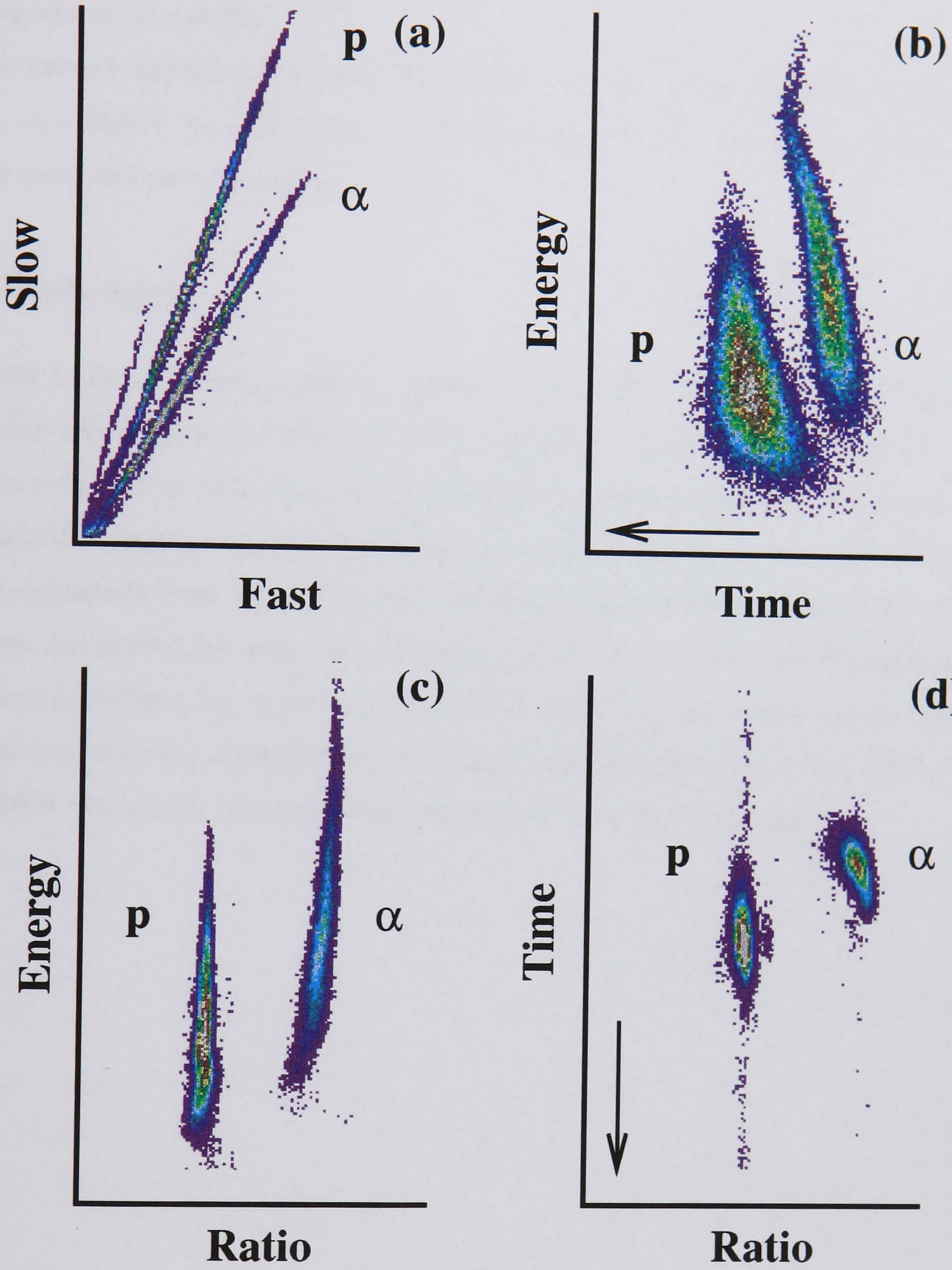

Figure 3.12: Pulse shape discrimination (PSD) using the MICROBALL to identify charged particle emission from the reaction ^{105}Pd(^{35}Cl,xα,yp,zn). (a) PID resolution for a single CsI(Tl) detector. (b) Plot of energy (fast component) versus zero crossover time (ZCT) for the same reaction. (c) Plot of energy versus the ratio R=fast/slow. (d) Optimum PSD method obtained by plotting ZCT versus ratio using the data from (b) and (c). The arrows in the figure indicate the direction of time flow.

in subsequent γ-ray spectra.

Once correct identification has been made, γ rays from a particular channel can be selected in software by demanding only those γ rays that are in coincidence with any required combination of particles.

3.7 Summary

The major tools of current γ-ray spectroscopy have been detailed in this chapter. It has been shown that high-spin states in neutron deficient nuclei can be produced using heavy ion fusion evaporation reactions. Large spectrometer arrays composed of many high-purity germanium detectors have recently become the foremost apparatus to detect the subsequent γ-ray de-excitation from these reactions. Recent improvements in semiconductor detector technology, integrated circuitry and data acquisition innovations mark an ongoing development towards better γ-ray spectrometers. Furthermore the use of channel selection devices in conjunction with the capability for detecting and analysing high-fold coincidence events has heralded the advent of an exciting new era for γ-ray spectroscopy.

Chapter 4

Lifetimes and Relative Deformations in ^{131,132,133}Ce

The isotopes ^{131}Ce and ^{132}Ce have been investigated in previous experimental studies aimed at understanding the properties of superdeformation in the A≈130 region. This chapter documents the results of a recent spectroscopic study using the GAMMASPHERE detector array based at LBNL, USA. The aim of the study is to use lifetime measurements to deduce the relative deformations of the SD bands in an effort to understand the deformation driving effects of the N=6 intruder orbitals at high angular momentum. The results also give an important insight into the role of the sidefeeding and its effect on the deformation of band structures. A brief introduction to previous studies of these isotopes precedes an account of the experimental details. A review of the Doppler shift attenuation method (DSAM) is followed by a presentation of the results. A discussion in terms of the cranked shell model follows.

Furthermore, a triaxial band in ^{133}Ce is also populated in this experiment. Previous investigations have suggested that the band is based upon a prolate configuration involving a single $i_{13/2}$ intruder orbital. Doppler broadened lineshape analysis has been performed to deduce the transition and sidefeeding quadrupole moments and lifetimes for the band. The results indicate that this band is not superdeformed and cranking calculations instead suggest a normally deformed oblate structure.

4.1 Previous Studies of ^{131,132}Ce

The earliest evidence of collective behaviour in the A≈132 cerium nuclei came from a study by Ward *et al.* [War68] that identified trends in the low-lying collective levels of bands belonging to the even-A nuclei $^{128-136}$Ce. Dehnhardt *et al.* [Deh74] extended the level schemes and showed through angular distribution and lifetime measurements that the transitions were consistent with a rotational band composed of stretched E2 γ-rays with transition strengths around 100 Wu. The conclusions of Dehnhardt *et al.* established that A≈ 132 cerium nuclei are permanently deformed at low excitation energies. Furthermore the A≈ 130 rare-earth nuclei were predicted to have more deformed shapes that become yrast at high angular momentum and possess deformation parameters around $\beta_2 \approx 0.4$ [BR85]. This prediction was confirmed experimentally by Nolan *et al.* [Nol85] in a study that revealed a rotational band with a high moment of inertia extending to high spin. Subsequent lifetime measurements have verified that the band is based upon a rapidly rotating prolate deformed nucleus and the experimentally deduced quadrupole moment Q_t=8.8eb (β_2=0.45), is consistent with a superdeformed nuclear shape with a 3:2:2 axis ratio [Kir87].

A similar cascade was observed in ^{131}Ce shortly after the superdeformed nature of the ^{132}Ce band had been established [Luo88]. The measurement of the quadrupole moment of this band was the focus of a study using the TESSA3 spectrometer. Using the same reaction as Kirwan (^{100}Mo(^{36}S, xn)$^{136-x}$Ce), the highly deformed character of the ^{131}Ce band was confirmed. The band was interpreted as a cascade produced by a similar prolate deformed nucleus with a somewhat lower deformation ($Q_t \approx$ 6eb, β_2≈0.35) [He90].

The advent of large γ-ray spectrometers such as EUROGAM heralded an exciting opportunity to identify much weaker structures than the first superdeformed bands. A great deal of interest developed in the search for excited superdeformed bands in the same nuclei in which bands had already been observed. Comparison with cranked shell model calculations revealed that there was often a high density of states into which nucleons could be excited and so observations of excited bands would be extremely useful in confirming band configurations. The first observation of excited superdeformed bands was made by Johansson *et al.* who observed three bands in ^{153}Dy using the 8π-spectrometer [Joh89]. Since the SD bands observed in ^{131,132}Ce were strongly populated at ≈ 5% of their respective reaction channels,

it was puzzling that excited bands had not hitherto been observed. An experiment using the EUROGAM spectrometer at Daresbury however led to the observation of two excited bands in ^{132}Ce [San95] and a single excited band in ^{131}Ce [Sem96]. These observations have led to much discussion about the possible configurations of the bands.

4.2 Current Motivation

The EUROGAM experiment successfully uncovered three new superdeformed bands, however the configuration assignments for the bands could not be defined as clearly as expected. At $\beta_2 \approx 0.4$, cranked shell model calculations clearly show a proton shell closure at Z=58 leading to the conclusion that the excited bands were formed by particle-hole excitations involving neutrons. The deformed shell gap at N=72 is diminished at large deformation and high frequency by high-j N=6 $\nu i_{13/2}$ intruder orbitals. The role of high-j intruder orbitals in stabilising large deformations has been a central theme in studies of superdeformation. With the introduction of large nuclear deformations, orbitals that normally lie at high excitation energies are reduced in energy and approach the immediate vicinity of the Fermi surface. In the superdeformed nuclei ^{131,132}Ce, the $i_{13/2}$ neutron orbitals from the N=6 shell are predicted to play an important role in enhancing quadrupole deformation. Calculations based upon the TRS formalism suggest that the occupation of the $i_{13/2}$ neutrons in the $[660]1/2^+$ orbit are directly responsible for stabilising high deformations and consequently studies involving these levels are expected to reveal much about the shape driving properties of these orbitals and those involved in excited configurations.

The single-particle Routhians pictured in Fig. 4.1 show the difficulty in trying to elucidate the configurations from which the bands originate. In ^{131}Ce, the 73rd neutron is expected to fill the $[660]1/2^+$ (α=+1/2) orbital whilst the extra neutron in ^{132}Ce occupies the neighbouring $[660]1/2^+$ (α=–1/2) orbital. There are a large number of possible excitations from which excited bands might be formed. Looking at Fig. 4.1 one might expect many bands with similar excitations energies and therefore similar population intensities. The fact that there have only been two bands observed in ^{131}Ce and three in ^{132}Ce has led to much discussion regarding the whereabouts of possible missing bands.

As the bands are not definitely fixed in spin or excitation energy earlier analysis relied heavily on the evidence from the dynamic moment of inertia, $\Im^{(2)}$. The $\Im^{(2)}$ parameter is

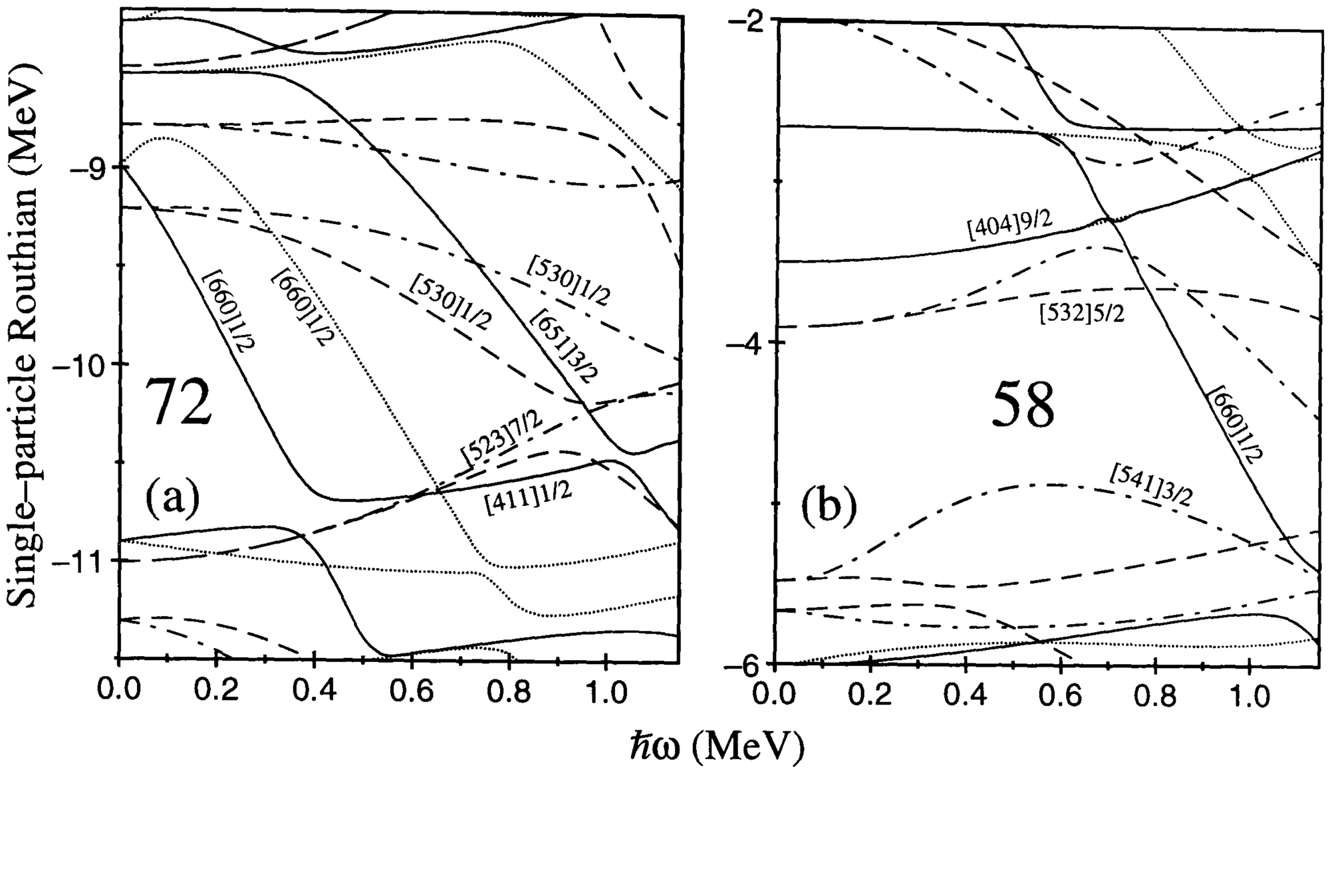

Figure 4.1: Routhian diagrams for β_2=0.4 assuming β_4=0, γ=0°. Each orbital is labelled according to its parity and signature (π, α): Solid lines = (+,+1/2), dotted lines = (+,-1/2), dot-dash lines = (-,+1/2) and dashed lines = (-,-1/2).

very sensitive to changes in nuclear structure and the variation of the $\Im^{(2)}$ with rotational frequency has been central to identifying interactions that give clues to the orbitals involved in the structure. The differences in $\Im^{(2)}$ between the bands have led previous experimenters to suggest that the structures may have different deformations. Interpretations based on the $\Im^{(2)}$ have led to a number of anomalies which have been difficult to explain in terms of the cranked shell model. The evidence obtained from the dynamic moments of inertia will be reviewed in the discussion.

The ideal method for resolving many of the questions that have arisen from previous experiments is to measure the deformations of the excited bands directly. Until the present experiment, the quadrupole moments and lifetimes of the excited bands had not

been measured. The standard method for obtaining the decay time of excited nuclear states, the Doppler shift attenuation method (DSAM), has two major limitations. Firstly, the stopping powers used to model the slowing down of the recoil in the target and backing are poorly known and result in large absolute uncertainties around the 10-15% level. Also the lifetimes of unobserved transitions feeding the in-band transitions must be accounted for in calculations and lead to further uncertainties in the measurement. The current experiment was proposed to reduce the effects of these limitations. Since all five structures are populated under the same experimental conditions it is possibly to directly compare the experimental fractional Doppler shifts (F(τ) curves), thus limiting systematic errors and allowing a comparison of the relative deformations of the structures. Using a large statistics data set from the latest generation γ-ray spectrometer, GAMMASPHERE, it has been possible to limit the unknown sidefeeding. Setting gates above the states of interest removes the the sidefeeding on lower energy states within the cascade. This is the first time such an accurate measurement has been made of the relative deformations of of yrast and excited superdeformed (SD) bands in more than one nucleus in this mass region.

4.3 Experimental details

4.3.1 The Experiment

The experiment was performed at the Lawrence Berkeley National Laboratory using the GAMMASPHERE γ-ray spectrometer. High-spin states in A$\approx$ 132 cerium isotopes were populated with the ^{100}Mo(^{36}S,xn)$^{136-x}$Ce fusion-evaporation reaction. The 88 Inch cyclotron provided a ^{36}S beam at an energy of 155 MeV, incident upon a target comprised of a thin ^{100}Mo foil (600μg/cm^2) backed by a thick (12mg/cm^2) layer of ^{197}Au in which recoiling nuclei stopped. For this experiment, GAMMASPHERE contained 55 Compton suppressed HPGe detectors with the following angular configurations, θ, relative to the beam axis: three at $\theta = 17.3°$, five at 31.7°, five at 37.4°, three at 50.1°, one at 58.3°, one at 79.2°, six at 90.0°, one at 100.8°, five at 121.7°, ten at 129.9°, five at 142.6°, five at 148.3° and five at 162.7°. The data were gainmatched online to fully stopped peaks in ^{132}Ce in order to compensate for the varying detector gains. Approximately, 9×10^8 γ^n (n $\geq$ 4) coincidence events were recorded to tape for subsequent analysis. The population intensities,

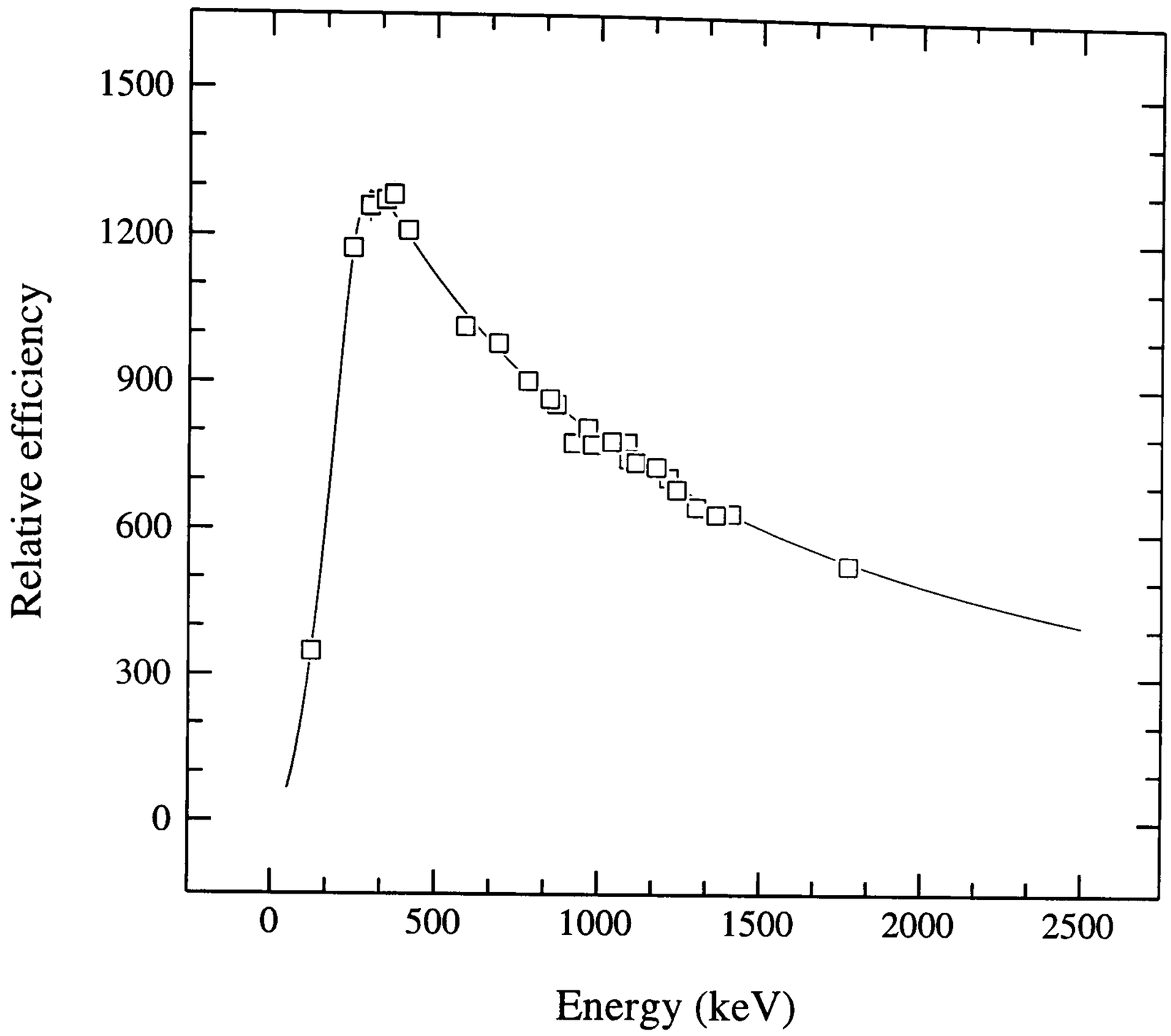

Figure 4.2: Efficiency curve for the GAMMASPHERE spectrometer array. The data points are taken from ^{56}Co and ^{152}Eu radioactive sources.

estimated by comparing the intensities of low lying normally deformed transitions in an ungated matrix, reveal that ^{132}Ce (4n) and ^{131}Ce (5n) are the strongest reaction channels while the 3n channel producing ^{133}Ce was relatively weaker. The measured relative population ratios were estimated to be 5:4:1 for ^{132}Ce, ^{131}Ce and ^{133}Ce, respectively.

Energy and efficiency calibrations were obtained using standard ^{56}Co and ^{152}Eu sources. The efficiency curve defining the response of the spectrometer array is pictured in Fig. 4.2.

4.3.2 Spectral contamination

There are a number of unavoidable sources of contamination in this experiment. This section describes some of the origins of systematic contamination and methods of reducing their influence on spectral quality using the timing properties of the spectrometer.

The major source of contamination is Coulomb excitation of the ^{197}Au backing. The inelastic scattering of the recoil against nuclei in the backing material leaves the backing nuclei in an excited state. The Coulomb excitations contribute to a random background in the spectra. The time differences corresponding to true coincidence events have a definite time relationship whereas random coincidences such as those generated from Coulomb excitation of the backing do not have a correlated timing relationship. Sorting spectra with a selection criterion around the TAC peak selects events with correlated timing relations and greatly reduces the contamination due to Coulomb excitations. An E_γ–Time matrix is shown in Fig. 4.3 to clarify the principle. Events with correlated timing lie in the central region of the energy-time plane. The long vertical lines correspond to the Coulomb excited lines the the ^{197}Au backing foil. Setting limits or gates around the central region and rejecting events outside these limits from subsequent analysis improves the spectral quality. Fig. 4.4a shows the total projection from this data set while Fig. 4.4b and Fig. 4.4c show the events removed from the spectra and the final total projection respectively.

Decay of compound nuclei produced in heavy ion fusion evaporation reactions in the A$\approx$ 130 region can proceed via a number of open particle channels. In this experiment, the isotopes of interest are populated via x-n channels (x = 3, 4 or 5) and it is likely that fast neutrons will strike the germanium detectors. When such events occur, germanium nuclei in the detector crystal are excited by inelastic neutron scattering and the subsequent γ-ray de-excitation produce spurious peaks in the γ-ray spectra. The peaks produced in n-n$'$ reactions are easily recognisable since they are usually wider than prompt γ-ray events. Broadening occurs due to a fraction of the excitation energy transferring into the kinetic energy of the recoiling germanium nucleus, which in turn produces a variable number of electron-hole pairs adding to those produced by the n–n$'$ de-excitation γ-ray. These events are delayed relative to the prompt γ-ray events and can removed from spectra by suitable TAC gating. The n–n$'$ events are displayed in the inset of Fig. 4.4b.

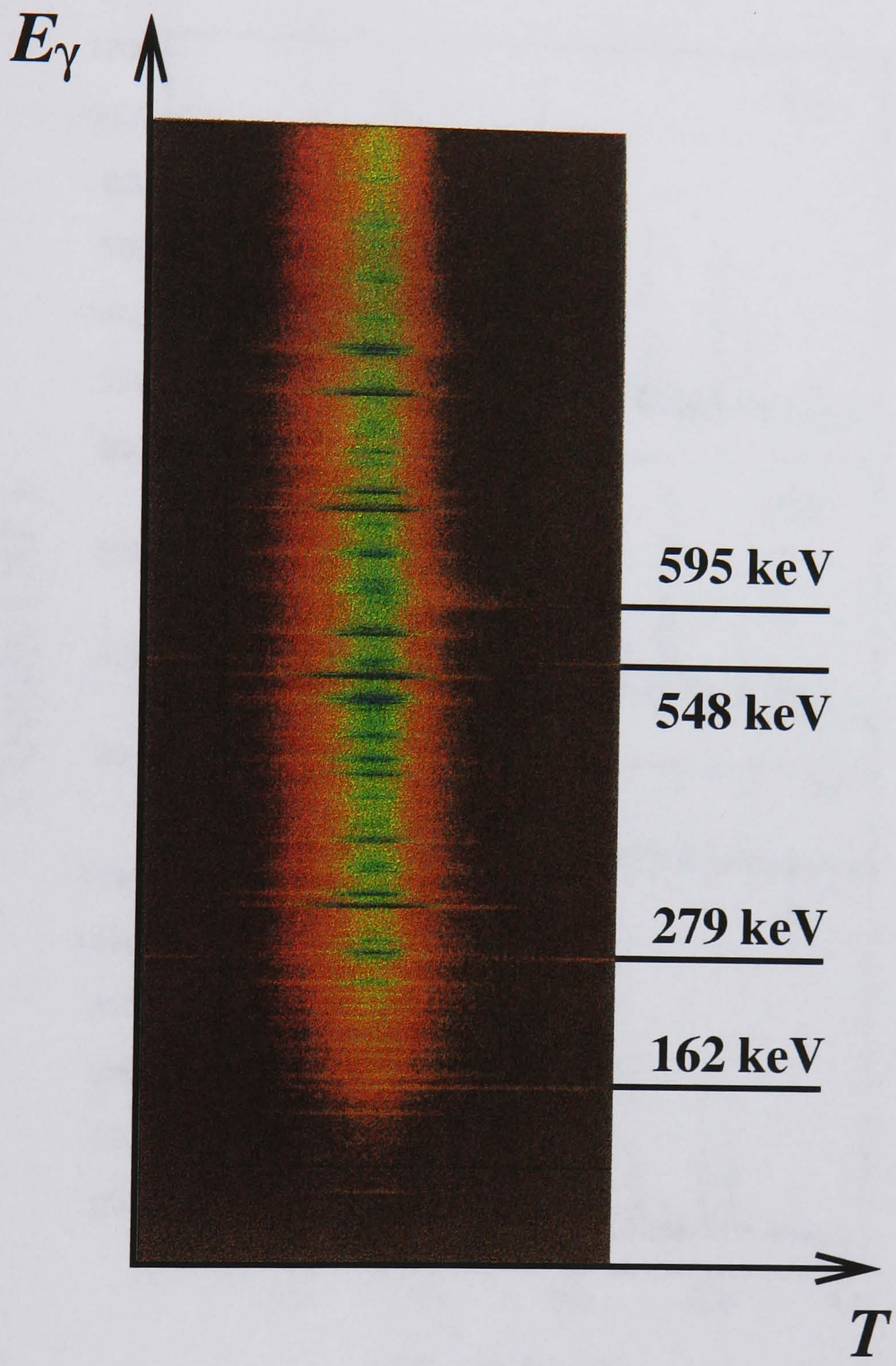

Figure 4.3: An E_γ-TAC matrix. γ-ray events which are correlated in time lie in the central ridge. Coulomb excited lines are represented by continuous lines along the time axis. n-n′ events are noted as extrusions on the right hand side of the central ridge. There is also a 162 keV transition which corresponds to the decay of a short lived isomer in ^{131}Ce.

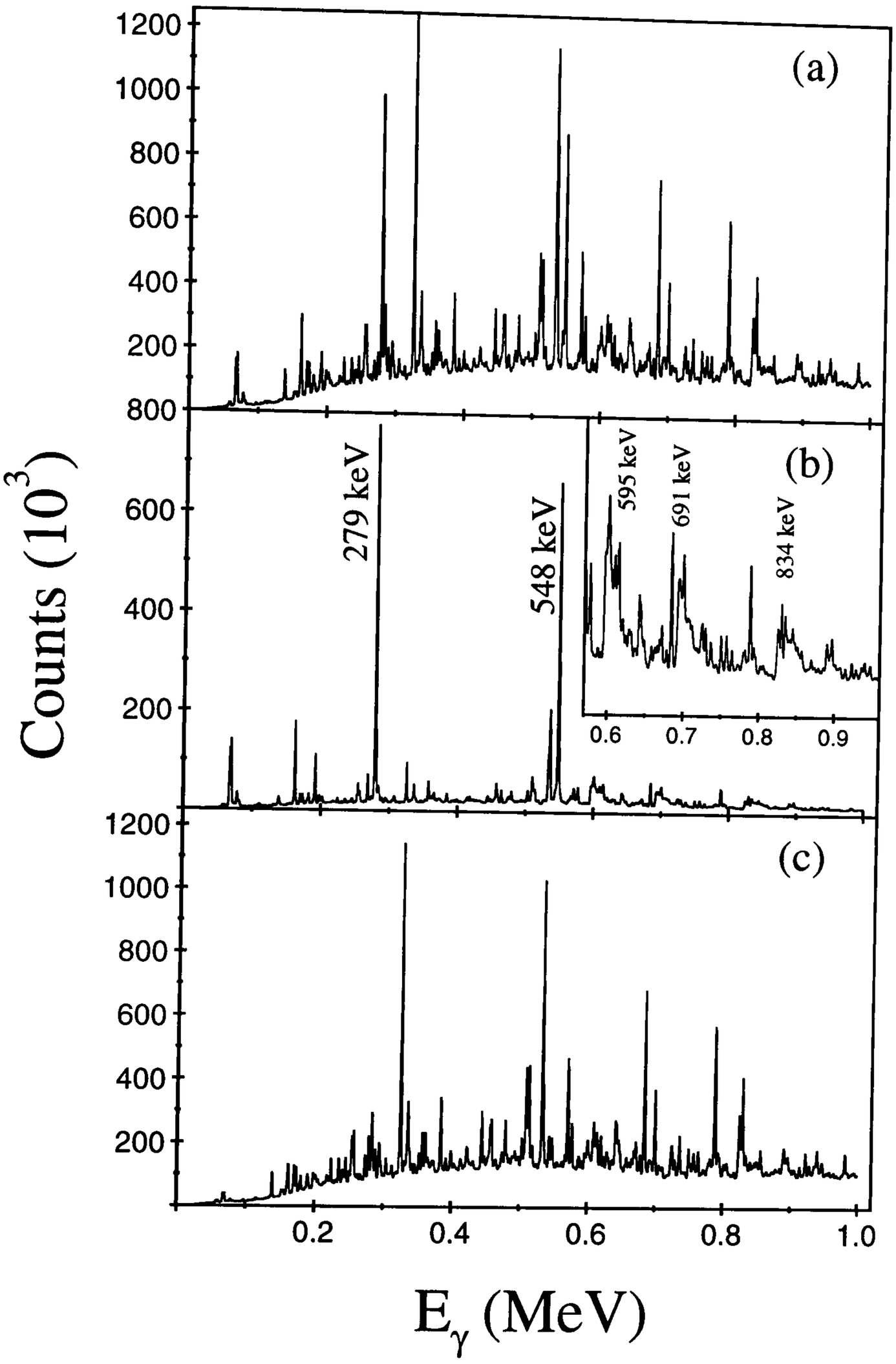

Figure 4.4: Figure displaying the influence of gating on the TAC spectra. (a) The raw data collected in the experiment. There are large contaminant peaks arising from the Coulomb excitation of the ^{197}Au backing. (b) The γ rays removed by selecting events within a time gate. (c) The final total projection after applying a TAC gate.

4.4 Doppler Shift Attenuation Method

The Doppler Shift Attenuation Method (DSAM) is used to measure the lifetimes of states within the range of 10^{-15} – 10^{-12} seconds. The technique is based on the fact that the time taken by a recoiling nucleus to slow down in a metal foil is comparable to the lifetimes of excited nuclear states. A recoil nucleus is formed in the target with an initial velocity, v_0, and is gradually slowed down in the target and backing until it eventually comes to rest. The recoil is continually losing angular momentum by emitting electric quadrupole γ rays as it slows down. The gamma rays are emitted at some average time $\bar{t}$ which is related to the average lifetime of the state. At the time of emission, the recoiling nucleus will possess an attenuated velocity, $\bar{v}$. This process is shown schematically in Fig. 4.5.

There are two methods of extracting lifetime measurements. It is expected that the lifetimes of the excited states should become shorter with increasing deformation (see Eq. 1.56). For example, for a rotational band built on a highly deformed structure with very short lifetimes, it is possible that the band will de-excite before the peak lineshapes have started to exhibit stopped components. Conversely, for lower deformed shapes, the lifetimes of the band members will be longer and so will possess a different stopping character to the highly deformed structure in the previous example. These differences will be reflected in the peak lineshapes as the band de-excites. For states with short lifetimes the γ-rays will be shifted and the centroid shift and lineshape analysis methods can be used to relate the Doppler

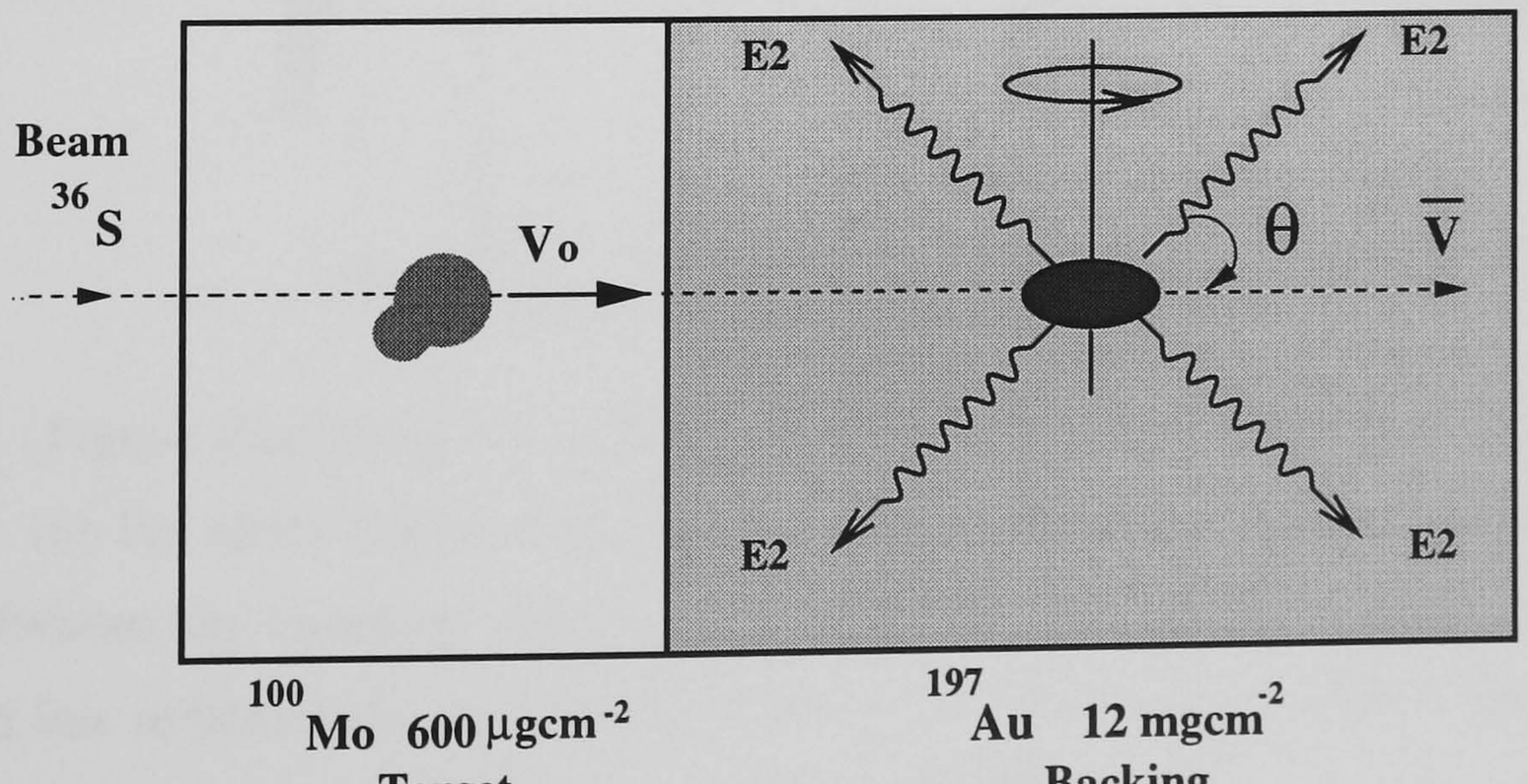

Figure 4.5: Schematic diagram for the Doppler shift attenuation method.

shifted energy to the velocity at which the state decays. If the peaks display significant stopped and shifted components the centroid shift method is inaccurate and lineshape analysis is preferred. The two lineshape regimes are illustrated schematically in Fig. 4.6. Both methods are explained in the following sections.

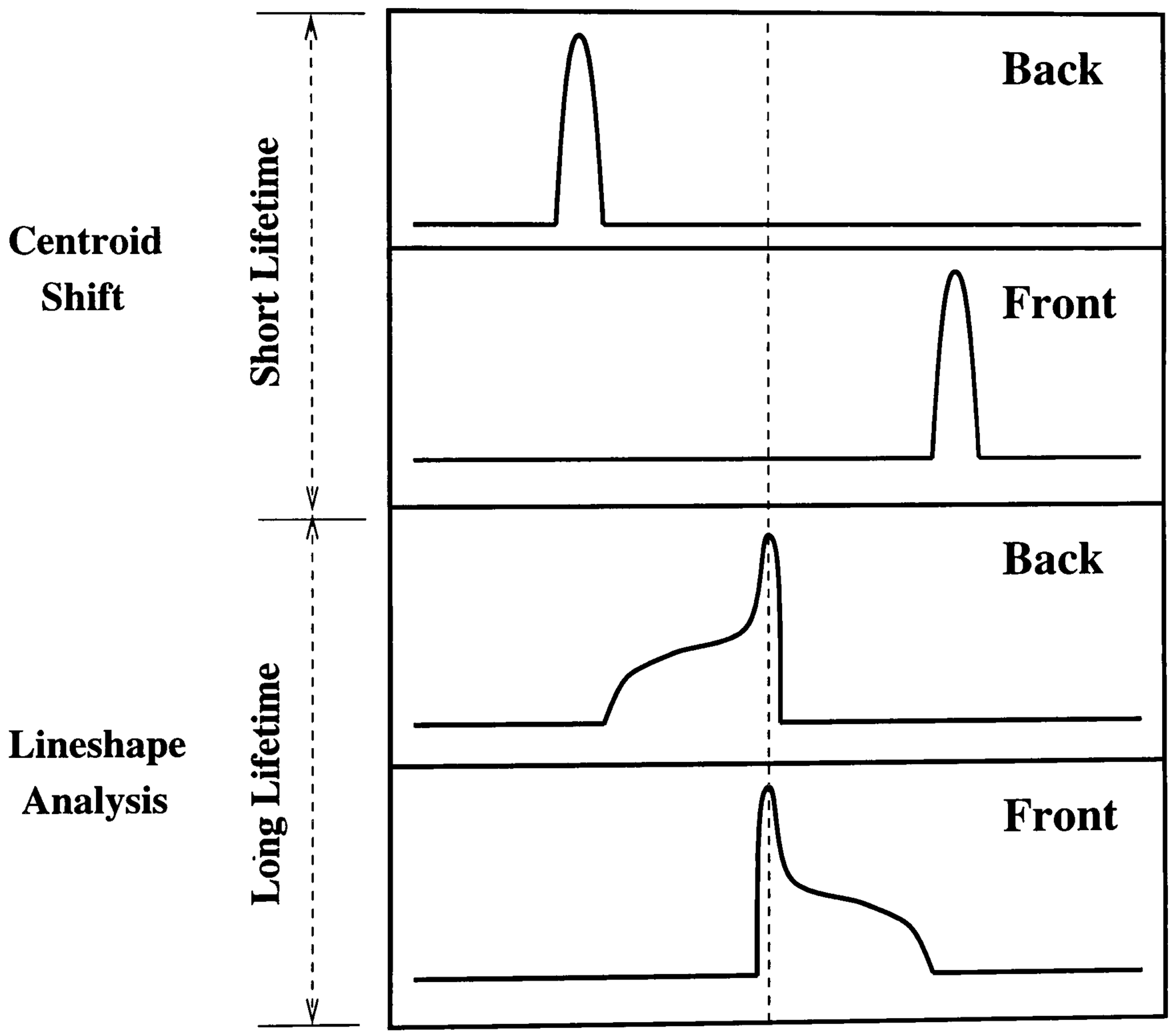

Figure 4.6: Figure displaying the influence of lifetimes on the Doppler broadened peak lineshapes. (a) For short lifetimes the lineshape does not have a stopped component. (b) For long lifetimes the lineshape may possess significant stopped and shifting components. The dashed line indicates the true energy of the γ-ray. The relevant method for measuring lifetimes in the two regimes is stated to the left of the figure.

4.4.1 Centroid Shift Method

The DSAM measures the lifetimes relative to the stopping times of heavy ions in a material. The velocity at which the nucleus de-excites can be deduced by measuring the Doppler shift of the γ-ray transitions. The velocity of the recoil as a function of time can be obtained through the force equation

$$\frac{dE}{dx} = -M\frac{dv}{dt}. \tag{4.1}$$

where dE/dx is the rate of energy loss in the target and backing, M is the mass of the recoil and dv/dt is the rate of change of velocity. Thus the time at which a state decays can be deduced from the measured velocity. This is dependent upon a knowledge of the stopping powers of the target and backing where the recoil is slowing down.

The formula for the Doppler shift of an electromagnetic transition to first order is

$$E_s = E_0\left(1 + \frac{\bar{v}}{c}\cos\theta\right). \tag{4.2}$$

The fractional Doppler shift can be obtained from spectra generated from gated matrices that register coincidences from specific angular groups of detectors as described in section 3.4.1. The spectra produced for the extreme angles of the array are shown in Fig. 4.7 The shifted energies at the forward and backward angles of the spectrometer are given by

$$E_f = E_0\left(1 + \frac{\bar{v}}{c}\cos\theta_f\right), \tag{4.3}$$

$$E_b = E_0\left(1 + \frac{\bar{v}}{c}\cos\theta_b\right). \tag{4.4}$$

Since the forward and backward angles are symmetric about the 90° position

$$\theta = \theta_f = 180° - \theta_b, \tag{4.5}$$

and subtracting Eq. 4.4 from Eq. 4.3 gives

$$E_f - E_b = 2E_0\frac{\bar{v}}{c}\cos\theta. \tag{4.6}$$

The attenuated velocity at the time of emission can be defined as

$$\frac{\bar{v}}{c} = \frac{\bar{v}}{v_0}\frac{v_0}{c} = F(\tau)\beta_0, \tag{4.7}$$

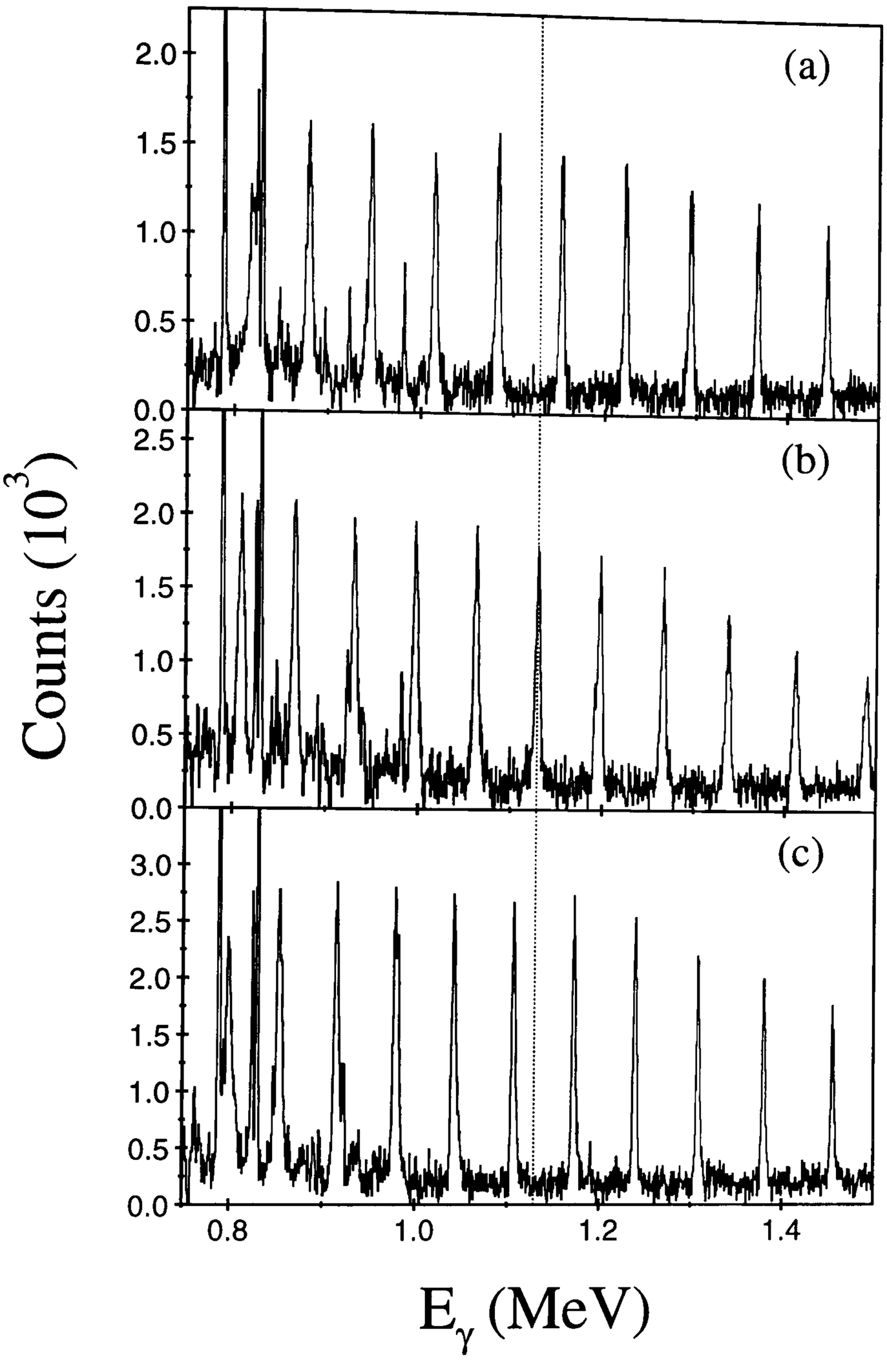

Figure 4.7: Spectra displaying Doppler shifted peaks at (a) forward angles (17.3°), (b) centre (90°) and (c) backward angles (162.7°) of the GAMMASPHERE array. The dotted line marks the unshifted position of the 1129 keV transition. It can be seen that the peak is shifted to the right in (a) and to the left in (b).

where $\beta_0 = v_0/c$ and denotes the unattenuated v/c value. Note, β_0 has been calculated with the assumption that the compound nucleus is formed at the centre of the target. The attenuation of the beam at this point in the target has been calculated using the stopping powers of Ziegler [Zie95] and the initial recoil velocity v_0= 0.0253 has been deduced using reaction kinematics.

Thus, the fractional Doppler shift F(τ) is defined as

$$F(\tau) = \frac{E_f - E_b}{2E_0\beta_0 \cos\theta}. \tag{4.8}$$

4.4.2 Lineshape Fitting Method

The lineshape fitting method compares the lineshapes of individual peaks at different angles with simulated theoretical lineshapes using the definition of the fractional Doppler shift factor, F(τ) in terms of the peak lineshape such that

$$F(\tau) = \frac{1}{v_0}\left(\int_0^{v_0} v\frac{dN(v)}{dv}dv\right) \Big/ \left(\int_0^{v_0} \frac{dN(v)}{dv}dv\right). \tag{4.9}$$

Since the Doppler shifted energy is proportional to the recoil velocity, information contained in the lineshape is derived from $dN(v)/dv$ with

$$dN(t) = \frac{1}{\tau}\exp\left[-\frac{t}{\tau}\right]dt. \tag{4.10}$$

which can also be written in terms of τ,

$$F(\tau) = \frac{1}{v_0\tau}\int_0^{\infty} v(t)\exp\left[-\frac{t}{\tau}\right]dt, \tag{4.11}$$

The lineshape fitting method is especially useful for extracting the lifetimes of states where the lineshape has broadened into stopped and shifted components. For example, the triaxial band in ^{133}Ce detailed in section 4.7 has states in which both stopped and shifted components are apparent, implying that lineshape analysis is the most appropriate method to achieve accurate lifetime measurements.

4.4.3 Stopping Powers

Modelling the recoil velocities of ions in matter depends on knowledge of the stopping powers. Generally, the experimental stopping powers for specific reactions are not widely available and it is necessary to provide an approximation for the stopping powers used. The stopping of recoils in matter is often separated into two distinct physical regimes. Ions can be stopped by interactions with either electrons or nuclei in the stopping medium. Electronic stopping arises from the Coulomb interaction of the recoil nucleus with the atomic electrons in the stopper. Since the mass of the recoiling nucleus is many magnitudes greater than the electron mass, energy is lost in small amounts and the recoil direction is not significantly deflected. Electronic stopping is modelled as a continuous energy loss process and is dominant for recoil velocities v/c $\geq$2%. Nuclear stopping is dominant at low recoil velocities. At v/c $\leq$0.3% the cross sections for interaction between the recoil nucleus and the stopper nuclei become significant. Since the stopper nuclei have comparable sizes to the recoil nuclei, collisions between them are influenced by the Coulomb and strong interactions which can cause large energy losses and major directional changes.

The stopping powers may be defined as the sum of the electronic and nuclear contributions [LSS63].

$$\frac{dE}{dx} = \left(\frac{dE}{dx}\right)_e + \left(\frac{dE}{dx}\right)_n, \tag{4.12}$$

where the subscripts e and n refer to electronic and nuclear stopping respectively. Corrections are usually applied to Eq. 4.12 to provide a better fit to experimental stopping powers to allow for charge oscillation effects observed by Currie [Cur69]

$$\frac{dE}{dx} = f_e\left(\frac{dE}{dx}\right)_e + f_n\left(\frac{dE}{dx}\right)_n, \tag{4.13}$$

where f_e and f_n are the correction coefficients for electronic and nuclear stopping respectively. The nuclear stopping component is usually treated using the Blaugrund approximation [Bla66],

$$\overline{v\cos\theta} = \overline{v}\ \overline{\cos\theta}, \tag{4.14}$$

which effectively separates the nuclear scattering from the stopping and treats both processes independently. The stopping powers used in this work are taken from tables formulated by Ziegler [Zie95].

4.5 Results for ^{131,132}Ce

4.5.1 Fractional Doppler Shifts

Since superdeformed bands have short lifetimes (e.g. F(τ)$\geq$0.5) it is possible to perform a centroid shift analysis for the bands in ^{131,132}Ce. The data were sorted into gated $E_{\gamma 1} - E_{\gamma 2}$ correlation matrices as described in section 3.4.1. Each matrix required a single gate set on an in-band transition to be satisfied before the matrix was incremented. Five matrices were sorted for each band according to detector angle as shown in Table 4.1. Spectra were produced by subsequent gating on the 'all' axis and projecting out coincidences at specific angles. The resulting spectra are selective with regard to the detectors that are used in the analysis and consequently leads to a reduction in statistics compared with spectra produced by demanding coincidences with all detectors on both axes. The lower number of counts in the spectra is more serious for the excited bands which have lower population intensities. To overcome this limitation matrices were sorted where coincidences with detectors at θ=31.72° and 37.38° and θ= 142.62° and 148.28° were incremented into matrices with $\bar{\theta}$=34.55° and $\bar{\theta}$=145.45° respectively. The energy of shifted γ-ray transitions using the bands were measured by fitting Gaussian lineshapes to peaks in spectra within the RADWARE GF2 code. The errors on the γ-ray transitions were calculated to include the

Matrices sorted for DSAM analysis

Detector angles (x-axis)	Detector angles (y-axis)	No. Detectors
All	17.27°	3
All	34.55°*	10
All	90°	6
All	145.45°*	10
All	162.73°	5

Table 4.1: Matrices sorted for the DSAM analysis of superdeformed bands in ^{131,132}Ce. 'All' refers to all remaining detectors in the array recorded in an event. * denotes an average angle sorted from two separate angles.

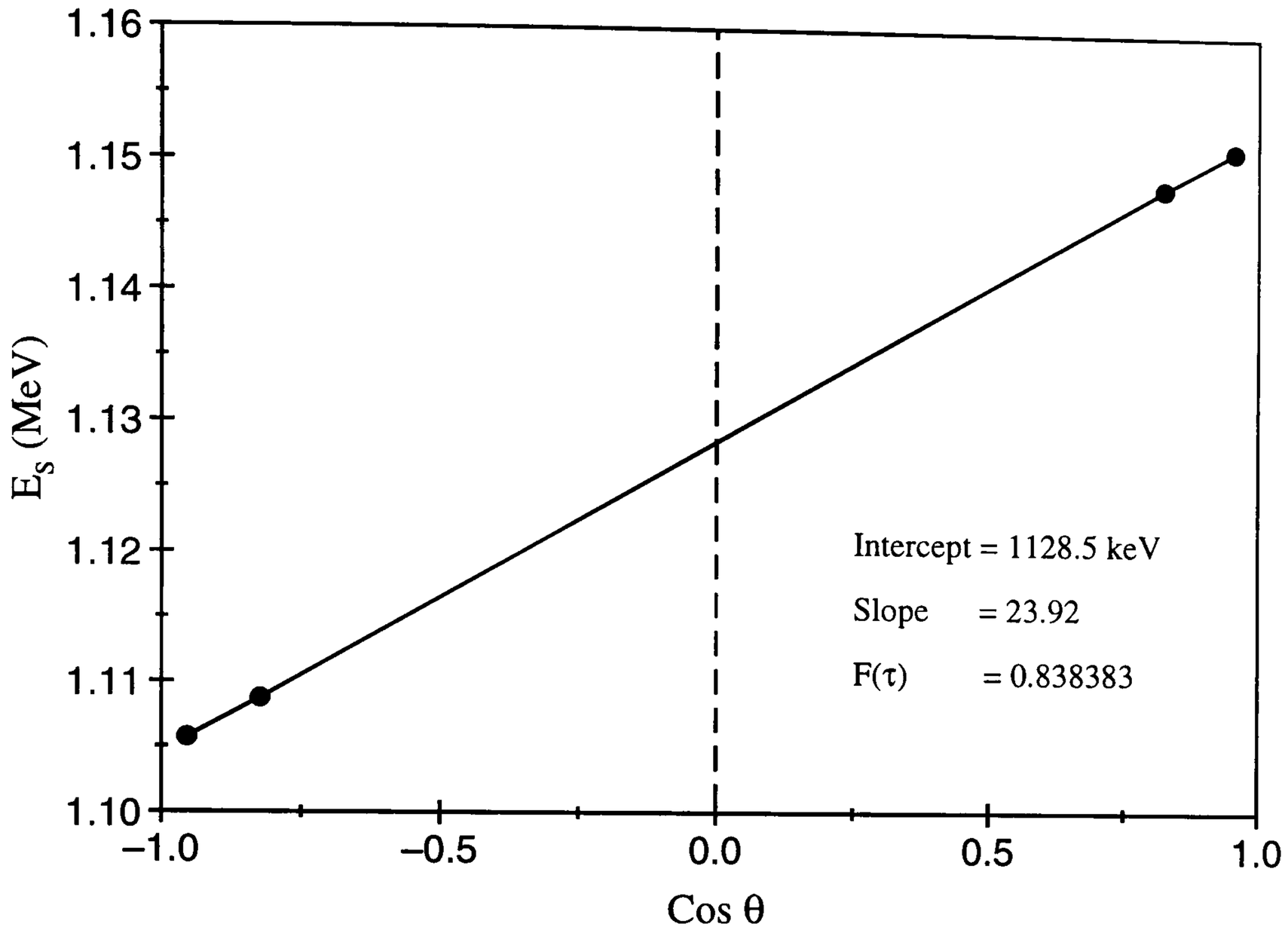

Figure 4.8: A typical fit to experimental values using the graphical method to extract $F(\tau)$ values. This fit is for the 1129 keV transition in ^{132}Ce superdeformed band 1.

contributions from the background spectra. The measured Doppler shifted energies can be substituted into Eq. 4.8 to extract the attenuation factor F(τ). An alternative method can be used which utilises the equation

$$E_s = E_0 F(\tau)\beta_0 \cos\theta + E_0, \tag{4.15}$$

to obtain an average F(τ) value graphically. Eq. 4.15 has the form of the equation defining a straight line. Plotting the shifted energies measured from spectra as a function of the cosine of detector angle yields a gradient of $E_0 F(\tau)\beta_0$ and an intercept of E_0. This method is advantageous over direct substitution into Eq. 4.8 as it clearly shows any rogue points at a particular angle that may deviate from the line and can be discarded in the fit. As a further check all detector angles except the 90° detectors can be used in the fit and the fitted intercept values should be consistent with 90° value corresponding to the true γ-ray energy. A typical fit is displayed in Fig. 4.8. The F(τ) values are plotted as a function of γ-ray energy in Fig. 4.9.

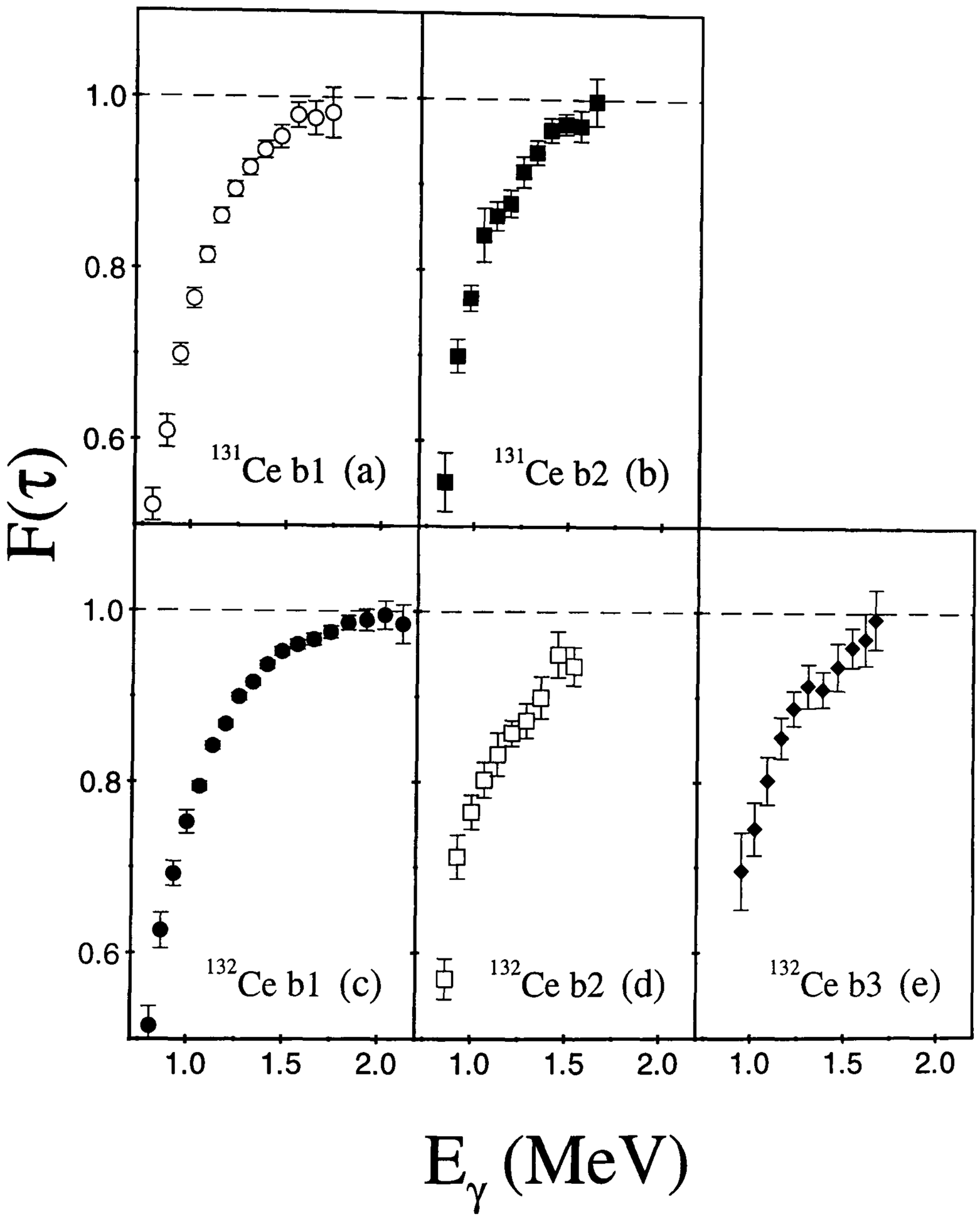

Figure 4.9: Doppler shift attenuation factor, F(τ), for superdeformed bands in ^{131,132}Ce. (a) ^{131}Ce yrast SD band (b) ^{131}Ce SD band 2 (c) ^{132}Ce yrast SD band (d) ^{132}Ce SD band 2 and (e) ^{132}Ce SD band 3. The dashed line denotes F(τ)=1 which corresponds to a γ ray decay at the initial recoil velocity, v_0.

4.5.2 Quadrupole Moments

The F(τ) value is the ratio of the attenuated velocity at the time of emission to the initial recoil velocity and so by modelling the rate of change of velocity for different quadrupole moments it is possible to generate theoretical attenuation curves. The quadrupole moment for superdeformed bands is obtained through comparison of the extracted F(τ) curves with theoretical calculations. The measured quadrupole moments were deduced from χ^2-minimisation to calculated curves generated using the stopping powers of Ziegler and are recorded in Table 4.2. In order to allow direct comparison with cranked shell model calculations the quadrupole deformation parameter has been inferred from the expansion of Q_t in terms of β_2 given in [LVH70] assuming no hexadecapole deformation, such that

$$Q_t = \frac{3}{\sqrt{5\pi}} Z R_0^2 \beta_2 \left[1 + \frac{1}{8}\sqrt{\frac{5}{\pi}}\beta_2 + \frac{5}{8\pi}\beta_2^2 - \frac{5}{192\pi}\sqrt{\frac{5}{\pi}}\beta_2^3 + ... \right]. \tag{4.16}$$

Note $Q_t = Q_0$ for axially symmetric shapes. The β_2 parameter is also listed in Table 4.2. Calculated F(τ) curves, assuming a constant quadrupole moment of either Q_t=5.4 or 9.4 eb are shown for comparison with the data in Fig. 4.10. A cursory inspection of the Fig. 4.10 allows several important points to be stated. The yrast superdeformed bands in ^{131,132}Ce have very similar Q_t values suggesting that the two structures have similar deformations. The ^{131}Ce band extends to lower excitation energies via three transitions of energy 591, 662, and 732 keV. The 662 and 732 keV transitions are contaminated in the spectra and

Structure	Q_t (eb)	β_2
^{131}Ce Band 1	7.3 ± 0.3	0.408 ± 0.015
^{131}Ce Band 2	8.2 ± 0.4	0.452 ± 0.021
^{132}Ce Band 1	7.4 ± 0.3	0.411 ± 0.015
^{132}Ce Band 2	7.2 ± 0.4	0.401 ± 0.021
^{132}Ce Band 3	7.0 ± 0.4	0.391 ± 0.021

Table 4.2: The quadrupole moments Q_t extracted for the superdeformed bands in ^{131,132}Ce. The quadrupole deformation parameter, β_2 is also shown.

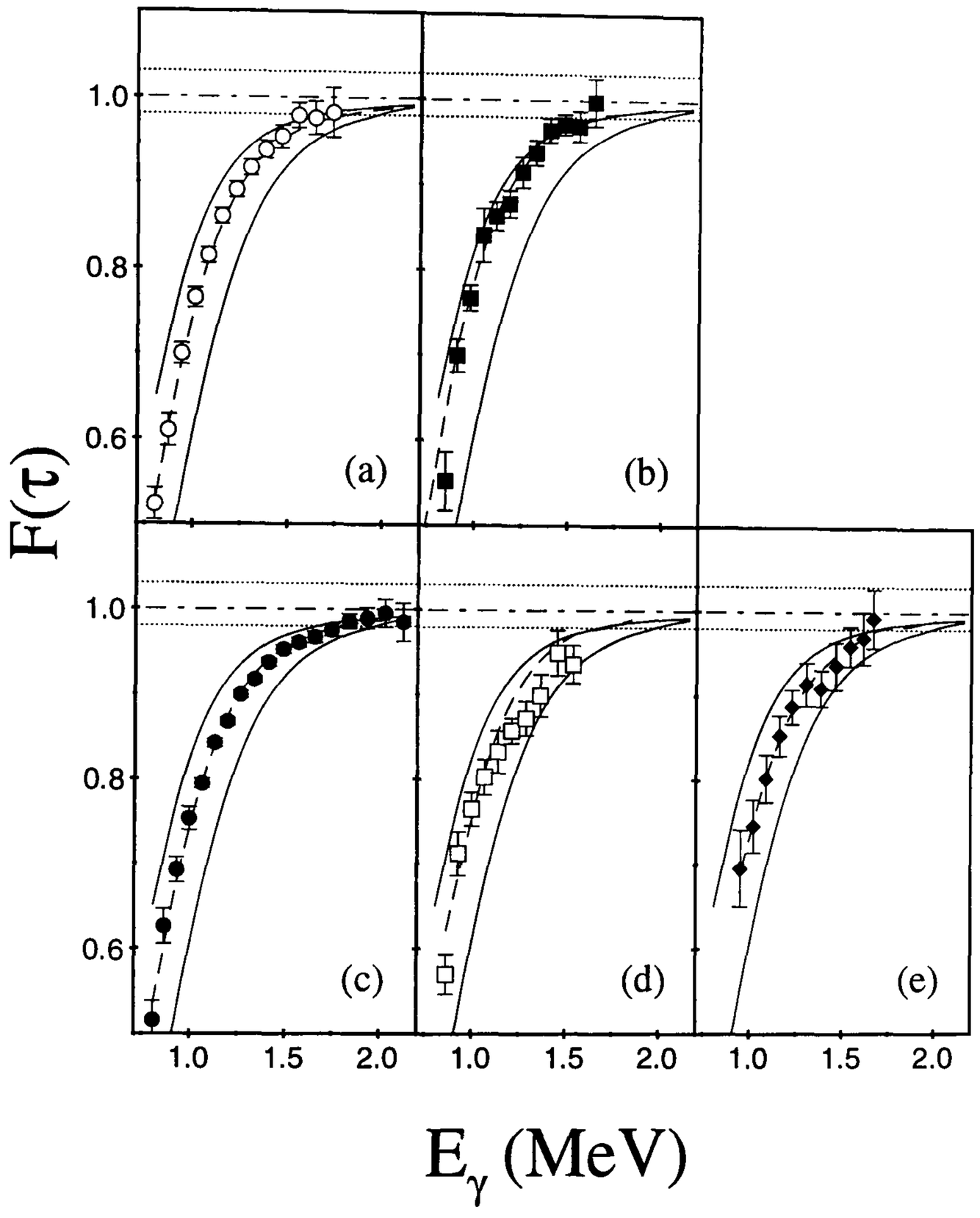

Figure 4.10: Experimental F(τ) curves for SD bands in ^{131,132}Ce compared with calculated curves. The solid lines above/below the experimental values are calculated for Q_t=9.4 and Q_t=5.4 eb. The dashed lines display the F(τ) curves for the measured Q_t values. The dot-dashed line denotes F(τ)=1 which corresponds to a γ ray decay at the initial recoil velocity, v_0. The dotted lines above/below F(τ)=1 indicate an estimate of the spread in F(τ) values obtained when v_0 is calculated assuming the recoil is formed at back/front of the target. (a) ^{131}Ce yrast SD band (b) ^{131}Ce SD band 2 (c) ^{132}Ce yrast SD band (d) ^{132}Ce SD band 2 and (e) ^{132}Ce SD band 3.

consequently there is little confidence in using values extracted for these transitions. Only transitions above these are used in the fitting procedure. The excited bands in ^{132}Ce are also of consistently similar deformations to the yrast bands in ^{131,132}Ce indicating that four of the five structures have nuclear shapes of similar deformations. This is an important result since it implies that the second minimum in ^{132}Ce is extremely stable in the presence of single-particle excitations. The remaining band, ^{131}Ce band 2 clearly possesses a larger deformation. The extracted value Q_t =8.2(4) is approximately 12% higher than the yrast SD band.

These results are largely unexpected since previous experiments have all concluded that ^{131}Ce band 1 is much less deformed than the yrast structure for ^{132}Ce. The configurations for these bands have not been definitely assigned, however these deformation values will be used to generate cranked shell model calculations that will assist configuration assignments.

4.5.3 Lifetimes and Transition Strengths

The quadrupole moments extracted from the centroid shift measurement have been used to obtain transition strengths ($T(E2)_{expt}/T(E2)_{sp}$) and lifetimes (τ) for the SD bands in ^{131,132}Ce. These quantities are extremely useful for estimating the collectivity of the nucleus. Fig. 4.11 shows the lifetimes for all the bands and the complete measurements are listed in Tables 4.3, 4.4 and 4.5.

Comparison of the experimental transitions probabilities ($T(E2)$) with the single-particle Weisskopf estimates implies that all the bands are highly collective with transition strengths of the order of $T(E2)_{expt}/T(E2)_{sp}\approx$480 Wu. These measurements are much larger than the normally deformed yrast states in the ^{132}Ce ground state band that have been measured at $\approx$100 Wu. Although the transition strengths are not as large as those extracted for superdeformed bands in other mass regions ($T(E2)_{expt}/T(E2)_{sp}\approx$2000 Wu for the superdeformed A$\approx$150 region), they are consistent with superdeformed prolate shapes defined by 3:2 major-minor axis ratios. The excited band in ^{131}Ce has much larger transition strengths than the other bands with $T(E2)_{expt}/T(E2)_{sp}\approx$610 Wu. These values are $\approx$27% larger than the other bands in this discussion. These results suggest that the excited band in ^{131}Ce is clearly based on a more deformed structure. The remaining bands appear to possess very

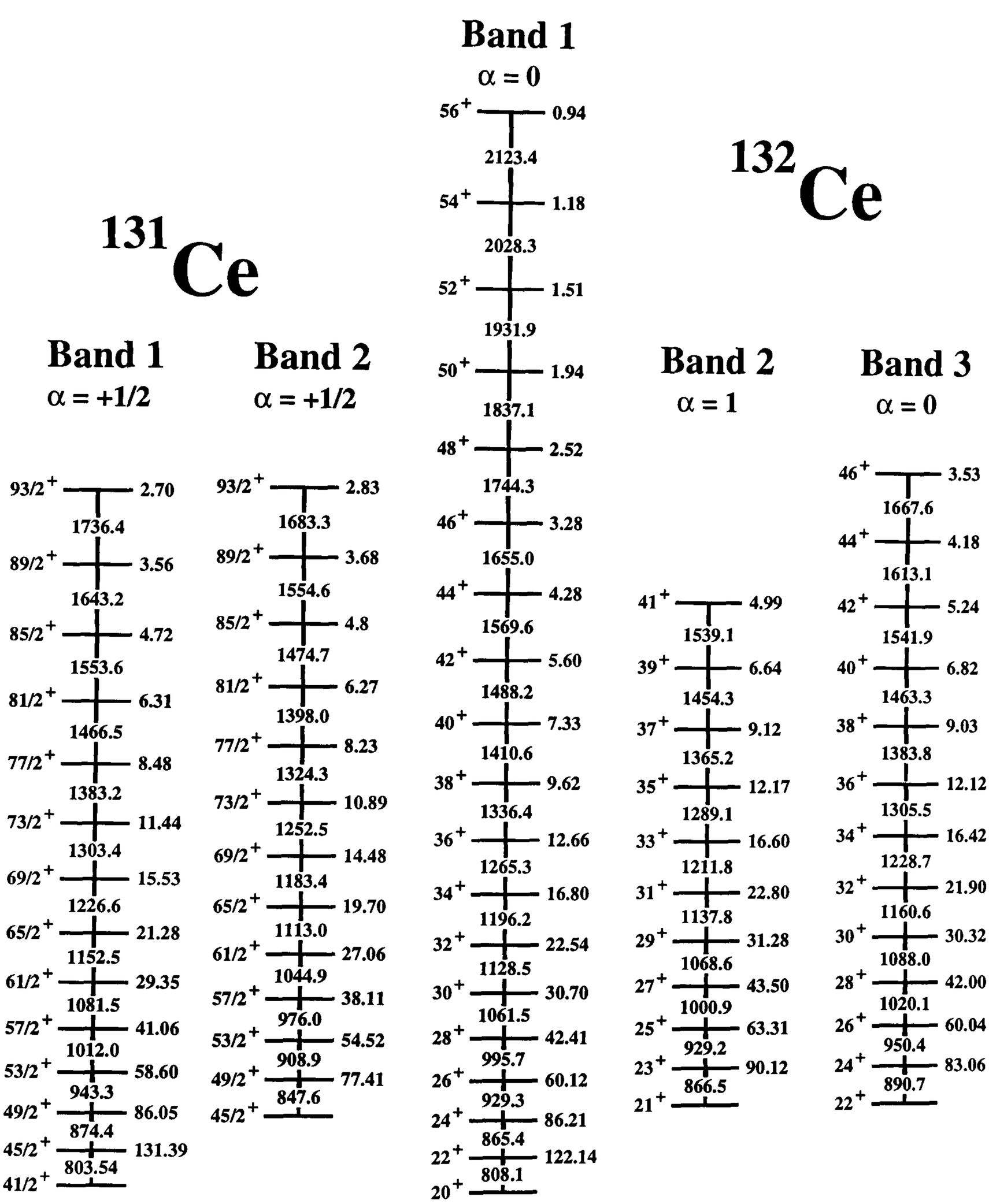

Figure 4.11: Figure detailing the deduced lifetimes for the superdeformed bands. Tentative spins are noted to the left of the levels while the lifetimes in femtoseconds are labelled to the right. The bands are labelled with a proposed signature based upon arguments presented later in this chapter.

^{131}Ce Superdeformed Band 1		
E_γ (MeV)	$T(E2)_{expt}/T(E2)_{sp}$ (Wu)	τ (fs)
0.8035(2)	468	131.39
0.8744(2)	488	86.05
0.9433(2)	470.4	58.60
1.0120(2)	472.4	41.06
1.0815(2)	474.2	29.35
1.1525(2)	475.8	21.28
1.2266(2)	477.3	15.53
1.3034(2)	478.6	11.44
1.3832(2)	479.7	8.48
1.4665(3)	480.8	6.31
1.5536(3)	481.8	4.72
1.6432(4)	482.7	3.56
1.7364(5)	483.5	2.70
^{131}Ce Superdeformed Band 2		
0.8476(6)	608.0	77.41
0.9089(5)	609.0	54.52
0.9760(6)	610.0	38.11
1.0449(3)	611.0	27.06
1.1130(4)	611.9	19.70
1.1834(3)	612.7	14.48
1.2525(3)	613.5	10.89
1.3243(4)	614.2	8.23
1.3980(4)	614.9	6.27
1.4747(3)	615.5	4.80
1.5546(4)	616.1	3.68
1.6383(5)	616.7	2.83

Table 4.3: Transition strengths $(T(E2)_{expt}/T(E2)_{sp})$ and lifetimes (τ) for the stretched E2 transitions in the ^{131}Ce superdeformed bands.

^{132}Ce Superdeformed Band 1

E_γ (MeV)	$T(E2)_{expt}/T(E2)_{sp}$ (Wu)	τ (fs)
0.8081(4)	484.2	122.14
0.8654(4)	487.0	86.21
0.9293(3)	489.2	60.12
0.9957(3)	491.1	42.41
1.0615(1)	492.7	30.7
1.1285(1)	494.02	22.54
1.1962(1)	495.2	16.80
1.2653(1)	496.3	12.66
1.3364(1)	497.2	9.62
1.4106(1)	498.0	7.33
1.4882(1)	498.7	5.60
1.5696(2)	499.4	4.28
1.6550(2)	500.0	3.28
1.7443(2)	500.5	2.522
1.8371(2)	501.0	1.94
1.9319(4)	501.5	1.51
2.0283(5)	501.5	1.18
2.1234(6)	501.5	0.942

Table 4.4: Transition strengths ($T(E2)_{expt}/T(E2)_{sp}$) and lifetimes (τ) for the stretched E2 transitions in ^{132}Ce superdeformed band 1.

^{132}Ce Superdeformed Band 2		
E_γ (MeV)	$T(E2)_{expt}/T(E2)_{sp}$ (Wu)	τ (fs)
0.8665(2)	463.1	90.12
0.9292(2)	464.9	63.31
1.0009(2)	466.4	43.50
1.0686(2)	467.7	31.28
1.1378(3)	468.8	22.80
1.2118(3)	469.8	16.60
1.2891(4)	470.7	12.17
1.3652(4)	471.4	9.12
1.4543(5)	472.1	6.64
1.5391(5)	472.7	4.99
^{132}Ce Superdeformed Band 3		
0.8907(2)	437.7	83.06
0.9504(2)	437.7	60.04
1.0201(2)	439.4	42.00
1.0880(2)	440.8	30.32
1.1606(2)	442.1	21.90
1.2287(3)	443.1	16.42
1.3055(3)	444.1	12.12
1.3838(4)	444.9	9.03
1.4633(4)	445.6	6.82
1.5419(5)	446.3	5.24
1.6131(5)	446.9	4.18
1.6676(6)	447.4	3.53

Table 4.5: Transition strengths ($T(E2)_{expt}/T(E2)_{sp}$) and lifetimes (τ) for the stretched E2 transitions in the ^{132}Ce excited bands.

similar deformation characteristics and therefore, the enhanced collectivity is probably due to some characteristic structure that is not apparent in the other superdeformed bands.

4.5.4 Role of Sidefeeding

A major aim of this work was to substantially reduce the effects of the unknown sidefeeding transitions. If the unseen transitions have long lifetimes the increased contribution to the total lifetime can dramatically lower the apparent deformation. The effect of sidefeeding is removed by gating on transitions that lie above the measured state. It is also possible to extract a measurement where the sidefeeding has been allowed to take full effect. For example, a schematic superdeformed band is pictured in Fig. 4.12a, where the bold arrows describe in-band transitions while sidefeeding transitions are depicted as diagonal dashed lines. If a gate is set on γ_1 in Fig. 4.12a the resulting spectra should contain all the γ rays in Fig. 4.12b. Selecting coincidences with transitions at the bottom of the band will thus include the unseen feeding transitions. For the opposite extreme case, coincidences with γ_6 completely remove the influence of the sidefeeding transitions. In reality, different gating criteria produce spectra with varying degrees of sidefeeding. If γ_5 is demanded with γ_6, an albeit smaller contribution to the total lifetime of level 6 will arise from γ_c.

In order to deduce information on the magnitude of the sidefeeding, matrices were sorted with different gating criteria. Matrices for the two yrast SD bands in ^{131,132}Ce were sorted using gates set on γ-ray transitions either above (gated high) or below (gated low) 1150 keV. In the region below $E_\gamma \approx 1150$ keV both bands are fully fed and the superdeformed states will be most sensitive to the effects of sidefeeding. Fig. 4.13 shows the resultant $F(\tau)$ values extracted with full sidefeeding and reduced sidefeeding. Quadrupole moments deduced from χ^2-minimisation to calculated $F(\tau)$ curves in the sensitive region are displayed in Table 4.6. The effects of sidefeeding appear to be greater for ^{131}Ce band 1 resulting in lower $F(\tau)$ values in the sensitive region. If sidefeeding is not correctly accounted for in calculations the extracted Q_t values will be lower than the true value. The difference in the Q_t values extracted from the curves is approximately 10%. Consequently the lifetimes of the sidefeeding transitions are expected to be significantly longer than the in-band transitions ($\approx 2-3$ times longer). This suggests that band 1 in ^{131}Ce is fed by a states of different character to the in-band transitions, probably with a lower deformation.

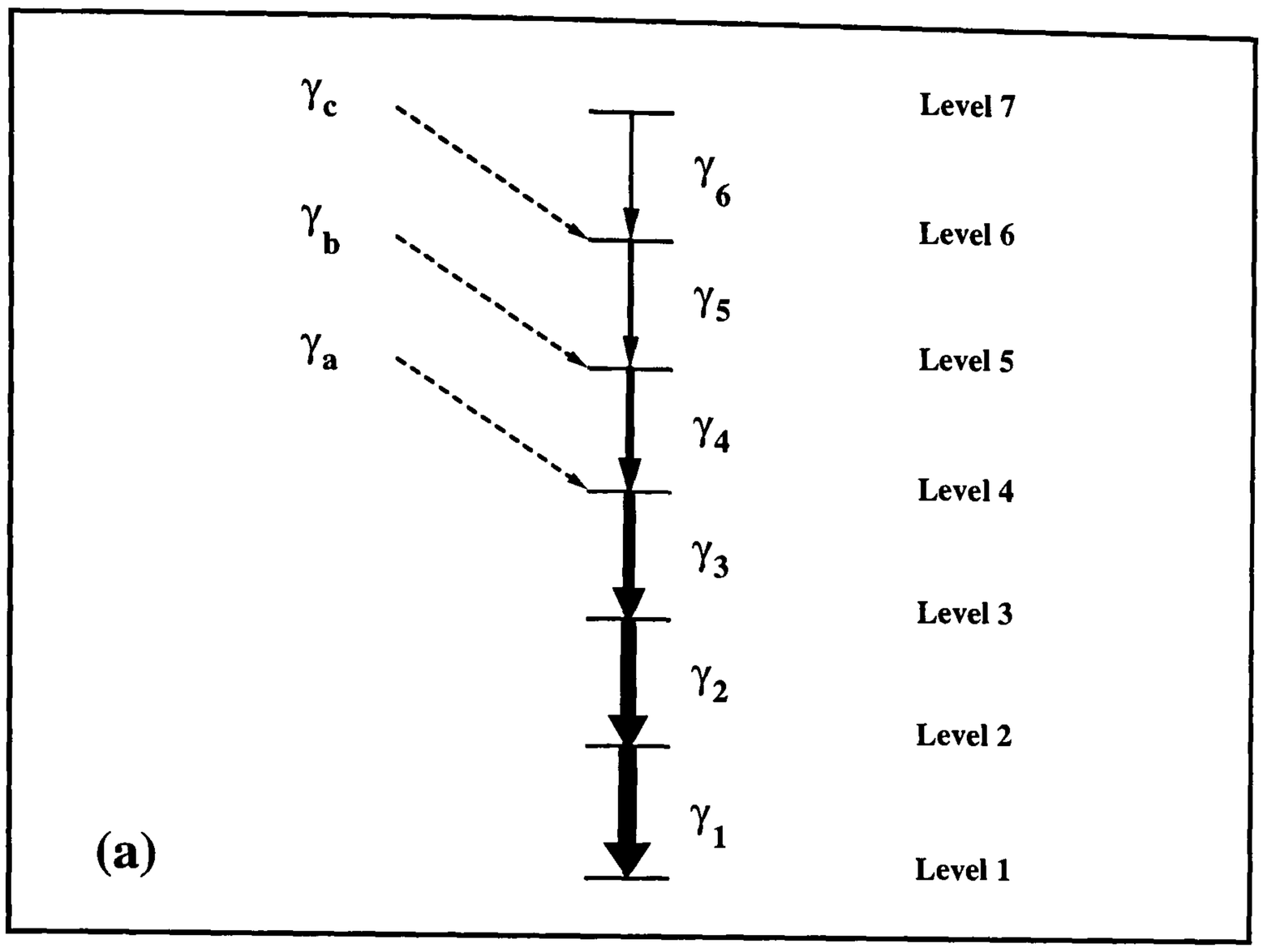

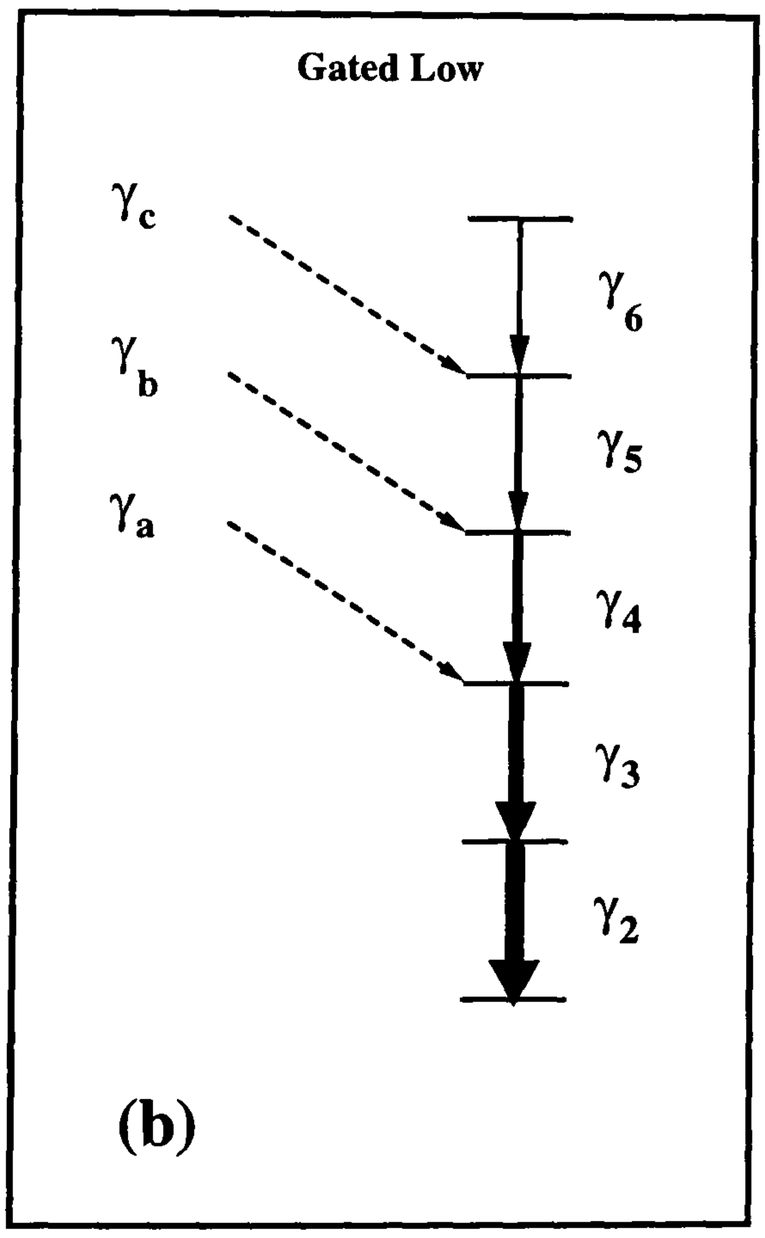

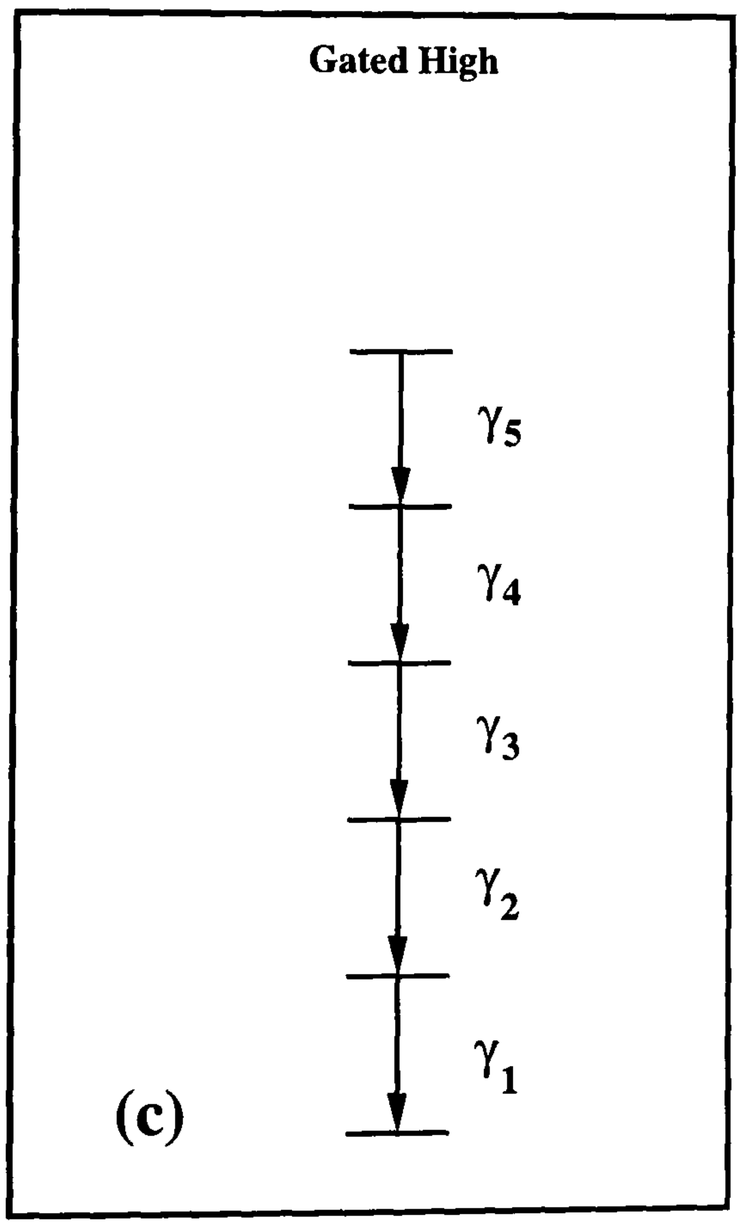

Figure 4.12: A figure illustrating the role of sidefeeding in superdeformed bands. (a) A schematic illustration of a superdeformed band. (b) γ rays in coincidence with γ_1. (c) γ rays in coincidence with γ_6. The width of the arrows represent the γ-ray intensities.

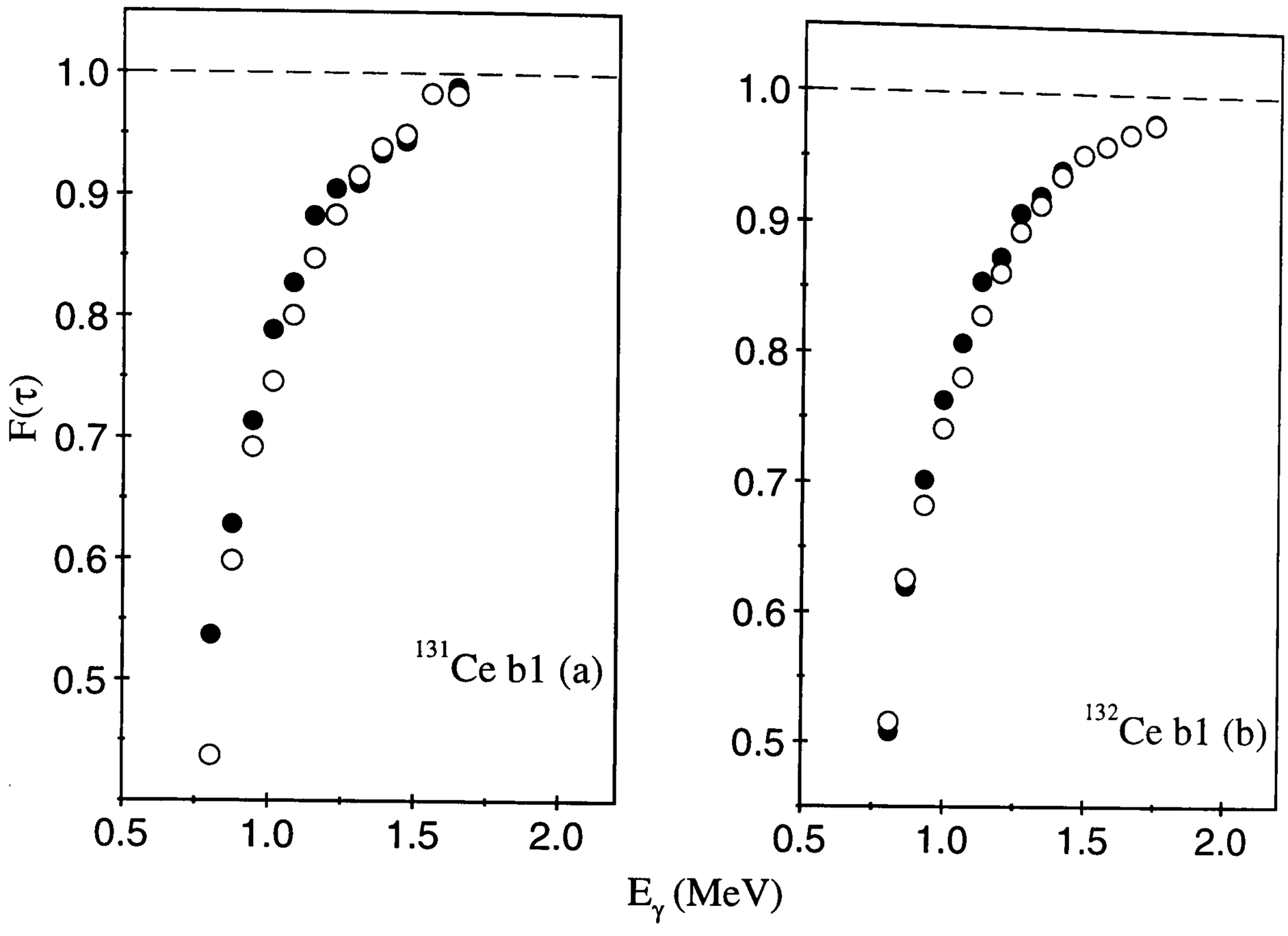

Figure 4.13: $F(\tau)$ values extracted from spectra formed by gating on transitions above 1150 keV ('gated high', closed circles) and below 1150 keV ('gated low', open circles) for (a) ^{131}Ce band 1 and (b) ^{132}Ce band 1.

Structure	Q_t (eb) Gated High	Q_t (eb) Gated Low
^{131}Ce Band 1	7.5(4)	6.8(4)
^{132}Ce Band 1	7.3(4)	7.2(4)

Table 4.6: Q_t values extracted from a χ^2-minimisation of experimental $F(\tau)$ values to calculated $F(\tau)$ values.

The apparent inconsistency between the Q_t values obtained from this and earlier experiments is probably due to the sidefeeding. Experiments using earlier spectrometer arrays could not eliminate the effects of sidefeeding transitions since there would have been insufficient statistics available to allow 'high-gating'. Consequently previous Q_t measurements of the ^{131}Ce yrast SD band would be lower due to sidefeeding contributions. These results emphasise the sensitivity of the present generation of γ-ray spectrometer arrays.

Superdeformed band 1 in ^{132}Ce is also fed across the same frequency range as ^{131}Ce. The Q_t values for ^{132}Ce obtained from high and low gated spectra is consistent with no change suggesting that the lifetimes of the feeding states are much shorter than in the ^{131}Ce case.

4.5.5 Dynamic Moments of Inertia

The dynamic moment of inertia, $\Im^{(2)}$ is especially relevant to the analysis of superdeformed bands since it is spin-independent and the spins of superdeformed bands are usually indefinite. Since this quantity is highly sensitive to single-particle alignments and level interactions, the $\Im^{(2)}$ offers an opportunity to note the presence of characteristics that can identify the underlying nuclear structure.

In this work it has not been possible to measure the energy of the topmost transitions in some of the bands with total confidence. Inaccuracies in the measurements of transition energies can translate into large changes in $\Im^{(2)}$ thereby introducing spurious features into the $\Im^{(2)}$ pattern. The $\Im^{(2)}$ patterns in this work have been calculated using only transitions in which there are total confidence. Previous work has documented two further transitions in ^{132}Ce band 2 and one further in ^{132}Ce band 3 than are reported in this work [Sem95]. In this earlier study, band 2 in ^{132}Ce was found to show a moderate increase in $\Im^{(2)}$ at $\hbar\omega \approx 0.8$ MeV suggesting the possibility that a level interaction occurs. In any case, the final points in a $\Im^{(2)}$ pattern are extremely sensitive to the measured transition energy and should be treated with caution. The $\Im^{(2)}$ patterns from this data as a function of rotational frequency are displayed in Fig. 4.14. Apart from the absence of the extreme high energy transitions, the $\Im^{(2)}$ plots reproduce the results of Santos *et al.* (note the transition energies measured in this work deviate from those of Santos due to a minor calibration error in the previous

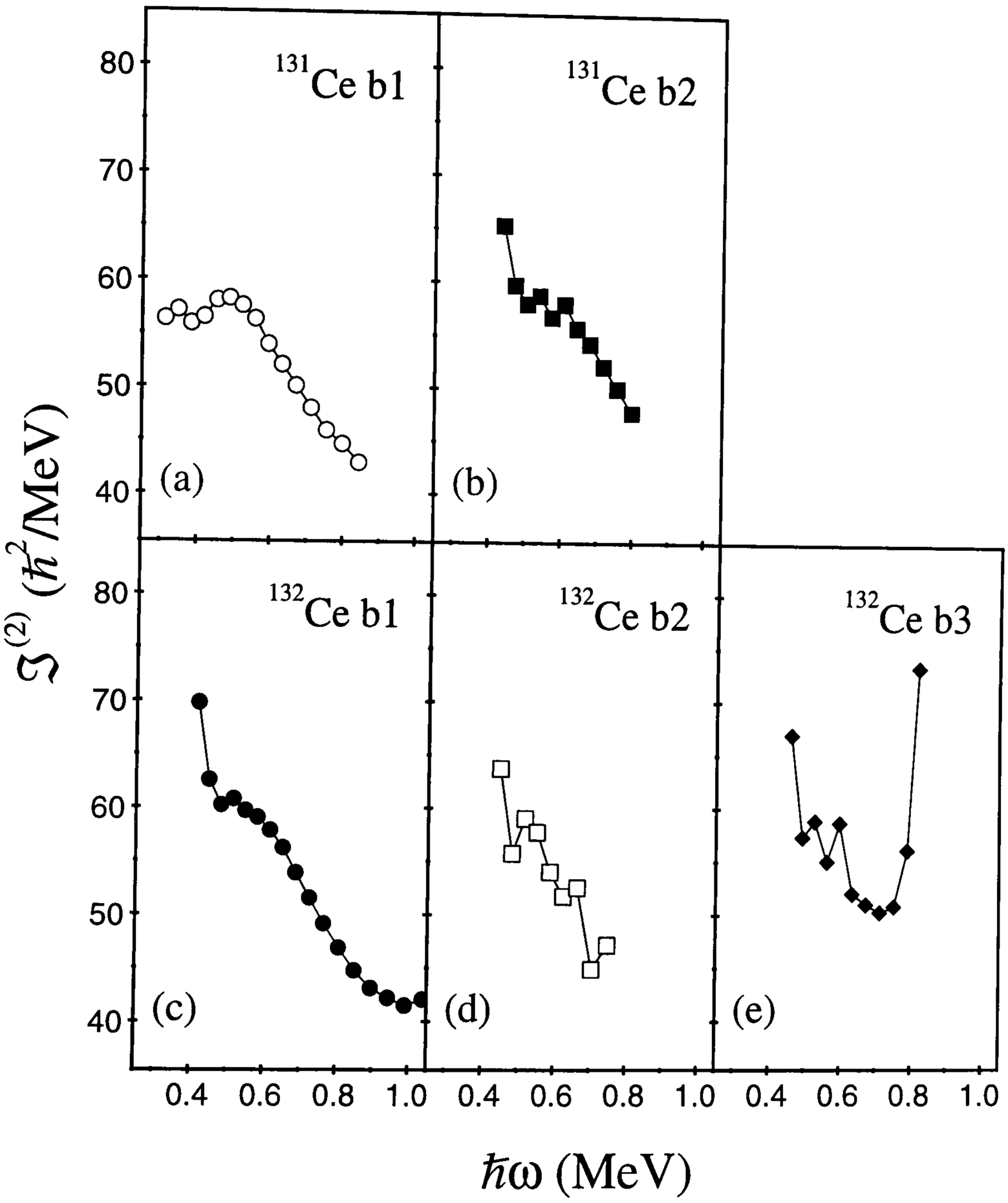

Figure 4.14: Dynamic moments of inertia for the superdeformed bands in ^{131,132}Ce. (a) ^{131}Ce yrast SD band (b) ^{131}Ce SD band 2 (c) ^{132}Ce yrast SD band (d) ^{132}Ce SD band 2 and (e) ^{132}Ce SD band 3.

work) [San95]. Fig. 4.14 highlights some interesting features that will be discussed in greater depth later in this chapter. Firstly, all bands except ^{131}Ce band 1 appear to exhibit a sharp increase at $\hbar\omega \approx$0.4 MeV indicative of an alignment process. Also, the excited bands in ^{132}Ce have a somewhat irregular $\Im^{(2)}$ pattern compared with the other structures. Band 3 exhibits a marked increase at $\hbar\omega \approx$0.8 MeV. The $\Im^{(2)}$ characteristics will form a central part of the discussion regarding configuration assignments later in this chapter.

4.5.6 Decay of ^{132}Ce Band 1

It was mentioned in section 2.4.1 that the decay mechanism of superdeformed bands is of great contemporary interest. At the present time, discrete linking transitions that connect the superdeformed second minimum states in ^{132}Ce to the normally deformed level scheme have not been observed. Although the decay process is thought to be highly fragmented, it has been possible to estimate the lifetime of the decay from the yrast superdeformed band in ^{132}Ce. This band is the strongest superdeformed band in this data set and can be clearly observed down to its lowest transitions. The band has been observed to strongly feed the S-band and a 4-quasiparticle high-K dipole band [Pau97]. The normally deformed yrast states can be traced up to the 823 keV ($18^+ \rightarrow 16^+$) transition in the S-band and the I^π=19^- level in the dipole structure. A partial level scheme of ^{132}Ce is shown in Fig. 4.15.

Spectra generated from a matrix gated on in-band transitions are pictured in Fig. 4.16. The 823 keV ($18^+ \rightarrow 16^+$) transition is fully stopped in both spectra. The 939 keV ($20^+ \rightarrow 18^+$) transition in the S-band is not seen in any spectra. The 808 keV transition in the superdeformed band has been found to decay at 50% of the initial recoil velocity (F(τ)=0.52(2), τ=122.14$\pm$14 fs). Given that the 823 keV transition does not exhibit any Doppler shift in different spectra under various gating conditions, the decay from the second minimum to the normally deformed well for ^{132}Ce is expected to be greater than 122 fs. This result places a limit on the lifetime of the decay process although it does not elucidate the mechanism itself. It is possible that the decay is a statistical highly fragmented process. If the decay is assumed to decay through statistical E1 γ-ray transitions with lifetimes approximately 1 fs and energies around 1 MeV, the ratio $T(E1)_{expt}/T(E1)_{sp}$ would be around $\approx 10^{-3}$ Wu which would not be unreasonable for statistical decays. An alternative suggestion for the decay mechanism would be the low-spin termination of the superdeformed band. Such a

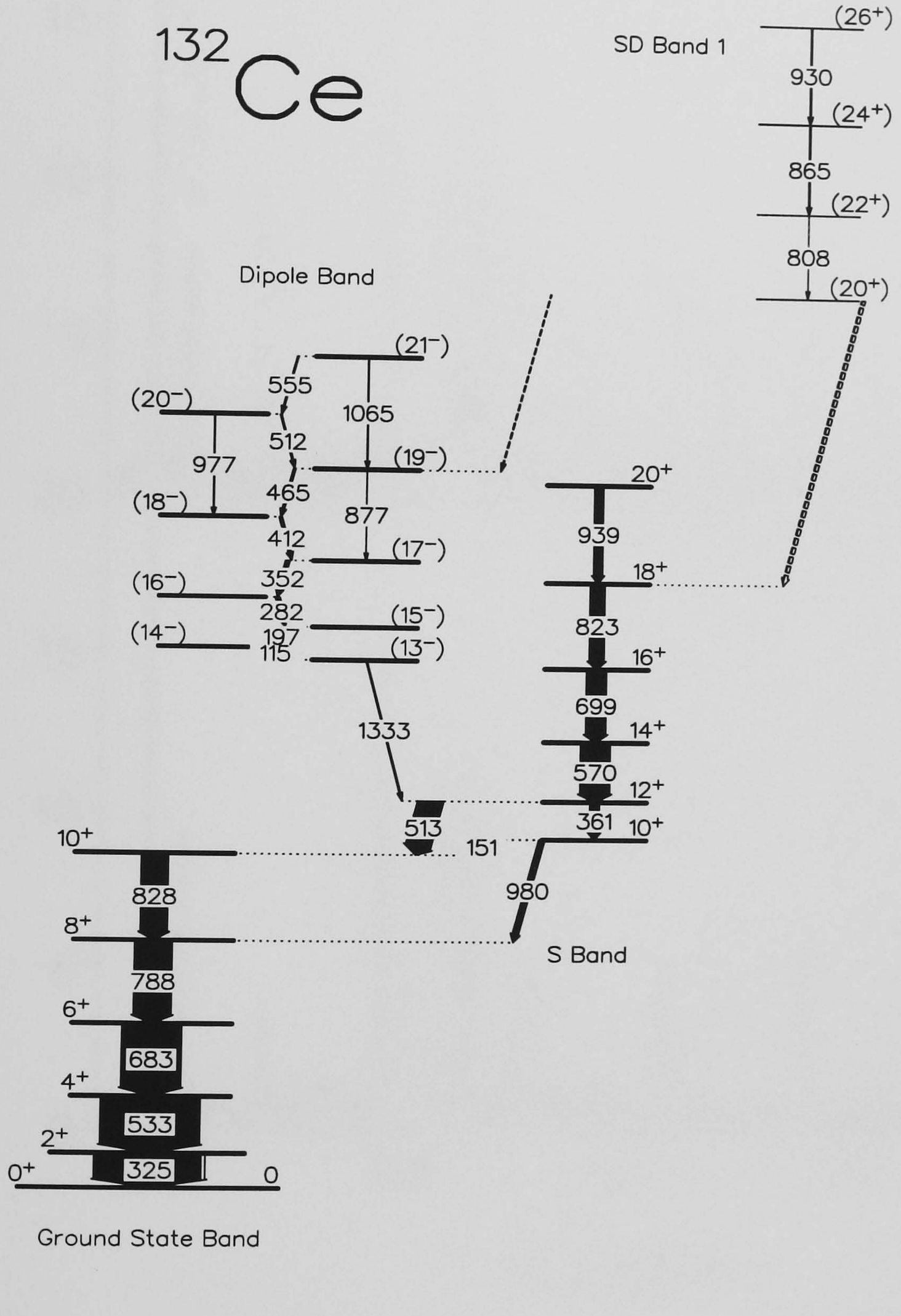

Figure 4.15: Partial level scheme of ^{132}Ce indicating the decay path from SD band 1 into the normally deformed sequences. The band strongly feeds the S-Band and a 4-quasiparticle dipole band.

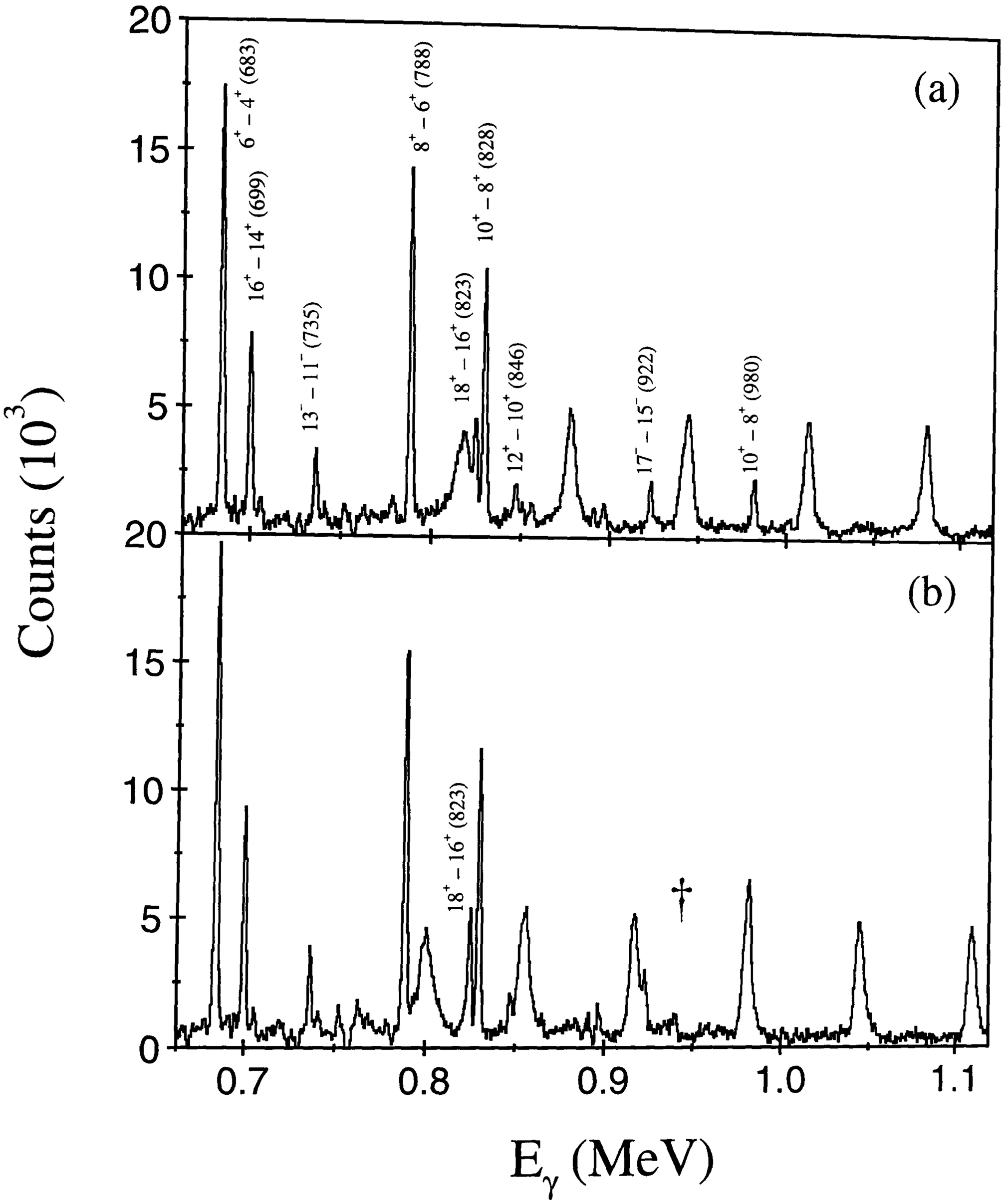

Figure 4.16: Spectra for (a) forward and (b) backward Doppler shifted γ rays generated from a matrix gated on ^{132}Ce SD band 1. Transitions in the normally deformed level scheme appear fully stopped and are labelled by $I_i - I_f$ (E_γ keV). The dagger marks the position of the E_γ=939 keV transition.

termination would involve protons and neutrons shifting out of the orbital configuration that defines the band into nearby orbitals forming a completely different structure. This mechanism has been proposed by Deleplanque *et al.* to describe the decay of ^{135}Nd [Del95]. It should be noted that all the bands in this work except the ^{131}Ce yrast band are thought to involve configurations involving two $i_{13/2}$ neutrons. Also, these bands appear to decay into the normally deformed level scheme at similar rotational frequencies to the predicted $i_{13/2}$ neutron de-alignment suggesting that the decay process could involve some intimate connection to the de-alignment of an intruder pair.

4.6 Discussion for ^{131,132}Ce

The previous sections have highlighted the difficulties in assigning definite nucleon configurations for the ^{131,132}Ce bands on the sole basis of the dynamic moments of inertia, $\Im^{(2)}$. This section reviews the information gained from relative deformation measurements in the present experiment as a more direct method of identifying the deformation driving roles of nucleons at the Fermi surface. Comparisons are also made with theoretical calculations based on the TRS formalism and the cranked shell model.

4.6.1 The Yrast Superdeformed Bands in ^{131,132}Ce

It has been proposed that superdeformation in ^{131,132}Ce is stabilised by the proton shell closure at Z=58 and the core polarising effects of the $i_{13/2}$ neutron orbitals. At low deformation the $i_{13/2}$ neutrons are situated at high excitation energy above the Fermi surface, however the combined effects of deformation and rotation lower the $i_{13/2}$ levels to the immediate vicinity of the Fermi surface. As the two isotopes are expected to have the same proton configuration, differences in deformation are supposed to arise from the successive occupation of the $i_{13/2}$ neutron intruder orbitals. Fig. 4.17a shows the variation of $\Im^{(2)}$ for the bands. A comparison of the $\Im^{(2)}$ pattern for the two bands reveals a sharp upturn at $\hbar\omega \approx$0.4MeV for ^{132}Ce whilst this feature is not apparent for ^{131}Ce. This feature has been attributed to the alignment of $i_{13/2}$ neutrons which is blocked in ^{131}Ce. There is a small hump in the ^{131}Ce $\Im^{(2)}$ pattern which is thought to be due to the alignment of the $h_{11/2}$ protons. Comparison with theoretical $\Im^{(2)}$ calculations by Wyss *et al.* [Wys88] also suggests that gradual alignments of the $h_{9/2}$ and $h_{11/2}$ neutrons contribute to the $\Im^{(2)}$ at intermediate frequencies. It can be seen that the $\Im^{(2)}$ for ^{132}Ce is generally higher than the ^{131}Ce pattern.

The larger $\Im^{(2)}$ of ^{132}Ce has been interpreted as evidence of a larger deformation. The evidence reported in [Kir87], [He90] would seem to support this argument placing the ^{132}Ce yrast band $\approx$ 3eb higher than the ^{131}Ce yrast band. Theoretical calculations based on the TRS formalism imply that the occupation of the second $i_{13/2}$ neutron orbital drives the nuclear shape to larger deformation producing a difference of $\approx$ 10% in the quadrupole deformation parameter β_2. Fig. 4.17b compares the F(τ) curves for the bands. As can be seen from Fig. 4.17b, the measurements are extremely similar to each other

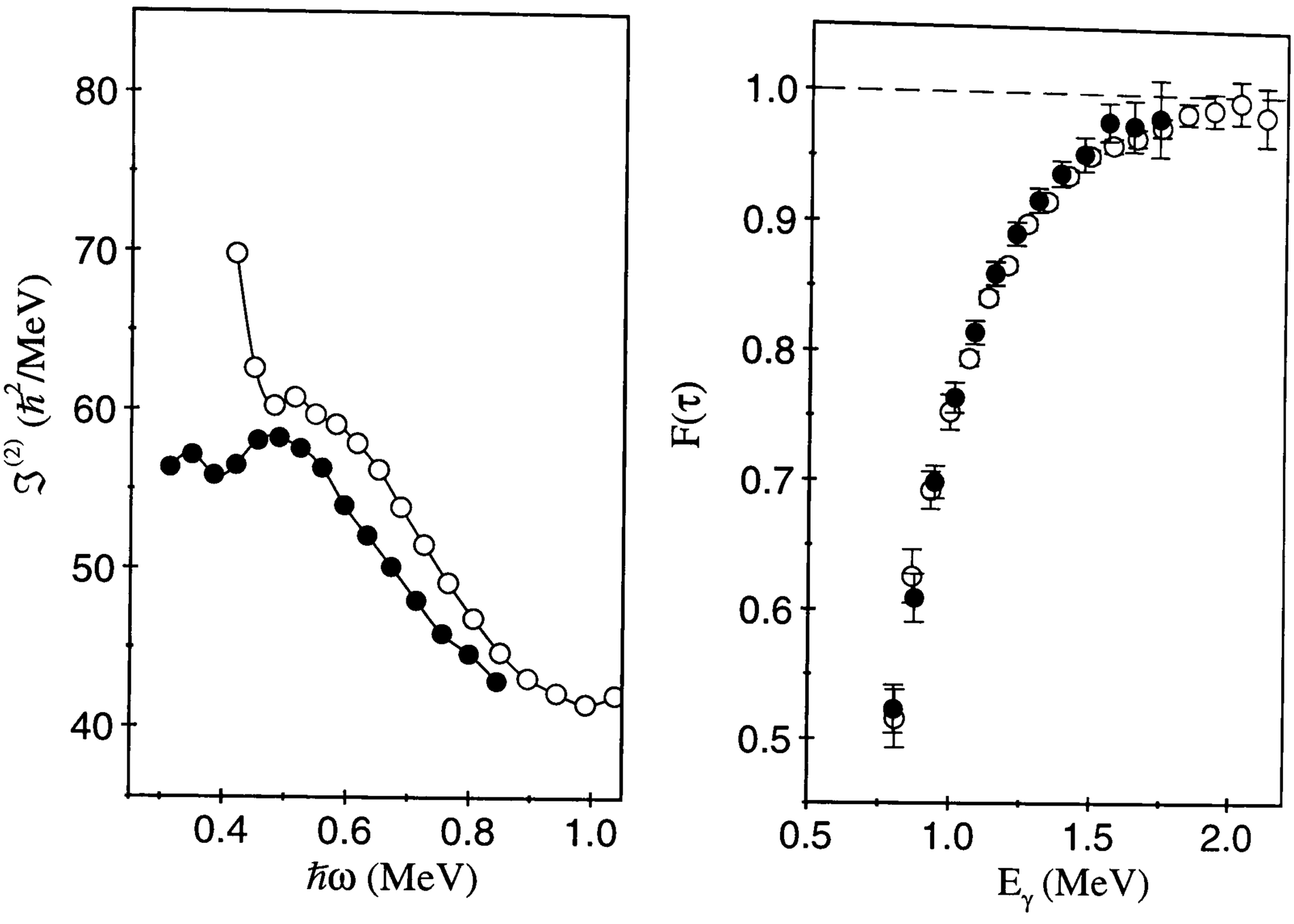

Figure 4.17: Comparison of experimental results for the yrast sequences in ^{131,132}Ce. (a) The variation of $\Im^{(2)}$ with rotational frequency. (b) Comparative F(τ) curves for the yrast bands. The filled/open circles correspond to ^{131}Ce/^{132}Ce.

indicating that both nuclei have very similar deformations. These results are at considerable variance with the previous measurements for the bands. Table 4.7 compares the present observations with the results for quadrupole moments extracted from previous experiments. If the results from Table 4.7 were used to generate Routhian diagrams it would be almost impossible to determine configuration assignments, illustrating the difficulty in gaining information by comparing results from different experiments where large systematic errors can be introduced in the analysis. There are two possible conclusions that can be used to explain the present observations. If the deformation driving properties of the $i_{13/2}$ intruders orbitals are as significant as the theory predicts, the similarities might arise from an identical intruder configuration. The evidence from the the $\Im^{(2)}$ plots and comparison

(a) Structure	Q_t (eb)	(b) Structure	Q_t (eb)	Reference
^{131}Ce Band 1	7.3(3)	^{131}Ce Band 1	≈6	[He90]
		^{131}Ce Band 1	5.5(5)	[Mul93]
		^{131}Ce Band 1	≈ 6.4	[War94]
^{132}Ce Band 1	7.4(3)	^{132}Ce Band 1	7.5(6)	[Reg90]
		^{132}Ce Band 1	8.8(8)	[Kir87]
		^{132}Ce Band 1	≈7.1	[War94]

Table 4.7: (a) The quadrupole moments Q_t extracted in this work for the yrast superdeformed bands in ^{131,132}Ce. (b) The quadrupole moments extracted for the yrast bands in previous studies. Note, all the values quoted are subject to large absolute errors (10-15%) due to uncertainties in the stopping powers. [Reg90] result came from reanalysis of the data described in [Kir87].

with cranked shell model calculations in Fig. 4.1 suggest that it is difficult to reconcile the results with this argument. It is hard to imagine the bands belonging to a different configuration to the one previously assigned without introducing other features into the dynamic moments of inertia. The other possibility leads to the conclusion that the core polarising effects of the aligned $i_{13/2}$ neutrons are not as dramatic as previously thought.

4.6.2 The Excited Band Configurations

The yrast superdeformed bands in ^{131,132}Ce are expected to fill either one or two of the N=6 $i_{13/2}$ intruder orbits. The excited bands are proposed to arise from particle-hole excitations involving the negative-parity $\nu h_{11/2}$ (N=5) valence orbitals or the positive-parity $\nu d_{3/2}$ (N=4) states. Cranked shell model calculations indicate that excitations from either the N=4 or N=5 sub-shells are equally likely at representative deformations for this mass region. The deformation measurements allow a more definite discussion.

4.6.3 The ^{131}Ce Excited Band

The dynamic moment of inertia extracted for ^{131}Ce band 2 as a function of rotational frequency is plotted in Fig. 4.18a where it is compared with ^{132}Ce band 1. The moments of inertia of ^{131}Ce band 2 follows that of the ^{132}Ce yrast band very closely. The major point of interest is the upturn in dynamic moment of inertia at $\hbar\omega \approx 0.4$ MeV which suggests that the $\nu i_{13/2}$ intruder alignment is present in addition to the $h_{11/2}$ proton alignment. If both bands have an identical intruder configuration, one might expect that the bands have similar deformations. The Q_t values obtained from a χ^2-minimisation procedure using the F(τ) curves for the bands illustrated in Fig. 4.18b imply that the bands have significantly different quadrupole deformations.

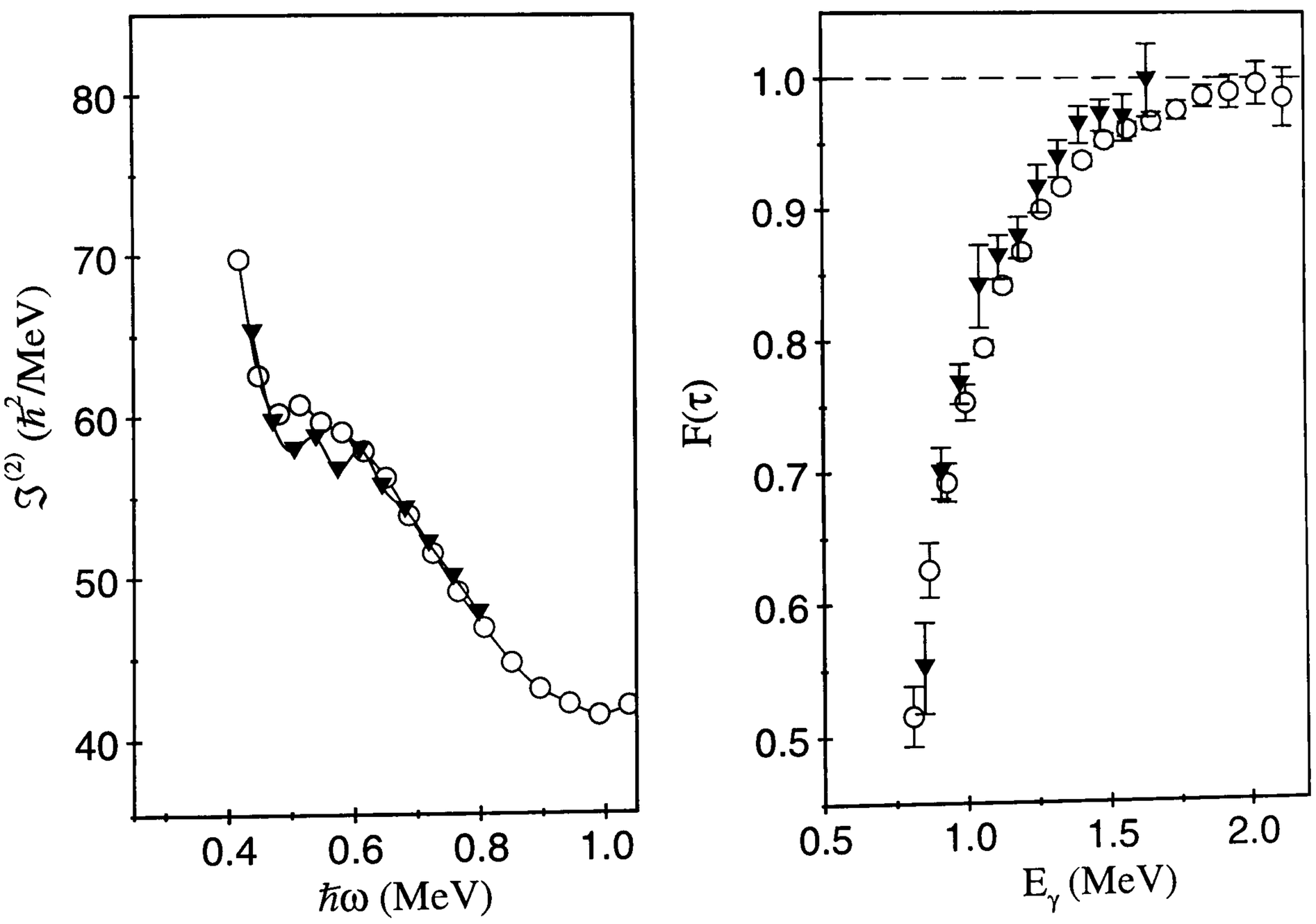

Figure 4.18: Comparison of experimental results for the excited band in ^{131}Ce with the yrast structure in ^{132}Ce. (a) The variation of $\mathcal{S}^{(2)}$ with rotational frequency. (b) Comparative F(τ) curves for the bands. The filled triangles represent ^{131}Ce band 2 whilst the open circles correspond to ^{132}Ce band 1.

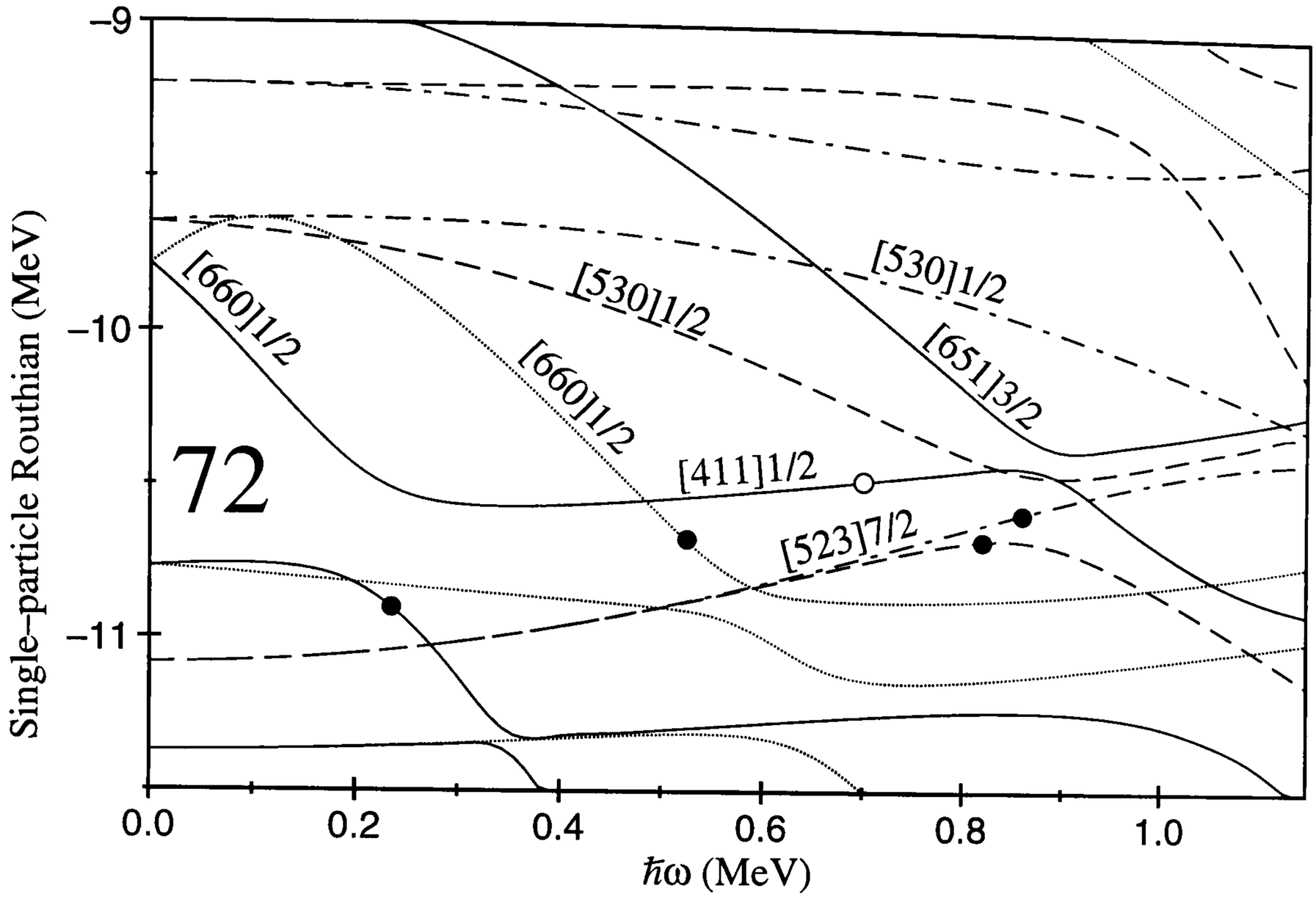

Figure 4.19: Routhian diagrams for β_2=0.452 assuming β_4=0, γ=0°. The filled circles indicate that the level is occupied by a neutron and open circles illustrate vacant orbitals (holes). Each orbital is labelled according to its parity and signature (π, α)): Solid lines = (+,+1/2), dotted lines = (+,–1/2), dot-dash lines = (–,+1/2) and dashed lines = (–,–1/2).

For the excited band in ^{131}Ce to have the same intruder configuration as ^{132}Ce, a neutron must be excited from a nearby orbital into the [660]1/2$^+$ (α=–1/2) orbital. Cranked single-particle calculations using a deformed Woods-Saxon potential defined by the experimental deformation parameters β_2=0.452 are displayed in Fig. 4.19. The calculations indicate that there are three possible excitations. A neutron can be promoted from the [411]1/2$^+$ (α=1/2) orbital or from either signature of the [523]7/2$^-$ orbital. At β_2=0.452, the [411]1/2$^+$ (α=1/2) state is predicted to lie above the Fermi surface while the [660]1/2$^+$ (α=–1/2) is occupied. This configuration would be consistent with the observation of only one excited band in ^{131}Ce. If the excitation was assigned to arise from one of the [523]7/2$^-$ states, a further signature partner band with a similar population intensity would be expected. Since the signature splitting of the [523]7/2$^-$ levels is very small at low rotational

frequencies, any signature partner band might be expected to lie at the mid-points of the observed band. Such a band is not observed.

A neutron Nilsson diagram appropriate for ^{131,132}Ce calculated using a deformed Woods-Saxon single-particle potential is shown in Fig. 4.20. A superdeformed shell closure at N=72 is clearly evident for $\beta_2 \approx$ 0.4. As the deformation increases beyond $\beta_2 \approx$ 0.4 the positive parity [660]1/2$^+$ orbitals are lowered in energy and the upward sloping [411]1/2$^+$ levels approach the Fermi surface from below. Around $\beta_2 \approx$ 0.45 it is likely that neutrons from the [411]1/2$^+$ states are closer to the Fermi surface than the neighbouring valence orbitals.

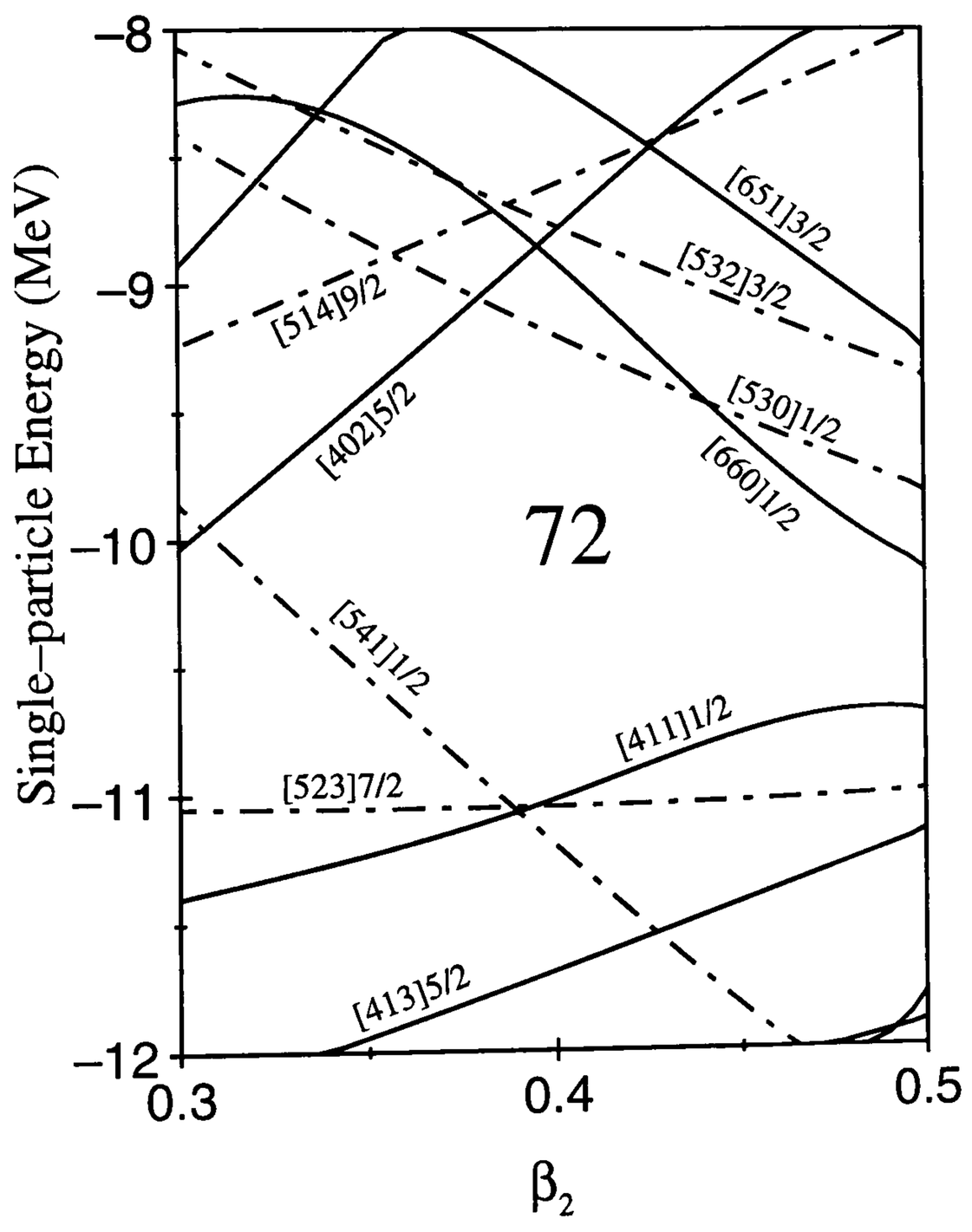

Figure 4.20: Nilsson diagram for A$\approx$ 132 nuclei. Each orbital is labelled according to its parity: Solid lines = (π=+) and dot-dashed lines = (π=−).

Another way to view band 2 in ^{131}Ce is by coupling a hole in the [411]1/2$^+$ state to the SD ^{132}Ce core. The [411]1/2$^+$ (α=1/2) level is quoted as having a negative quadrupole moment [Sat96], thus leaving a hole in this level will have a shape driving effect on the nucleus. One way of conveniently labelling SD configurations in the literature is to note the number of protons and neutrons in intruder orbitals. In this notation, the yrast SD band of ^{132}Ce has the configuration $\pi 5^4 \nu 6^2$ i.e. there are four N=5 protons and two N=6 neutrons. The excited band in ^{131}Ce can thus be denoted $\pi 5^4 \nu 6^2 \otimes (\nu[411]1/2^+)^{-1}$. This configuration has an interesting parallel in the A$\approx$150 region. The configuration of ^{131}Ce band 2 can be compared with band 4 in the superdeformed nucleus ^{151}Dy. In both cases the bands are formed by coupling a hole in the [411]1/2$^+$ state to the superdeformed core of the A+1 nucleus; ^{132}Ce and ^{152}Dy respectively. The ^{151}Dy band is formed by promoting a neutron from the [411]1/2$^+$ orbital to the [770]1/2$^-$ intruder state. A number of interesting features arise from this comparison. The dynamic moments of inertia of ^{151}Dy band 4 is found to be identical to the ^{152}Dy yrast band. Fig. 4.18a also exhibits the identical $\Im^{(2)}$ of ^{131}Ce band 2 to ^{132}Ce band 1. Recent relative deformation measurements by Nisius *et al.* [Nis97] have provided some illuminating results. Nisius has showed that the excited bands in ^{151}Dy that adopt the same $\pi 6^4 \nu 7^2$ configuration as the ^{152}Dy core have larger deformations than the ^{151}Dy yrast band. Another significant observation was that the Q_t values for the excited bands in ^{151}Dy are larger than that of the ^{152}Dy yrast band. The large errors on the band 4 measurement are too large to be absolutely conclusive about the role of the [411]1/2$^+$ state, however this result offers further credence to the argument for the increased deformation driving effects of specific non-intruder configurations. Although there are many similarities between these two cases, there are also two fundamental differences. Firstly, the occupation of successive intruder orbitals in the N=7 shell appears to drive the nucleus to larger deformations. Secondly, in the strongly coupled limit of the pseudospin coupling scheme, the [411]1/2$^+$ orbital is expected to be associated with a decoupling parameter of a=–1. As a consequence of this decoupling parameter value, one would expect the transitions of the excited band based on this configuration to lie at the half-way points of the A+1 nucleus yrast band. This is observed experimentally for ^{151}Dy band 4 and ^{152}Dy band 1, however ^{131}Ce band 2 lies at the quarter points of the ^{132}Ce yrast band leaving an open question in the A$\approx$130 region.

4.6.4 The ^{132}Ce Excited Bands

The configurations for the excited bands in ^{132}Ce have been the subject of much discussion in recent years. Single particle Routhian calculations performed for a typical quadrupole deformation parameter ($\beta_2 \approx 0.4$) are shown in Fig. 4.1 and indicate that there are a number of possible excitations that have comparable excitation energies. Excitations could possibly arise from either the $[411]1/2^+$ (α=1/2), $[523]7/2^-$ (α=$\pm$1/2) or the $[660]1/2^+$ (α=-1/2) states into the orbits close to the Fermi surface which include the $[530]1/2^-$ (α=$\pm$1/2) and $[651]3/2^+$ (α=1/2) levels.

The dynamic moments of inertia for the ^{132}Ce excited bands are illustrated in Fig. 4.21. The $\Im^{(2)}$ patterns for the yrast SD bands are also plotted in the figures to allow comparison between the structures. It is interesting to note that the moments of inertia for the excited bands are lower than the yrast sequence in ^{132}Ce and generally have magnitudes similar to the ^{131}Ce yrast structure. Both of the excited bands show an up-turn around $\hbar\omega \approx$0.4MeV, a feature already suggested to be defined by the alignment of the $i_{13/2}$ neutron intruder orbitals. Another distinct feature arises at higher frequency around $\hbar\omega \approx$0.8MeV. Band 3 shows a very sharp up-turn at $\hbar\omega \approx$0.8MeV, whilst band 2 appears to exhibit a smaller increase at a similar frequency. The up-bend at $\hbar\omega \approx$0.8MeV is indicative of a level interaction or a band crossing. Two possible candidates for this interaction are manifested in the frequency range $\hbar\omega$=0.8–1.1 MeV. A ΔN=0 interaction arises between the $[530]1/2^-$ (α=+1/2) and the $[523]7/2^-$ (α=+1/2) levels. This is a gradual interaction occurring over a frequency range spanning around 0.3 MeV. A much sharper ΔN=2 interaction occurs between the $[411]1/2^+$ (α=+1/2) and the $[651]3/2^+$ (α=+1/2) levels.

The initial report on the excited SD bands in ^{132}Ce suggested a number of possible excitations. Using single-particle Routhians employing the deformation parameters β_2=0.4, β_4=0.014 and γ=3°, Santos *et al.* suggested that it would be energetically favourable to promote a neutron from the $[411]1/2^+$ (α=+1/2) level to the $[530]1/2^-$ (α=+1/2) level, whilst the second excited band might arise from an excitation from the $[523]7/2^-$ (α=+1/2) level to the $[530]1/2^-$ (α=+1/2) state. The absence of the second signature partner was accounted for by suggesting that the ΔN=0 interaction repels the $[523]7/2^-$ (α=+1/2) level further below the Fermi surface, thus more excitation energy is required to populate the second signature partner band. A comparison of experimental and theoretical dynamic

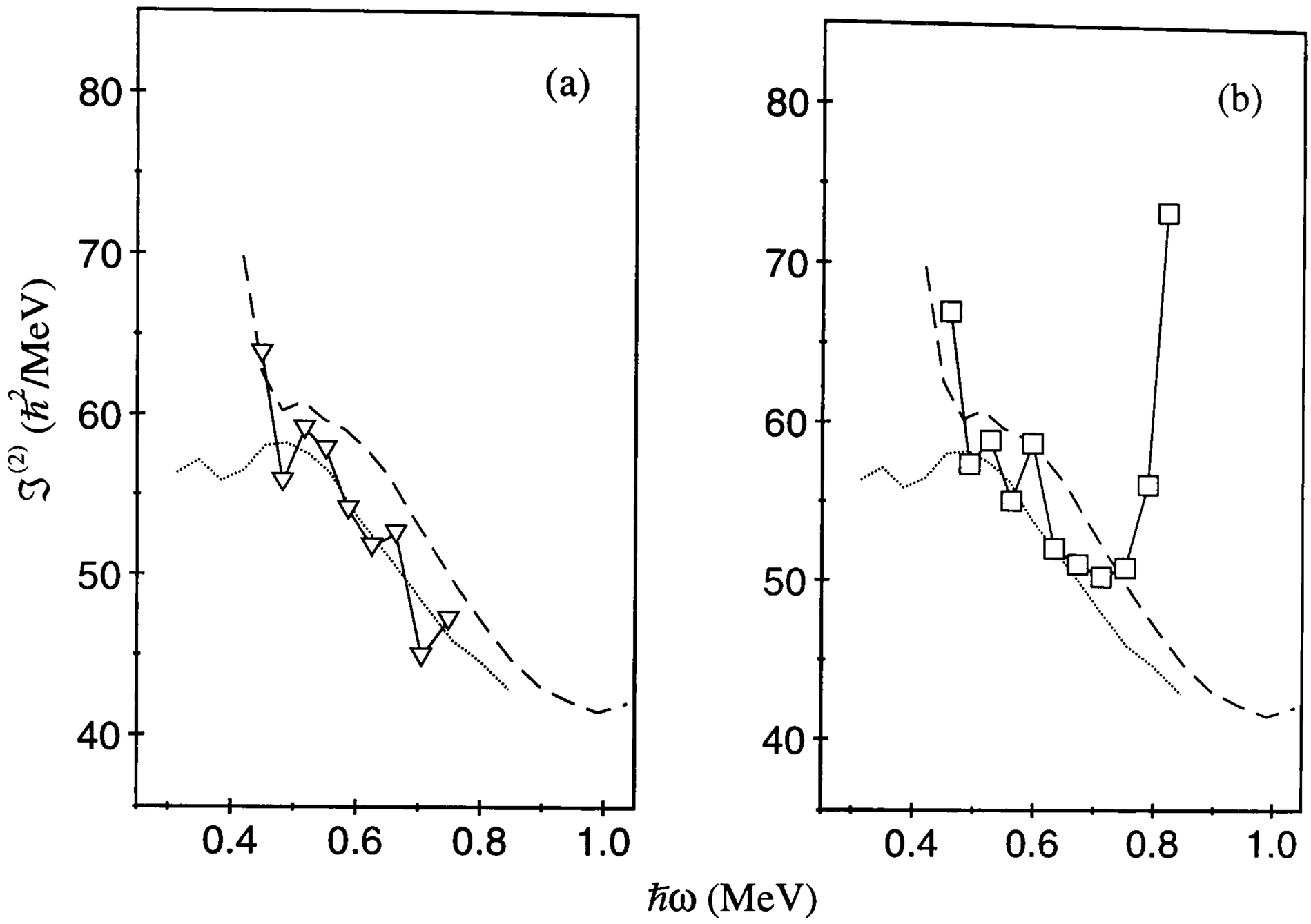

Figure 4.21: Dynamic moments of inertia for the excited bands in ^{132}Ce (a) The variation of $\Im^{(2)}$ for ^{132}Ce band 2. (b) The variation of $\Im^{(2)}$ for ^{132}Ce band 3. The dashed lines represent the dynamic moment of inertia for ^{132}Ce band 1 whilst the dotted lines correspond to ^{131}Ce band 1.

moments of inertia [San95] revealed that the best fits were made forming excitations from the $[523]7/2^-$ signature partner levels and assuming the bands possessed different quadrupole deformations and moderate triaxiality. Similar comparisons assuming an excitation from the $[411]1/2^+$ (α=+1/2) level to the $[530]1/2^-$ (α=+1/2) level also provided a reasonable correlation and could not be dismissed as a configuration candidate [San95].

The distinct upbend at $\hbar\omega \approx$0.8 MeV was suggested by Semple [Sem95] to arise from the ΔN=2 crossings mentioned earlier. In order to reproduce both the crossings Semple proposed that band 2 was formed by promoting a neutron from the $[411]1/2^+$ (α=+1/2) level to the $[651]3/2^+$ (α=+1/2) level. The second excited band (band 3) was suggested to arise from a neutron excitation from the $[523]7/2^-$ (α=+1/2) state to the $[530]1/2^-$

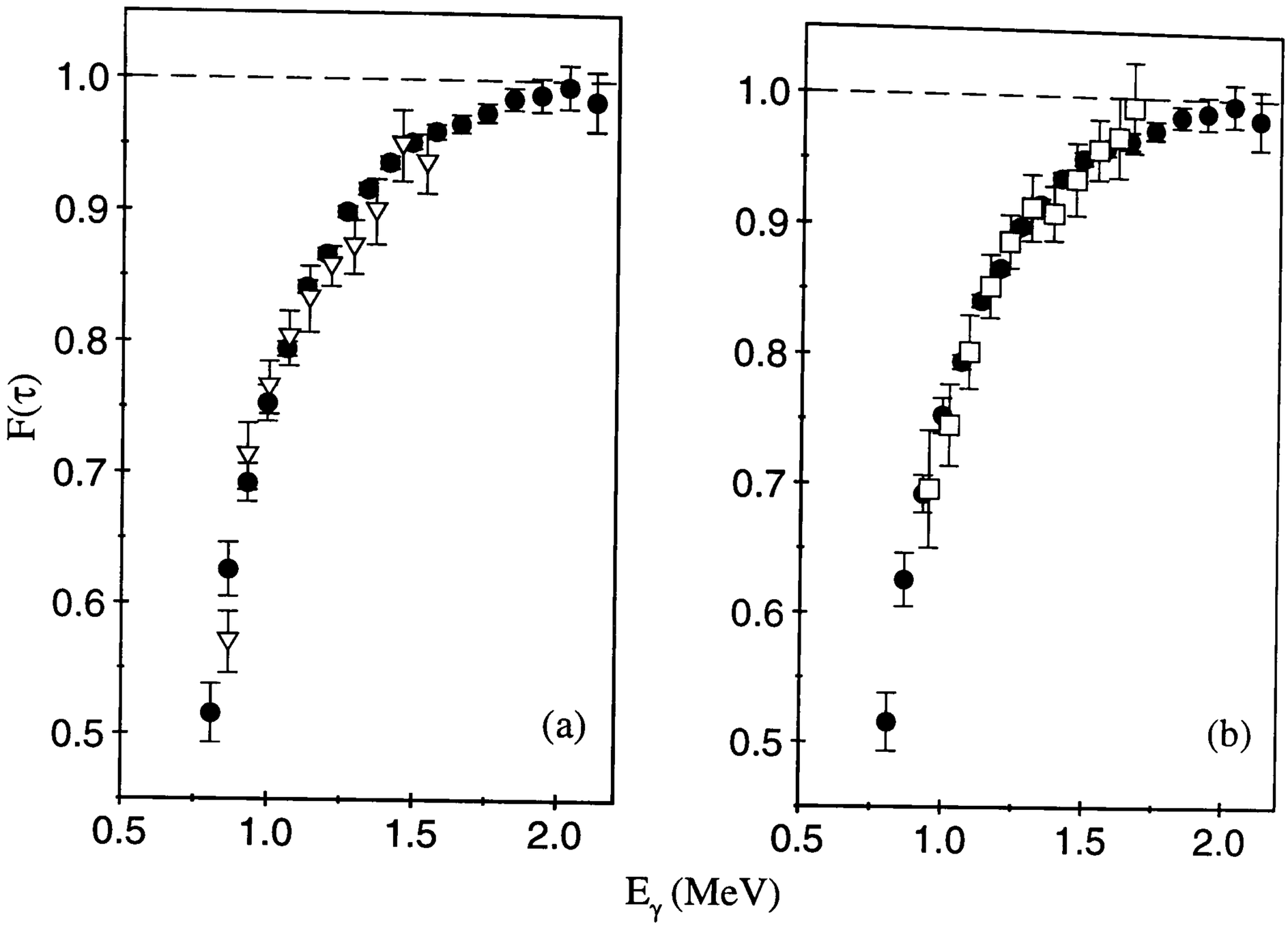

Figure 4.22: Comparison of experimental fractional Doppler shifts for the excited bands in ^{132}Ce with the yrast structure in ^{132}Ce. (a) ^{132}Ce band 2 (open triangles) compared with ^{132}Ce band 1 (filled circles) (b) ^{132}Ce band 3 (open squares) compared with ^{132}Ce band 1 (filled circles)

(α=−1/2) level. Both of these assignments were proposed on account that identicality relationships between the excited bands do not appear to suggest that the bands are signature partners. These assignments have highlighted a problem that has hindered the study of superdeformation in this mass region - missing bands. The previous assignments leave a missing signature partner band based on the excitation from the [523]7/2$^-$ (α=−1/2) level to the [530]1/2$^-$ (α=−1/2) state.

The quadrupole moments obtained from the present experiment reveal that both excited bands have similar deformations. The F(τ) curves for both bands are compared with the yrast SD band in ^{132}Ce in Fig. 4.22. It is apparent that the deformation of both the excited bands are not only comparable to each other but also to the yrast SD bands in ^{131,132}Ce.

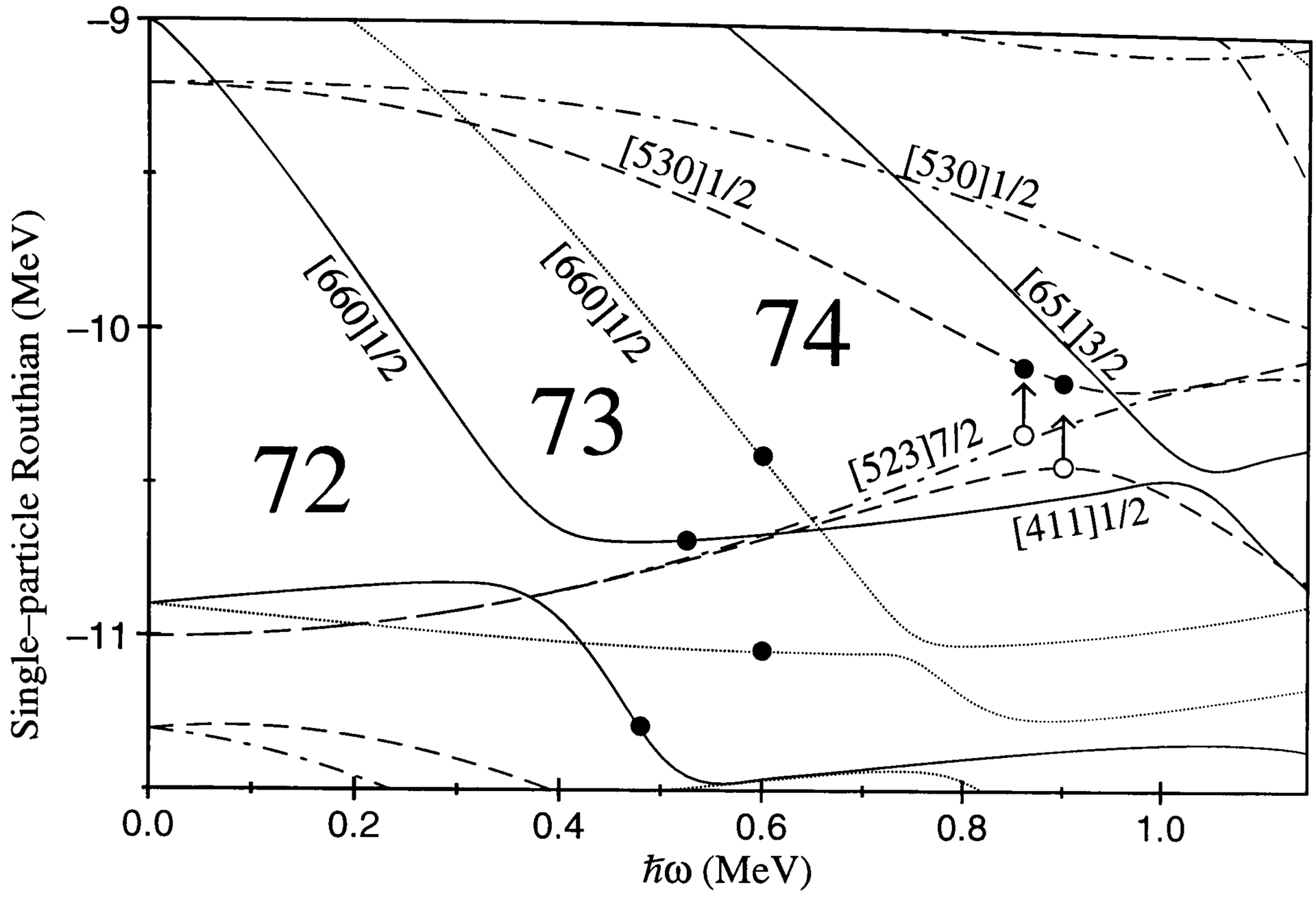

Figure 4.23: Single particle Routhian diagram appropriate to ^{132}Ce (N=74). Excitations from the $[523]7/2^-$ states into the $[530]1/2^-$ ($\alpha = -1/2$) level are displayed.

This result is a clear step forward since it eliminates the possibility of the bands possessing different deformations.

Cranked shell model calculations performed for the experimental deformation parameter β_2=0.411 are displayed in Fig. 4.23. Excitations from the $[523]7/2^-$ signature partners are energetically favourable at this deformation. The nearest orbital into which a neutron can be placed is the $[530]1/2^-$ (α=−1/2) level. The Nilsson diagram calculated for A≈ 132 nuclei displayed earlier in Fig. 4.20 indicates that with decreasing deformation it becomes energetically favourable to promote from the $[523]7/2^-$ states into the nearby intruder levels. Woods-Saxon calculations would suggest that the bands are indeed signature partners.

Fig. 4.24 displays the deviation (ΔE) of the ^{132}Ce band 3 transition energies from the ^{132}Ce band 2 mid-points. It can be seen that the deviation is quite large at moderate frequencies and increases with increasing frequency which is consistent with the non-

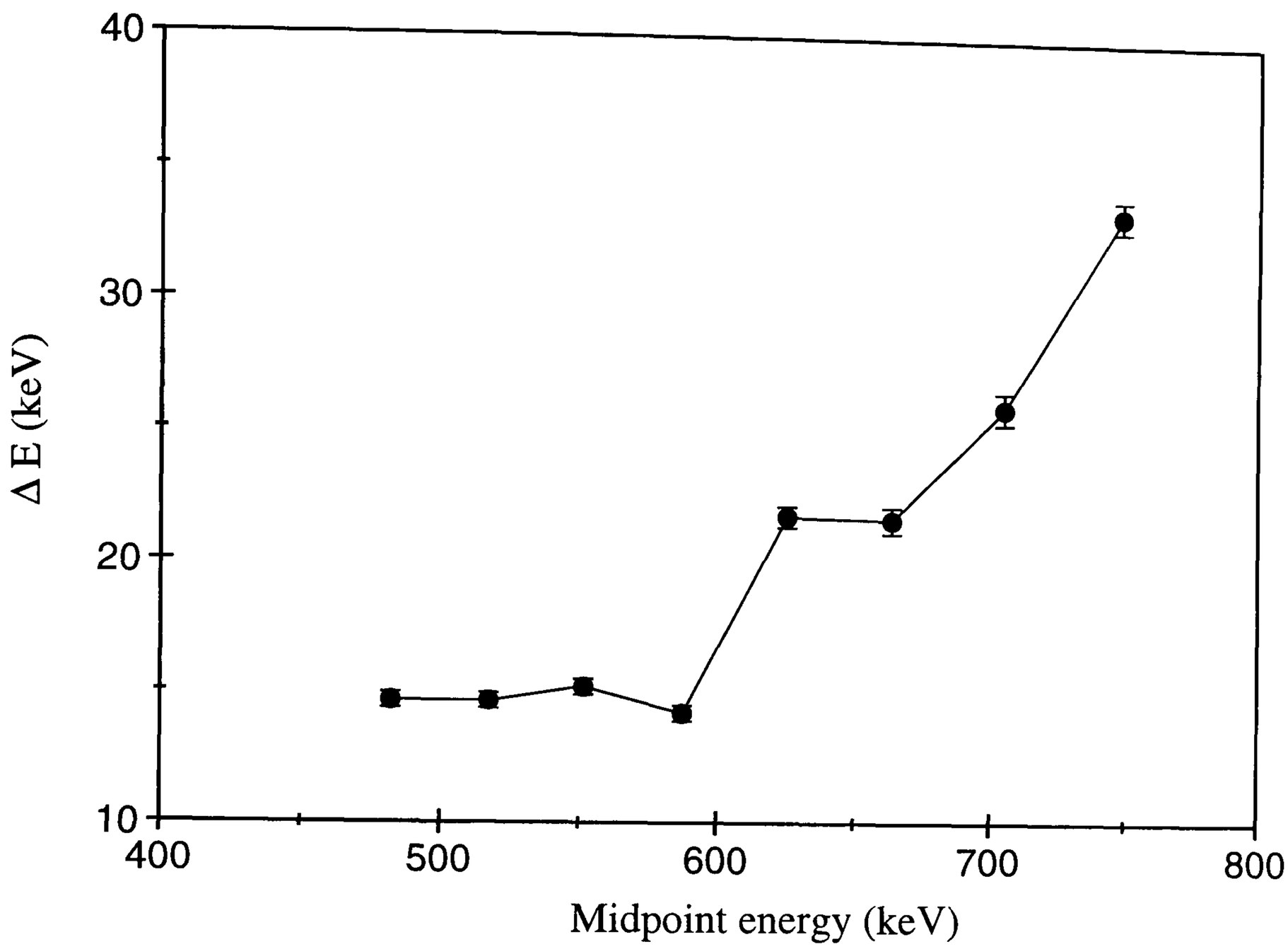

Figure 4.24: Deviation of the transition energies in ^{132}Ce band 3 from the midpoint energies of ^{132}Ce band 2.

degenerate signature partner scenario. This assignment would remove the need to search for a missing signature partner band, however certain problems remain. In the Nilsson diagram in Fig. 4.20, the $[411]1/2^+$ (α=+1/2) state crosses the $[523]7/2^-$ states implying from the close proximity of these levels that a further band should be observed corresponding to an excitation from the $[411]1/2^+$ (α=+1/2) orbital. A band based upon the excitation from the $[411]1/2^+$ (α=+1/2) level has not been observed. The deformation properties of the bands point towards an excitation from the $[523]7/2^-$ (α=$\pm$1/2) states into the $[530]1/2^-$ (α=−1/2) level. The similar quadrupole moments of the excited and yrast SD bands in ^{132}Ce suggest that the excitation should happen between orbitals which do not have an effect on the global deformation properties of the bands. In Fig. 4.20, the $[523]7/2^-$ states are exceedingly flat with respect to changes in deformation, thus placing particles or holes in this level is not expected to enhance or diminish quadrupole deformation. The deformation

driving properties of the [530]1/2$^-$ (α=$\pm$1/2) and [651]3/2$^+$ orbitals has been probed in a study of the superdeformed bands in ^{133}Ce [Hau95], [Ha96a]. The yrast SD band in ^{133}Ce is formed by coupling a neutron in the [530]1/2$^-$ (α=–1/2) level to the superdeformed ^{132}Ce core. The two excited bands attributed to ^{133}Ce are expected to be formed by exciting the odd neutron into the [530]1/2$^-$ (α=+1/2) and the [651]1/2$^+$ (α=+1/2) states. The dynamic moments of inertia for the ^{133}Ce bands are compared with the yrast band in ^{132}Ce in Fig. 4.25a and Fig. 4.25b. There are obvious similarities between the bands 1 and 2 in ^{133}Ce and ^{132}Ce band 1. The moment of inertia for ^{133}Ce band 3 shows marked differences from the other bands. The most notable difference is the upturn at $\hbar\omega \approx$0.7 MeV. Although this upbend strongly suggests that an alignment is occurring, cranking calculations displayed in Fig. 4.23 do not display any interactions that might account for this observation. The ^{132}Ce excited bands are plotted in Fig. 4.25c and Fig. 4.25d where they are compared with the $\Im^{(2)}$'s of bands belonging to ^{133}Ce. The ^{132}Ce excited bands appear to be considerably different to the other bands and it is difficult to assign configurations on the basis of moments of inertia.

Lifetime measurements based upon target thickness induced Doppler broadening have shown that bands 1 and 2 in ^{133}Ce have a similar quadrupole moments at Q_t=7.4(7) and Q_t=7.5(8) respectively [Ha96a]. Since ^{132}Ce band 1 was populated in the same reaction it has been possible to compare relative deformations of the bands in ^{132,133}Ce. The quadrupole moment of ^{132}Ce yrast band was measured to be Q_t=7.4(9). This would imply that the core polarising effects of the [530]1/2$^-$ (α=$\pm$1/2) states do not have a significant deformation driving role. The probable excitations based on the evidence from relative deformation measurements are proposed to arise from exciting a neutron from either signature of the [523]7/2$^-$ level into the [530]1/2$^-$ (α=–1/2) state. These excitations are unlikely to enhance the nuclear shape beyond the deformation of the ^{132}Ce intruder configuration.

Assuming that the excited bands in ^{132}Ce are the [523]7/2$^-$ signature partners it is possible to assign which band is associated with a particular signature from comparisons between cranking calculations and the $\Im^{(2)}$ plots. The sharp crossing apparent for ^{132}Ce band 3 at $\hbar\omega \approx$0.8 MeV is attributed to the ΔN=0 interaction between the [523]7/2$^-$ (α=–1/2) level and the [530]1/2$^-$ level (α=–1/2). This suggests that band 3 in ^{132}Ce is based on an excitation from the (α=–1/2) signature into the [530]1/2$^-$ (α=–1/2) state.

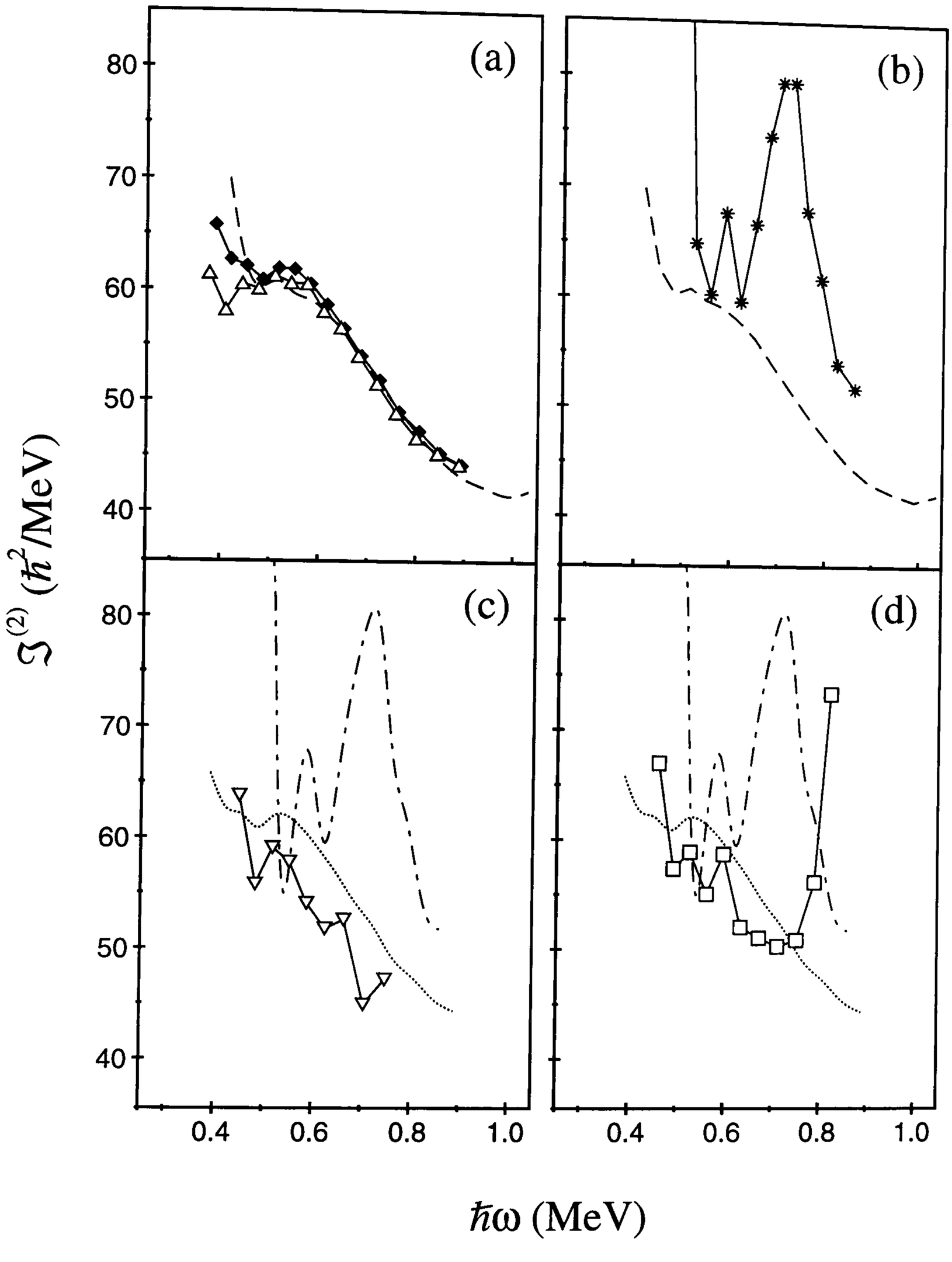

Figure 4.25: Comparison of experimental dynamic moments of inertia. (a) Band 1 (filled diamond) and band 2 (open delta) in ^{133}Ce with ^{132}Ce band 1 (dashed line). (b) ^{133}Ce band 3 (stars) compared with ^{132}Ce band 1 (dashed line). (c) and (d) show ^{132}Ce band 2 (open triangles) and ^{132}Ce band 3 (open squares) respectively, compared with ^{133}Ce band 1 (dotted lines) and ^{133}Ce band 3 (dot-dashed lines).

This assignment implies that band 3 has total signature α=1 and odd spins. Band 2 in ^{132}Ce is assigned to arise from the excitation of the [523]7/2$^-$ (α=+1/2) into the [530]1/2$^-$ (α=–1/2) level resulting in total signature α=0 and even spins. The excitations on which these configurations are based are displayed in Fig. 4.23.

4.6.5 Summary

In summary, the lifetimes and quadrupole moments of superdeformed bands in ^{131,132}Ce have been measured in the same experiment using the GAMMASPHERE spectrometer array. This relative deformation measurement has allowed the contribution of specific configurations to the deformation properties to be deduced. The quadrupole moments of the yrast superdeformed structures in ^{131,132}Ce are measured to be Q_t=7.3(4) and 7.4(4) eb respectively, implying that the bands are based upon nuclei with very similar deformations. The bands are restated to involve the occupation of one and two N=6 intruder orbits, respectively. The core polarising effects of occupying the $\nu i_{13/2}$ intruder states is concluded to have less effect than previously thought.

The quadrupole moments of the excited bands in ^{132}Ce have been measured for the first time and reveal quadrupole moments of Q_t=7.2(4) and 7.0(4)eb, respectively. These results indicate that the excited bands in ^{132}Ce have similar deformations to each other and to the yrast structures in ^{131,132}Ce indicating the stability of the second minimum against single-particle excitations. It is concluded that these bands are based upon exciting a single neutron from either signature of the available N=5 valence [523]7/2$^-$ orbital into the [530]1/2$^-$ (α=–1/2) level based on these measurements and comparison with results of Hauschild *et al.* [Ha96a].

The deformation of the excited band in ^{131}Ce is measured to be larger than the other bands at Q_t=8.2(4). This enhancement in deformation is proposed to arise from a hole in the [411]1/2 (α=+1/2) state originating from the $d_{3/2}$ shell. The $d_{3/2}$ state is predicted to be upward sloping with increasing deformation and therefore a hole in this orbital is a reasonable candidate for driving the nucleus to a greater prolate shape.

The lifetime of the decay process for the strongest band ^{132}Ce band 1 has been limited to greater than 122 fs. A discrete decay path cannot be discerned, however, the decay process is suggested to be intimately linked to the dealignment of an $i_{13/2}$ pair.

The role of sidefeeding in the deduced deformation properties has been investigated. It is found that there is a slow sidefeeding component to the ^{131}Ce yrast structure implying that the superdeformed states are fed by a lesser deformed structure. The effects of sidefeeding appear to have little influence on the deformation of ^{132}Ce yrast superdeformed band leading to the conclusion that lifetimes of the sidefeeding transitions are much shorter than the in-band lifetimes. This may also imply that ^{132}Ce band 1 is fed by a more deformed structure. Before the present generation of arrays it was not possible to remove the effects of sidefeeding transitions by gating high in the bands. Due to the sensitivity of the GAMMASPHERE array, these results have allowed an explanation for the discrepancies between the present deformation measurements and earlier observations for the yrast bands in terms of sidefeeding.

4.7 Lifetime measurements of a Triaxial Band in ^{133}Ce

Rotational band structures, characterised by long regular cascades of gamma rays, have been well established in different mass regions across the chart of nuclides [HW96]. These structures are based upon secondary minima in the nuclear potential energy surface that are stabilised by the combined effects of quantal shell structure and collective dynamics. In recent years there has been great interest in the origin of stable nuclear deformations in axially symmetric nuclei due to the role of specific single-particle orbits at the Fermi surface [Wys88]. It is also apparent that the relative position of the Fermi surface within a high-j subshell can produce significant differences in nuclear deformation properties [LFM83]. A particularly interesting scenario occurs when the occupation of shape-driving orbitals at the Fermi surface removes axial symmetry and forces the nucleus to adopt a triaxial shape. This is particularly so for rare-earth nuclei in the mass 130 region which exhibit a softness to γ, the triaxiality coordinate in the polar description of rotating quadrupole shapes. The recent observation of triaxial band structures in ^{133}Ce [Ha96b] includes a relatively strongly populated band that extends to high spin but possesses a lower dynamic moment of inertia, $\Im^{(2)}$, than the known superdeformed (SD) bands [Hau95] that coexist across the same frequency and spin range. Previous work has proposed that this band is based upon a prolate $\nu i_{13/2} \otimes \pi(h_{11/2})^2$ configuration where the $\nu i_{13/2}$ orbital was deemed to be responsible for enhancing the deformation beyond the normally deformed states characterised by $\beta_2 \approx 0.2$ [Ma87]. The present results, however, rule out this interpretation since a low Q_t is found. The results suggest that the band is based on a near-oblate deformed shape rather than a SD shape, consistent with the triaxial interpretation of [Ha96b]. This section documents new information on (i) the lifetimes of in-band and sidefeeding transitions, (ii) the transition quadrupole moment of this band, and (iii) the relative deformations of coexisting nuclear shapes.

4.7.1 Experimental Details

The triaxial band in ^{133}Ce was populated in the same experiment as the superdeformed bands discussed earlier in this chapter. The band intensity is approximately 10% of the 3n-reaction channel producing ^{133}Ce and this investigation has only been possible due to the resolving power of the GAMMASPHERE spectrometer. In order to study ^{133}Ce, the data

were sorted off-line into gated matrices ($E_{\gamma 1} - E_{\gamma 2}$ coincidences). Coincidences with in-band transitions were projected into spectra defined by particular angular groups of detectors. Specifically, spectra were produced from detectors at (a) forward angles (31.7° + 37.4°), (b) 90.0°, and (c) backward angles (142.6° + 148.3°).

4.8 Lineshape Analysis

The Doppler shift attenuation method (DSAM) was used to determine the transition lifetimes of the triaxial band by Doppler-broadened lineshape (DBLS) analysis [AF79]. Inspection of the spectra indicated that the higher energy transitions show Doppler shifts, while the lowest members of the band are fully stopped. The intermediate transitions showed both stopped and moving components suggesting a lineshape analysis is more appropriate than a simple centroid shift analysis. The analysis of the data was carried out using the computer program LINESHAPE [WJ91]. The program employs Monte Carlo techniques based on the formalism of Currie [Cur69] to simulate the velocity and directional history of recoils formed at various positions in the target. It should be noted that the Monte Carlo technique can trace both the scattering directions and low recoil velocities due to nuclear stopping. Five thousand recoil histories were generated and converted into time-dependent velocity profiles for particular angular configurations of detectors. The slowing-down processes were modelled using the stopping powers of Ziegler [Zie95]. Spectra were obtained by summing gates on the clean stopped lower energy transitions of the triaxial band in ^{133}Ce (422, 488, 643, 888 keV). The sidefeeding intensities were estimated by using relative intensities extracted from this data set and checked with thin target data [Ha96b] for each transition. The sidefeeding intensities are fixed parameters in the program. The sidefeeding has been modelled as a five-state rotational band with a fixed moment of inertia of 48 $\hbar^2 \mathrm{MeV}^{-1}$ (estimated from an average of the experimental values for in-band transitions). The LINESHAPE program treats the transition quadrupole moment, Q_t, sidefeeding quadrupole moment, Q_{SF}, intensities of contaminant peaks and various background and normalisation factors as variables in the fit. Spectra for forward angles, backward angles and 90° spectra were fitted simultaneously. The best fit was obtained through the least squares minimisation procedures SEEK, SIMPLEX, and MIGRAD outlined in [WJ91]. Errors on the fitted quantities were found using the MINOS routine. A minimum acceptable error

limit has been set at 8% of the measured values and MINOS errors lower than this limit have been adjusted upwards as prescribed in [Joh97].

4.9 Results for ^{133}Ce

The mean lifetimes extracted from the lineshapes can be used to determine the transition strengths ($T(E2)$), reduced electric quadrupole transition probabilities ($B(E2)$) and electric quadrupole moments (Q_t) through the equations

$$T(E2; I \rightarrow I-2) = 1.23 \times 10^{13} E_\gamma^5 B(E2), \tag{4.17}$$

$$B(E2; I \rightarrow I-2) = \frac{5}{16\pi} \langle I\ 2\ 0\ 0 | I-2\ \ 0 \rangle^2 Q_t^2, \tag{4.18}$$

where E_γ is the γ-ray transition energy in MeV, B(E2) is in units of (e^2b^2) and Q_t is in (eb). The term in the angled brackets is a Clebsch-Gordan coefficient. The unobserved states in the modelled sidefeeding band have their energies estimated through the expression

$$E_\gamma(SF) = \frac{\hbar^2(4I-2)}{2\Im_{SF}}, \tag{4.19}$$

where the moment of inertia of the sidefeeding band has been assumed to be 48 $\hbar^2$MeV^{-1} as stated earlier. The estimate of sidefeeding energies are tentative since Eq. 4.19 is dependent on the spin, I, and no linking transitions have been observed connecting the triaxial band into the normally deformed level scheme. The results of the DBLS analysis for transitions possessing lineshapes are displayed in Table 4.8 and lineshape fits for the 999.3 and 1097.6 keV transitions are illustrated in Fig.4.26.

The results show that the triaxial band is formed by a low deformation rotor with a quadrupole moment $Q_t \approx$2.4 eb. Fig. 4.27 shows the variation of Q_t and Q_{SF} as a function of angular momentum. It can be seen that the triaxial bands transition quadrupole moment of the triaxial band, Q_t, is fairly constant with increasing spin. It also interesting to note that the results for the sidefeeding quadrupole moments, Q_{SF}, of the modelled feeding cascade have similar values to the quadrupole moments of the in-band transitions, suggesting that the band is fed by states of similar deformation.

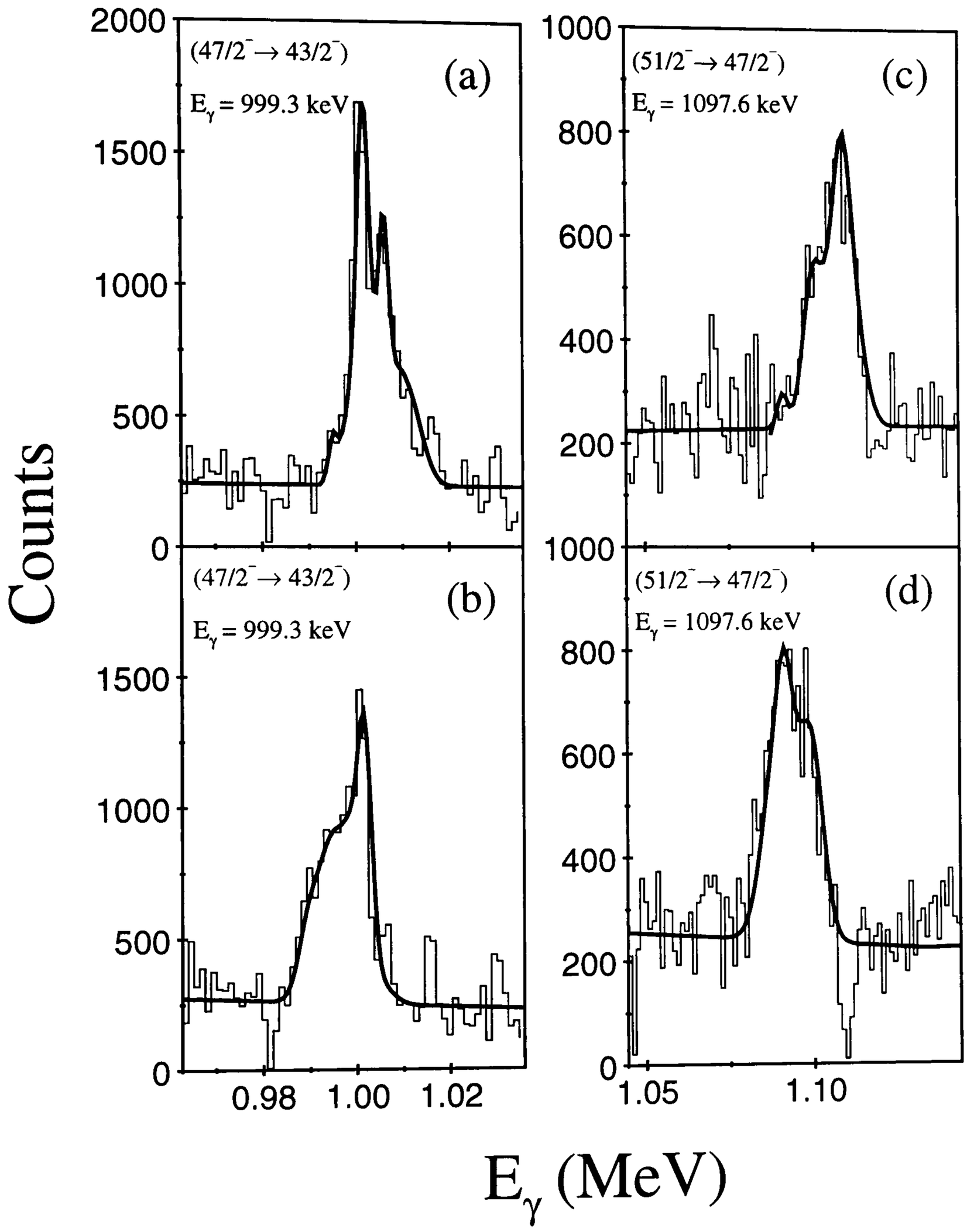

Figure 4.26: Fitted lineshapes for the 999.3 keV and 1097.6 keV transitions in ^{133}Ce. (a) and (c) display the forward angle spectra for the two transitions and (b) and (d) display the backward angle spectra. The solid line displays the total fitted lineshape.

$I_i^\pi \rightarrow I_f^\pi$	E_γ (keV)	Q_t (eb)	τ (ps)	Q_{SF} (eb)	τ_{SF} (ps)
$(43/2^- \rightarrow 39/2^-)$	887.4	1.94 ± 0.10	1.11 ± 0.13	3.93 ± 0.62	0.48 ± 0.11
$(47/2^- \rightarrow 43/2^-)$	999.3	2.65 ± 0.16	0.33 ± 0.04	3.01 ± 0.24	0.49 ± 0.01
$(51/2^- \rightarrow 47/2^-)$	1097.6	2.66 ± 0.21	0.20 ± 0.02	2.76 ± 0.22	0.37 ± 0.04
$(55/2^- \rightarrow 51/2^-)$	1188.1	2.15 ± 0.15	0.21 ± 0.02	2.33 ± 0.19	0.34 ± 0.04

Table 4.8: Summary of results for transition quadrupole moments (Q_t) and lifetimes (τ) for high-spin states in ^{133}Ce.

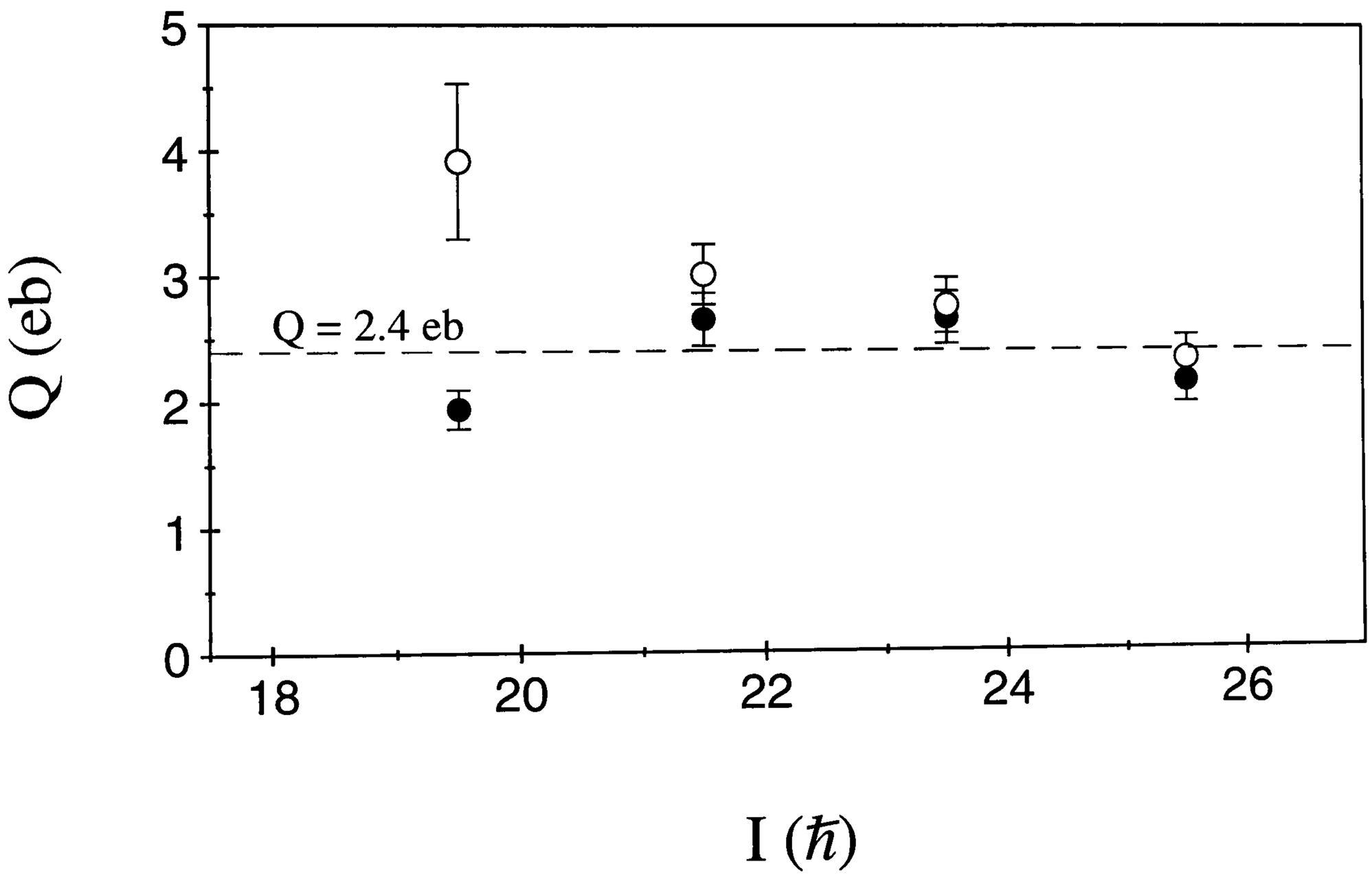

Figure 4.27: Variation of quadrupole moments as a function of spin. In-band transitions are represented by filled circles. Sidefeeding transitions are described by open circles.

This is not entirely unexpected since two other triaxial bands are observed to decay into the band around spin I=39/2 [Ha96b].

4.10 Discussion for ^{133}Ce

Deformation self-consistent Woods-Saxon cranking calculations based on the total Routhian surface TRS formalism [Wys88, NLD87, NLW88] have been performed for quasiparticle configurations in ^{133}Ce. The negative-parity one-quasineutron $\nu h_{11/2}$ bands are predicted to possess triaxial shapes lying midway between the collective prolate and oblate axes with deformation parameters $\beta_2 \approx 1.9$ and $\gamma = -30°$. Calculations predict that another minimum in the potential energy surface is formed at a notably larger γ deformation ($\gamma = -85°$) displayed in the TRS contour map in Fig. 4.28a, and is based on a $(\nu h_{11/2})^3$ 3-quasineutron configuration.

For nonaxial shapes, Q_t is related to the intrinsic quadrupole moment, Q_0, by the equation [AR95]

$$Q_t = Q_0 \frac{\cos(\gamma + 30°)}{\cos 30°}. \tag{4.20}$$

Assuming $\gamma = -85°$, the above equation yields $Q_0 = 3.62 \pm 0.30$ eb and corresponds to a quadrupole deformation $\beta_2 = 0.211 \pm 0.017$; the β_2 value was obtained from the expansion of Q_0 in terms of β_2 given in [LVH70] assuming no hexadecapole deformation. The extracted value of $Q_t = 2.4 \pm 0.2$ eb is considerably lower than the measured quadrupole moments of the superdeformed bands in this nucleus ($Q_t \approx 7.5$ eb). Fig. 4.28b displays the potential energy surface for negative parity structures at higher spin. Several coexisting minima can be observed in Fig. 4.28b including the γ=–85° triaxial minimum and a superdeformed prolate minimum that is lowered in energy at higher spin. The three known superdeformed bands in ^{133}Ce [Hau95] are much less intense than the triaxial band in these data and are not observed in this experiment due to the weaker nature of this particular reaction channel. Previous lifetime measurements of SD bands in ^{132,133}Ce, based upon target-thickness induced Doppler broadening [Ha96a], have indicated that the excited SD bands in ^{133}Ce possess similar quadrupole moments to the yrast SD band in ^{132}Ce. Table 4.9

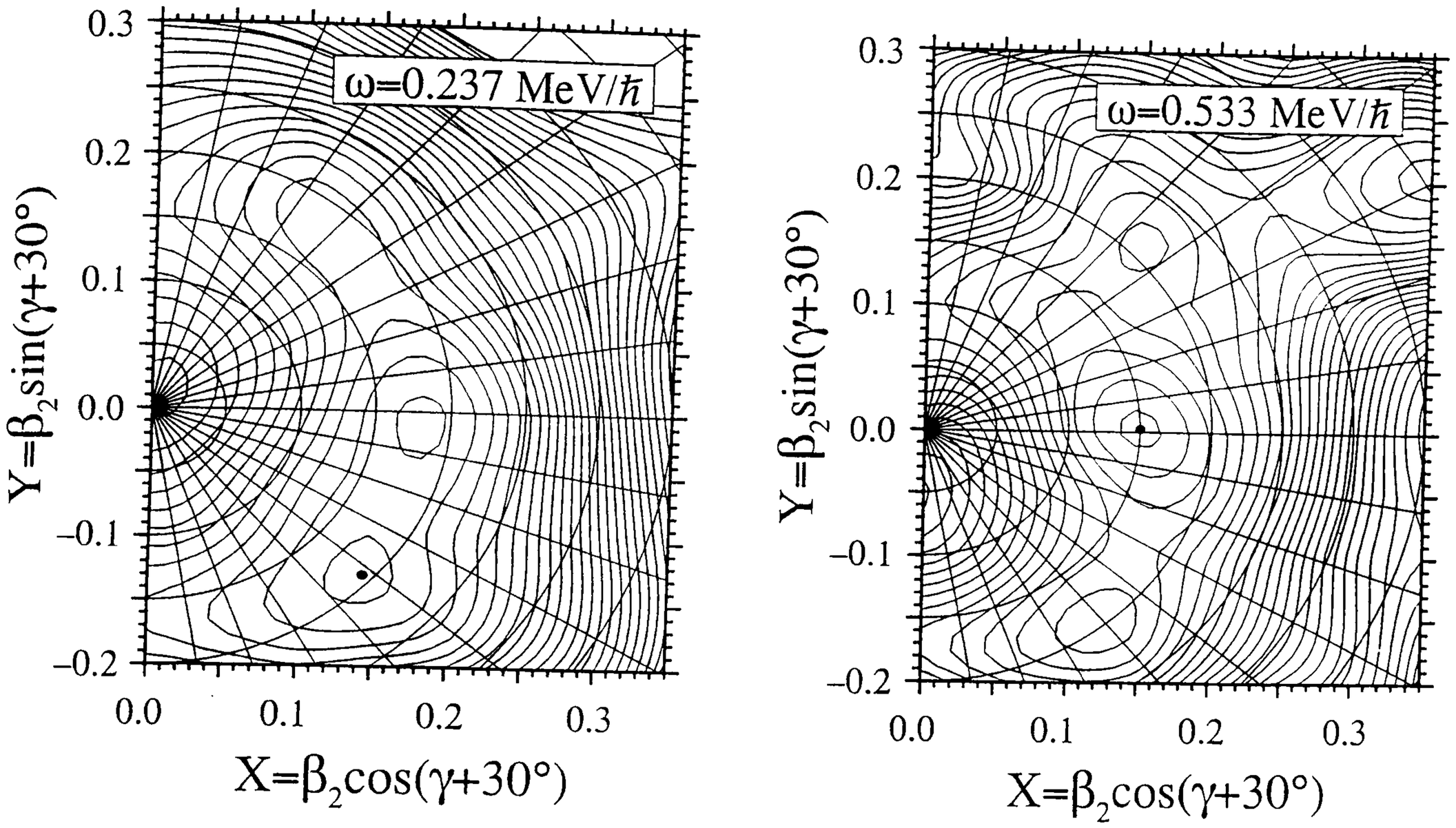

Figure 4.28: Total Routhian surface (TRS) maps for (π, α)=(–,–1/2). (a) displays the triaxial minimum at γ=–85°. A number of coexisting minima are pictured in (b) at higher spin.

Band	Q_t (eb)	β_2	γ	Reference
^{133}Ce Triaxial Band	2.4 ± 0.2	0.173 ± 0.014	–85°	
^{132}Ce SD Band 1	7.4 ± 0.4	0.411 ± 0.021	0°	
^{132}Ce SD Band 1	7.4 ± 0.9	0.411 ± 0.045	0°	[Ha96a]
^{133}Ce SD Band 1	7.4 ± 0.7	0.409± (0.04)	0°	[Ha96a]
^{133}Ce SD Band 2	7.5± 0.8	0.414 ± 0.040	0°	[Ha96a]

Table 4.9: Comparison of experimental Q_t values for rotational bands in ^{132,133}Ce.

compares the present deformation measurements for rotational bands in ^{132,133}Ce with prior experiments. The yrast band in ^{132}Ce is intensely populated in this data set and the similar nature of the quadrupole moments of these bands allows a direct comparison to be made between highly deformed prolate bands and the much less deformed triaxial structure. Since both structures are populated concurrently and recoil with the same stopping conditions, we can directly contrast the deformation measurements and overcome large uncertainties [≈10-15 %] in the absolute Q_t values that arise due to poor knowledge of the recoil stopping in the target foils. Experimental F(τ) curves are displayed in Fig. 4.29a and Fig. 4.29b. Fig. 4.29a obtained from a centroid shift analysis indicate that the Q_t value is consistent with a low deformed shape with Q_t=2.0(2)eb. The large errors on the centroid shift measurement suggest that this measurement is consistent with the lineshape measurements. A comparison with the superdeformed yrast band in ^{132}Ce clearly displays the difference in Q_t values between the coexisting minima.

The lifetimes, τ, of the in-band transitions also show marked differences between the triaxial and superdeformed bands. Transition strengths (T(E2)/T(E2)$_{sp}$) obtained using the experimental lifetimes and Weisskopf estimates, were found to be ≈ 35 Wu which are lower than those derived for the yrast SD band in ^{132}Ce with magnitudes ≈ 490 Wu. A further comparison can be made with the normally deformed ground state band in ^{132}Ce that is known to have transition strengths of the order of 100 Wu [Kir89]. This implies that the degree of collectivity is lower in the triaxial structure than in normally deformed and superdeformed prolate shapes. This is entirely consistent with TRS calculations that suggest that the minimum in which the band is formed lies between the non collective prolate (γ = –120°) and collective oblate (γ = –60°) axes.

4.11 Summary

In summary, the lifetimes of a triaxial band in ^{133}Ce have been measured and transition quadrupole moments deduced. The band is formed by a rotating triaxial shape at large γ deformation and possesses a quadrupole moment of average value Q_t=2.4 eb. TRS calculations predict that the band is based on a 3-quasineutron $(\nu h_{11/2})^3$ configuration suggesting that the $\nu i_{13/2}$ orbital is not involved in the band's configuration. Comparisons of transition strengths of the triaxial band and neighbouring structures in ^{132}Ce suggest that the triaxial

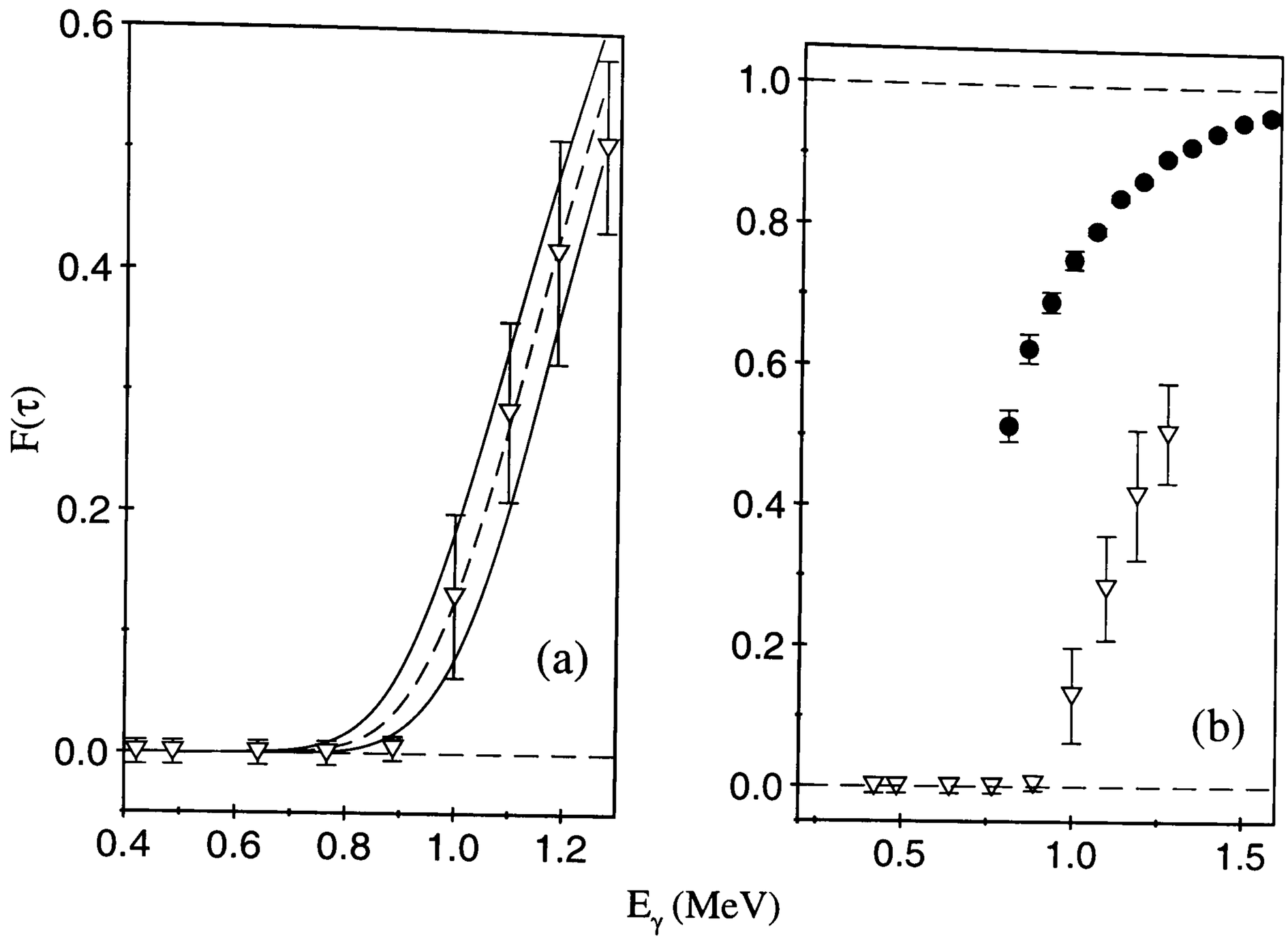

Figure 4.29: (a) F(τ) curve for ^{133}Ce triaxial band. The dashed line is the calculated curve for Q_t=2.0 eb and the solid lines for comparison above/below are calculated for Q_t=2.2 eb and 1.8 eb respectively. (b) Comparison of centroid shift measurements between the ^{133}Ce triaxial band (open triangles) and superdeformed band 1 in ^{132}Ce (filled circles).

band is not as collective as prolate normally deformed or superdeformed shapes. The relative deformations of coexisting minima have been measured and it has been established that the triaxial ($\gamma = -85°$) configuration has a much lower deformation than coexisting shapes formed in the superdeformed prolate minimum.

The results of the DBLS analysis appear to suggest that the band is fed by states of similar deformation. This is not unreasonable since other weaker triaxial structures are known to feed this band.

Chapter 5

Multiple Superdeformed Bands in ^{132}Nd

High-spin states have been studied in neutron deficient ^{132}Nd, produced in the ^{105}Pd(^{35}Cl,α, $p, 3n$) reaction, using the GAMMASPHERE γ-ray spectrometer in conjunction with the MICROBALL charged particle detector array. Three new, weakly populated rotational bands have been found, which are believed to be associated with a superdeformed prolate shape. Comparison of the properties of these bands with Woods-Saxon cranking calculations suggests that they are built upon negative-parity configurations that involve only one intruder orbital ($i_{13/2}$) from the N=6 shell. One of the bands has been linked into the normally deformed states allowing an estimation of the spin, parity and excitation energy of the band.

5.1 Current Motivation

In the light rare-earth region around A≈130, the superdeformed structures roughly correspond to a prolate nuclear shape with a 3:2 axis ratio (β_2≈0.35-0.45) and the superdeformed configurations are predicted to involve intruder orbitals from the N=6 oscillator shell. The initial discovery of superdeformation in ^{132}Ce was predicted to be stabilised at high-spin by a stable proton shell closure and the core polarising effects of the $(\nu i_{13/2})^2$ intruder configuration. Similar configurations are expected for the neighbouring even-even nuclei. In the light neodymium isotopes, the scenario is different. With decreasing neutron number it is energetically favourable to occupy available N=5 negative-parity valence orbitals rather than the second N=6 intruder state. For example, the yrast superdeformed band in ^{134}Nd has been interpreted in terms of a negative-parity structure involving only one of the $i_{13/2}$ intruder states, while a second excited band has been assigned a positive-parity configuration involving two N=6 intruders [Pet94].

The nucleus ^{132}Nd is also predicted to possess superdeformed shapes at high spin, however until the present work such structures had not been observed. Nilsson diagrams appropriate to ^{132}Nd are displayed in Fig 5.1 and show the relevent single particle states as a function of deformation. Both proton and neutron diagrams indicate the presence of shape driving orbitals at the Fermi surface. Fig 5.1a indicates that at β_2 >0.3, the neutron potential is occupied up to the [541]1/2$^-$ intruder state originating from the $h_{9/2}$ sub-shell. The proton Nilsson diagram (Fig 5.1b) predicts that the Fermi surface lies above the [404]9/2$^+$ state originating from the $g_{9/2}$ sub-shell. At larger deformations it becomes energetically favourable to occupy the negative-parity [532]5/2$^-$ $h_{11/2}$ states where superdeformed states might be expected to be stabilised by the $(\pi g_{9/2})^{-2} \otimes (\pi h_{11/2})^2$ proton configuration in a similar manner to superdeformed bands observed in ^{133}Pr [Wil95]. Calculations based on the TRS formalism and using a deformed Woods-Saxon single particle potential using a monopole pairing force residual interaction have been performed for various quasiparticle configurations in ^{132}Nd and predict the presence of highly deformed stable minima that become yrast at medium-spin ($I \geq 30\hbar$).

Recent work on superdeformed bands in other neodymium isotopes has revealed the presence of linking transitions that connect the superdeformed states into the normally deformed level scheme allowing an estimation of the spin, parity and excitation energy of

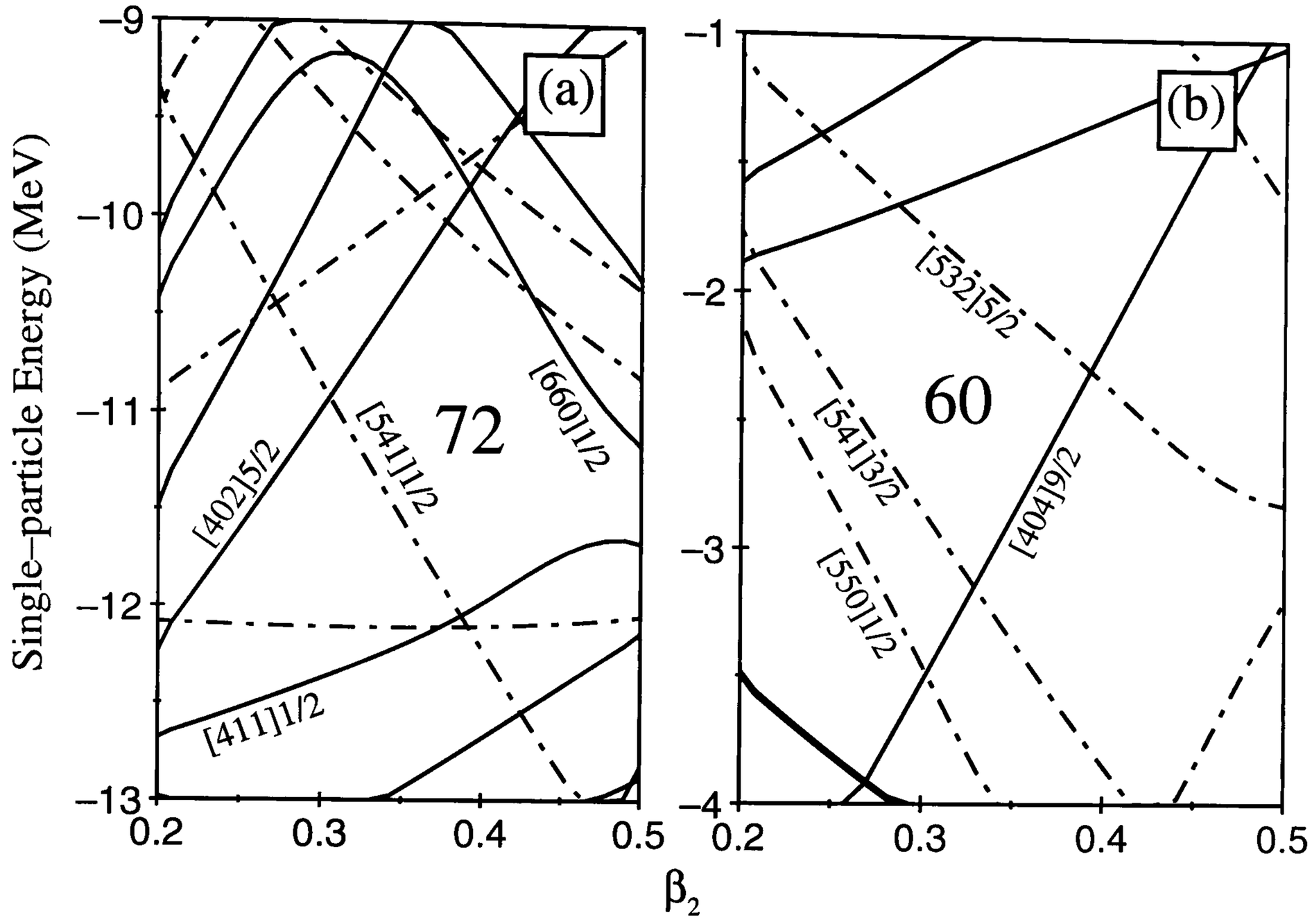

Figure 5.1: Single particle energies as a function of quadrupole deformation for ^{132}Nd calculated using a deformed Woods-Saxon potential. (a) Neutron Nilsson states around the N=72 closure. (b) Proton Nilsson states around the Z=60 shell closure. Each orbital is labelled according to its parity: Solid lines = (π=+), dot-dash lines = (π=−).

the bands. To date, linking transitions have been observed in ^{133}Nd [Baz94], ^{134}Nd [Pet96], ^{135}Nd [Del95] and ^{137}Nd [Lun95]. Any superdeformed bands in ^{132}Nd might be expected to follow the trend adding further information to the systematics of the neodymium isotopes.

5.2 Experimental details

High spin states in A$\sim$135 nuclei were populated using the ^{105}Pd(^{35}Cl,$x\alpha, yp, zn$) fusion evaporation reaction. The 88 Inch cyclotron at the Lawrence Berkeley National Laboratory provided a 180 MeV ^{35}Cl beam which was incident on a thin self-supporting target foil of nominal thickness 500μg/cm^2. Coincident high-fold γ-ray events ($\gamma^n, n \geq 4$) were recorded

with the GAMMASPHERE γ-ray spectrometer [Lee90] containing 57 Compton suppressed HPGe detectors, while the evaporated charged particles were detected simultaneously with the MICROBALL charged particle detector array [Sar96], located within the GAMMASPHERE target chamber.

In order to study the light neodymium isotopes, the MICROBALL was used to select γ-ray events in coincidence with both an evaporated α particle and a proton (1α,$1p$, zn). Approximately 270 million such events were selected off-line, unpacked into constituent triple γ-ray coincidences (γ^3) and sorted into a RADWARE cube ($E_{\gamma 1}$-$E_{\gamma 2}$-$E_{\gamma 3}$) [Rad95]. In this cube, ^{132}Nd ($\alpha p3n$) and ^{133}Nd ($\alpha p2n$) dominated while ^{131}Nd($\alpha p4n$), ^{134}Nd(αpn) and other $2\alpha pzn$ (cerium) and $\alpha 2pzn$ (praseodymium) channels were present below the 1% level.

5.3 Results

5.3.1 New Superdeformed Bands in ^{132}Nd

Prior to this work superdeformed bands had not been observed in ^{132}Nd. Three new weakly populated superdeformed bands have been found in this work. All three bands have been assigned to ^{132}Nd in view of their coincidence relationships with low-spin transitions of ^{132}Nd. The population intensities are estimated to be 0.7% (band 1), 0.4% (band 2) and 0.4% (band 3) of the $2^+ \rightarrow 0^+$ transition. This is the lightest neodymium isotope in which superdeformation has been observed.

Double-gated spectra generated from the cube are pictured in Fig 5.2. All bands shows similarities to the known superdeformed bands in this mass region. The energy separation between γ rays is $\approx$70 keV leading to moments of inertia of the same magnitude as SD bands in the cerium/neodymium region.

The spectrum for band 1 has been produced by double-gating on all the transitions in the superdeformed band that are labelled in (Fig.5.2a). It is apparent that the band is in coincidence with the known negative-parity 2-quasiproton sideband [Wad89] and a large 764 keV γ-ray that was previously unknown. The 764 keV transition (labelled by an asterisk in Fig. 5.2a) appears to be a self-coincident doublet that is involved in the decay of the superdeformed band into the known normally deformed level scheme.

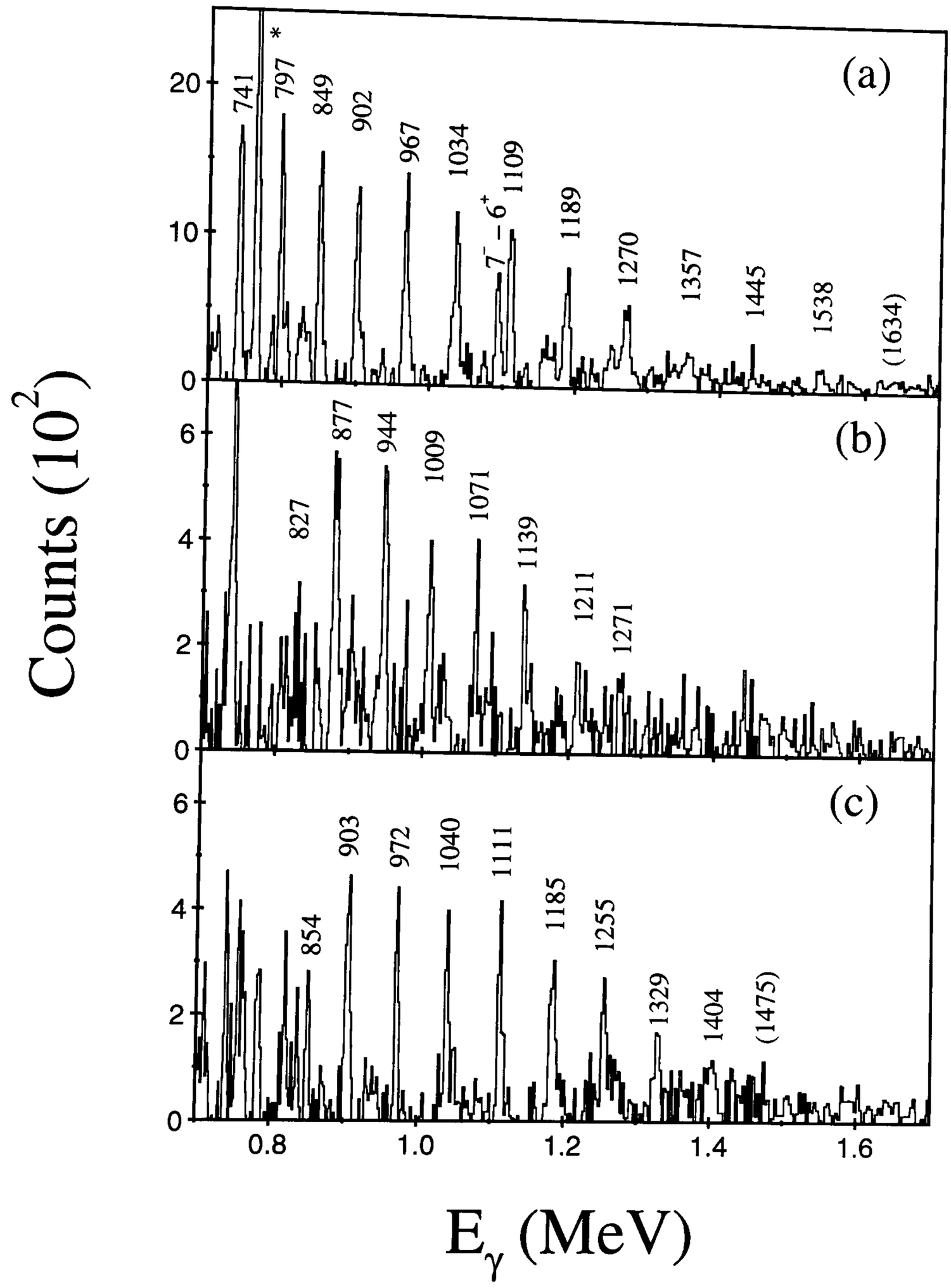

Figure 5.2: Double-gated spectra, generated from the cube, showing the new SD bands in ^{132}Nd. The energies of the transitions are labelled in keV, and all these transitions have been used as gates. The low-lying 1094-keV E1 transition ($7^- \rightarrow 6^+$) is indicated in (a) while a self-coincident 764-keV doublet, involved in the decay of band 1, is labelled by an asterisk.

It is hoped that since all three bands are attributed to the same nucleus, ^{132}Nd offers a further opportunity to investigate the deformation driving effects of specific configurations involving the $\nu i_{13/2}$ intruder states.

5.3.2 Transition Energies and Relative Intensities.

The transition energies and relative intensities were extracted from the cube using the RADWARE LEVIT8R code. LEVIT8R is an graphical analysis code that determines energy and intensity values from a least squares fitting routine. This has been especially useful since it has been possible to account for the intensities of γ rays from contaminant channels. The measured γ-ray transition energies are recorded in Table 5.1. The uncertainties in the transition energy measurements increase with increasing frequency. This is due to the effects of Doppler broadening, diminishing detector efficiency and larger statistical errors on the peak fit at higher frequencies.

The relative intensity measurement reflects the intensity of various γ-ray transitions within a rotational band with respect to the maximum intensity of the band. The relative intensity distributions as a function of γ-ray energy is pictured in Fig 5.3. All measurements are taken from the cube and have been normalised to the most intense transition in SD band 1. The intensities have been corrected for the efficiency of the spectrometer array within the RADWARE LEVIT8R code. The relative intensity profiles of superdeformed bands are often characterised by three major regions. The feeding region is defined where the intensity gradually increases with each successive transition to lower energy. In some bands the feeding regions leads to a plateau region where the transitions are observed to have equal intensities. The depopulation region occurs at low frequency when the band becomes non-yrast and depopulates to some other yrast structure. The band 1 profile indicates that the band is fed across the frequency range of $\hbar\omega$=1.2–1.7 MeV before levelling into a plateau of even intensity. Band 2 appears to be populated over the top four transitions of the band while the distribution for band 3 indicates that feeding occurs across most of the band. These profiles are typical for superdeformed bands in this mass region.

γ-ray transition energies in ^{132}Nd

Band 1 (keV)	Band 2 (keV)	Band 3 (keV)
741.4 ± 0.2		
797.0 ± 0.2		
849.2 ± 0.2	826.9 ± 0.4	854.0 ± 0.3
902.1 ± 0.2	877.0 ± 0.5	903.3 ± 0.3
967.3 ± 0.3	943.9 ± 0.5	971.6 ± 0.3
1034.1 ± 0.4	1008.9 ± 0.5	1039.9 ± 0.5
1108.8 ± 0.6	1070.8 ± 0.6	1111.4 ± 0.5
1188.8 ± 0.6	1139.1 ± 0.8	1184.6 ± 0.5
1270.5 ± 0.9	1210.6 ± 0.8	1254.5 ± 0.5
1357.0 ± 1.3	1270.8 ± 1.3	1329.0 ± 0.5
1445.0 ± 1.4		1404.1 ± 0.5
1538.3 ± 1.2		(1475.0 ± 1.0)
(1634.0 ± 1.2)		

Table 5.1: γ-ray transition energies for the superdeformed bands in ^{132}Nd. Tentative transitions are shown in brackets.

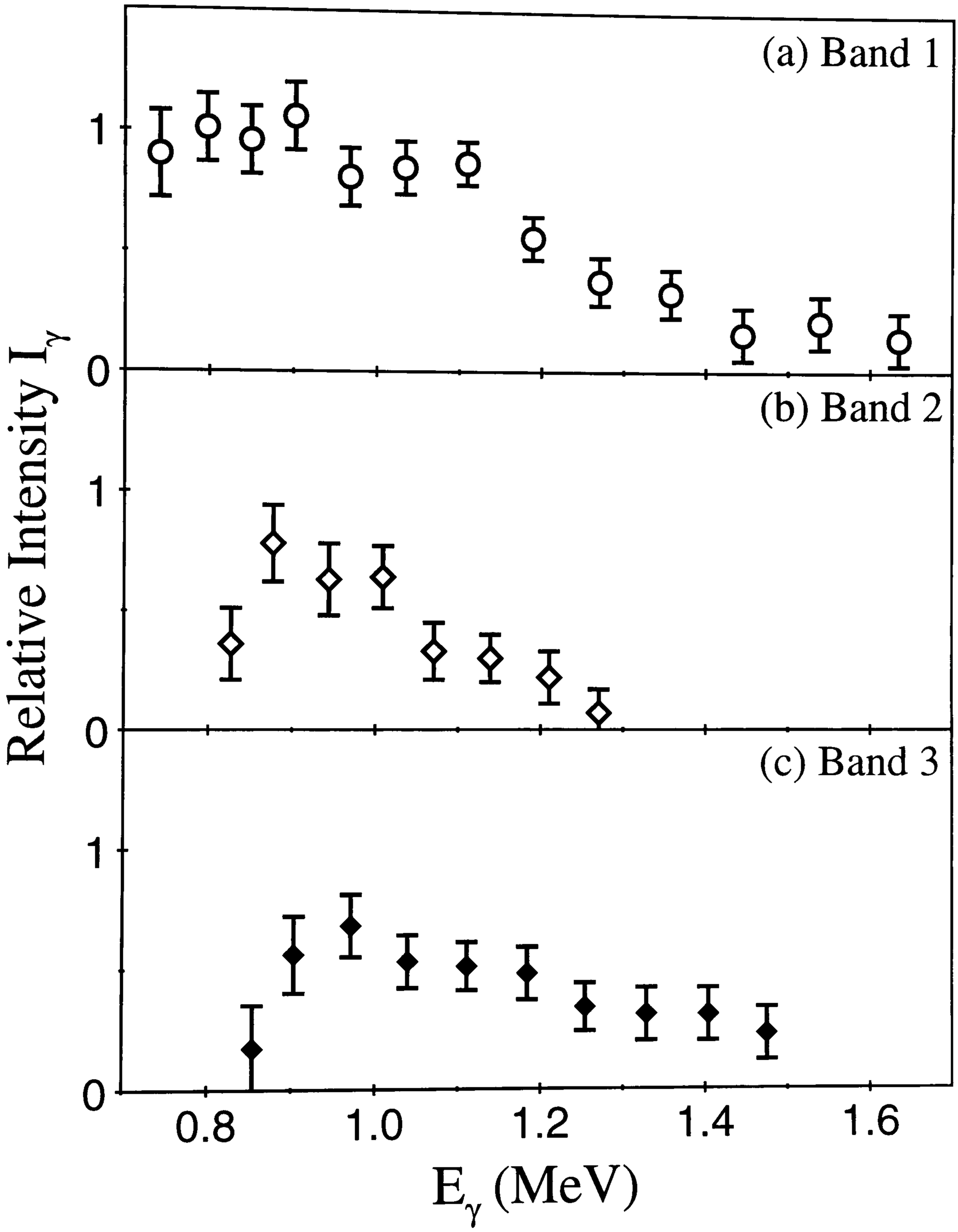

Figure 5.3: Relative intensity profiles for the superdeformed bands in ^{132}Nd.

5.3.3 Dynamic Moments of Inertia

The dynamic moments of inertia for the bands in ^{132}Nd are shown in Fig 5.4 as a function of rotational frequency. The $\Im^{(2)}$ is related to the energy spacing between peaks in rotational bands and since it can be evaluated independently of spin, it is appropriate to discuss this quantity in relation to superdeformed bands. The dynamic moments of inertia will be discussed with regards to configuration assignments later in this chapter, however the main features will be mentioned here.

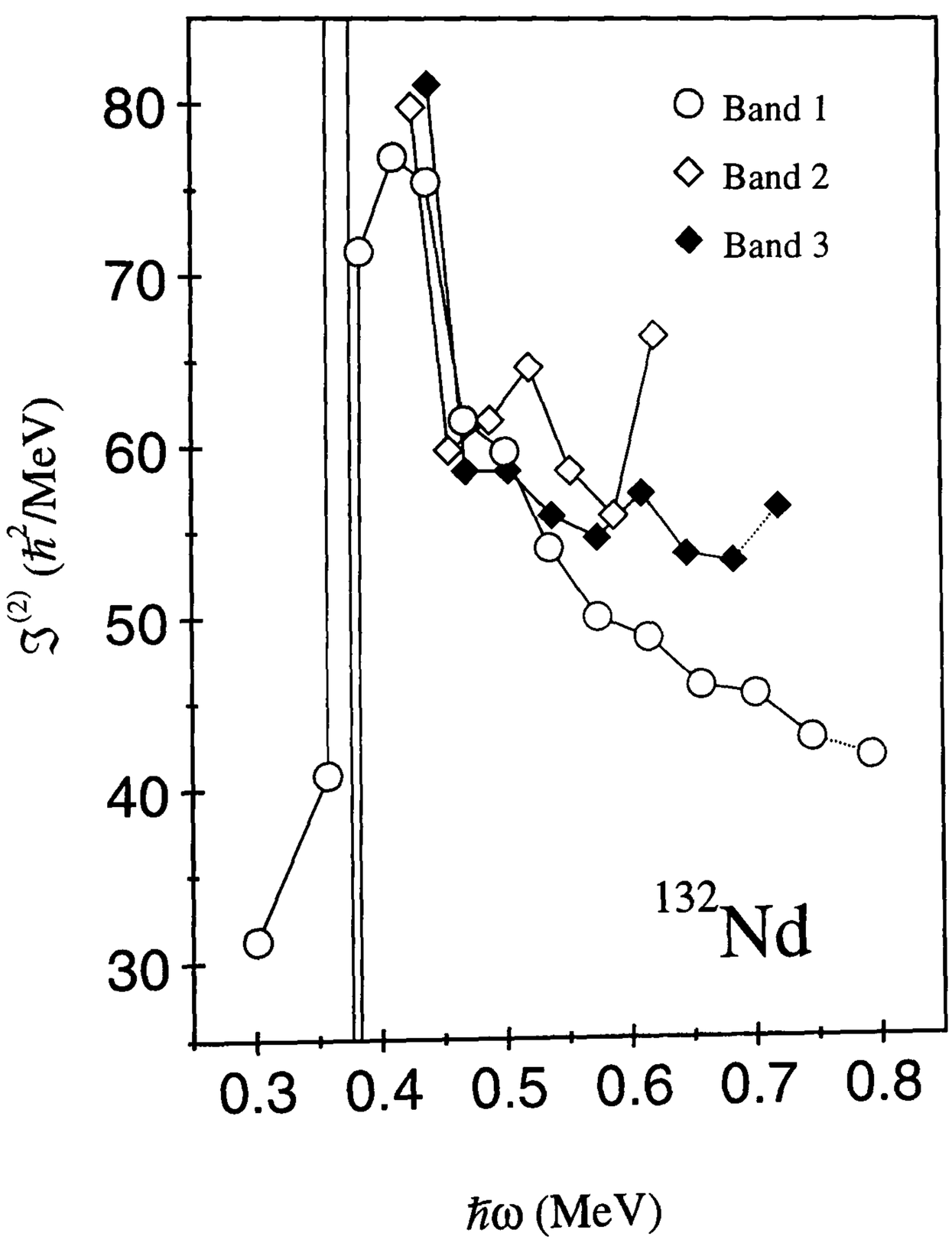

Figure 5.4: Dynamic moments of inertia extracted for the three SD bands in ^{132}Nd.

1. All three superdeformed bands exhibit a large rise in dynamic moment of inertia at $\hbar\omega \leq 0.45$ MeV which is indicative of an alignment process.
2. A large perturbation arises at $\hbar\omega \approx 0.35$ MeV corresponding to the transition through the self-coincident 764 keV γ-ray pair.
3. The profiles for band 2 and band 3 are generally larger than the band 1 dynamic moment of inertia pattern.
4. Band 2 and band 3 display abrupt rises in moments of inertia at $\hbar\omega \approx 0.50$ MeV and $\hbar\omega \approx 0.60$ MeV respectively.

5.4 Discussion

The discussion of the experimental results is separated into two major topics of interest. The first discussion concerns the underlying structures upon which the bands are built. The second aspect considers the decay mechanism of the new superdeformed bands in ^{132}Nd.

5.4.1 Configurations of Superdeformed Bands in ^{132}Nd

Deformation self-consistent cranking calculations, based on the total Routhian surface (TRS) formalism [NLD87, Wys88, NLW88] and using a deformed Woods-Saxon single-particle potential with a monopole pairing force residual interaction [Naz85, Cwi87] have been performed for quasiparticle configurations in ^{132}Nd. In these calculations, the pairing strength has been calculated at zero frequency and modelled to decrease with increasing rotational frequency such that the pairing has fallen by 50% at ω =0.7 MeV/$\hbar$, for details see [Wys88]. The known ground-state and negative-parity two-quasiproton bands ($\pi h_{11/2} \otimes \pi g_{7/2}$) are predicted to possess prolate shapes with deformation parameters $\beta_2 \approx$0.27, $\beta_4 \approx -0.005$. However, negative-parity two-quasineutron configurations, formed by coupling the $\nu i_{13/2}$ (N=6) intruder orbital to the available $\nu h_{9/2}$ and $\nu h_{11/2}$ (N=5) valence orbitals, possess a larger average deformation ($\beta_2 \approx 0.34, \beta_4 \approx 0.022$) and become yrast with respect to the normally deformed states for I $\geq 30\hbar$. In particular, three such SD structures show up, namely the $\nu i_{13/2} \otimes \nu h_{9/2}$ ($\alpha = 1$) configuration and the $\nu i_{13/2} \otimes \nu h_{11/2}$ ($\alpha =$ 0,1) pair of near degenerate signature partners. These three negative-parity configurations are predicted at a lower excitation energy than the positive-parity $(\nu i_{13/2})^2$ configuration,

involving two N=6 intruders. Fig 5.5 displays a rigid rotor plot generated using TRS parameters, comparing potential SD configurations with the normal deformed yrast band.

Results of Woods-Saxon cranking calculations, using representative SD TRS deformation parameters, are shown in Fig. 5.6, with the relevant quasiparticle orbitals labelled (note that the TRS calculations suggest that both the quadrupole and hexadecapole deformation parameters decrease with increasing frequency, which tends to lower the energy of the $\nu h_{9/2}$ orbital relative to the $\nu h_{11/2}$ orbital). Table 5.2 relates the labels to the underlying Nilsson labels. Since bands 2 and 3 are populated with the same intensity and both decay differently to band 1, we may associate these bands with the near-degenerate signature partner $\nu i_{13/2} \otimes \nu h_{11/2}$ configurations. Furthermore, the transition energies of band 2 lie approximately midway between those of band 3 (see Fig 5.2), consistent with the signature partner scenario. The stronger band 1 may then be associated with the $\alpha = 1$ (odd-spin) $\nu i_{13/2} \otimes \nu h_{9/2}$ configuration.

Neutrons

Shell model	(π, α)	Nilsson label	High-spin quasiparticle label
$i_{13/2}$	(+,+1/2)	[660]1/2$^+$	a
$h_{9/2}$	(−,+1/2)	[541]1/2$^-$	h
$h_{11/2}$	(−,±1/2)	[514]9/2$^-$	e/f
$d_{5/2}$	(+,±1/2)	[402]5/2$^+$	c/d

Protons

Shell model	(π, α)	Nilsson label	High-spin quasiparticle label
$g_{9/2}$	(+,±1/2)	[404]9/2$^+$	A/B
$h_{11/2}$	(−,±1/2)	[541]3/2$^-$	E/F

Table 5.2: Parity-signature labels and their relationship to conventional shell model and quasiparticle labels.

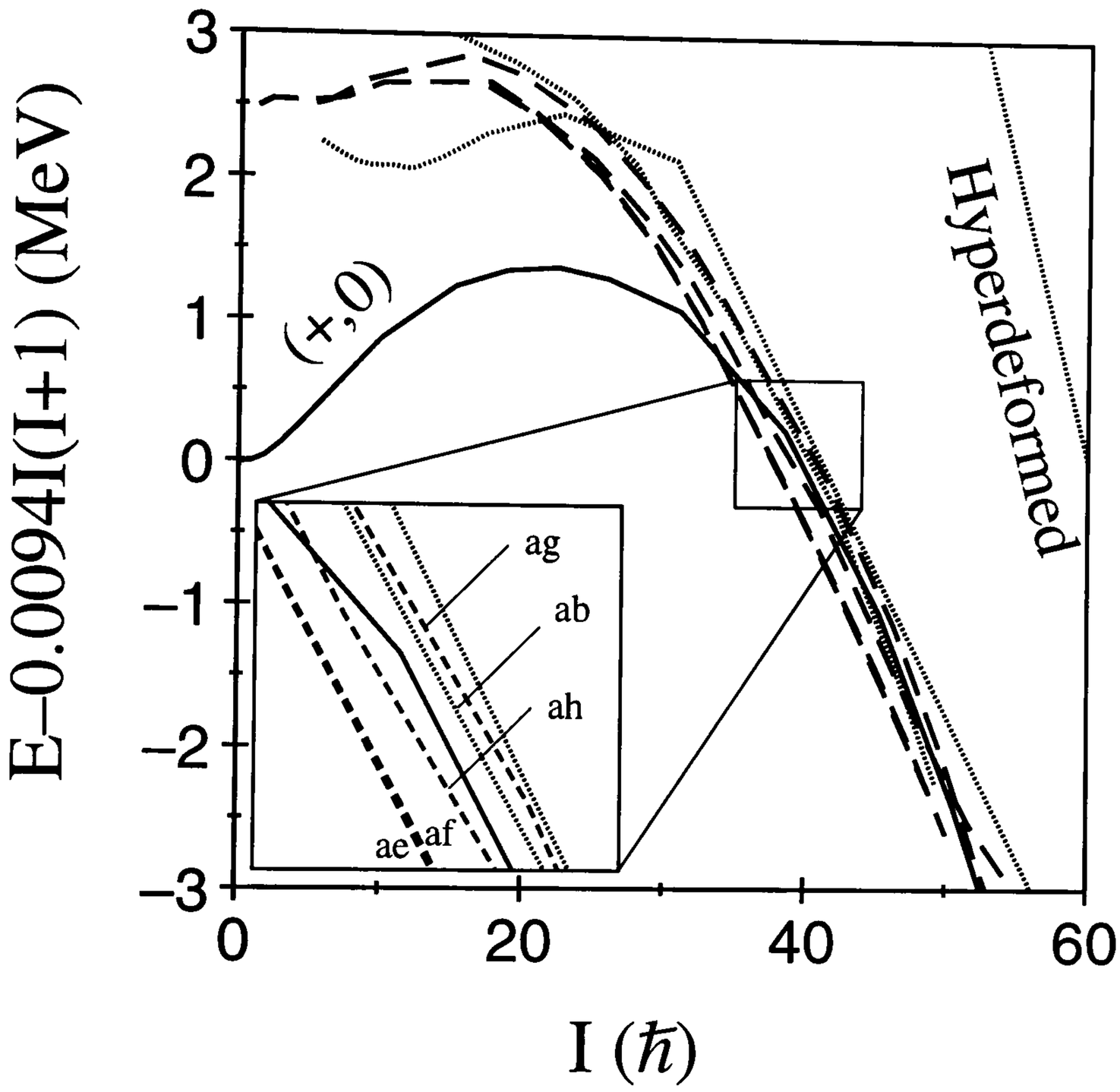

Figure 5.5: TRS rigid rotor plot for ^{132}Nd comparing predicted SD configurations with the (+,0) band. The inset shows that negative-parity configurations are favoured at high-spin. These configurations are predicted to be lower in energy compared with the $(\nu i_{13/2})^2$ (ab) configuration. The inset labels correspond to the standard convention for labelling quasiparticles orbitals.

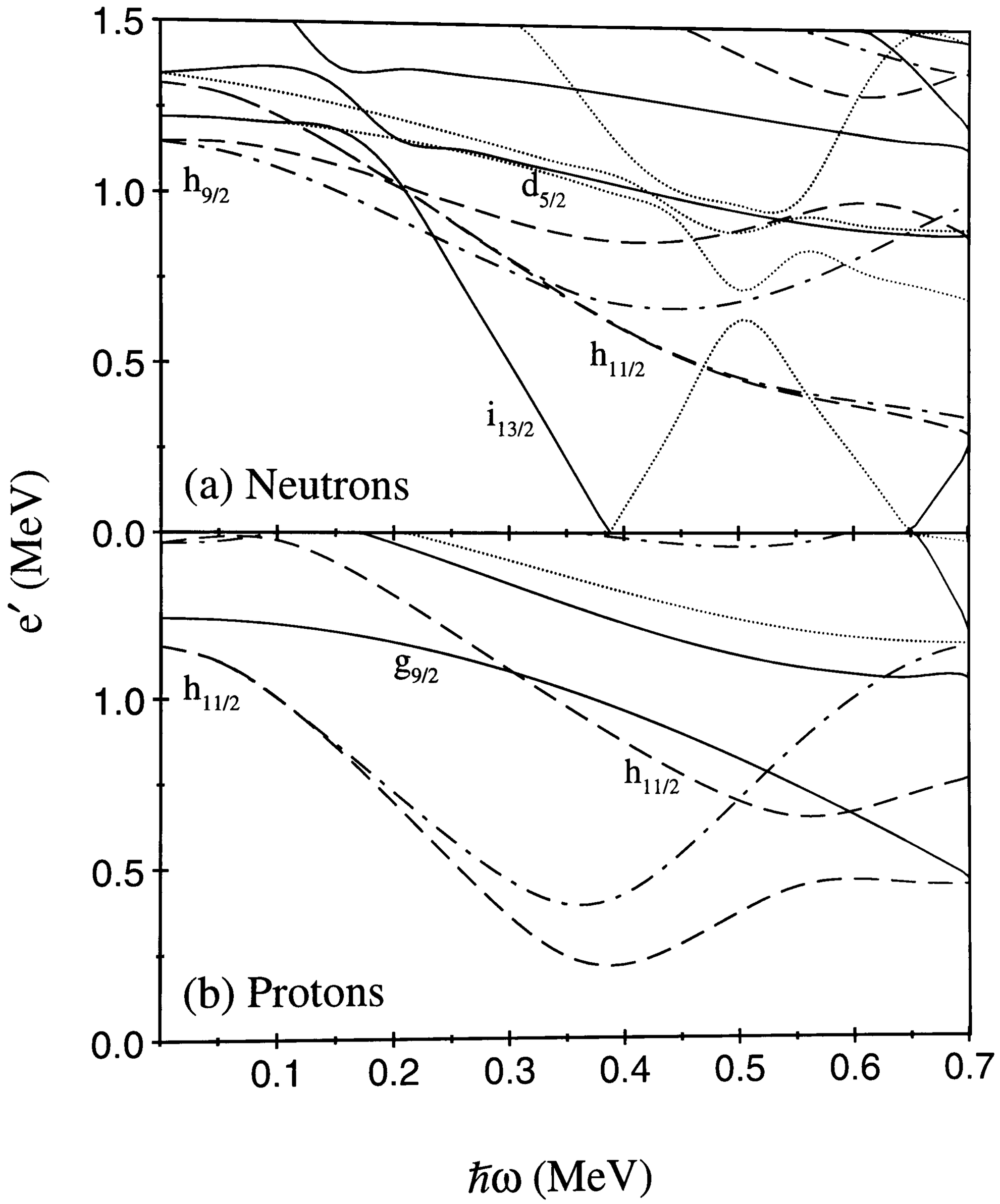

Figure 5.6: Representative cranked Woods-Saxon Routhians for neutrons (a) and protons (b) in superdeformed ^{132}Nd. The parity and signature (π, α) of the levels are: (+,+1/2) solid lines; (+,–1/2) dotted lines; (–,–1/2) dashed lines; (–,+1/2) dot-dashed lines. Shell model labels are also given for the valence orbitals.

The dynamic moments of inertia of the three bands all show a large rise at low frequencies ($\omega \leq 0.45$ MeV/$\hbar$; see Fig 5.4), which is consistent with an alignment process. The Woods-Saxon cranking calculations of Fig. 5.6 predict the rotational alignment of a pair of $\pi h_{11/2}$ quasiparticles at $\omega \approx 0.38$ MeV/$\hbar$, in reasonable agreement with the rise in the moments of inertia. The moments of inertia of bands 2 and 3 are generally higher than that of band 1. This may be caused by the gradual alignment of a pair of $\nu h_{9/2}$ quasineutrons, which is blocked for the assigned band 1 configuration. Similar smooth alignments are predicted for other SD bands in this mass region [Wys88]. The exact nature of the sharp, abrupt rises in the moments of inertia of bands 2 and 3 at $\omega \approx 0.50$ MeV/$\hbar$ and $\omega \approx 0.60$ MeV/$\hbar$ is unclear. The moment of inertia of band 1 exhibits a large perturbation around at $\hbar\omega \approx$ 0.35 MeV corresponding to the transition through the self-coincident 764 keV γ-ray pair. This is thought to be indicative of a further change in alignment.

The variation of total aligned angular momentum, I_x as a function of rotational frequency for band 1 is plotted in Fig. 5.7. There is a change in angular momentum of $\Delta I_x \approx 4\hbar$ at $\hbar\omega \approx$0.4MeV. The experimental value could represent the sharp crossing between the $\nu d_{5/2}$ level and the $\nu i_{13/2}$ state. The alignment contributions of particular orbitals can be estimated from the slopes of the quasiparticle Routhians. The difference in slopes (Δi_x) between two interacting orbitals should correspond to the increase of the experimental I_x value. Since $\Delta i_x \approx 5\hbar$ for the $\nu d_{5/2}$-$\nu i_{13/2}$ crossing, the new structure below band 1 may represent a negative-parity configuration involving the $\nu d_{5/2}$ orbital. The experimental crossing frequency is larger than the predicted frequency in Fig. 5.6, however it should be noted that the crossing frequency is sensitive to changes in deformation. At lower deformations (β_2=0.3) the crossing occurs at a similar frequency to the experimental value.

5.4.2 Depopulation of Superdeformed bands in ^{132}Nd

The depopulation mechanism of superdeformed bands is of great contemporary interest. In the A≈130 region, the superdeformed bands possess lower average deformations compared with the superdeformed structures in other mass regions. For example, in the A≈150 region superdeformed nuclei have quadrupole deformations around β_2 ≈0.6 whereas bands in the A≈130 region tend to have lower average deformations (β_2 ≈0.3–0.4). Also, A≈130

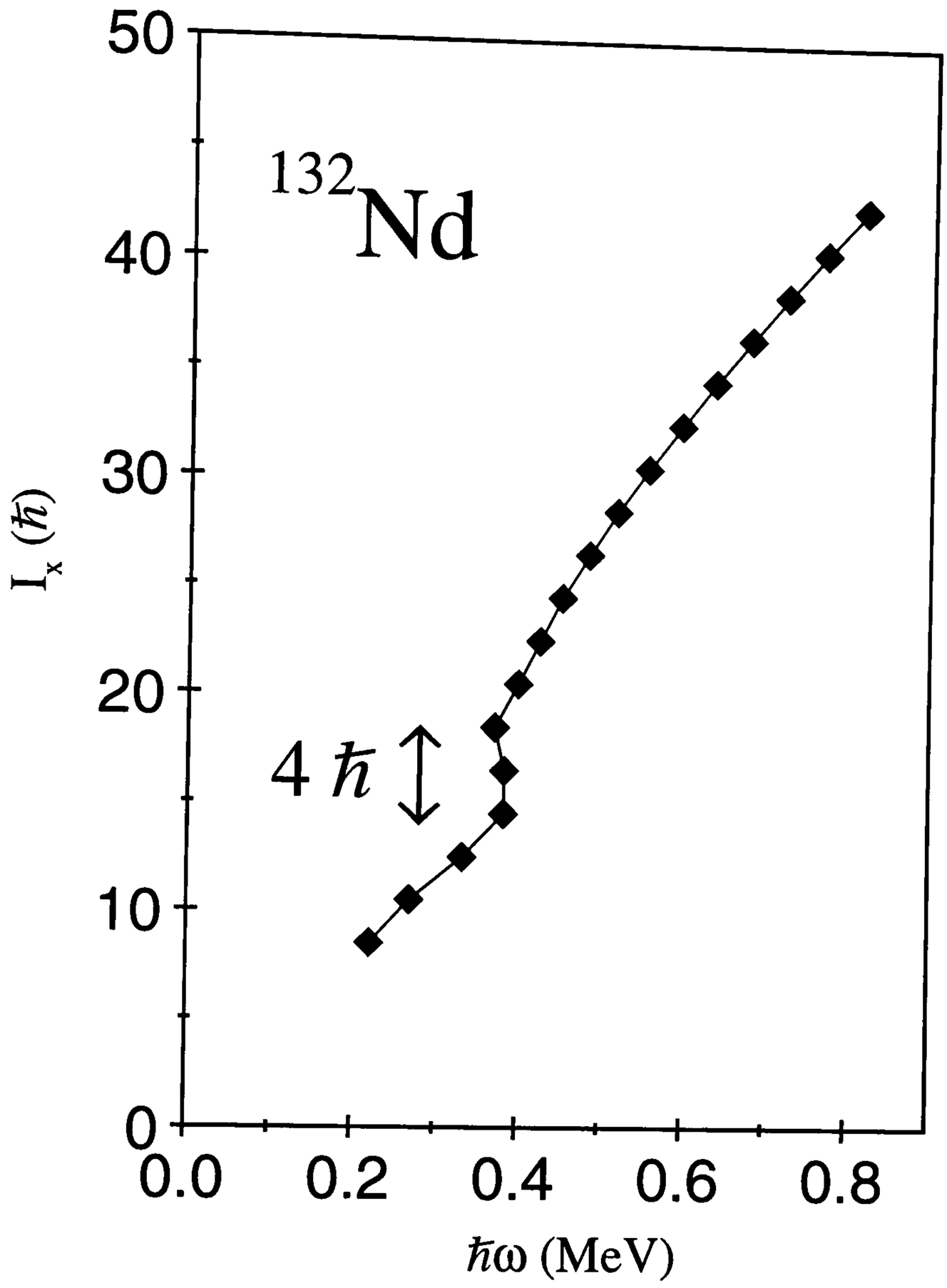

Figure 5.7: Total aligned angular momentum (I_x) plot for SD band 1 in ^{132}Nd.

nuclei exhibit large ground state deformations with $\beta_2 \approx 0.2$. Consequently the difference in β_2 between the second minimum and the normally deformed states is not as large when compared to other mass regions. The observation of discrete linking transitions between the wells is thought to be more likely in A≈130 because of the comparable deformations between structures in the different minima. In recent years an increasing amount of data has become available on the odd-N neodymium isotopes [Baz94], [Del95], [Lun95]. In all of these studies it has been possible to unambiguously define the decay path to the normally deformed states. The even-N neodymium isotopes are generally more weakly populated

compared with their odd-N neighbours and so fewer cases of linking transitions have been reported. Recently, the superdeformed bands in ^{134}Nd have been linked into the normally deformed level scheme allowing for the first time an opportunity to compare the decay of even-N and odd-N neodymium isotopes [Pet96]. In order to augment understanding of the decay process from superdeformed bands it is desirable to investigate other even-N neodymium nuclei. Analysis of the present data has revealed linking transitions between superdeformed band 1 in ^{132}Nd and the known level scheme.

The strongest sequence (band 1), consisting of thirteen transitions, feeds into the known (π,α)=(–,1) two-quasiproton sideband [Wad89] at the $I^{\pi} = 9^{-}, 11^{-}$ levels. The decay proceeds via a self-coincident pair of γ-ray transitions of energy 764 keV; gamma rays in coincidence with the self-coincident pair of 764 keV transitions are shown in Fig. 5.8, and a partial decay scheme defining the pathway from band 1 into the normally deformed states is shown in Fig. 5.9. The links define the excitation energy of band 1, and allow an estimate of the spin and parity to be made (the new structures are too weak for a meaningful angular correlation analysis to be performed on this data set). Band 1 feeds into an intermediate structure before decaying into the (–,1) band, via weak low energy (257 and 242 keV) and stronger high energy (807 and 908 keV) transitions. Assuming that no I $\rightarrow$ I+1 transitions are involved in the decay, suggests odd spins and negative-parity for these new structures including band 1. This assumption implies that the 242 keV and 257 keV transitions must be nonstretched magnetic dipole transitions, while the 807 keV and 908 keV transitions are stretched quadrupoles. Comparison of the γ-ray intensities of in-band and out-band transitions from a particular level allows estimates of the reduced transition strength $B(\sigma\lambda)$. Such estimates may be compared with typical experimental $B(\sigma\lambda)$ values to elucidate the likely multipolarity of the γ-ray. The experimental ratios $B(E1)/B(E2)$ and $B(M1)/B(E2)$ can be determined through the expressions

$$\frac{B(E1)}{B(E2)} = \left[\frac{1}{1\times10^{6}}\frac{1}{\lambda_{in/out}}\frac{E_{\gamma}(in)^{5}}{E_{\gamma}(out)^{3}}\right] fm^{-2}, \tag{5.1}$$

$$\frac{B(M1)}{B(E2)} = \left[0.697\frac{1}{\lambda_{in/out}}\frac{E_{\gamma}(in)^{5}}{E_{\gamma}(out)^{3}}\right] (\mu_{N}/eb)^{2}, \tag{5.2}$$

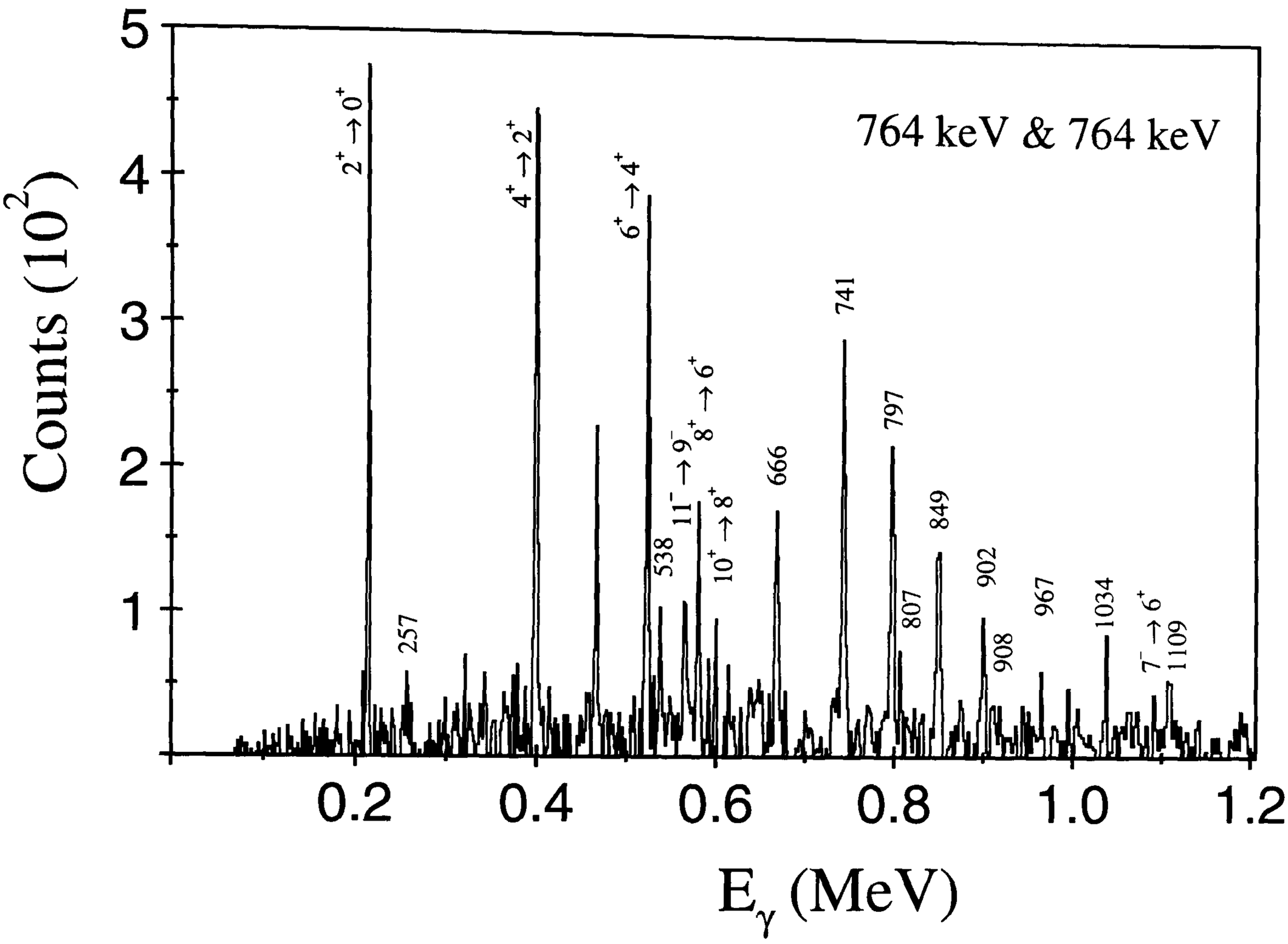

Figure 5.8: Double-gated spectrum showing γ rays in coincidence with the two self-coincident 764 keV transitions. The energies of of the transitions in band 1 are labelled in keV, together with linking transitions, while the known low-lying transitions in ^{132}Nd are labelled by their spins. Most of the unlabelled transitions correspond to the (–,1) band into the yrast band through intermediate structures, namely the (–,0) and γ-vibrational bands.

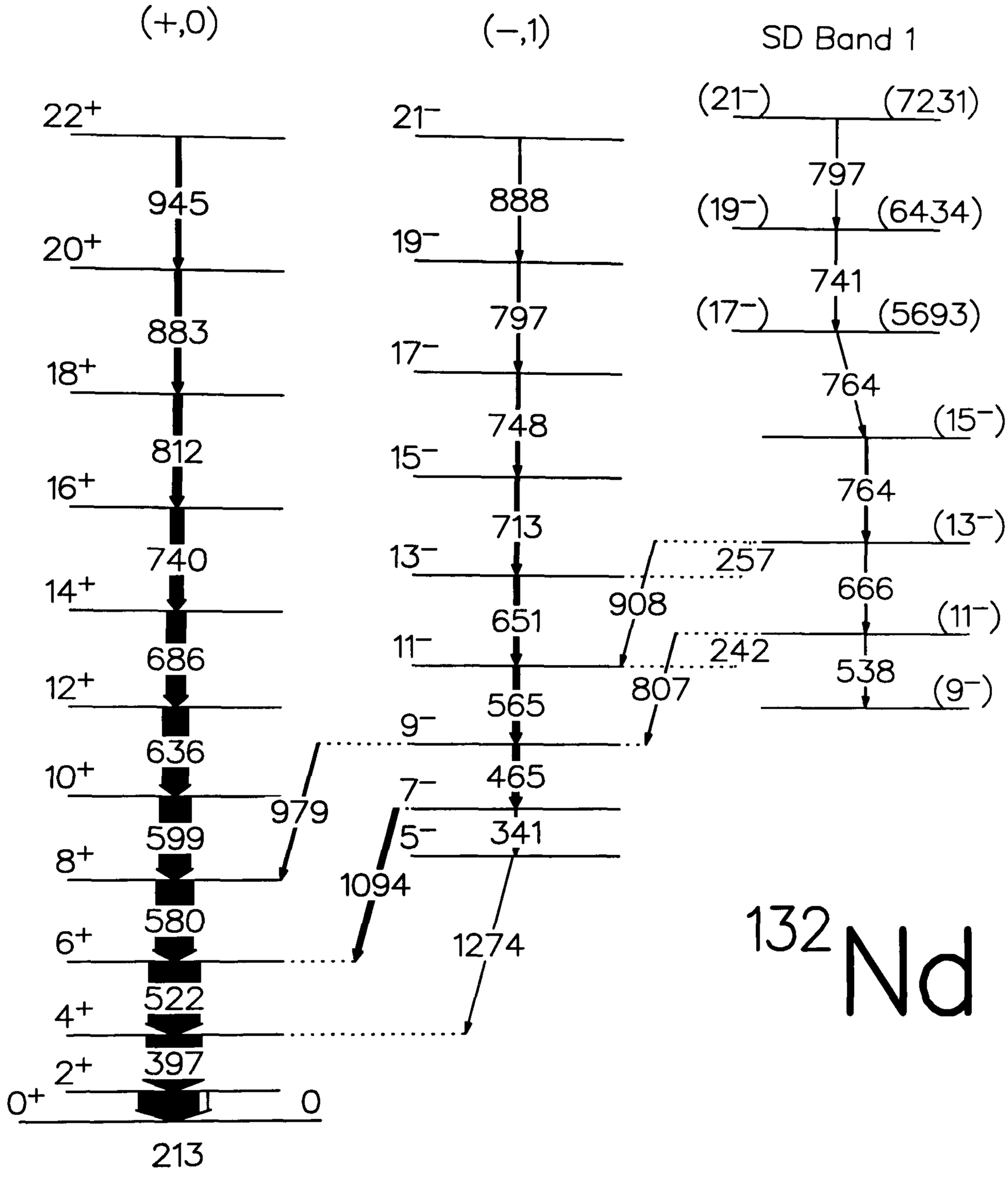

Figure 5.9: Partial level scheme showing the proposed decay path of SD band 1 into the known levels of ^{132}Nd. The transition energies and level energies are labelled in keV.

where E_γ is measured in MeV. The branching ratio is defined as

$$\lambda_{in/out} = \left[\frac{I_\gamma(in)}{I_\gamma(out)}\right] \tag{5.3}$$

where I_γ is the γ-ray intensity. Since the $B(E2)$ value can be calculated using Eq. 1.54 with a rough value for Q_t, reasonable estimates for the experimental $B(E1)$ and $B(M1)$ values can be obtained. The quadrupole moment is estimated as $Q_t \approx$6eb from comparison with TRS calculations and experimental lifetime measurements of the neighbouring isotopes [Mul92]. The $B(\sigma\lambda)$ values compared with the Weisskopf estimates are found to yield values for electric transitions at or above the recommended upper limit of $B(E1) \approx 10^{-2}$ Wu, while the magnetic values are estimated below the $B(M1) \approx$1 Wu limit. This implies that the low-energy linking transitions must have magnetic character. The bandhead of band 1 is thus tentatively assigned $I^\pi = (17^-)$ at an excitation energy $\approx$5.693 MeV. Fig. 5.10 shows an experimental rigid-rotor plot for band 1, using the assumed spins, compared with the normally deformed structures in ^{132}Nd. A rotating liquid-drop energy reference, equal to $(\hbar^2/2\Im_{rig})$I(I+1) MeV, has been subtracted. The rigid-body moment of inertia $\Im_{rig}$ has been normalised to ^{158}Er, [Sim94] such that

$$\left(\frac{\hbar^2}{2\Im_{rig}}\right) = 0.007\left(\frac{158}{A}\right)^{5/3} MeV, \tag{5.4}$$

where A is the mass number. Band 1 is seen to become yrast above I=30$\hbar$ where it crosses the (+,0) band which is in excellent agreement with the TRS calculations. The two weaker structures consist of eight (band 2) and ten (band 3) transitions, respectively. The decay paths of bands 2 and 3 could not be established, although unlike band 1, these bands are not in coincidence with the known negative-parity structures and decay directly into the positive-parity states of ^{132}Nd, at spin $I \geq 16\hbar$.

Investigation of the decay of neodymium isotopes seems to suggest that two principal mechanisms are responsible for depopulation. The decay from ^{133}Nd [Baz94], ^{134}Nd [Pet96] and ^{137}Nd [Lun95] has been interpreted in terms of small admixtures of normally deformed and superdeformed wavefunctions. Another proposal for the decay mechanism has been suggested by Deleplanque *et al.* for the decay of ^{135}Nd [Del95]. In ^{135}Nd there are no

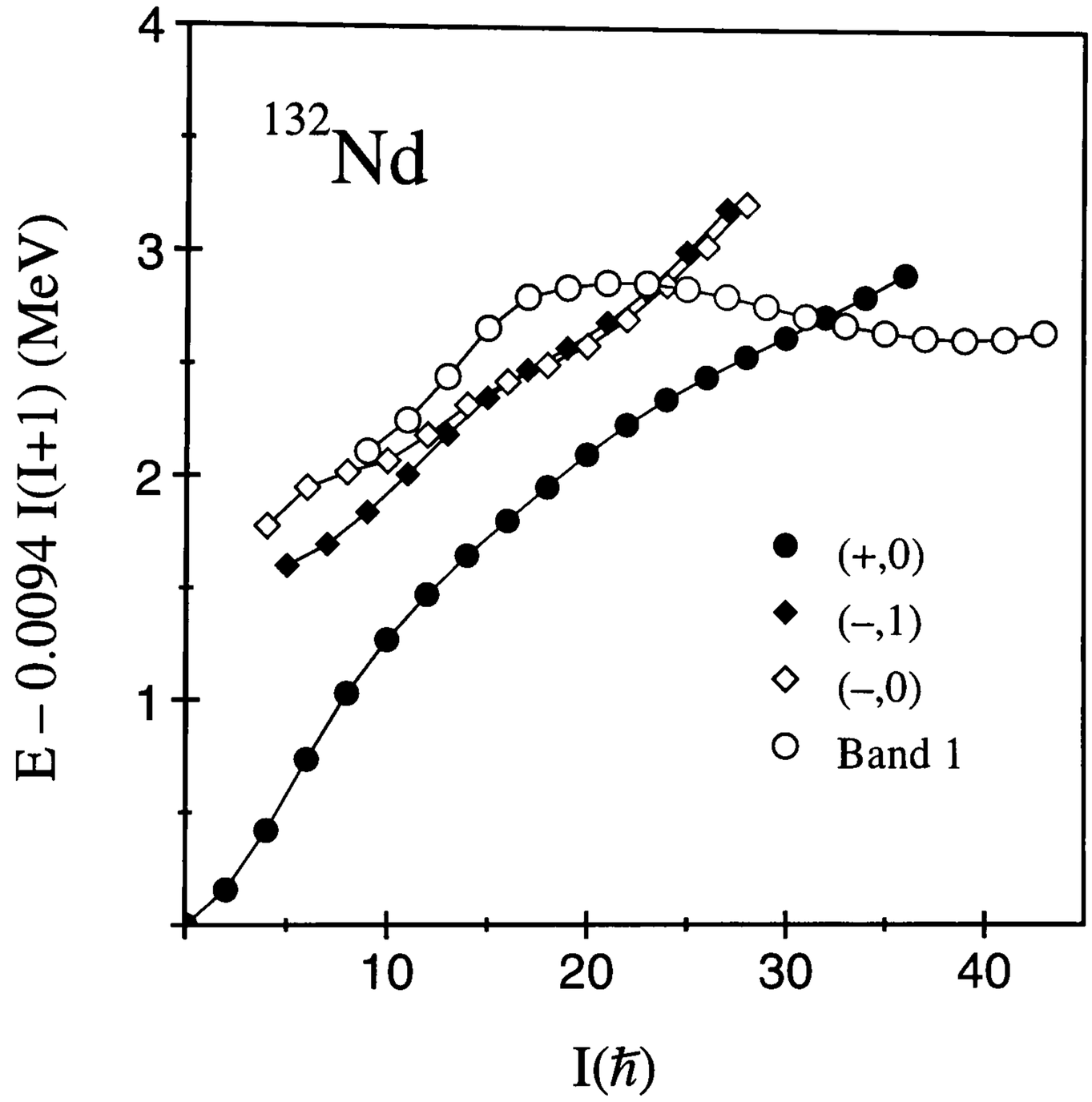

Figure 5.10: Rigid-rotor plot for band 1 and the normally deformed structures in ^{132}Nd.

accidentally close lying levels for normal-superdeformed mixing to occur. The superdeformed ^{135}Nd band is observed to abruptly end (terminate) and the intensity is fragmented through a number of discrete pathways. In this process the second minimum disappears due to shifting nucleons out of shape driving orbitals. It is also apparent that depopulating shape driving orbitals might trigger decay through mixing. For example, the decay of ^{134}Nd has been interpreted as mixing triggered by the crossing of $\nu i_{13/2}$ and $\nu d_{5/2}$ levels.

In all cases the disappearance of the second minimum appears to be related to the frequency at which the superdeformed band decays. TRS calculations detailed in [Lun95] and calculated for the odd-N neodymium nuclei are shown in Fig 5.11. It is clearly seen that that the barrier effectively disappears allowing a smooth transition to a different nuclear shape at the decay frequency. This is also true of superdeformed band 1 in ^{132}Nd. TRS contours displayed in Fig 5.12 calculated for negative-parity configurations in ^{132}Nd around the decay frequency clearly show the same effect as the second minimum evolves. The normally deformed prolate minimum gradually slides over to a more deformed well at $\hbar\omega \approx$0.3-0.4 MeV corresponding to the decay frequency from the $\nu i_{13/2} \otimes \nu h_{9/2}$ configuration. The Nilsson diagram pictured in Fig 5.1 shows that the N=72 shell closure is stabilised by the $\nu i_{13/2}$ and $\nu h_{9/2}$ intruder states. A probable interpretation for the decay mechanism is a low-spin band 'termination' where valence neutrons vacate the shape driving $\nu i_{13/2}$ orbital and occupy the N=4 $[402]5/2^+$ $d_{5/2}$ valence orbital. This is consistent with the change in total aligned angular momentum described in section 5.4.1. Since superdeformed band 1 is formed by neutron intruder configurations it also seems credible that the destruction of the second minimum is entirely due to vacating intruder states rather than invoking the mixing of neutron and proton states between normal and superdeformed wells.

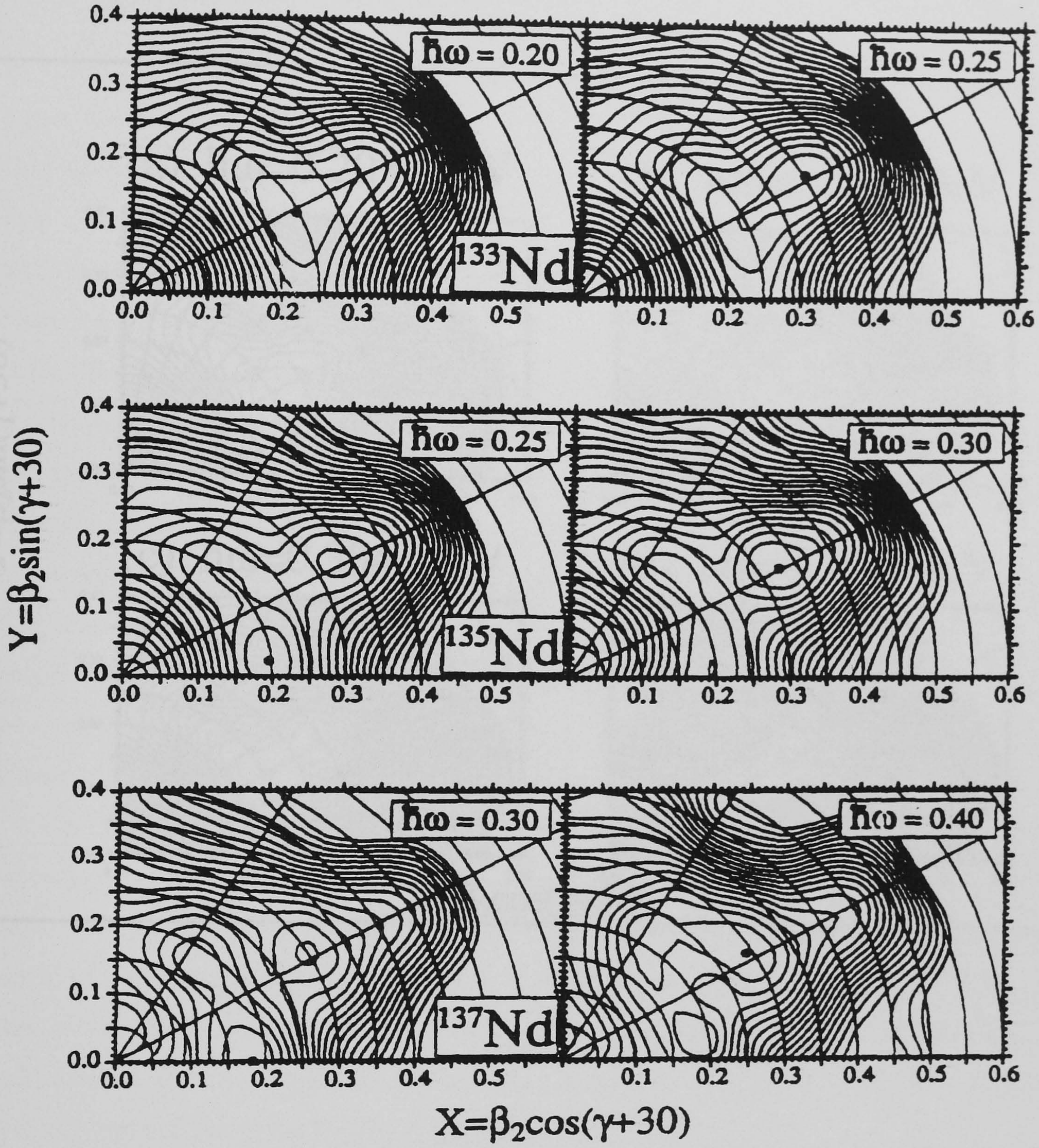

Figure 5.11: Total Routhian surface calculations for the lowest (π, α)=(+,+1/2) configurations for the odd-N neodymium isotopes taken from [Lun95]. The prolate minimum at β_2=0.30-0.36 is associated with the $\nu i_{13/2}$ configuration. At lower frequency a less deformed minimum appears associated with an odd neutron in an N=4 configuration.

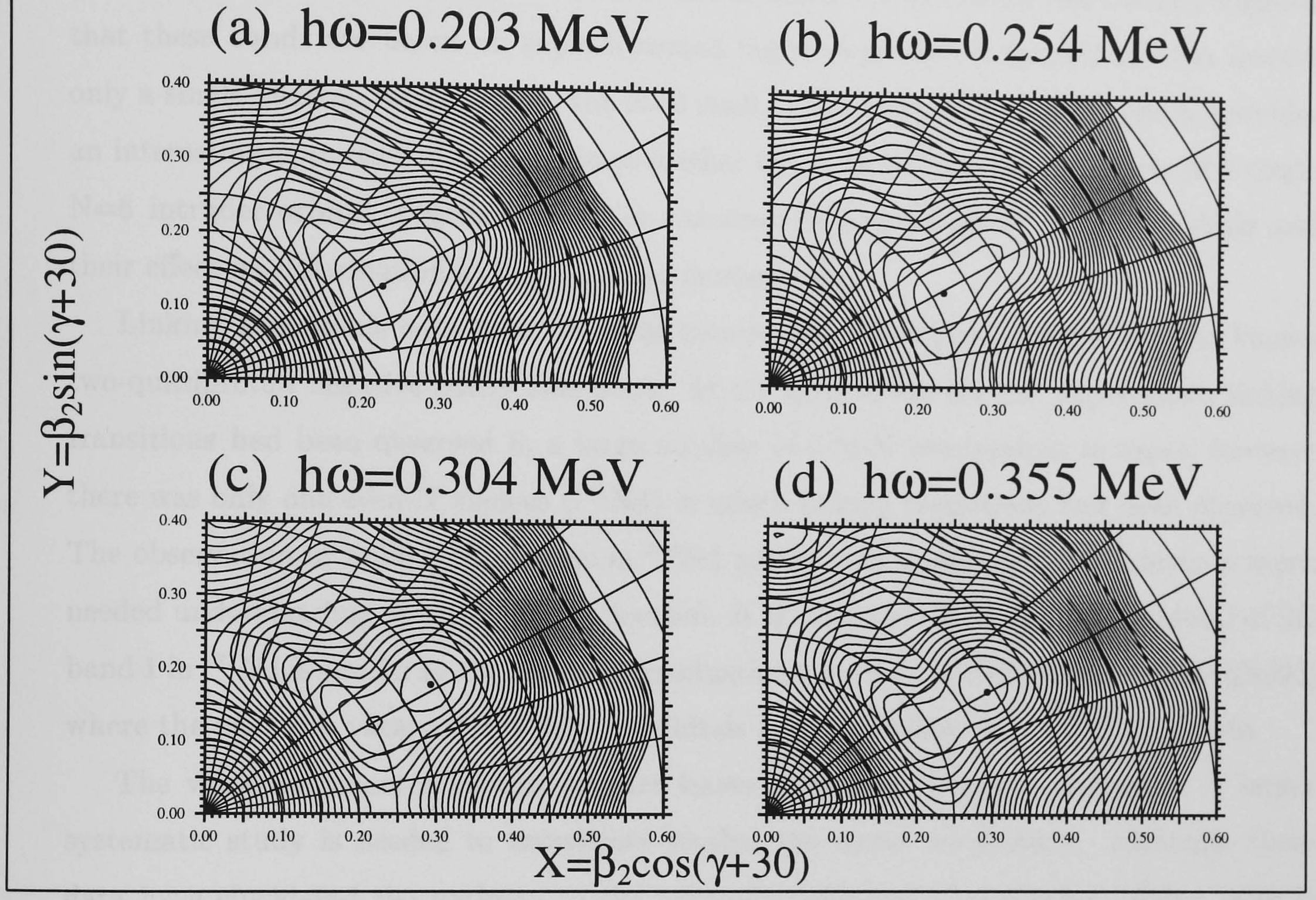

Figure 5.12: Total Routhian surface calculations for the lowest (π, α)=(−,1) configurations for ^{132}Nd. The prolate minimum at $\beta_2 \approx 0.25$ evolves into a $\nu i_{13/2} \otimes h_{9/2}$ configuration with $\beta_2 \approx 0.34$.

5.5 Conclusions and Future Prospects

In summary, three new bands have been observed in ^{132}Nd, with a population intensity below the 1% level. Comparison with TRS and cranked Woods-Saxon calculations suggests that these bands are based on superdeformed negative-parity configurations that involve only a single neutron intruder from the N=6 shell. The observation of these bands provides an interesting opportunity to investigate further the deformation-driving effects of a single N=6 intruder orbital, together with the character of normal-parity valence orbitals and their effect on deformation at high angular momentum.

Linking transitions have been observed between superdeformed band 1 and the known two-quasiproton negative-parity side-band. At the time of the present experiment, linking transitions had been observed in a large number of odd-N neodymium isotopes, however there was only one even-N nucleus (^{134}Nd) in which linking transitions had been observed. The observation of linking transitions in ^{132}Nd presents an opportunity to achieve a much needed understanding of the decay mechanism. It is concluded that the depopulation of SD band 1 in ^{132}Nd is similar to the low-spin termination proposed by Deleplanque *et al.* [Del95] where the neutrons vacate shape driving orbitals and destabilise the second minimum.

The work documented in this chapter leaves a number of open questions. A larger systematic study is needed to investigate further the decay mechanism. Although these data have elucidated the pathway to the normally deformed level scheme further work is needed to unambiguously define the electromagnetic nature of the linking transitions. Using the next generation of spectrometer arrays such as EUROBALL it may be possible to perform experiments with high counting statistics to determine the angular correlations and linear polarisations of the γ-ray linking transitions.

In addition to the three bands presented in this work, a recent experiment on the GASP array using the reaction ^{104}Pd(^{32}S, $2p2n$) at 160 MeV to populate high-spin states in ^{132}Nd has revealed two further SD bands [Pet97]. The configurations of these bands have been suggested to arise from coupling the N=4 $\nu d_{5/2}$ valence orbitals to a single $i_{13/2}$ intruder state. Total Routhian surface calculations predict that these bands have a lower deformation than the SD bands built on negative-parity configurations. The observation of the bands in this work and by Petrache *et al.* [Pet97] offer an exciting opportunity to investigate the role of specific non-intruder configurations in the deformation properties of the A$\approx$132

region. A thick-backed target experiment using the same experimental setup as detailed in this work has been performed recently to measure the relative deformations of these new structures. It is hoped that this data will provide further understanding of the deformation driving role of specific configurations in the A≈132 region.

References

[AF79] T.K. Alexander and J.S. Forster, in *Advances in Nuclear Physics*, edited by J. Negele and E. Vogt (Plenum, New York, 1979), Vol. 10, Chap.3

[And76] G. Andersson, *et al.* Nucl. Phys. **A268**, (1976) 438.

[AR95] A.V. Afanasjev and I. Ragnarsson, Nucl. Phys. **A591**, (1995) 387 .

[Bax92] A.M. Baxter *et al.* Nucl.Instr.Meth **A317**, (1992) 101.

[Baz94] D. Bazzacco *et al.* Phys. Rev. C. **49**, (1994) R2281.

[Bla66] A.E. Blaugrund, Nucl. Phys. **A88**, (1966) 501.

[BMP58] A. Bohr, B.R. Mottelson and D. Pines, Phys. Rev. **110**, (1958) 936.

[BR85] T. Bengtsson and I. Ragnarsson, Nucl. Phys. **A436**, (1985) 14.

[Bea95] C.W. Beausang *et al.* Nucl.Instr.Meth **A364**, 2 (1995) 560.

[Bro97] T.B. Brown *et al.* Phys. Rev. C. **55**, 2 (1997) R985.

[BS96] C.W. Beausang and J. Simpson, J. Phys. G. **22**, 2 (1996) 527.

[Cla95] R.M. Clark *et al.* Phys. Lett. B. **343**, (1995) 59.

[Cla96] R.M. Clark *et al.* Phys. Rev. Lett. **76**, (1996) 3510.

[Cur69] W.M. Currie *et al.* Nucl. Phys. **A134**, (1969) 325.

[Cwi87] S. Cwiok, J. Dudek, W. Nazarewicz, W. Skalski, and T. Werner, Comp. Phys. Comm. **46**, (1987) 379.

[Deh74] W. Dehnhardt *et al.* Nucl. Phys. **A225**, (1974) 1.

[Del95] M.A. Deleplanque *et al.* Phys. Rev. C. **52**, (1995) R2302.

[Dev96] M. Devlin, L. Sobotka, D.G. Sarantites and D.R. LaFosse. Nucl. Instr. and Meth. in Phys. Res. **A383**, (1996) 506.

[Dia95] R.M. Diamond *et al.* Phys. Rev. C. **41**, (1990) R1327.

[God89] M.J. Godfrey, Y. He, I. Jenkins, A. Kirwan P.J. Nolan, R. Wadsworth and S.M. Mullins, J. Phys. G **15**, (1989) L163.

[Gal94] A. Galindo-Uribarri *et al.* Phys. Rev. C **50**, (1994) R2655.

[Go94a] F.S. Goulding, D.A. Landis, N. Madden, M. Maier and H. Yaver, IEEE Trans. Nucl. Sci. **41**, (1994) 1140.

[Go94b] F.S. Goulding, D.A. Landis, N. Madden, M. Maier and H. Yaver, IEEE Trans. Nucl. Sci. **45**, (1994) 1145.

[Go94c] F.S. Goulding, D.A. Landis, N. Madden, M. Maier and H. Yaver, IEEE Trans. Nucl. Sci.

[GLN67] C. Gustafson, I.L. Lamm, B. Nilsson, and S.G. Nilsson, Arkiv Fysik **36**, (1967) 613.

[HW96] X. Han and C.Wu, Atomic Data and Nuclear Data Tables **63**, (1996) 1.

[Har97] D.J. Hartley *et al.* Phys. Rev. C. **55**, (1997) R985.

[Hau94] K. Hauschild *et al.* Phys. Rev. C. **50**, (1994) 707.

[Ha96a] K. Hauschild *et al.* Phys. Rev. C **52**, (1996) R2281.

[Ha96b] K. Hauschild *et al.* Phys. Rev. C **54**, (1996) 613.

[Hau95] K. Hauschild *et al.* Phys. Lett. B. **353**, (1995) 438.

[Hax49] O. Haxel, J. Hans, D. Jensen and H. Suess, Phys. Rev. **75**, (1949) 1766.

[He90] Y. He, M.J. Godfrey, I. Jenkins, A.J. Kirwan, P.J. Nolan, S.M. Mullins, R. Wadsworth and, D.J.G. Love, J. Phys. G: Nucl. Part. Phys. **16**, (1990) 657.

[Ing54] D.R. Inglis, Physics Review **96**, (1954) 1059.

[JK91] R.V.F. Janssens and T.L. Khoo, Ann. Rev. Nucl. Part. Sci. **41**, (1991) 321.

[Joh89] J.K. Johansson *et al.* Phys. Rev. Lett. **63**, (1989) 2200.

[Joh97] N.R. Johnson *et al.* Phys. Rev. C. **55**, (1997) 652 .

[Jos96] D.T. Joss *et al.* Phys. Rev. C. **54**, (1996) R969.

[Kir87] A.J. Kirwan, G.C. Ball, P.J. Bishop, M.J. Godfrey, P.J. Nolan, D.J. Thornley, D.J.G. Love and, A.H. Nelson, Phys. Rev. Lett. **58**, (1987) 467.

[Kir89] A.J. Kirwan, P.J. Bishop, D.J.G. Love, P.J. Nolan, D.J. Thornley, A. Dewald, A. Gelberg and K. Schiffer and, K.O. Zell, J. Phys. G: Nucl. Part. Phys. **15**, (1989) 85.

[Kno89] G.F. Knoll, Radiation Detection and Measurement, Second Edition, Wiley (1989).

[LaF95] D.R. LaFosse *et al.* Phys. Lett. B **354**, (1995) 34.

[LFM83] G.A. Leander, S. Frauendorf, and F.R. May, in *Proceedings of the Conference on High Angular Momentum Properties of Nuclei, Oak Ridge, 1982,* edited by N.R. Johnson (Harwood Academic, New York, 1983), p. 281.

[LVH70] K.E.G. Löbner, M. Vetter, and V. Hönig, Nucl. Data Tables **A7**, (1970) 495.

[Lee90] I.Y. Lee, Nucl. Phys **A520**, (1990) 641c.

[LSS63] J. Lindhard, M. Scharff and H.E.Schiott, Mat. Fys. Medd. Dan. Vid. Selsk. **33**, (1963) No.14.

[Lun95] S. Lunardi, R. Venturelli, D. Bazzacco, C.M. Petrache, C. Rossi-Alvarez, G. De Angelis, G. Bonsignori, M. Savoia, and, D. Vretenar, Phys. Rev. C. **52**, (1995) R6.

[Luo88] Y.X. Luo *et al.* Z. Phys. A **329**, (1988) 125.

[Ma87] R. Ma, E.S. Paul, C.W. Beausang, S. Shi, N. Xu and, D.B. Fossan, Phys. Rev. C. **36**, (1987) 2322.

[May49] M.G. Mayer, Phys. Rev. **75**, (1949) 1969.

[Mul92] S.M. Mullins, I. Jenkins, Y.J. He, A.J. Kirwan, P.J. Nolan, J.R. Hughes, R. Wadsworth and, R.A. Wyss, Phys. Rev. C. **45**, (1992) 2683.

[Mul93] S.M. Mullins, J. Nyberg, A. Maj, M.S. Metcalfe, P.J. Nolan, P.H. Regan, R. Wadsworth and, R.A. Wyss, Phys. Lett. **B312**, (1993) 272.

[New69] J.O. Newton, F.S. Stephens, R.M. Diamond, W.H. Kelly and D. Ward, Nucl. Phys. **A141**, (1969) 631.

[Naz85] W. Nazarewicz, J. Dudek, R. Bengtsson and I. Ragnarsson, Nucl. Phys. **A435**, (1985) 285.

[Nil55] S.G. Nilsson, Mat. Fys. Medd. Dan. Vid. Selsk. **29**, (1955) No 16.

[Nis97] D Nisius *et al.* Phys. Lett. B **392**, (1997) 18.

[NLD87] W. Nazarewicz, G.A. Leander, and J. Dudek, Nucl. Phys. **A467**, (1987) 437.

[NLW88] W. Nazarewicz, R. Wyss, and A. Johnson, Nucl. Phys. **A503**, (1989) 285.

[Nol85] P.J. Nolan, A. Kirwan, D.J.G. Love, A.H. Nelson, D.J. Unwin and, P.J. Twin, J. Phys. G: Nucl. Part. Phys. **11** (1985) L17.

[NBF94] P. J. Nolan, F.A. Beck and D.B. Fossan, Ann. Rev. Nucl. Part. Sci **45**, (1991) 561.

[Nya84] B.M. Nyakó *et al.* Phys. Rev. Lett. **52**, (1984) 507.

[OBr97] N.J. O'Brien *et al. to be published.*

[Pau97] E.S. Paul, Private communication (1997).

[Pet94] C.M. Petrache, S. Lunardi, D. Bazzacco, D. Bucurescu, G. De Angelis, C. Rossi-Alvarez, C. Ur and, R. Wyss, Phys. Lett. **B335**, (1994) 307.

[Pet96] C.M. Petrache *et al.* Phys. Rev. Lett. **77**, (1996) 239.

[Pet97] C.M. Petrache *et al. to be published.*

[Pfo97] J. Pfohl *et al. to be published.*

[Pol62] S.M. Polikanov *et al.* Sov. Phys. JETP **15**, (1962) 1016.

[Rad95] D.C. Radford, Nucl. Instrum. Methods. Phys. Res **A361**, (1995) 297. (1996) 418.

[Rag96] I. Ragnarsson, Acta Physica Polonica **27**, (1996) 33. (1996) 418.

[Reg90] P.H. Regan *et al.* Phys. Rev. C. **42**, (1990) R1805. (1996) 418.

[Reg92] P.H. Regan *et al.* J. Phys. G. **18**, (1992) 847. (1996) 418.

[San95] D. Santos *et al.* Phys. Rev. Lett. **74**, (1995) 1708. (1996) 418.

[Sar96] D.G. Sarantites, P.F. Hua, M. Devlin, L.G. Sobotka, J. Elson, J.T. Hood, D.R. LaFosse, J.E. Sarantites and, M.R. Maier, Nucl.Instr. and Meth. in Phys. Res. **A381**, (1996) 418.

[Sat96] W. Satula, J. Donaczewski, J. Dudek and W. Nazarewicz, Phys. Rev. Lett. **77**, (1996) 5182.

[Sch97] G. Schmidt *et al. to be published.*

[Sem95] A.T. Semple Ph.D, thesis, University of Liverpool (1995).

[Sem96] A.T. Semple *et al.* Phys. Rev. C. **54**, (1996) 425. (1996) 418.

[Sem97] A.T. Semple *et al. to be published*

[Sim94] J. Simpson *et al.* Phys. Lett. B **327**, (1994) 187.

[Str66] V.M. Strutinsky, Sov. J. Nucl. Phys. **3**, (1966) 449.

[Str67] V.M. Strutinsky, Nucl. Phys. A. **95**, (1967) 420.

[Sve97] C.E. Svensson *et al.* Phys. Rev. Lett. **79**, (1997) 1233.

[Twi86] P.J. Twin *et al.* Phys. Rev. Lett. **57**, (1986) 811.

[Wad89] R. Wadsworth, S.M. Mullins, J.R. Hughes, P.J. Nolan, A. Kirwan, P.J. Bishop, I. Jenkins, M.J. Godfrey, and D.J. Thornley, J. Phys. G. **15**, (1989) L47.

[War68] D. Ward *et al.* Nucl. Phys. **A117**, (1968) 309.

[War94] D. Ward *et al.* Proceedings of the Conference on Physics from Large γ-ray Arrays, Berkeley, Vol. 1 (1994), 4

[WM73] M.J. Weber and R.R. Monchamp, J. Appl. Phys., 4 44, (1973) 5495.

[WJ91] J.C. Wells and N.R. Johnson, "LINESHAPE: A Computer Program for Doppler-Broadened Lineshape Analysis," Report No. ORNL-6689 (1991).

[WS54] R.D. Woods and D.S. Saxon, Phys. Rev. **95**, (1954) 577.

[Wil95] J.N. Wilson *et al.* Phys. Rev. Lett. **74**, (1995) 1950.

[Wys88] R. Wyss *et al.* Phys. Lett. **B215**, (1988) 211.

[Zie95] J.F. Ziegler, *The Stopping and Ranges of ions in Matter*, (Pergamon, London. 1985), Vols. 3 and 5.